LBL-3529
c.1

MOLECULAR BEAM KINETICS

Richard Behrens, Jr.
(Ph. D. thesis)

November 1975

Prepared for the U. S. Energy Research and
Development Administration under Contract W-7405-ENG-48

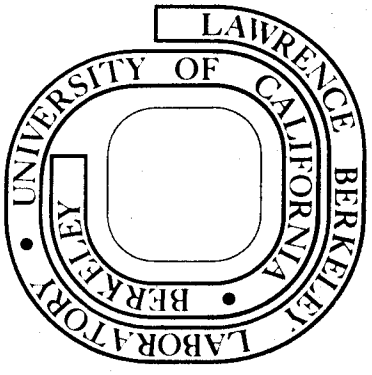

LBL-3529
c.1

DISCLAIMER

To my wife

and

my parents

MOLECULAR BEAM KINETICS

Contents

MOLECULAR BEAM KINETICS

Richard Behrens, Jr.

Inorganic Materials Research Division, Lawrence Berkeley Laboratory
and Department of Chemistry; University of California,
Berkeley, California

ABSTRACT

The design of a crossed molecular beam "supermachine" for neutral-neutral collisions is discussed. The universal electron bombardment ionizer, mass filter, and ion detection system of the detector, the supersonic nozzle sources, the differential pumping arrangement for the sources and detector, the time-of-flight detection of scattered products, and the overall configuration of the apparatus are described.

The elastic scattering of two systems, CH_4 + Ar and NH_3 + Ar, have been measured using the supermachine with two supersonic nozzle sources. The rainbow structure and the interference oscillations are seen in each system. The best fit to the data was found using a Morse-Spline-Van der Waals (MSV) potential. The three potential parameters ϵ, r_m, and β were found to be $2.20(\pm.04)\times10^{-14}$ ergs, $3.82(\pm.04)$Å, and $7.05\pm.20$ for CH_4 + Ar, and $2.21(\pm.04)\times10^{-14}$ ergs $3.93(\pm.05)$Å, and $8.45\pm.30$ for NH_3 + Ar.

A new phenomena in crossed molecular beams of condensation of a molecule on a cluster to form a complex was observed. A bromine molecule condensed on clusters of chlorine $(Cl_2)_\chi$ and ammonia $(NH_3)_\chi$. The value of χ for measurements in these experiments ranges from 7 to 40 for chlorine clusters and from 10 to 70 for ammonia clusters.

Angular and time-of-flight distributions are presented for detected ions ranging in size from $BrCl^+$ to $Br_2Cl_{10}^+$ for the $Br_2 + (Cl_2)_\chi$ system and from $Br(NH_3)^+$ to $Br_2(NH_3)_5^+$ for the $Br_2 + (NH_3)_\chi$ system. When the Br_2 forms a condensation complex with the cluster, the complex either lives long enough to reach the detector or fragments with a very small recoil velocity. Products have not been observed corresponding to the reaction of Br_2 with Cl_4.

I. INTRODUCTION

The field of chemical kinetics to many simply entails the determination of rate constants for a multitude of reactions. But to the true kineticist the interest extends past the measurement of reaction rates to the dynamics of the individual reactions themselves. The real interest lies in how the various chemical properties of different atoms or molecules will influence the dynamics of a particular type of reaction. Since the first measurement of an angular distribution in a crossed molecular beam experiment[1] in 1955, a tremendous amount of knowledge on the dynamics of chemical reactions has been learned from crossed molecular beam experiments.[2,3] The early crossed molecular beam neutral-neutral scattering experiments have been primarily confined to alkali reactions due to the ease with which alkalis can be detected by surface ionization techniques.

With the advent of the electron bombardment molecular beam detector[4] and a very clever arrangement of sources and vacuum pumps,[5] the field of crossed molecular beam chemical dynamics was extended from alkali reactions to reactions encompassing most of the elements in the periodic table. To perform the ultimate beam experiment,

$$A(n,v,J) + B(n',v',J') \rightarrow C(n'',v'',J'') + D(n''', v''', J'''),$$

where the electronic, vibrational, and rotational state of each reactant and product were known would require very intense beam sources and an extremely long length of time. A more realistic approach to a good crossed molecular beam experiment would have two well defined

beams with narrow velocity distributions and have the ability to determine the velocity of the scattered products. Knowing these two parameters along with the measured angular distribution as in more primitive experiments permits a much more detailed analysis of the kinematics of the reaction. The design considerations necessary to build a beam machine capable of doing these experiments and the description of the actual crossed beam apparatus, MBA-Kathy, is discussed at length in Chapter II.

One of the first projects undertaken on the new "supermachine" was the study of elastic and inelastic scattering of the hydride molecules, CH_4, NH_3, and HF, with Argon. Since the molecular beam "supermachines" have been able to produce high quality data on rare gas-rare gas intermolecular potentials from elastic scattering and good quality data on diatomic-rare gas systems such as N_2, O_2, HCl + Ar, it seemed reasonable to study the elastic scattering of a slightly more complex atom-molecule pair such as the hydride molecules. The hydride molecules with their large rotational spacings also provide good systems for the study of inelastic scattering by utilizing time-of-flight velocity analysis. However, due to the necessity to move the molecular beam apparatus from Berkeley only the elastic scattering of CH_4 and NH_3 with Argon has been studied up to the present time. The results from these experiments are presented in Chapter III.

Typically crossed molecular beam experiments have elucidated the mechanisms of bimolecular reactions. Recently, Lee et al.[6] have formed a complex with a fluorine atom and various olefin molecules and observed the unimolecular decay. Now that it is possible to form many interesting types of Van der Waals molecules,[7] it is feasible to study termolecular reaction kinetics in crossed molecular beams by looking at reactions such as particle growth initiation

$$ArHCl + NH_3 \rightarrow NH_4Cl + Ar \ ,$$

or atomic recombination

$$ArCl + Cl \rightarrow Cl_2 + Ar \ .$$

During the course of these studies on Van der Waals molecules King, Dixon, and Herschbach[8] published their results on the facile six-centered reaction

$$Br_2 + Cl_4 \rightarrow 2BrCl + Cl_2$$

where Cl_4 is the Van der Waals molecule. In trying to reproduce the experimental results of this reaction, a new complex was formed by the condensation of Br_2 on heavy chlorine clusters ($(Cl_2)_\chi$ where χ has a range of approximately 10 to 25). This condensation phenomena is described in Chapter IV along with possible future experiments with these clusters.

These two experimental studies are only a small fraction of the large number of studies that this molecular beam apparatus was designed to perform. They are in a way two experiments that deomonstrate the potential of this apparatus for doing many more interesting molecular beam experiments.

Chapter 1 References

1. E. H. Taylor and S. Datz, J. Chem. Phys. 23, 1711 (1955).
2. J. L. Kinsey, Ch. 6, MTP International Review of Science, Phys. Chem. Series One, Vol. 9, Chemical Kinetics, (Butterworth's, London, 1972).
3. J. M. Farrar and Y. T. Lee, Annual Review of Physical Chemistry, 1974.
4. G. O. Brink, Rev. Sci. Instr. 37, 857 (1966).
5. Y. T. Lee, J. D. McDonald, P. R. LeBreton, and D. R. Herschbach, Rev. Sci. Instr. 40, 1402 (1969).
6. a. J. M. Parson, K. Shobatake, Y. T. Lee, and S. A. Rice, J. Chem. Phys. 59, 1402 (1973).
   b. K. Schobatake, J. M. Parson, Y. T. Lee, and S. A. Rice, J. Chem. Phys. 59, 1416 (1973).
   c. K. Shobatake, J. M. Parson, Y. T. Lee, S. A. Rice, J. Chem. Phys. 59, 1427 (1973).
   d. K. Shobatake, Y. T. Lee, and S. A. Rice, J. Chem. Phys. 59, 1435 (1973).
7. S. E. Novick, P. B. Davies, T. R. Dyke, and W. Klemperer, J. Am. Chem. Soc. 95, 8547 (1973).
8. D. L. King, D. A. Dixon, and D. R. Herschbach, J. Am. Chem. Soc. 96, 3328 (1974).

II. APPARATUS AND EXPERIMENTAL CONSIDERATIONS

A. Introduction and Design Criteria

For the past twenty years beam machines have had many different configurations for studying elastic, inelastic, or reactive scattering on a large range of chemical systems. Early neutral beam studies were mainly concerned with the chemistry of the alkali metals since they can be detected with up to 100% efficiency using surface ionization techniques. Of course the limitation with surface ionization detection is that it can only be used for chemical systems involving the alkali metals and a few other metals with low ionization potentials. During the last 10 years a universal detector has been developed which has extended crossed molecular beam experimentation to chemical systems encompassing many more regions of the periodic table.

The main goal for the design of this "supermachine" was to make it as versatile as possible for studying either elastic, inelastic, or reactive scattering and to be able to study the widest range of chemical species as possible. In order for this goal to be attained there are several basic properties which the apparatus must possess. First, the machine must utilize a universal detector which will be able to detect any type of atom or molecule. Second, the detector must be able to scan as large an angular range as possible in the plane of the beams. Third, the beam sources should be as interchangeable as possible since for some experiments monoenergetic well collimated gas sources are needed, whereas, for others either a high temperature or discharge sources are needed. Fourth, the vacuum chambers must be made of a material that is strong enough to maintain

the geometric alignment of the beam and detector and is resistant to corrosion since many of the experiments will use corrosive chemicals. Fifth, the detector must be as sensitive toward scattered signal as possible. Last, the velocity of the beams and scattered species should be able to be determined. With the above criteria and the cognition of the fact that someone must be able to run this apparatus, the machine was designed.

In order to see where the emphasis should be placed for the most efficient design of the apparatus, it is necessary to look at how intense a signal can be expected for a given cross section. This signal must then be compared to various size background signals in order to determine what the background signal must be in order to see a signal after counting for a reasonable length of time.

For the purposes of this calculation, it is assumed that there are two beams of particles intersecting at 90° with fluxes I_{10} and I_{20}, cross sectional areas of A_1^1 and A_2 and beam widths w_1 and w_2 respectively. The number of particles scattered out of beam 2 (N) is

$$N = A_2 I_{20}(1 - e^{-n_1 w_1 Q}) \tag{1}$$

where n_1 is the number density of beam 1 and Q is the scattering cross section which is typically angle dependent but for this case is considered angle independent. For $n_1 w_1 Q \ll 1$ the number of particles scattered out of the beam is given by

$$N = A_2 I_{20}\, n_1 w_1 Q \tag{2}$$

The number of particles scattered into a solid angle Ω per second (S), assuming an isotropic distribution, is then

$$S = I_{20}\, A_2 n_1 w_1 Q\, \Omega/4\pi \tag{3}$$

or

$$S = I_{20}\, n_1\, QV\Omega/4\pi \qquad (4)$$

where V is the volume of the collision zone define by the intersection of the two beams.

Particles which pass through the collision zone but are not scattered will make up the background for this calculation, although, in practice a beam catcher can be used to pump a large portion of these particles out of the system before they can contribute to the background. In particular experiments, usually involving gases which constitute a large fraction of the atmosphere, there are other sources of background but they will not be considered here. The background will be determined by the number density at the detector. To a large extent this background will determine the configuration and the pumping requirements of the apparatus.

To get a rough idea of what the signal will be, a beam and detector geometry will be assumed and the signal calculated for various beam fluxes and cross sections given in Table II-1. The assumptions made for the calculations in Table II-1 are as follows: the collision zone volume is .015 cm^3; the signal is scattered isotropically and the detector subtends an angle of 1° by 1° or 9.69×10^{-4} steradians; the particles are detected 15 cm from the collision zone; and the velocity of reactants and scattered products is 4×10^4 cm/sec.

Since this apparatus will utilize a "universal detector", an electron bombardment ionizer is used which is a number density detector. Therefore, in designing the geometrical configuration and pumping requirements of the apparatus the scattered signal number density and the background number

Table II-1. Detector Signal & Background

	Beam 1 Intensity $\left(\frac{\text{Molecules}}{\text{cm}^2\text{-sec}}\right)$	Beam 2 Intensity $\left(\frac{\text{Molecules}}{\text{cm}^2\text{-sec}}\right)$	Cross Section $\left(\text{Å}^2\right)$	Scattered Products $\left(\frac{\text{Molecules}}{\text{sec}}\right)$	Scattered Number Density $\left(\frac{\text{Molecules}}{\text{cm}^3}\right)$
1	1×10^{15}	1×10^{15}	1	3.63×10^{4}	4.16
2	1×10^{16}	1×10^{16}	1	3.63×10^{6}	4.16×10^{2}
3	1×10^{17}	1×10^{17}	1	3.63×10^{8}	4.16×10^{4}
4	1×10^{18}	1×10^{18}	1	3.63×10^{10}	4.16×10^{6}
5	1×10^{19}	1×10^{19}	1	3.63×10^{12}	4.16×10^{8}
6	1×10^{20}	1×10^{20}	1	3.63×10^{14}	4.16×10^{10}

density at detector must be compared. If the sources are two supersonic nozzle sources, beam intensities listed in row 4 of Table II-1 give a conservative estimate of what the total number of scattered products should be. For sake of comparison, if the beam with intensities listed in Row 4 were put into a chamber with a 5000 1/sec. pump the background number density at the detector would be approximately 2.5×10^{10} molecules/cm^3. This number is nearly 4 orders of magnitude larger than the scattered product number density. This simple calculation illustrates the point that the detector must be isolated from the collision chamber and sources of background gas.

Before proceeding to the detailed description of the configuration of the apparatus, statistical noise, the main contributor to noise in most molecular beam experiments, should be mentioned. Using a universal electron bombardment detector will at best give an ionization efficiency of 0.1%. Looking at Table 4, it is apparent that at times the count rate could be several hundred counts per second but coupled with a time of flight system could be less than a few counts per second. At these low count rates the predominent source of noise will be the statistical variation in the number of counts.[1] In order to measure the background signal, one of the beams is modulated with a chopping wheel. The scattered signal can be obtained by measuring the signal with both beams on and then with one beam on and then subtracting the counts in the background channel from the counts in the signal plus background channel. If the counts per second of signal plus background is S and of background is B then in time t the noise N is

$$N = \sqrt{St + 2Bt} \qquad (5)$$

The signal to noise ratio (R) as a function of t is

$$R = \frac{St}{\sqrt{(S + 2B)t}} \tag{6}$$

or the counting time required for a given signal to noise ratio is

$$t = \frac{R^2(S+2B)}{S^2} \tag{7}$$

If S>B then t scales as S^{-1} and if S<<B then t scales as S^{-2}. To achieve short count times S and S/B should be as large as possible.

A large signal and signal to background ratio requires the use of intense beams, beam modulation, a good resolution mass filter to eliminate all background ions except the one of interest, a high efficiency detecter system, and extensive differential pumping.

Since the development of the universal detector over 10 years ago and through the development of new and better pumping techniques to obtain an ultra high vacuum, several groups have undertaken the construction of a molecular beam "supermachine". The basic criteria have been outlined here and further explanation can be found by Lee, et al.[1] The criteria for construction of the various machines are the same but the method of meeting them vary.

Several of the machines, including this one, are of similar design. The initial design by Lee, et al.[1] has been used by Grice[2] and us with various modifications. The design essentially consists of two stationary sources with differential pumping and rotating lid from which are suspended three differentially pumped chambers which house various parts of the detecter. Both source chambers and detecter chambers are housed in a large collision chamber which is pumped by oil diffusion pumps and cryogenic liquid nitrogen surfaces. The detecter chambers are pumped by ion pumps,

titanium sublimation pumps and a liquid helium pump. An apparatus of somewhat similar design by McFadden et al.[3] utilizes the same general configuration but extensive liquid helium pumping is used to trap each of the beams. One of the earlier "supermachine" designs is by Bickes and Bernstein.[4] Their design utilizes a round scattering chamber which contains the oven, a differentially pumped nozzle source and a detecter chamber pumped by a 4 inch liquid nitrogen baffled diffusion pump. They also use dual beam modulation and detect the scattered signal at the beat frequency. Their detecter utilizes the typical Paul mass filter but unlike the machines previously mentioned it utilizes the Weiss[5] type ionizer rather than the Brink[6] design.

Another configuration used by two other molecular beam groups (Blais and Cross[7,8] and Grosser and Haberland[9]) has the detecter in a stationary position and the beams moving around the collision zone. Machines of this type usually have reduced pumping speeds for gases that are not condensable and therefore are not as versatile as the previously mentioned machines. Both of these machines employ the Weiss type ionizer. Blais and Cross utilize a dual beam modulation technique. Grosser and Haberland have observed both in plane and out of plane scattering.

An apparatus for studying the $D + H_2$ reaction has been constructed by Geddes, Krause, and Fite.[10] Their apparatus is constructed with the usual differential pumping idea but with extensive use of liquid helium pumping to trap the hydrogen. Their apparatus also measures a velocity distribution using a phase detection technique. Geddes[11] has also used a similar apparatus to study the $O + CS_2$ reaction.

Even with these many machines now operational the new chemical systems that have been studied is relatively small which tends to accentuate the fact that molecular beam experiments are still extremely diffucult even with the advances of modern technology.

B. Vacuum Chamber Configuration

The vacuum chambers have been designed to utilize extensive differential pumping. The different vacuum chambers can be divided into three categories - the source chambers and collimation chambers which define the geometry of the parent beams, the main chamber where the collision between the two beams takes place, and the detector chamber which houses the various detector parts. The geometrical configuration is simply two beams crossing at an angle of 90° and the detector rotating about the collision zone in the plane defined by the beams. This is the best general arrangement for most experiments although for certain experiments it is better to have the detector rotate in a plane perpendicular to one of the beams.[9] The vacuum chambers were designed so the beams and detector could be as close as possible to the collision zone without sacrificing pumping speed or angular resolution. One of the main criteria in the design of the vacuum chambers was that the pumping speed be as large as possible for as many different parent species as possible. The last, and most difficult, problem was designing the parts with extremely close tolerances so as to have the beams and detector positioned accurately enough so as not to vary the relative geometry by more than .002 or .003 of an inch.

1. Source Chambers and Collimation Chambers

Although the source and collimation chambers have been designed to house various types of sources, their size and configuration were mainly

chosen so intense hypersonic nozzle beams could be used. The main criteria for the maximum intensity achievable from a nozzle source (see nozzle section of this chapter) is the speed that gas can be pumped away from the nozzle expansion region. To achieve a high pumping speed for non-condensable gases, the source chambers were designed to be pumped by 20 inch diffusion pumps. In order not to drastically reduce the pumping speed of a 20" diffusion pump, the source chambers also had to have a diameter of 20 inches.

The source chambers are constructed in two parts in order to facilitate aligning and working on the sources. One part, the inside source chamber, is bolted directly onto the main chamber and extends into the main chamber as shown in Figures II-1 and II-2. The inside source chambers slide into the two side chamber parts in the main chamber in such a way as to align the front face of these chambers with respect to each other and the detector. The nozzle source assembly is attached to the rear of the front face of these chambers as shown in Fig. II-2. The beam chopper-beam flag assembly bolts onto the front face of inside source chamber #1. Inside source chamber #2 has a beam flag assembly that bolts onto its front face. Both chambers also have an electrical feedthrough flange to bring power and signals in and out of the collimation chambers. The sloping portion of the inside source chamber near the lower front, shown in Fig. II-1, is necessary to increase the pumping speed between the volume downstream of the skimmer and upstream of the collimating slits and the NRC VHS 6 inch diffusion pumps.

The second part of the source chamber, the outside source chamber, is bolted on the top of a mobile stand so it can be rolled back and forth from the main chamber. This permits relatively easy access to the inside side chamber. An illustration of the outside side chamber is shown in Fig. II-3.

Figure II-1. Cross Sectional View of the Apparatus

1. Main chamber.
2. Collimation chamber #2.
3. Source chamber #2.
4. Detector chamber #1.
5. Detector chamber #2.
6. Ionization chamber.
7. Nozzle source #2.
8. Beam source #1.
9. Rotating detector lid.
10. Gate valve drive rod.
11. Detector gate valve.
12. Liquid nitrogen cooling reservoirs.
13. Rotating ring.
14. Rotating lid O-ring seal.
15. Kaydon KG350XPO 35 inch bearing.
16. Bearing retainer ring.
17. Tec-Ring seals #A-01926.
18. Ionizer
19. EAI Quad 250 quadrupole mass filter.
20. Quadrupole exit lenses.
21. EMI 9524S photomultiplier tube.
22. Pilot B plastic scintillator.
23. High voltage cathode.
24. Time of flight chopping wheel.
25. IMC time of flight motor.

Figure II-1 ((cont'd).

26. Access port.

27. Detector chamber 1 entrance slit.

28. Detector chamber 2 entrance slit.

29. Ionization chamber entrance slit.

30. Cold shield.

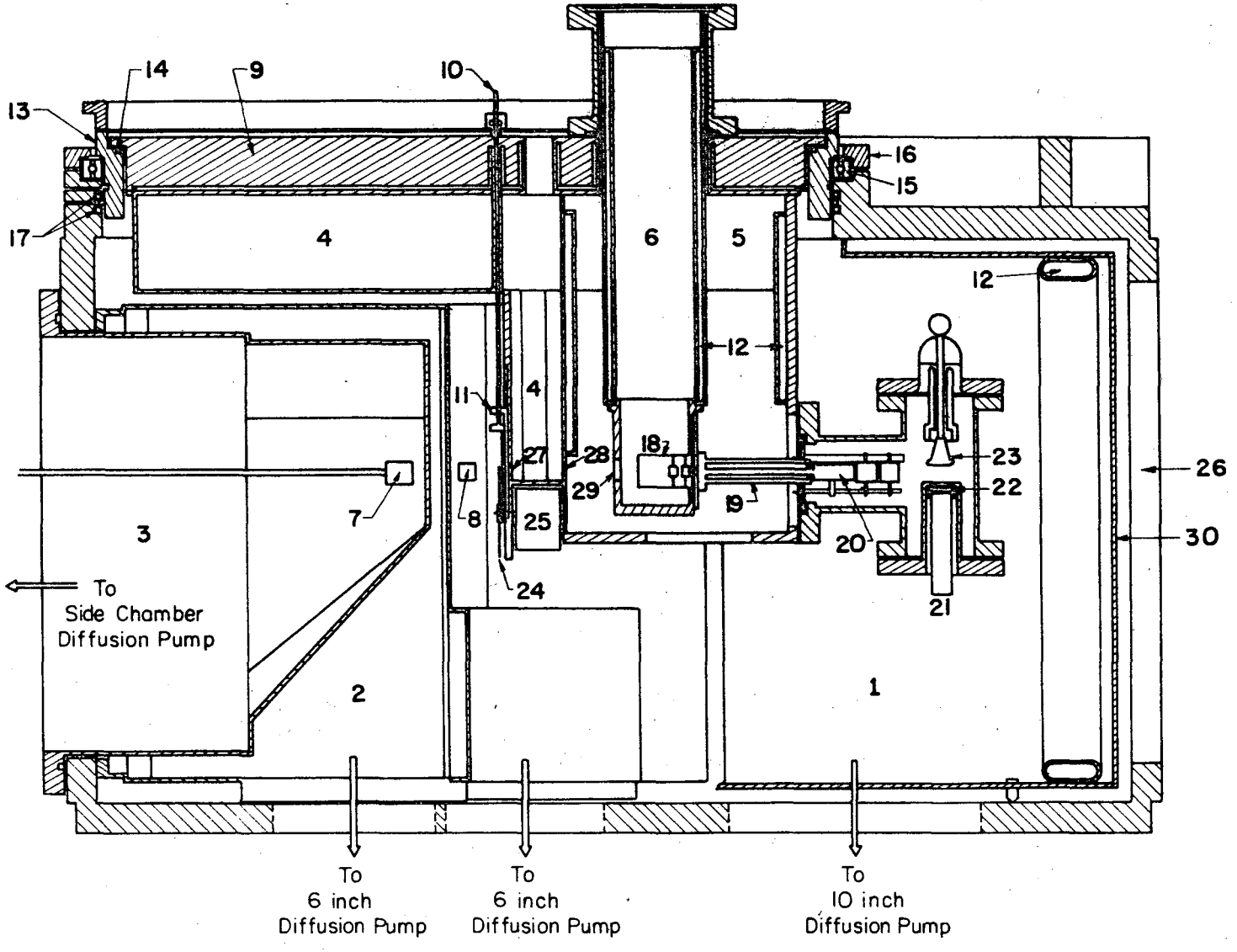

XBL 751-5449

Fig. II-1.

Figure II-2. Top Cross Sectional View of the Apparatus

1. Detection Chamber #1.
2. Detection Chamber #2.
3. Ionization Chamber.
4. Collimation Chamber 1.
5. Collimation Chamber 2.
6. Source Chamber 1.
7. Source Chamber 2.
8. Detector Chamber 1 entrance slit.
9. Detector Chamber 2 entrance slit.
10. Ionization Chamber entrance slit.
11. Beam 1 Collimating slit.
12. Beam 2 Collimating slit.
13. Skimmers
14. Nozzles
15. Heating or cooling fluid tubes.
16. Gas inlet.
17. Beam Flag 1.
18. Beam chopper.
19. Beam Flag 2.
20. Time-of-flight wheel.
21. Liquid nitrogen cooling.
22. Main Chamber.

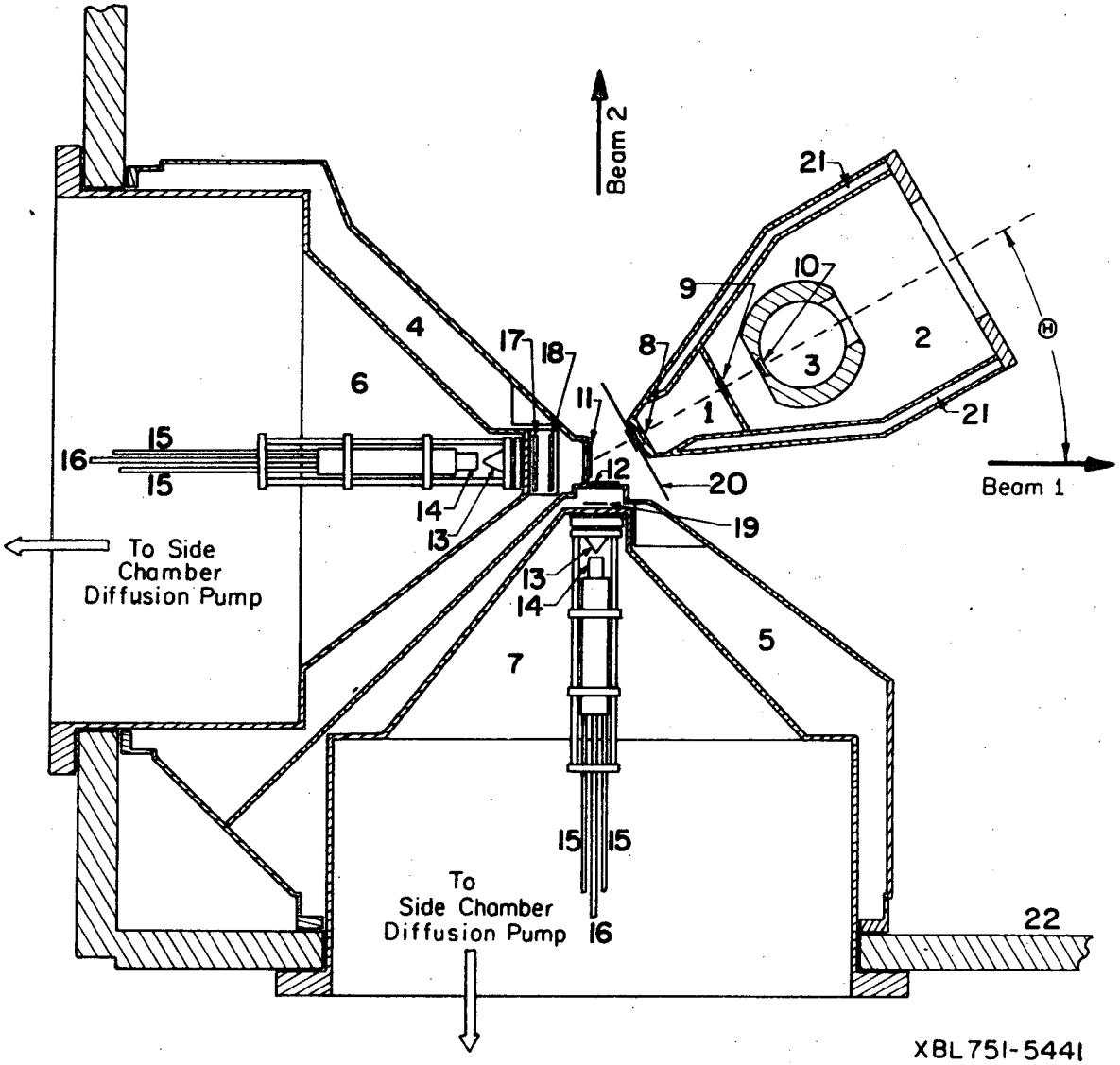
Beam 2
21
10
9
8
3
2
1
21
Beam 1
θ
4
17
18
11
6
15
16
15
12
20
14
13
19
To Side
Chamber
Diffusion Pump
13
14
5
7
15
15
To
Side Chamber
Diffusion Pump
16
22
XBL751-5441

Fig. II-2.

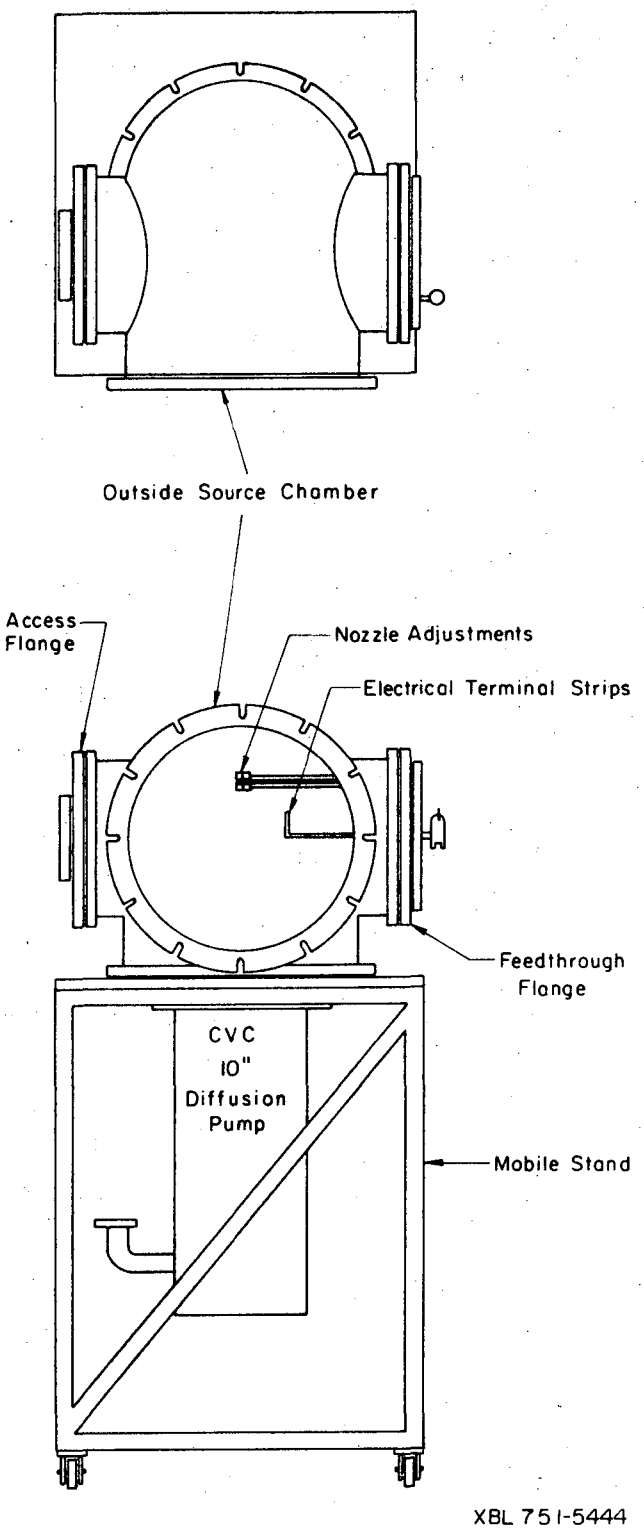

Fig. II-3. Outside Source Chamber.

The 24 inch diameter flange bolts into the main chamber through the inside source chamber flange. An O-ring seal is made between the outside and inside source chamber flanges. The outside source chamber also has two 16 inch flanges on opposite sides. One is for feedthroughs into the side chamber and the other is for access to the chamber to make final connections before pump down. The feedthrough flange configuration is shown in Fig. II-33. The chambers, although designed to use a Norton 20 inch diffusion pump, are now being operated with CVC 10" diffusion pumps which are bolted to the underneath side of the mobile stand. The two source chamber diffusion pumps are filled with Dow Corning 704 Silicon pump oil. The source chamber 1 diffusion pump is backed by the mechanical pumping combination of a Kinney KMB-230 Boostivac blower and a KDH-65 single stage mechanical pump. The source chamber 2 diffusion pump is backed by a Kinney KDH-80 mechanical pump. The pumping systems and interlocks for the side chambers are shown in block diagrams in Figs. II-5 and II-7. A detailed wiring schematic can be found on LBL blueprint #8S3175.[12] Specific wiring connections for terminal strips in each side chamber can be found in Appendix II-3.

The other chambers used in forming the beams are the two collimation chambers shown in Figs. II-1 and II-2. The collimation chamber is present for the sole purpose of differential pumping. In other words, if an atom or molecule passes through the skimmer hole from the source chamber into the collimation chamber and doesn't pass through the collimating slits and on through the collision zone, then it will get pumped out of the system through the collimation chamber diffusion pump before it can effuse through the collimation slits and into the main chamber. This reduces the number

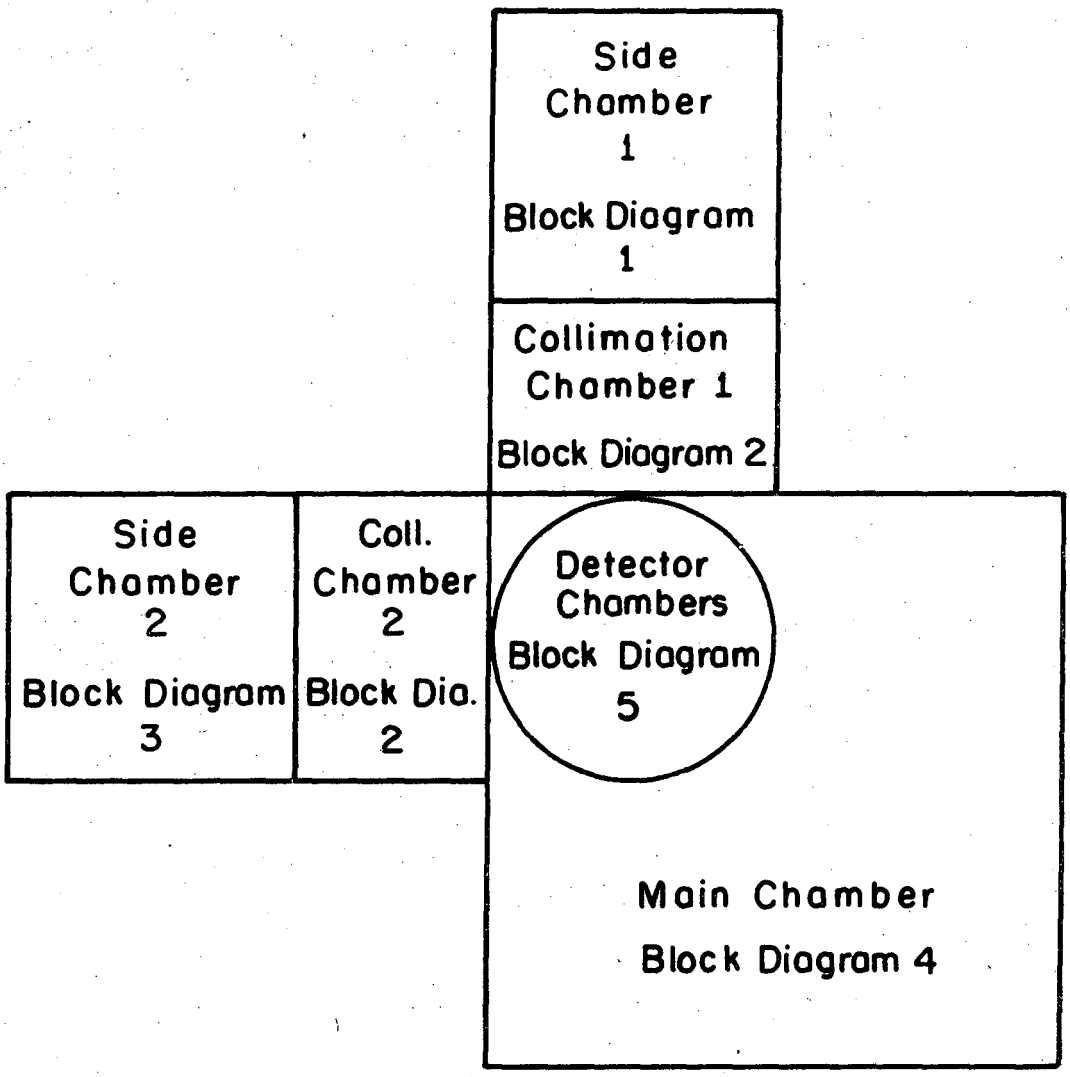

Fig. II-4. Block diagram location for various sections of the apparatus.

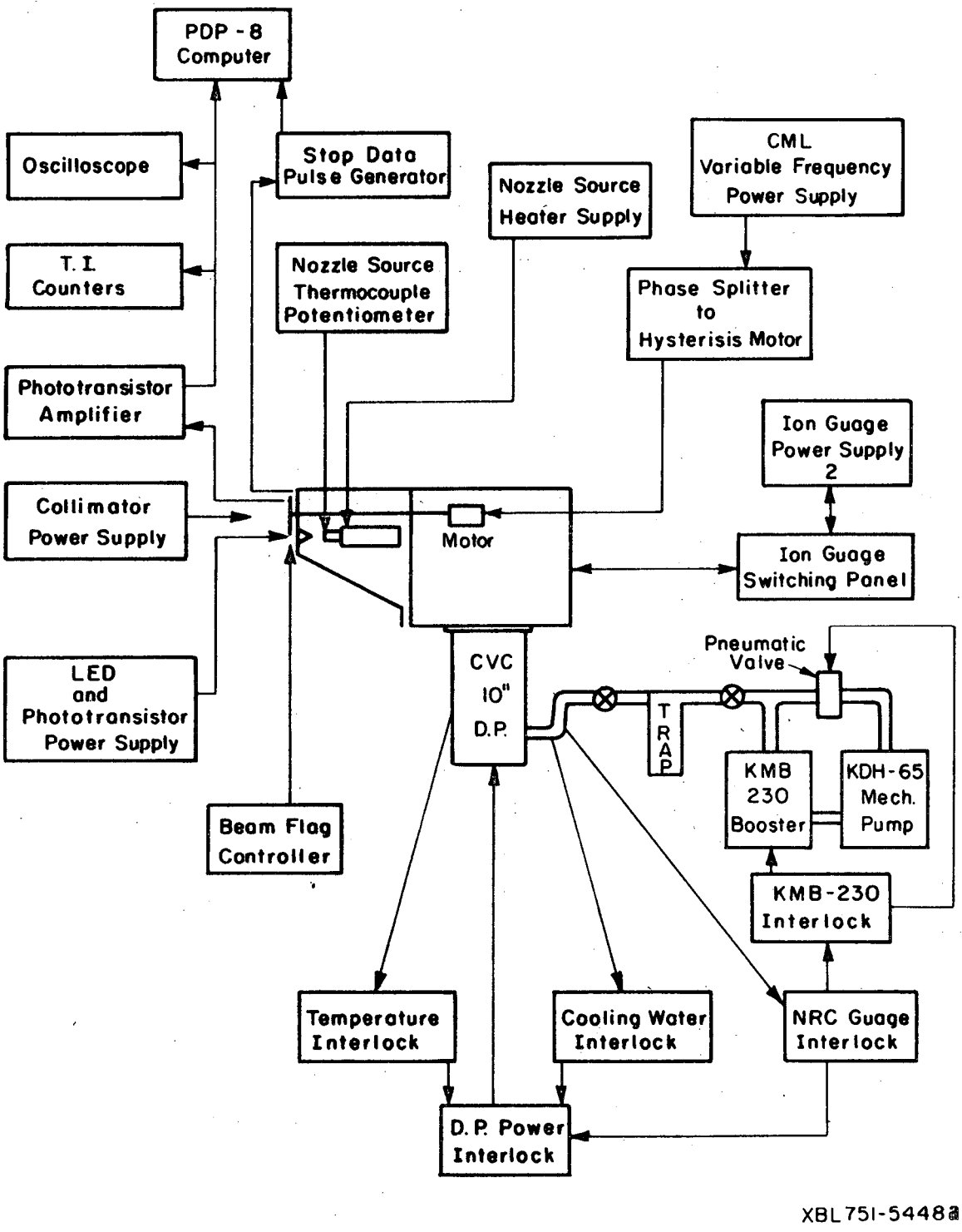

Fig. II-5. Block diagram 1 side chamber 1 electronics diagrams.

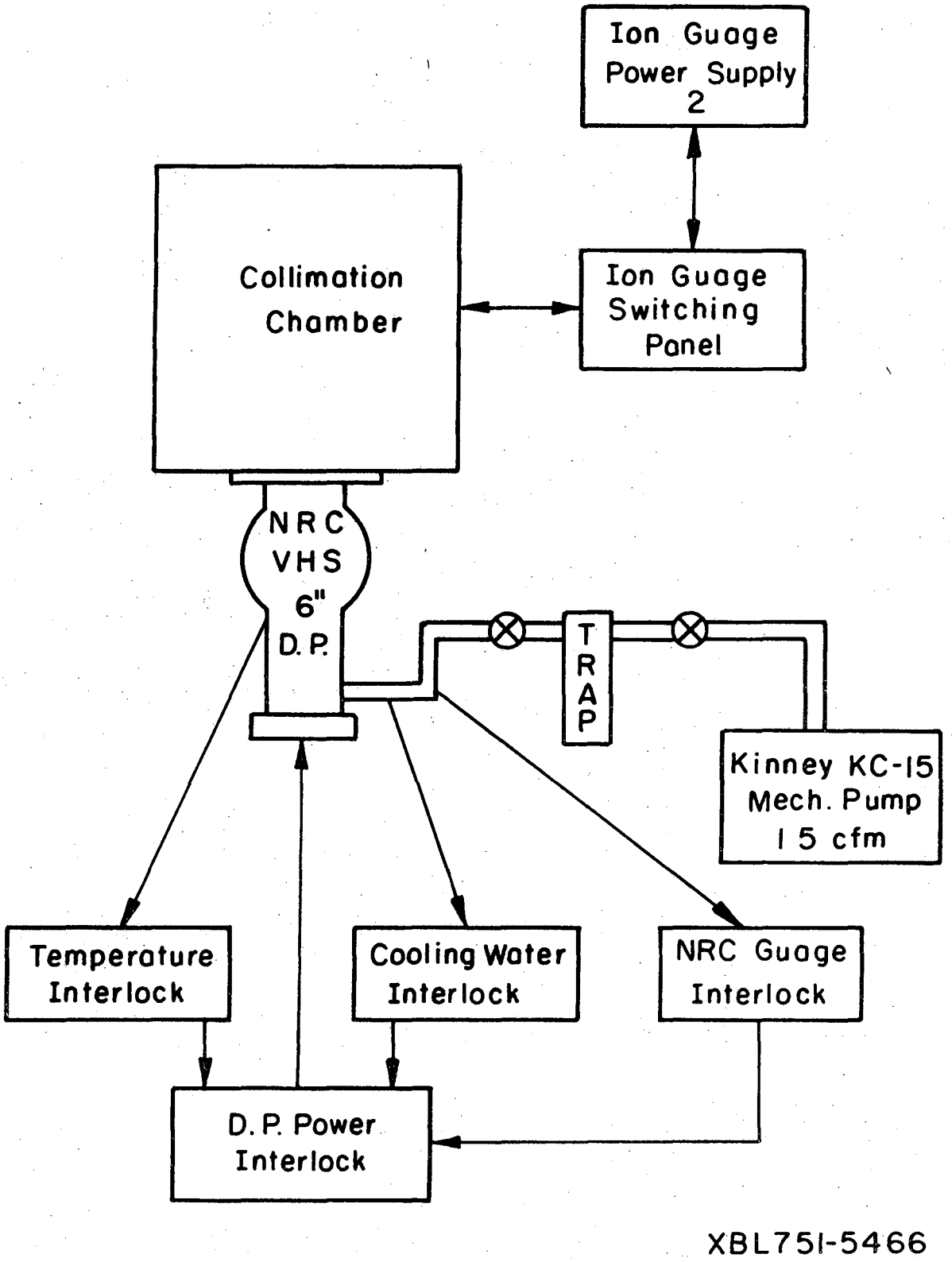

Fig. II-6. Block diagram 2 Collimation chamber electronics.

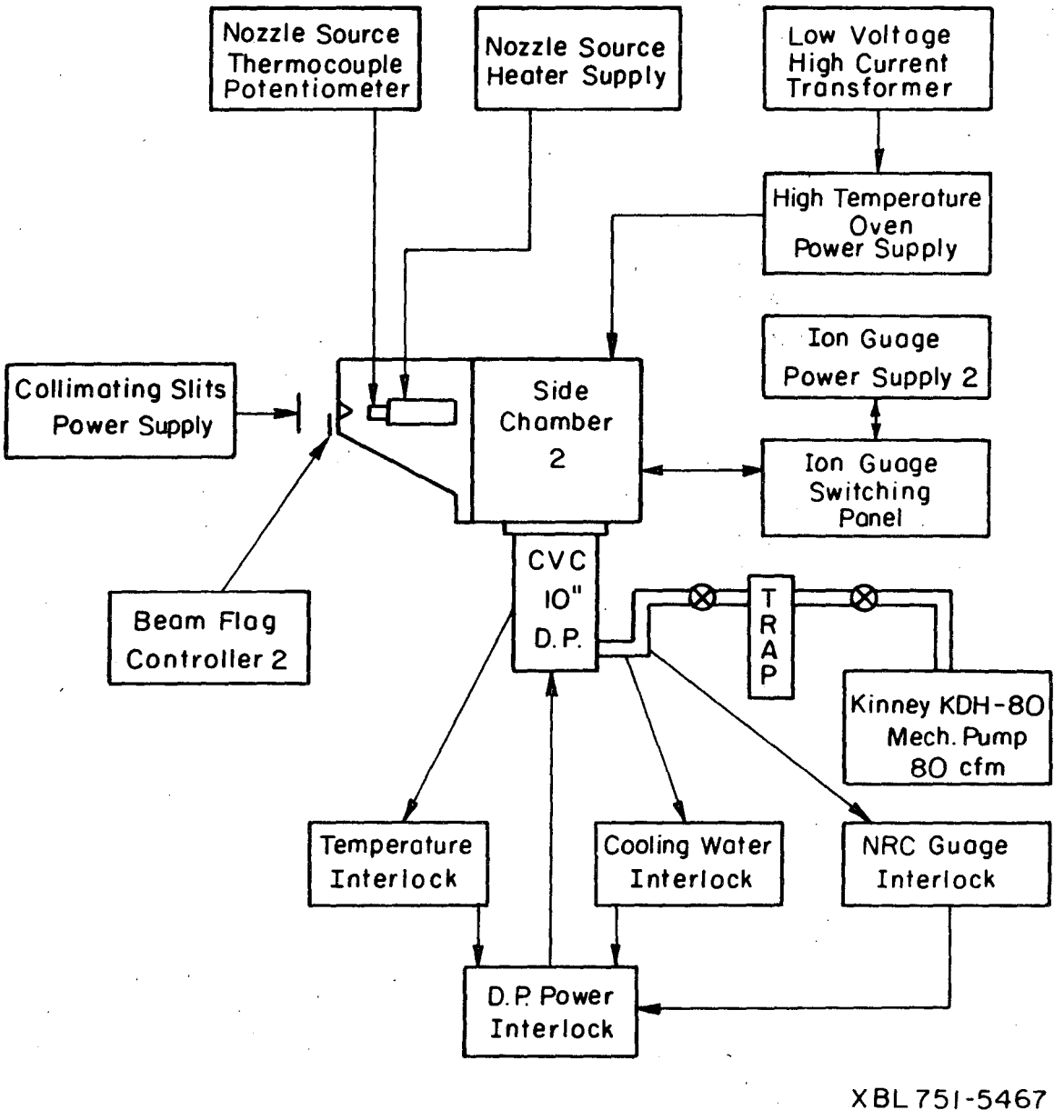

Fig. II-7. Block diagram 3 side chamber 2 electronics.

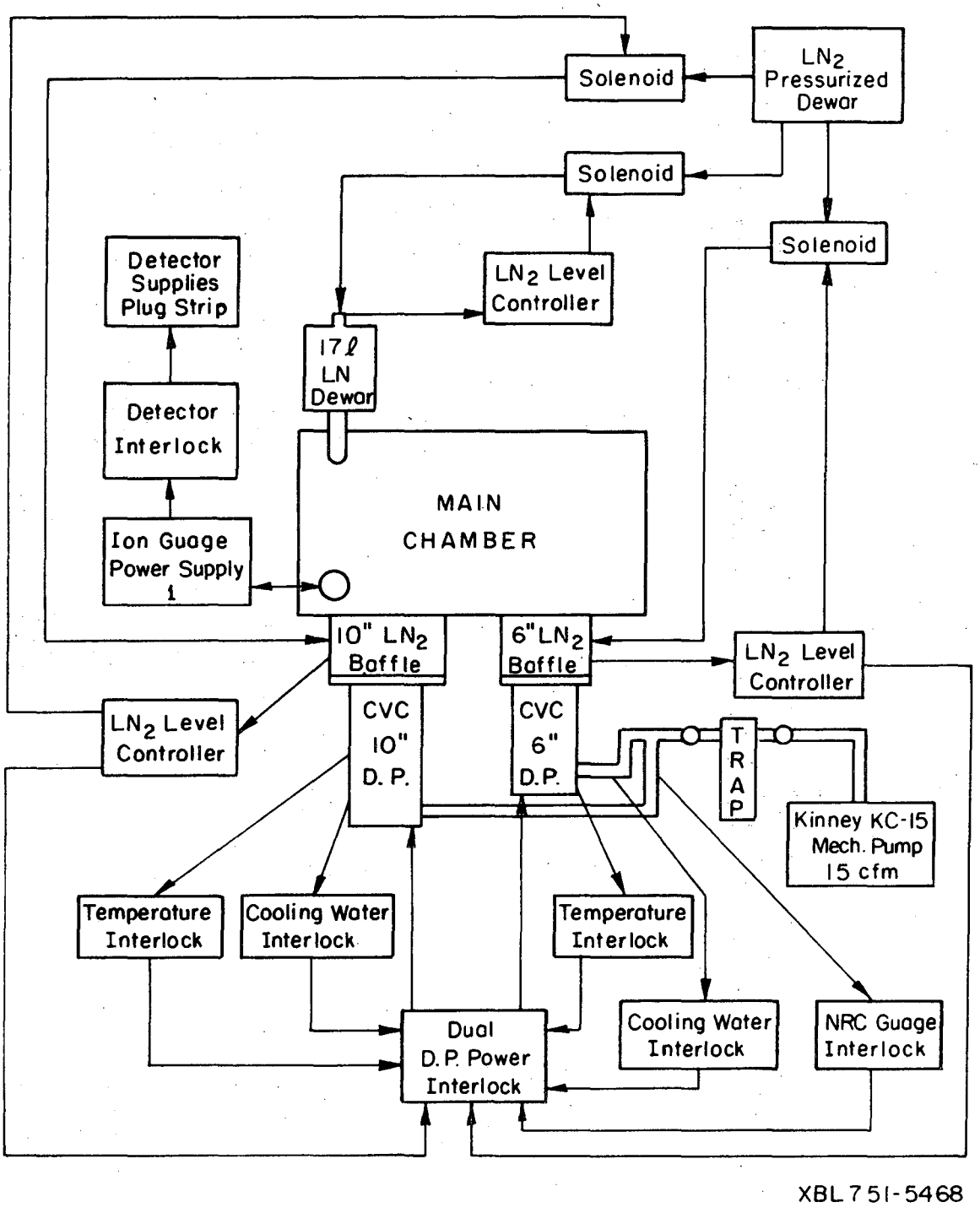

Fig. II-8. Block diagram 4 main chamber electronics.

Figure II-9. Block Diagram 5

1. Ultkek 150 1/sec Differential Ion Pump and Titanium Sublimation Pump.
2. Veeco 225 1/sec Mag-Ion Pump and E-Beam Titanium Sublimator Pump.
3. Veeco 100 1/sec Noble Gas Pump.
4. Janis Liquid Helium Pump.
5. 10 liter liquid notrogen dewars.
6. IMC Motor.

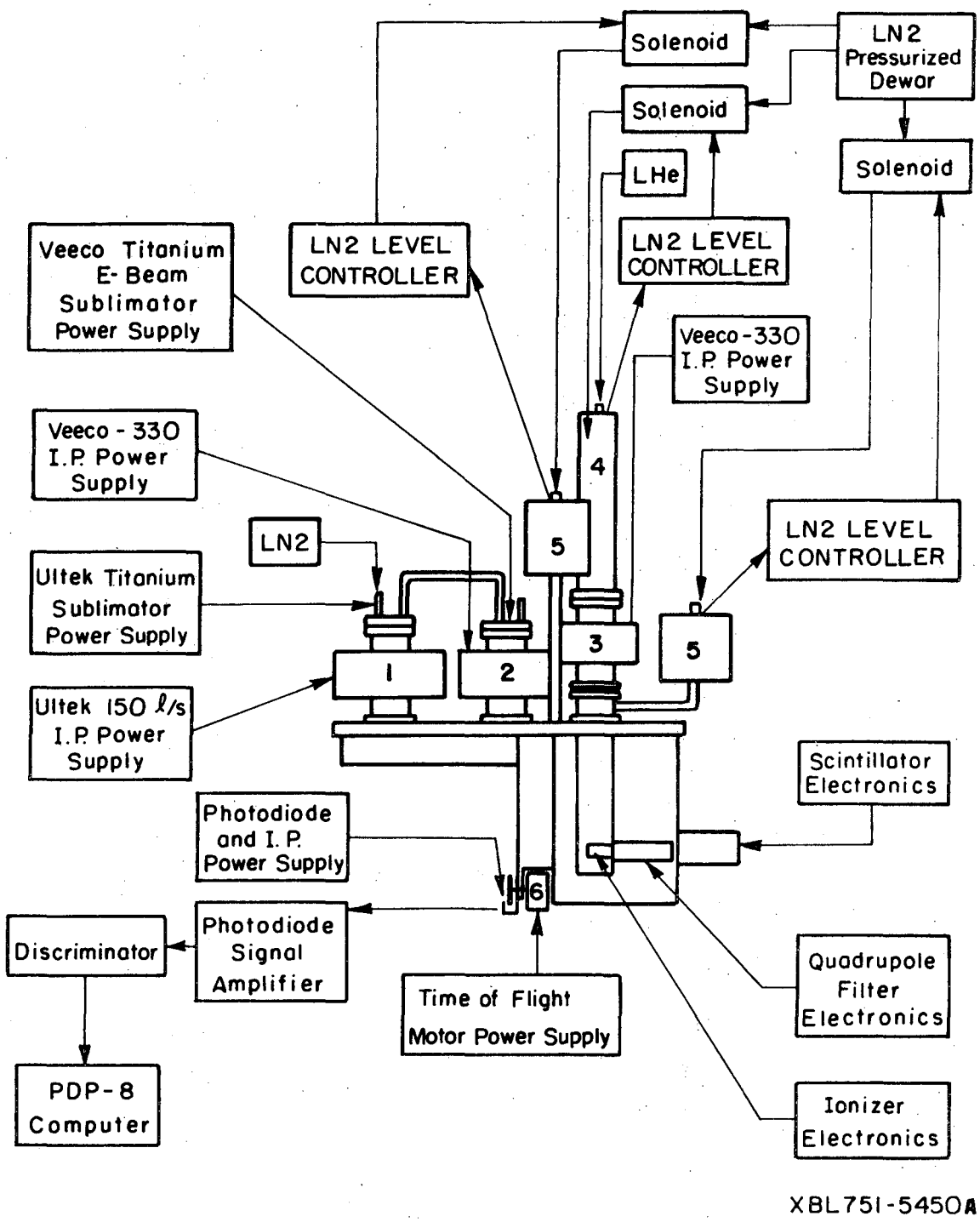

Fig. II-9.

of background molecules in the main collision chamber and ultimately the number of background molecules that can reach the detector. The two collimation chambers are both in one unit which must be the first chamber installed in the apparatus. Each collimation chamber is pumped by a NRC VHS-6 6 inch diffusion pump filled with a low vapor pressure silicon diffusion pump oil (Dow Corning 705) and backed by a Kinney KC-15 two stage mechanical pump. A block diagram of the pumping and interlock system is shown in Fig. II-6 and the detailed wiring schematic is in LBL blueprint #8S3175.

Two final points should be mentioned about the collimation chamber. First, the two cylindrical cutouts in each chamber are for the time-of-flight chopping wheel clearance. Second, there are two interchangeable sets of collimating slits which can be used. The exact dimensions and positions of the collimating slits will be given in another section. The collimating slits are put in place from the main chamber side of the collimation chamber. This makes alignment of the collimating slits quite simple (described in the apparatus alignment section of this chapter). The slits now made are sets of double collimation slits and collimation slits that can be heated but still installed from the main chamber side of the collimation chamber. (See Appendix II-1 for appropriate blueprints of the slits.).

2. Main Chamber Design

The main chamber of this molecular beam apparatus serves two purposes. First, it is the chamber in which the collision between the two beams takes place and second, and most important, it maintains the relative positions between the two sources and the detector. Since the collision zone is only about 0.2 cm wide, the main chamber must be able to maintain strict tolerances (.001 inch) between the source chambers and the detector chamber.

The size of the main chamber was indirectly determined by the size of the source chamber diffusion pumps, which were to be 20 inches in diameter, and the size of the rotating detector lid. The lid diameter was ultimately determined by the diameter of an obtainable bearing which in this case was 35 inches. The approximate dimensions of the vacuum chamber in order to accommodate these two items is 132 cm long, 130 cm wide, and 84 cm high.

In order to construct a vacuum chamber this size and still maintain its critical dimensions, the chamber was constructed from 304L stainless steel. Stainless steel was used instead of aluminum for two reasons: one, the stainless steel chamber can be made from thinner walls than aluminum since its strength and density are greater than aluminum; two, stainless steel can provide an ultimately cleaner vacuum system. The main chamber walls are 1 1/2 inch thick 304L stainless steel. This thickness is sufficient to maintain the required tolerances on all but the top (rotating detector) side of the vacuum chamber (see Fig. II-1). Due to the large opening necessary for the rotating lid and not wanting to make the top side out of an excessively thick plate of stainless steel, the chamber was constructed with three 1" × 3" strongbacks which skirt the outside of the rotating lid hole. Each strongback runs from one side wall to an adjacent side wall and is intermittently welded to the top 1 1/2 inch plate. The wall for the rotating ring assembly was made from a cast stainless steel ring and welded into the top plate. A detailed drawing of the main chamber may be found on LBL drawing #12N4126.

The main access to the apparatus is through one removable side flange. The bottom side has 5 port holes for diffusion pumps, 4 of which are now being used. Two holes pass through the bottom wall to pump the collimation

chambers when the apparatus is assembled, as shown in Fig. II-1. The other two diffusion pumps pump the main chamber itself. The main chamber pumps are a CVC-6 6 inch diffusion pump and a CVC-10C 10 inch diffusion. Both pumps are liquid nitrogen baffled. The 6 inch pump is baffled with a NRC 0326-6 liquid nitrogen long life trap and the 10" pump with a CVC BCN-101B liquid nitrogen baffle. Both diffusion pumps are backed by one 15 cfm Kinney KC-15 mechanical pump. The main chamber diffusion pumps are operated with Dow Corning 705 diffusion pump fluid. The pump system and associated electronics are shown in Fig. II-8. A diagram of the relative positions and orientation of the diffusion pumps is given in Appendix II-3.

The most critical part of the main chamber design is the rotating seal which allows the 35 inch detector chamber lid to rotate and still maintain a pressure in the main chamber of 1×10^{-7} torr. An overall assembly of the rotating seal and detector lid is shown in Fig. II-1 and a detailed cross section of the bearing, rotating ring, and O-ring are shown in Fig. II-10. The bearing used to support the rotating lid must be able to easily support the 15,000 lbs. of force which is exerted on the lid when the vacuum chamber is pumped out. The bearing used for this purpose is a Kaydon Reali-Slim type X ball bearing (Bearing Number KG350XPO).[13] The radial vacuum seal is made between the outer wall of the O-ring grooves in the main chamber and the outer radial surface of the rotating ring. Using a rotating ring for a sealing surface, rather than the outer radial surface of the rotating lid itself, facilitates the installation of sealing rings and removal of the rotating lid. The sealing rings are two special Tec-Rings made by the Tec Seal Corporation[14] (Seal #A01926). The Tec-Ring has

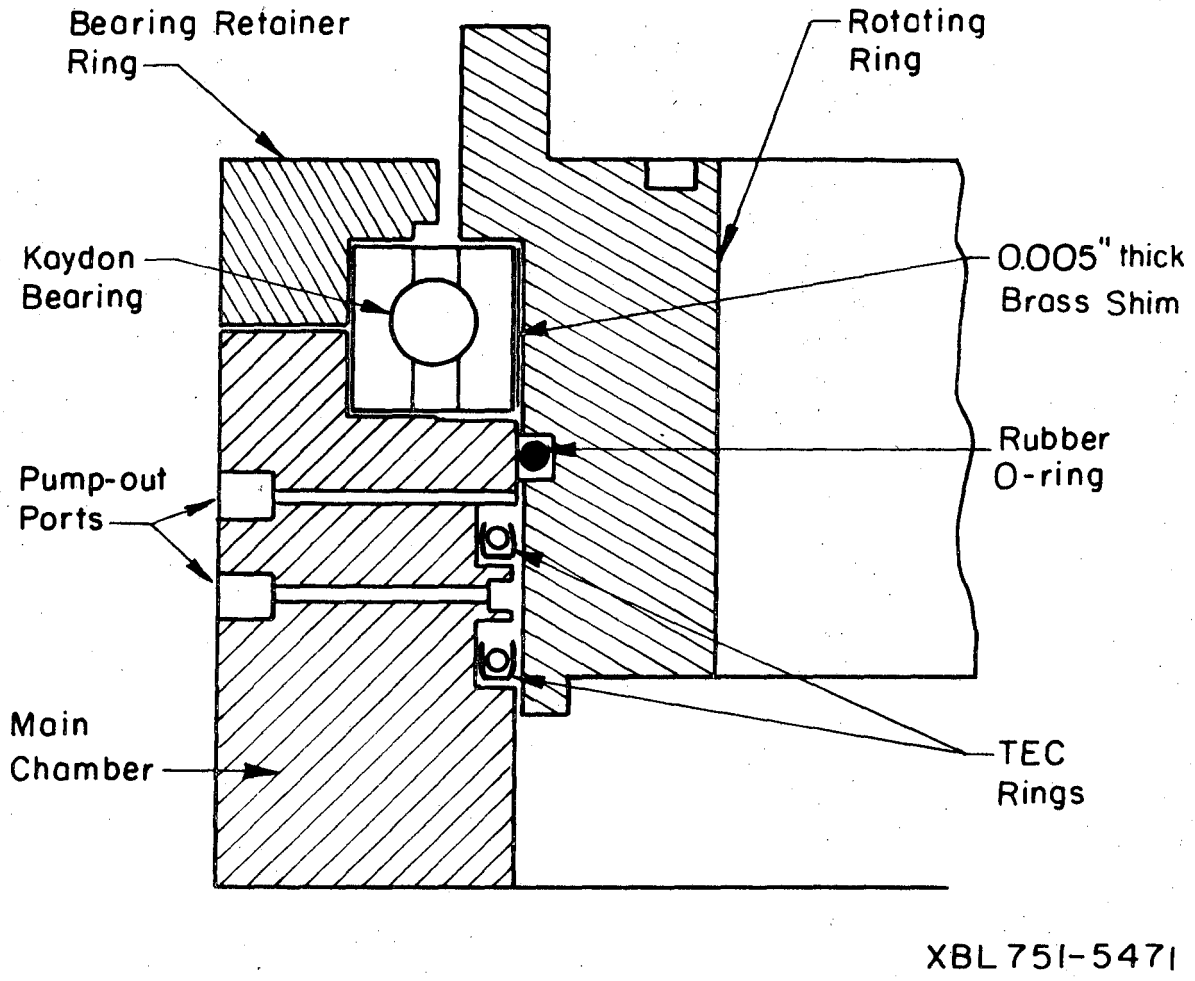

Fig. II-10. Cross sectional view of rotating ring seal.

a carbon inpregnated teflon sheath with a U-shaped cross section surrounding a coiled stainless steel expander spring which exerts a radial force that keeps the teflon sheath against the sealing surface as shown in Fig. II-10. It is necessary to use these teflon O-rings in order to reduce the turning friction of the seal. The rotating ring has an O-ring groove to accomodate an undersize rubber O-ring which keeps dirt and dust from getting into the Tec-Ring Seals. The main chamber rotating ring sealing area contains a smaller groove between the two Tec-Ring grooves. This groove is connected to the part of the vacuum system pumped by the main chamber mechanical pump. The pressure between the Tec-Rings is less than 0.1 torr so that any leak in either O-ring will only produce a minute leak into the main vacuum chamber. At present there is no measurable rise in pressure in the main chamber when the lid is rotated. The following is a list of the specifications for the Tec-Rings:

Gland Dimensions:

Inner Diameter = 34.993 inches

Outer Diameter = 35.469 inches

"W" Dimension = 0.238 inches

"D" Dimension = 0.375 inches

Since many experiments are run with condensable gases the main vacuum chamber contains a liquid nitrogen cooled nickel plated copper cold shield. The cold shield is made of 3/16" thick OFHC copper plates and is supported from the bottom of the main chamber by three needle point stainless steel screws to reduce heat conductivity. The shield is cooled by two U-shaped flattened copper pipe manifolds which are silver soldered onto the copper

cold shield plates. A cross section of part of the cold shield is shown in Fig. II-1 and a detailed drawing is shown on blueprint 12N4136. The liquid nitrogen reservoir for the cold shield is a Linde CR-17 gravity feed dewar located outside of the main chamber on a special feedthru shown in blueprint 12N4633.

Besides providing pumping for condensable gases the cold shield is designed to provide differential pumping by acting as a beam catcher. The cold shield has been designed with copper lips which extend from the cold shield to within 1/32 of an inch of the main chamber walls, thus, in effect, providing a separate chamber within the main chamber. There is a 10 inch hole in the bottom of the cold shield positioned over the CVC 10 inch diffusion pump. This diffusion pump pumps gas out of the main volume of the main chamber. The 6 inch CVC diffusion pump used to pump the main chamber is covered by the bottom plate of the cold shield and only pumps the volume contained between the outer wall of the cold shield and the inside wall of the main chamber. In the wall of the cold shield opposite each beam, there is a hole into which fits a stainless steel beam deflector. The beam deflector is simply a flange containing a hole which is the approximate size of the beam at the cold shield wall with a highly polished stainless steel wedge behind it to deflect molecules from the beam to behind the cold shield. These molecules are then more likely to be pumped out through the 6 inch diffusion pump than return to the main volume of the chamber.

3. Detection & Ionization Chamber

The detector and the vacuum chambers which house it are probably the most important parts of this apparatus. As shown in Section II-A, the

ability to see interaction with small cross sections depends on the total amount of scattered signal and the ratio of scattered signal to background signal. Both of these quantities can be maximized by the design of the detector itself and the latter can be maximized by a well designed vacuum and vacuum chamber system. Therefore, the detection chambers are designed to make maximum use of differential pumping.

The detection chamber system consists of three separately pumped vacuum chambers as shown in Fig. II-1. The detector parts (the ionizer, quadrupole mass filter, and exit lenses) are in a linear configuration which rotates about the collision zone in the plane defined by the two parent beams. Figure II-2 shows that there are three walls between the collision zone in the main chamber and the detector ionizer in the third chamber which is called the ionization chamber. Each wall contains an opening whose size depends on the particular angular resolution chosen. A detailed description of the slit dimensions is given in the alignment section of this chapter. The purpose of having three openings before the detector is to provide that the only atoms or molecules that will enter directly into the ionizer from the main chamber must have come from the collision zone and have been scattered at the angle for which the detector is set. The only other background molecules coming from the main chamber would have to be traveling in the direction of the narrow angle subtended by the ionizer slit. Background molecules, of course, can still enter the ionization chamber from detection chamber 2 but with sufficient pumping on each of the detector chambers this contribution is significantly reduced.

Another feature of this linear detector and detector chamber arrangement is its "fly-through" feature. Since an electron-bombardment ionizer, which

is only 0.1% efficient, is used in this apparatus most of the scattered product will not be ionized the first time it flies through the ionizer. To prevent this scattered product that is not ionized from building up in the region of the ionizer and contributing to the background, there is a hole in the back wall of the ionization chamber which permits any scattered atom or molecule that is not ionized to pass right through the ionization chamber and back into detector chamber #2. With sufficient pumping in chamber #2, only a small amount of the scattered product should reenter the ionization chamber.

In order to reduce the background of various types of scattered products three different kinds of pumps are used, plus liquid nitrogen cooling of the detector walls. Detector chamber #1 is pumped by an Ultek 150 liter/sec differential ion pump and a heated filament titanium sublimator pump with a liquid nitrogen cooled Cyro-shroud (Ultek #210-7020). Detector chamber #2 is pumped by a Veeco 225 liter/sec Mag-Ion pump (MI251) and an electron beam heated titanium sublimator (VeecoFH-270) with a liquid nitrogen cooled Cryo-shroud (Veeco SC-261). The ionization chamber is pumped by a Veeco 100 liter/sec noble gas ion pump (Veeco #PN-201) and a Janis 6 inch liquid helium pump (Janis No. 6CP). To further increase the pumping speed for condensable species the walls of all three detector chambers are liquid nitrogen cooled. A schematic diagram of the detector chambers and associated electronics is shown in Fig. II-9.

A cross section of the detector rotating lid and the ionization chamber is shown in Fig. II-1. The rotating detector chamber is supported by a 2 3/8 inch thick 304L stainless steel plate. This plate keeps the deflection of the lid after pump down to less than .001 inch. Detector

chambers 1 and 2 are suspended from this circular plate. The ionization chamber is a separate chamber that can be inserted through a hole in the rotating lid and down into detection chamber #2. The seal between the rotating lid and the ionization chamber and all seals to the detector chambers are copper gaskets between two Hall flanges. In order to form better weld joints all the vertical walls of the detector chambers are welded to a 3/16 thick stainless steel plate which in turn is welded to the 2 3/8 inch stainless steel plate. This 3/16 inch plate is suspended by a tube from each hole in the lid that goes into a detector chamber - which is seven tubes. The plate is also supported around its perimeter with small tabs welded between the 2 3/8 and 3/16 plates. The seven tubes were attached to the 2 3/8 plate by welding the end of the tube to a lip bored into each hole of the 2 3/8 inch plate.

Both detector chambers 1 and 2 are partially enclosed by a double wall jacket which holds liquid nitrogen. This keeps the entire chamber at liquid nitrogen temperature while an experiment is in progress. The walls that have liquid nitrogen cooling are shown in Figs. II-1 and II-2. A detailed drawing of this part can be found in blueprint # 12N4146.

Since large ion pumps are being used only the one on the ionization chamber is located directly over the chamber it is pumping. In order to connect detection chambers 1 and 2 to their respective ion pumps, the volume shown in Fig. II-1 that connects the two chambers is divided into two parts as shown by the dotted lines in Fig. II-29. The conductance of each of these volumes is sufficiently high so as not to drastically reduce the pumping speed of the ion pumps.

Detector chamber #1 has a 1 1/2 inch high vacuum flange immediately above it to provide access to this region which was needed for detector alignment. It also can accommodate a titanium sublimator pump to increase the pumping speed of detector chamber 1. Detector chamber 2 contains the two electrical feedthrough flanges. One is a 26 pin Ultek feedthru, and the other contains 3 high voltage feedthroughs for the quadrupole mass filter and an exit lens. The rear and bottom sides of detector chamber 2 each have a 5 inch ultra high vacuum flange seal. The rear flange mates to the exit lens - scintillator housing assembly and the bottom flange facilitates detector assembly.

The ionization chamber as mentioned before is removable from the detector chamber lid. This chamber is also double walled and liquid nitrogen cooled. The ionization chamber is shown in Fig. II-1 and in detail in blueprint #12N4724. The lower portion of the ionization chamber which houses the ionizer is constructed from a solid piece of OFHC copper which was silver soldered onto the double walled stainless steel part. The copper was silver soldered to the rest of the chamber before the final machining so as to obtain precise alignment between the ultra high vacuum flange and the opening in the copper. After final machining the copper portion was nickel plated. The rear opening in the copper piece is 2.001 inches by 4.126 inches. The ionizer plate on which the ionizer and the quadrupole are mounted is located in the correct position by these two dimensions. All of the collimating slits in the detector chamber are mounted in a similar manner.

The reason for machining larger precision holes in the detector chambers is twofold. First, since the detector chambers are all liquid nitrogen cooled it is difficult to accurately predict how far each chamber will move when it is cooled. Although the chambers should contract approximately .05 inch, it is difficult to calculate exactly, especially for detection chambers 1 and 2 because the length of liquid nitrogen cooling is not equal on all the walls. To solve this problem larger holes than necessary were made and measurements were taken to find out exactly how far each hole moved when the parts were cooled down to liquid nitrogen temperature. These measurements and also the size of the locating surfaces of the holes are listed in the alignment section of this chapter. The second reason for making the detector openings in this fashion is that it allows the angular resolution of the detector to be varied so as to accommodate the needs of a particular experiment. This has not been done to date since it requires the shut down and disassembly of the detector. This is not as prohibitive as it sounds since all the detector parts will automatically realign themselves when they are reassembled.

The detector chamber is also equipped with a gate valve which allows the detector to be shut off from the rest of the system enabling the detector to remain under vacuum while the rest of the apparatus is vented to atmosphere to be worked on. The gate valve and counter assembly are described in Appendix 3. The gate valve has one rectangular hole in it which is the beam defining entrance slit for looking at scattered signal and one smaller .003 inch diameter hole in it which is used for looking at the beams so as to prevent the unnecessary build up at background in the detector and also provide a narrow time of flight gate function. Both holes can be positioned

to better than .001 inch using the gear assembly and counter shown in Fig. II-36. The alignment procedure is in the alignment section of this chapter. The seal for the gate valve is made with a teflon Tec-Ring (#CR-012-CS-OF) with a stainless steel expander. There is no rise in detector chamber pressure when the rest of the apparatus is vented.

To estimate the effectiveness of the detector differential pumping, careful calculations must be made to estimate the total number of products scattered into the detector per second and the amount of background in the ionization chamber. Since this calculation is dependent on the parent beam geometry, the detector slit geometry and the angular resolution of the detector, it is located in the section of this chapter on alignment.

C. Beam and Detector Aperture Geometry and Alignment Procedures

This section will be divided into two parts. The first part will cover the detailed calculations for the angular resolution of the parent beams and the angular resolution of the detector. Also included in this part will be the effect of angular resolution on the number of particles scattered into the detector and the ratio of scattered signal to background signal in the ionization chamber. Finally, the effect of slight misalignments in various apertures will be examined and maximum misalignment dimensions will be tabulated. The second part of this section will discuss procedures for aligning the various parts of this molecular beam apparatus. Alignment of the detector chamber, detector slits and detector parts will be covered. Also the location of the center of rotation of the apparatus, the alignment of oven and nozzle sources, and the alignment of the parent beam collimating slits will be described.

1. Beam and Detector Geometry

The present geometrical configuration of the sources and detector are shown in Fig. II-11 and an exaggerated slit diagram is shown in Fig. II-12 in order to illustrate effects of misalignments.

The two criteria for determining the dimensions of the source slits and the detector slits are to obtain an angular resolution that is sufficient for an experiment and still get the maximum scattered signal, and to make the collision zone dimensions and the detector slit sizes such that there is no viewing factor.[15] The viewing factor is simply the fraction of the collision zone that the detector "sees" at different angles. To avoid having to correct for a viewing factor, the detector must be able to see all products scattered from the entire collision zone at the particular detector angle setting and within the angular resolution of the detector. Of course, experiments can be run while having a viewing factor but a suitable experimental correction factor must be obtained.[7,8,15] The angular resolution (Res) is defined here in laboratory coordinates as the sum of the two angles which represent the most deviant angle of scattered product from the collision zone when the detector is perpendicular to the widest part of the collision zone. This is shown as θ_R and θ_L in Fig. 12. The widest part of the collision zone occurs at the angle $\phi = \arctan \frac{W_1}{W_2}$. So the resolution of the apparatus is

$$\text{Res} = \theta_R + \theta_L \tag{8}$$

To obtain a realistic expression for the resolution, slit misalignment is included by specifying the actual slit width and the distance from the true beam axis to one side of each slit as shown in Fig. II-12. When a misalignment of either beam causes the colision zone to move closer to the

detector the resolution will get larger. Using the dimensions listed for Figs. II-11 and II-12, the resolution is given by

$$\text{Res} = \arctan\left(\frac{L + W_3 - W_{3L}}{d_1 + d_2 - C}\right) + \arctan\left(\frac{R + W_{3L}}{d_1 + d_2 - C}\right) \tag{9}$$

where

$$L = \sqrt{W_{2R}'^2 + (W_1' - W_{1L}')^2}\ \cos\left[\arctan\frac{W_1'}{W_2'} - \arctan\left(\frac{W_1' - W_{1L}'}{W_{2R}'}\right)\right] \tag{10}$$

$$R = \sqrt{W_{1L}'^2 + (W_2' - W_{2R}')^2}\ \cos\left[\arctan\frac{W_2'}{W_1'} - \arctan\left(\frac{W_2' - W_{2R}'}{W_{1L}'}\right)\right] \tag{11}$$

$$C = \sqrt{W_{1L}'^2 + (W_2' - W_{2R}')^2 - R^2} \tag{12}$$

These three variables just specify the position of the center of the misaligned collision zone from the perfectly aligned collision zone.

Now the dimensions of the umbra (W_{1L}, W_1, W_{2R}, W_2) and the penumbra (W_{1L}', W_1', W_{2R}', W_2') of the parent beams must be calculated for the various slit dimensions given in Figs. II-11 and II-12. The widths of the collision zone are given at the point where each beam passes through the center of the collision zone. Where there are circular slits rather than rectangular slits the dimension specified is the diameter of the circular oriface. This will not effect the location of the umbra and penumbra but only the intensity distribution between them. The following are the expressions for the collision zone beam widths and misalignment dimensions in terms of the slit dimensions:

$$W_1 = S_{1R} + (d_{11} + d_{12})\left(\frac{S_{1F} - S_{1R}}{d_{12}}\right) \tag{13}$$

$$W_1^1 = (d_{11} + d_{12})\left(\frac{S_{1F} + S_{1R}}{d_{12}}\right) - S_{1R} \tag{14}$$

$$W_{1L} = S_{1RL} + (d_{11} + d_{12})\left(\frac{S_{1FL} - S_{1RL}}{d_{12}}\right) \tag{15}$$

$$W_{1L}^1 = (d_{11} + d_{12})\left(\frac{S_{1FL} + S_{1R} - S_{1RL}}{d_{12}}\right) - \left(S_{1R} - S_{2RL}\right) \tag{16}$$

$$W_2 = S_{2R} + (d_{21} + d_{22})\left(\frac{S_{2F} - S_{2R}}{d_{22}}\right) \tag{17}$$

$$W_2^1 = (d_{21} + d_{22})\left(\frac{S_{2F} + S_{2R}}{d_{22}}\right) - S_{2R} \tag{18}$$

$$W_{2R} = S_{2RR} + (d_{21} + d_{22})\left(\frac{S_{2FR} - S_{2RR}}{d_{22}}\right) \tag{19}$$

$$W_{2R}' = (d_{21} + d_{22})\left(\frac{S_{2FR} + S_{2R} + S_{2RR}}{d_{22}}\right) - (S_{2R} - S_{2RR}) \tag{20}$$

The last two slit dimensions which must be found are the slit dimensions for detector chambers 1 and 2. Remembering that the detector chamber entrance slit must be large enough to prevent having a viewing factor given reasonable tolerances for slit misalignments. The detector chamber 1 slit width is

$$W_1 = W_{1L} + W_{1R} \tag{21}$$

where

$$W_{1L} = W_{3L} + d_2\left(\frac{L - W_{3L}}{d_1 + d_2} - C\right) \tag{22}$$

$$W_{1R} = (W_3 - W_{3L}) + d_2 \left(\frac{R - W_3 + W_{3L}}{d_1 + d_2 - C} \right) \tag{23}$$

With the above equations to describe the geometrical configuration of the parent beams and detector, the collision zone dimensions, the resolution of the apparatus, and size of the detector slits can be calculated for various parent beam slit dimensions. The effect of slit misalignment can also be calculated to find out the maximum deviation from perfect alignment without having a viewing factor.

Finally, a calculation, similar to the one made at the beginning of this chapter, is made to determine the amount of scattered signal and signal to background in the ionization chamber for various detector resolutions. The number of scattered product molecules that pass through the ionization chamber is given by

$$I_D = \frac{I_{20} n_1 \, QV \, W_3^2}{4\pi (d_1 + d_2)^2} \tag{24}$$

where I_{20} is the incident flux of beam 2, n_1 is the number density of beam 1 at the collision zone, Q is the cross section for the collision, V is the volume of the collision zone given by $W_1 \times W_2 \times W_i$ where W_i is the smaller of W_1 or W_2, and W_3, d_1, and d_2 are shown in Figs. II-11 and II-12. The background number density of the product being detected is calculated by assuming that the background can come from two sources outside of the detector chamber. The first source is the scattered product from the collision zone and the second source is from background gas in the main chamber. Once a molecule gets into a particular chamber it can get out in several ways. If it is a scattered product it can fly directly through the chamber and pass into the following chamber, if it makes it through the second

Figures II-11 and II-12. Apparatus Dimensions

	Name	Dimension
I.	Beam 1.	
	d_{11}	COR to collimating slits 1.
	d_{12}	Collimating slits 1 to skimmer oriface.
	S_{1F}	Width of collimating slits 1.
	S_{1FL}	Distance from true center to left edge of collimating slits 1.
	S_{1R}	Diameter of skimmer 1 oriface.
	S_{1RL}	Distance from true center to left edge of skimmer 1 oriface.
	W_1	Width of beam 1 umbra at collision zone.
	W_{1L}	Distance from COR to left side of umbra.
	W_1^1	Width of beam 1 penumbra at collision zone.
	W_{1L}^1	Distance from COR to left side of penumbra.
II.	Beam 2.	
	d_{21}	COR to collimating slits 2.
	d_{22}	Collimating slits 1 to skimmer oriface or oven crucible slit.
	S_{2F}	Width of collimating slits 2.
	S_{2FR}	Distance from true center to right edge of collimating slits 2.
	S_{2R}	Width of oven slits or diameter of skimmer oriface.
	S_{2RR}	Distance from true center to the right edge of oven slit or skimmer oriface.

Figures II-11 and II-12. Apparatus Dimensions (Cont'd.)

Name	Dimension
W_2	Width of beam 2 umbra at collision zone.
W_{2R}	Distance from COR to right side of umbra.
W_2^1	Width of beam 2 penumbra at collision zone.
W_{2R}^1	Distance from COR to right side of penumbra.

III. Detector

d_1	COR to detector chamber 1 entrance slit.
d_2	Detector chamber 1 entrance slit to ionization chamber entrance slit.
d_{12}	Detector chamber 1 entrance slit to detector chamber 2 entrance slit.
W_1	Width of detector chamber 1 entrance slit.
W_{1L}	Distance from true center to left edge of detector chamber 1 slit.
W_2	Width of detector chamber 2 entrance slit.
W_3	Width of ionization chamber entrance slit.
W_{3L}	Distance from true center to left edge of ionization chamber entrance slit.

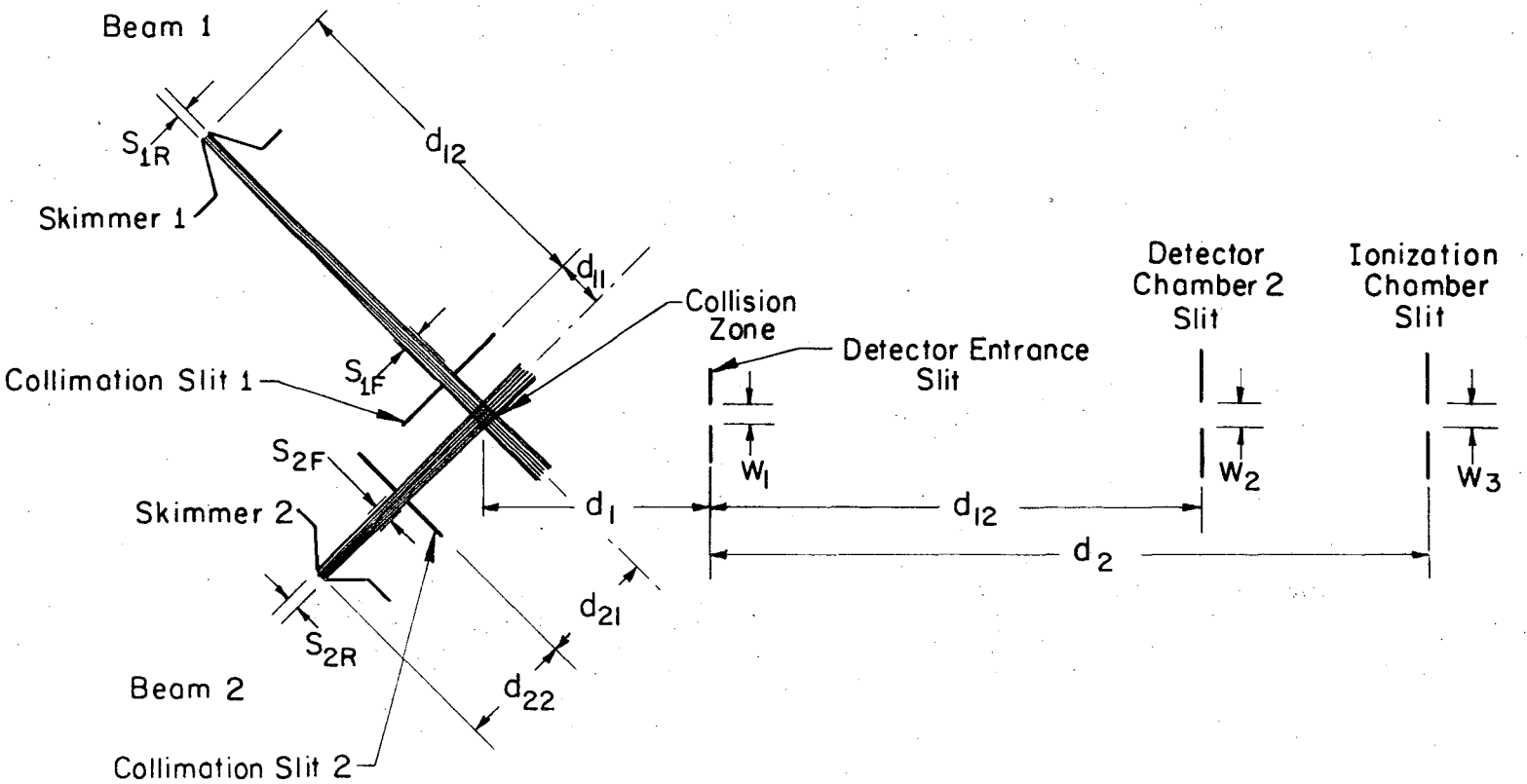

Fig. II-11.

XBL 751-5461

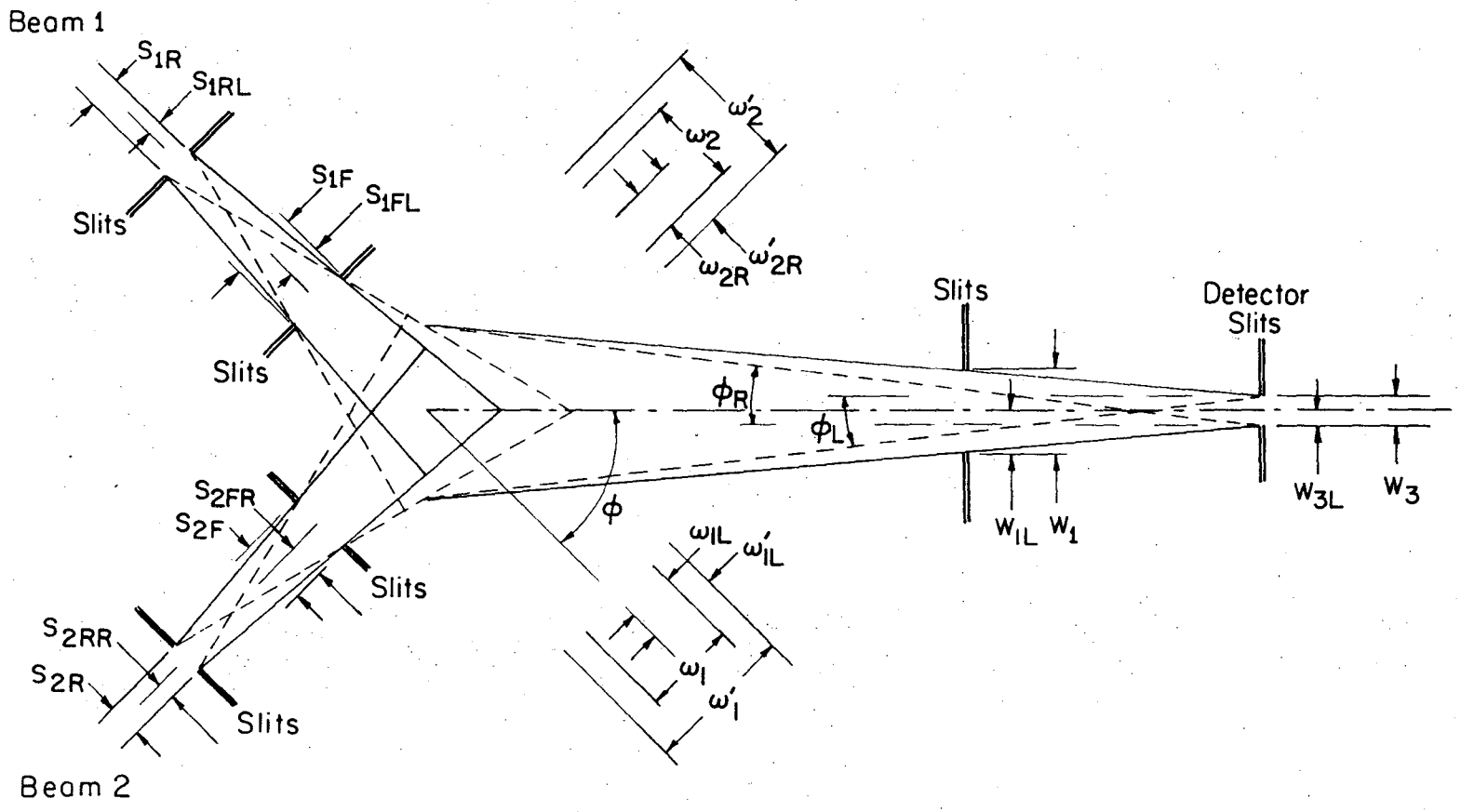

XBL 751-5462

Fig. II.12.

detector slit hole in that particular chamber. Once a molecule becomes background gas it may either effuse through one of the detector slits or be pumped out of the system by the pumps on that particular chamber. The equations used to determine the number density in each detector chamber are given in Table II-2. N_1, N_2, and N_3 are the number densities in detector chambers 1 and 2 and the ionization chambers respectively. S_1, S_2, and S_3 are the pumping speeds for each of the detector chamber and V is the average velocity of the gas.

To find the optimum slit geometry, Focal language computer programs were written to run on the PDP-8 computer. Slit geometries were determined that would give resolutions of 1.0, 1.5, and 2.0 degrees in laboratory angle. For a given size collision zone the detector slit widths were calculated to give an angular resolution of 2.0 degrees. Once the detector slit sizes were decided upon, the largest allowable source slit dimensions in order to avoid a viewing factor were determined by a method outlined by C. A. Mims.[16] Briefly, the calculation proceeds as follows. The signal at a given angle is the sum of the contributions from each point in the collision zone. Provided that the detector resolution in LAB angle is small and the distribution of relative collision velocity vectors throughout the collision zone is the same, then the contribution to the signal from one point in the collision zone is given by

$$dS(\theta) = A \cdot I(\theta) \cdot \tilde{n}_1(\tau) \cdot \tilde{n}_2(\tau) \cdot \Omega(\tau) \cdot d\tau \qquad (25)$$

where $\tilde{n}_i (i = 1,2)$ are the number density of reactant particles from beam i, $d\tau$ is the differential volume element, and $\Omega(\tau)$ is the solid angle subtended by the visible portion of the detector slits, A is the normalizing constant

Table II-2. Formula for detector Chamber Background Number Densities.

Chamber	Formula[a]
Detector 1	$N_1 = \dfrac{\frac{NmVW_1^2}{4} + \frac{I_d}{W_3^2}\left[\frac{W_1(d_1+d_2)^2}{d_1^2} - \frac{W_2^2(d_1+d_2)^2}{(d_1+d_{12})}\right]}{S_1 + \frac{VW_2^2}{4}}$
Detector 2	$N_2 = \dfrac{\frac{N_1VW_2^2}{4} + \frac{I_d}{W_3^2}\left[\frac{W_2^2(d_1+d_2)^2}{(d_1+d_{12})^2} + \frac{\pi D_4^2(d_1+d_2)^2}{4(d_1+d_2+d_4)^2} - W_3^2\right]}{S_2 + \frac{\pi VD_4^2}{16}}$
Detector 3	$N_3 = \dfrac{N_2V\left(W_3^2 + \frac{\pi D_4^2}{4}\right) + I_d - \frac{\pi I_d D_4^2(d_1+d_2)^2}{4W_3^2(d_1+d_2+d_4)^2}}{S_3 + \frac{1}{4}V\left(W_3^2 + \frac{\pi D_4^2}{4}\right)}$

a. W and d dimension given in Figs. 11 and 12 except d_4 is the distance from the center of rotation (COR) to the exit hole of the ionization chamber and D_4 is the diameter of the ionization chamber exit slit.

independent of angle or position, and $I(\theta)$ is the LAB angular differential cross section. The signal at a particular LAB angle, is then given by

$$S(\theta) = A \cdot I(\theta) \int \tilde{n}_1(\tau) \cdot \tilde{n}_2(\tau) \cdot \Omega(\tau) \cdot d\tau \qquad (26)$$

$I(\theta)$ can then be obtained by dividing the signal $S(\theta)$ by $A \cdot V(\theta)$, where

$$V(\theta) = \int \tilde{n}_1(\tau) \cdot \tilde{n}_2(\tau) \cdot \Omega(\tau) \cdot d\tau \qquad (27)$$

The method of evaluating this integral is described by Mims.[16]

The maximum slit widths for a resolution of 2.0 degrees and to avoid having a viewing factor are listed in Table II-3. The apparatus angular weighing function, $V(\theta)$, for several collimating slit widths is shown in Fig. II-13 and for different misalignments of each beam is shown in Fig. II-14. With the source slits set to give the largest collision zone without a viewing factor, the maximum misalignment of each beam is given in Table II-4.

The background number densities in each detector chamber for various beam intensities, scattering cross sections, background pressures, and slit geometries are shown in Table II-5. This table also shows the signal to noise ratio for various counting times, different beam intensities, and different scattering cross sections. Of course, some of the number densities seem low in the various detector chambers, but this is realistic if it is remembered that many background masses can be discriminated against with the quadrupole mass filter. So if the particle being observed is not the same mass as a typical background particle (see Fig. II-20), then these numbers are a realistic representation of the signal intensities that should be observed in this apparatus. Since the angular distribution of scattered particles has been assumed to be isotropic, the signals actually seen should

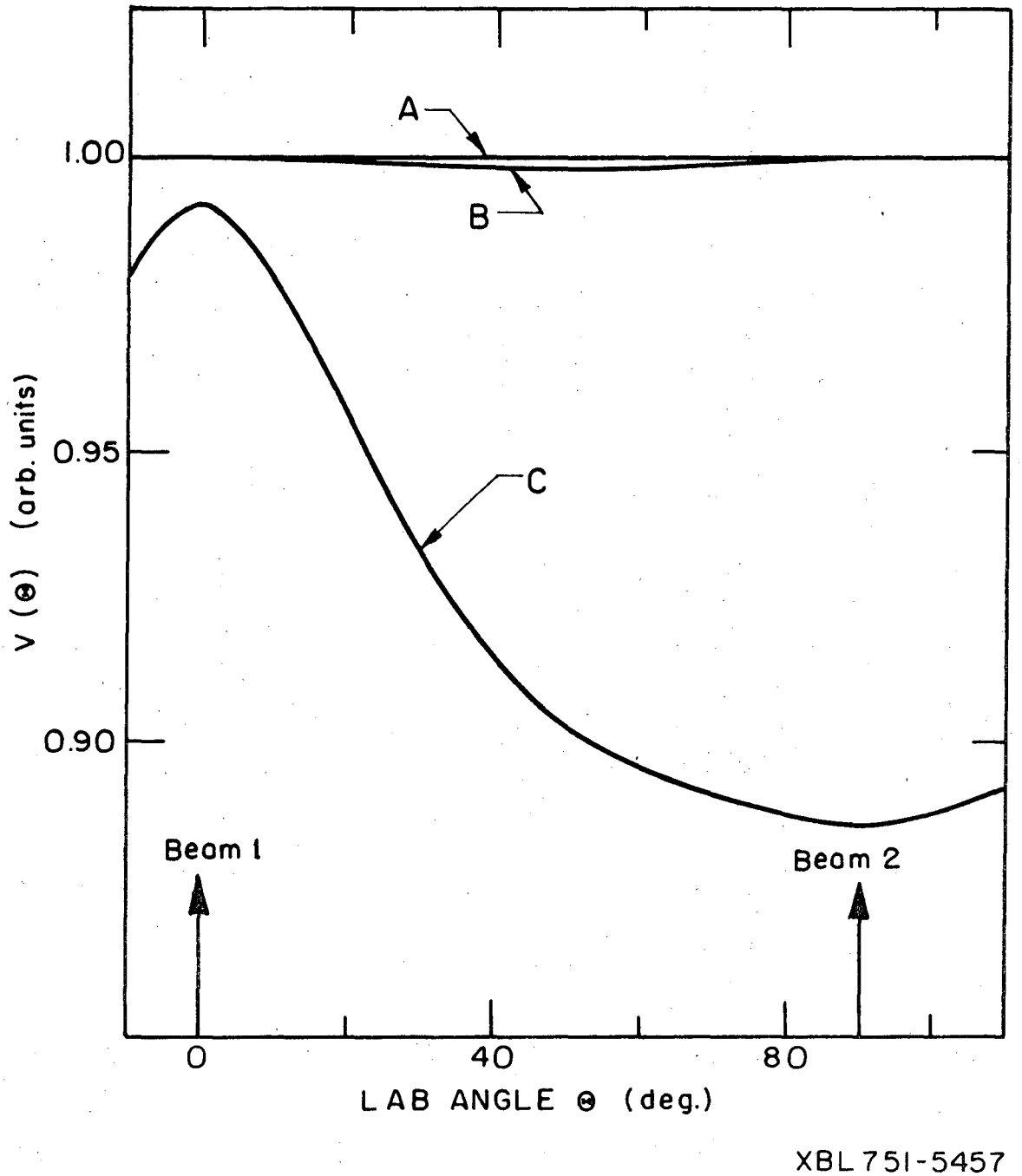

Fig. II-13. Apparatus angular wighting function, V(Θ) for three different collimating slit widths. A-collimating slit up to 0.250 cm wide, B-colimating slits 0.300 cm. wide, and c-colimating slits 0.400 cm wide.

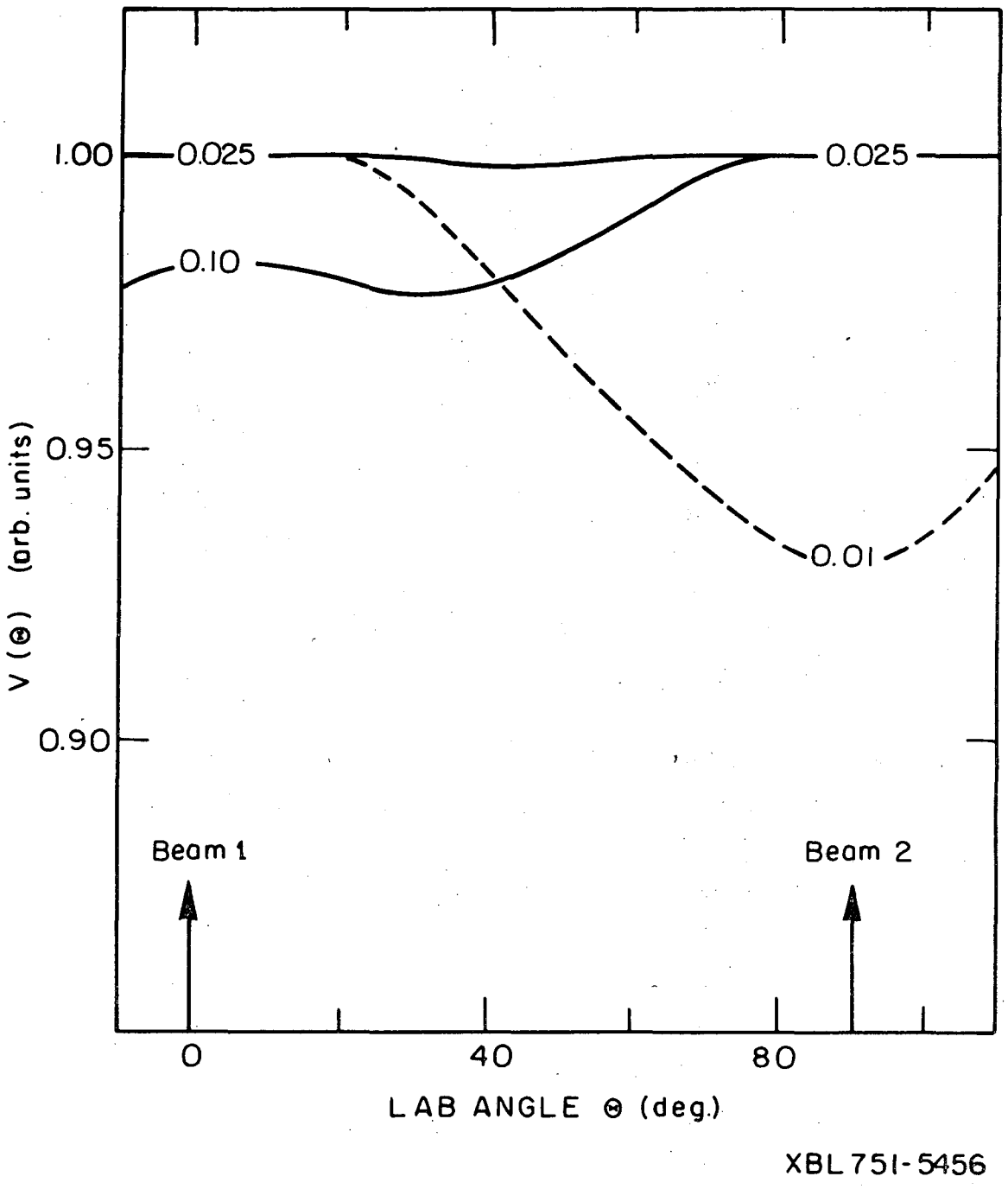

Fig. II-14. Apparatus angular wighting function, V(Θ) for various beam misalignments with collimating slit width of 0.250 cm. Numbers above each beam show the distance the beam is misaligned for each curve. A misalignment of 0.025 cm of either beam produces approximately the same wighting function.

Table II-3. Apparatus Slit Dimensions

Dimension Location	Width or Diameter[b] (cm)	Height (cm)	Distance to COR (cm)
I. Detector			
Detector Entrance Slit (W_1,d_1)	0.380	0.380	4.44
Detector Chamber 2 Slit (W_2,d_1+d_{12})	0.358	0.358	13.97
Ionization Chamber Entrance Slit (W_3,d_1+d_2)	0.300	0.300	18.40
Ionization Chamber Exit (D_4, d_4)	0.350		27.20
Entrance to Focusing Lenses	--	--	39.7
Umbra subtended by Detector Entrance Slit and Ionization Chamber Entrance Slit at COR	0.398	--	--
Penumbra subtended by Detector Slits	0.600	--	--
II. Collision Zone			
Maximum collision zone penumbra width			
Beam 1	0.243[a]		
Beam 2	0.243[a]		
Penumbra widest dimension	0.340[a]		

Table II-3 (Cont'd)

Dimension Location	Width or Diameter (cm)	Height (cm)	Distance to COR (cm)
III. Beam 1			
Maximum skimmer Dia. (S_{1R})	.150[a]D	--	10.53
Maximum collimating Slit Width(S_{1F})	.250	.320	0.95
Collimating slit width for 2° res.	.207	.320	0.95
Operating skimmer Dia.(S_{1R})	.075D	--	10.53
Operating collimating slits(S_{iF})	.180 to .240	.320	0.95
IVa. Beam 2 (Nozzle)			
Maximum skimmer Dia.(S_{2R})	.080[a]D	--	7.75
Maximum collimating Slit width(S_{2F})	.250[a]	.320	2.22
Operating Skimmer Dia.	.062D	--	7.75
Operating Collimating Slits(S_{2F})	.130 to .240	.320	2.22
IVb. Beam 2 (High Temperature Oven)			
Operating oven slit 1	0.025	0.625	8.47
Maximum Collimating Slit for oven slit 1	0.250[a]	0.320	2.22
Operating oven slit 2	0.062	0.625	8.47

Table II-3 (Cont'd)

Dimension Location	Width or Diameter (cm)	Height	Distance to COR
Maximum collimating slit for oven slit 2	0.160 to .240	0.320	2.22

[a]Maximum allowable valve so as to avoid having a viewing factor for given misalignment dimensions.

[b]Circular orifaces are specified by a D.

Table II-4. Maximum Beam Misalignment Dimensions

Slits	Maximum misalignment from perfect center cm	(inches)[a]
Beam 1 collimating	0.025	(.010)
Beam 1 skimmer	0.025	(.010)
Beam 2 collimating	0.025	(.010)
Beam 2 skimmer or oven	0.025	(.010)

[a]The location of the beam slit other than the one specified must be on center or off in the same direction as the one indicated.

Table II-5. Detector Background Conditions

Detector Conditions[a]	Beam 1[b] #Density	Beam 2[b] Intensity	Main[c] Chamber Pressure	Cross Section (Å)	Scattered #Density	Det. Chamber #Density[b] #1	#2	#3	Counting time (sec)	Signal to None Ratio[d]
HIGH PUMP	1×10^{13}	5×10^{17}	2×10^{-7}	1.0	5.1×10^{4}	7×10^{6}	6×10^{3}	39.	100	22
	1×10^{13}	5×10^{17}	2×10^{-7}	10.0	5.1×10^{6}	7×10^{6}	1.3×10^{4}	3×10^{3}	100	226
	1×10^{13}	5×10^{17}	2×10^{-7}	0.1	5.1×10^{3}	7×10^{6}	5.7×10^{3}	11.	100	7
	1×10^{13}	5×10^{17}	2×10^{-6}	1.0	5.1×10^{4}	7×10^{7}	5.7×10^{4}	110.	100	22
	1×10^{14}	5×10^{17}	2×10^{-6}	1.0	5.1×10^{5}	7×10^{7}	5.8×10^{4}	390	100	71
LOW PUMP	1×10^{13}	5×10^{17}	2×10^{-6}	1.0	5.1×10^{4}	7×10^{8}	5.8×10^{6}	8.0×10^{4}	100	11
	1×10^{13}	5×10^{17}	2×10^{-7}	1.0	5.1×10^{4}	7×10^{7}	5.8×10^{5}	8.3×10^{3}	100	19
	1×10^{13}	5×10^{17}	2×10^{-7}	1.0	5.1×10^{4}	7×10^{7}	5.8×10^{5}	8.3×10^{3}	10	6

a) The collision zone width is 0.243 cm, the detector slit widths for chambers 1, 2, and 3 are 0.380, 0.357, and 0.300 respectively. HIGH PUMP and LOW PUMP refer to the pumping speeds for each detection chamber which for HIGH PUMP are 1000 l/s for chambers 1 and 2 and 1500 l/sec for chamber 3, and for LOW PUMP are 150 l/s, 225 l/s, and 100 l/sec for chambers 1, 2, and 3 respectively.

b) Number densities in particles/cm^3 and intensities in particles/cm^2sec.

c) Torr

d) Ionization efficiency of 0.01%

be better than those listed. Exceptions to this will arise. For example, if elastic or inelastic scattering is being observed the detected particle will be the same mass as the parent particle so the background pressure will be higher than in the reactive scattering case. The situation is even worse for narrow angle elastic scattering since at small angles the fringes of the beams can get directly into detector chamber #1. Fortunately, it is often possible to measure this scattering since the cross section for this type of scattering is large.

2. Alignment Procedures

The first part of this section has described how the width of the various slits were determined and also listed what the maximum allowable slit sizes are, and what slit dimensions are actually used. The following section describes the practical aspects of how the slits are aligned in the apparatus and how their width and location are determined. The alignment procedures are divided into the following subsections:

A. Center of rotation (COR) determination.

B. Beam plane location.

C. Detector chamber alignment.

D. Detector alignment.

E. Parent beam alignment.

A. Center of Rotation (COR) Location

All the alignment procedures for this apparatus depend upon having an accurately located center of rotation (COR). The center of rotation in this apparatus consists of a #38 nickel wire (~ .0035 inch diameter) attached to a pair of metal slides which can move independently at right angles to one another. The metal slides are attached near the COR on the bottom of the

rotating detector lid. A lead weight is attached to the bottom of the nickel wire to keep it taut. To position the wire on the center of rotation would be easy if the detector lid could swing 180°, but once the collimation chambers are in place the detector lid can only be rotated approximately 120°. In order to locate the COR for this situation it is necessary to use two optical cathetometers. The nickel wire may be positioned on the COR as follows:

1. Set up the two cathetometers so there is an included angle between them of about 90° and they can both sight on the COR wire when the detector is in two different positions 90° apart.
2. Sight the two cathetometers on the COR wire.
3. Rotate the detector lid 90° and estimate how far the COR wire has moved from the vertical cross hair of each cathetometer. The diameter of the nickel wire may be used as an estimate of the COR wire distance from the cathetometer cross hair.
4. To determine which direction to move the COR wire draw a diagram as shown in Fig. II-15. The two axes represent the direction of sighting on the COR wire with the detector in its initial position. The detector is then rotated 90° (clockwise in the figure) and the COR wire is in a new position in each cathetometer. The distance the wire has moved in each direction is plotted on the figure. A circle with an appropriate diameter is drawn so that 90° of its arc in the direction the lid was rotated will connect the old COR wire location with the new location. The center of this circle is the true location of the COR.

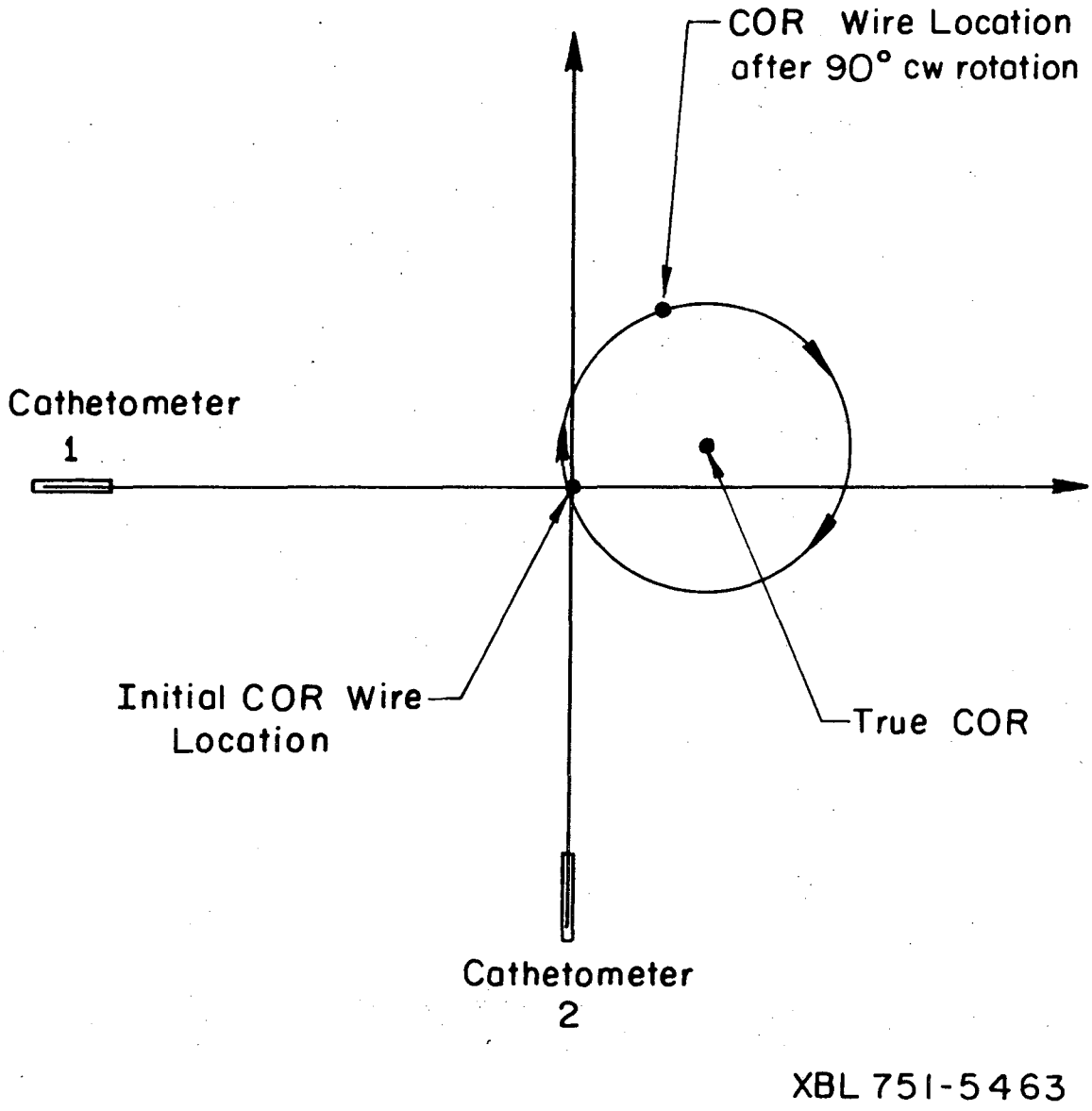

Fig. II-15. Center of rotation location diagram.

5. Move the two metal slides to try to position the COR wire on the true COR.

6. Repeat steps 3, 4, and 5 until the detector can be rotated and the COR wire does not move from the cathetometers vertical cross hair.

B. Beam Plane Location

The location of the beam plane for this apparatus was extremely critical in order to obtain accurate measurements for the initial alignment. To find the beam plane the rotating detector lid was assembled and the machine was leveled by placing a machine level on the rotating lid and adjusting the legs on the main chamber stand until the lid was level in orthogonal directions. This aligned the lid and the main chamber bearing surface to better than .0005 inch per foot.

The beams are located 3.375 inches above the center of the two source chamber ports on the vertical center line. To find this point a fixture was made from a bar of aluminum of a suitable length so as to span the port hole and bolt onto the main chamber. The bar contained a 3 inch long brass bushing with a half inch shaft. The shaft rotates inside the bushing. A rod with a machinists indicator attached to it and a rod with a point 3.375 inches from the center of the bushing rod were both clamped onto the bushing rod. The bushing rod was turned so the indicator ran on the inside bore of the 20 inch source chamber hole. The aluminum bar was moved until the bushing rod was centered to within .001 inch. The rod was then rotated until the point 3.375 inches from center was on the vertical center line of the hole. This point was marked as the beam position. This was done on both source chamber holes in the main chamber. A cathetometer was set up opposite each source hole and the cathetometer's cross hairs were positioned

so as to look at the respective beam point parallel to the plane defined by the detector rotating lid. The cathetometers can be positioned in a horizontal plane to better than .001 inch per foot. With the center of rotation and the beam plane determined, measurements for the source and detector slit locations could be made.

C. Detector Chamber Alignment

The movement of the detector chambers after the vacuum chambers were evacuated, and the detector chamber walls were cooled to liquid nitrogen temperature had to be measured. To do this a cathetometer was aligned on the beam plane as described in the previous section. The detector rotating lid was assembled and the ionization chamber was put in place. Five openings on the horizontal plane in the detector chambers were fitted with brass plates that enabled the detector chamber movement to be measured. Each plate had a square hole in its center with lines scribed .010 inch apart around the perimeter of the hole. The center of the accurately machined hole marked by a heavy horizontal and vertical line was precisely located with respect to the locating surface of each detector hole. This was done for the detector entrance hole, the detector chamber 2 entrance hole, the ionization chamber entrance hole, the ionizer support plate hole, and the 5 inch hole for the scintillation counting unit. Since the measurement had to be taken looking from the back of the detector toward the COR, each successive hole going toward the COR was smaller than the previous one. This allowed the simultaneous measurement of detector movement at all five positions. The chambers were temporarily equipped with light bulbs for these readings. After all the plates were in place the vacuum

chambers were sealed and the apparatus pumped down. The movement of the plates was measured with the optical cathetometer looking through a Pyrex porthole. Measurements were made in a cyclical fashion. First, the measurements were made with the vacuum chamber at atmospheric pressure, then the chambers were pumped out and again measurements were taken, then detector chambers were cooled to liquid nitrogen temperature and measured. Measurements were also taken when the chamber warmed up to room temperature, and finally when the apparatus was at atmospheric pressure. This process was repeated three times and the average of the three valves was used as the correct measurement. All the measurements are within about .002 or .003 of an inch. The dimension for the locating surfaces on the five plates and their distance to the center of the hole are listed in Table II-6. The distance that the center of each square hole is off from the true center defined by the line in the beam plane of beam 1 is given in Table II-7 for the chamber at atmosphere, under vacuum and at liquid nitrogen temperature.

The numbers listed in Table II-7 for the detector movement dimensions at liquid nitrogen temperature were used in making the actual detector slits and parts. The construction details of each of the five parts vary but their dimensions can be specified by listing the size of the locating surface, the distance from the left locating edge to the center of the aperture and the distance from the top locating edge to the center of the aperture, and finally the dimensions of the aperture itself. All dimensions and directions are looking from the back of the detector toward the COR. The detector entrance slit is on the sliding gate valve along with a .003 of an inch hole to look at each beam. The main aperture in the

Table II-6. Locating Plate Dimensions

Plate	Width (inches)	Left edge to hole center (inches)	Height (inches)	Bottom Edge to Hole center (inches)
Detector Entrance	0.715	0.357	0.309*	0.145*
Detector Chamber 2	0.624	0.317	0.748	0.375
Ionization Chamber	0.498	0.250	0.748	0.375
Ionizer Support	1.999	1.000	4.123	1.375
Rear Flange	4.500**	2.250**	--	--

*Actually diameter of circle and distance from the bottom of circle.

**Distance from locating pins.

Table II-7. Detector Chamber Movement Dimensions.†

Plate	At Atmospheric Pressure				Under Vacuum				At Liquid Nitrogen Temperature			
	Up and Down Dist.	Dir.*	Left & Right Dist.	Dir.*	Up & Down Dist.	Dir.*	Left & Right Dist.	Dir.*	Up & Down Dist.	Dir.*	Left & Right Dist.	Dir.*
Detector Entrance	0.000	OC	0.040	L	0.018	D	0.040	L	0.000	UC	0.047	L
Detector Chamber 2 Entrance	0.045	U	0.020	L	0.030	U	0.020	L	0.042	U	0.020	L
Ionization Chamber	0.028	U	0.060	L	0.017	U	0.060	L	0.071	U	0.060	L
Ionizer Support	0.024	U	0.057	L	0.015	U	0.057	L	.060	U	0.060	L
Rear Flange	0.001	U	0.017	L	0.018	D	0.015	L	.002	D	0.019	L

† All dimensions in inches.

* Direction Up(U) or Down(D) is the direction of the plate horizontal center line from the cathetometer horizontal cross hair. The direction Left(L) or Right(R) is the direction of the plate vertical center line from the vertical cross hair. These are the real directions not the apparent cathetometer directions.

gate valve has a small line scribed on the horizontal center line of the hole to aid in aligning the detector. The detector chamber 2 entrance slit, the ionization chamber entrance slit, and the ionizer plate all have horizontal and vertical scribe lines on the hole centers. The scintillator housing which attaches to the rear flange is different from the other four pieces. It is positioned by two locating pins, and it aligns the exit lens with the rear of the quadrupole mass filter. In this case the distances specified are between the center located by the pin in the detector chamber and the axis of the ion exit lenses, again, looking from the back of the detector toward the COR. The dimensions for these five pieces are listed in Table II-8.

The actual alignment of the detector apertures is straight forward. The cathetometer must be set up on a beam line in the beam plane. The gate valve and counter mechanism must be assembled (see Appendix 3) and the horizontal line set to line up with the cathetometer horizontal cross hair. The counter reading must be noted since this will be the position for the perfect alignment of the detector opening. The detector chamber 2 slit must now be put in place and its scribed lines should fall on the cross hairs of the cathetometer. The ionization chamber is now lowered into place but before tightening the UHV flange the chamber must be correctly positioned. To position the ionization chamber place the ionization chamber entrance slit in place and move the ionization chamber so as to line up the vertical center line. Place the ionizer support plate in position and move the ionization chamber so as to position the vertical line that is .010 of an inch off center on the vertical cross hair. Remove the ionizer support plate and recheck the ionization chamber entrance slit.

Table II-8. Detector Aperture Dimensions.[a]

Aperture	Locating Surfaces Width	Height	Left Edge to Hole Center[a]	Top Edge to Hole Center[a]	Aperture Dimension Width	Height
Detector Entrance (Gate Valve)	0.717	b	0.383	b	0.150(.381)	0.150(.381)
Detector Chamber 2 Entrance	0.620	0.748	0.323	0.417	0.141(.358)	0.141(.358)
Ionization Chamber Entrance	0.497	0.748	0.189	0.446	0.118(.300)	0.118(.300)
Ionizer Support Plate	2.000	4.124	1.060	2.810	.140 dia.	--
Rear Flange (Scintillator Housing)	2.250(radius)		-0.016[c,d]	0.002[c]	--	--

a Dimensions in inches except centimeter in parenthesis.

b Controlled by gate valve positioning device.

c Distance from flange center to exit lense axis.

d Distance to right of center when looking toward COR.

When both of these lines are lined up properly tighten the ionization chamber down until the two flanges are metal to metal. This completes the alignment of the detector chambers and the detector slits.

D. Detector Alignment

The detector is for the most part self aligning. The ionizer and exit lens - scintillator units are both self aligning. The only part of the detector that must be aligned is the quadrupole mass filter.

The EAI quadrupole mass filter is positioned in this system by a specially made adapter flange (Blueprint #12N5612). The quadrupole housing is screwed onto the adapter flange and the adapter flange is then bolted onto the back of the ionizer support plate. The critical adjustment is to get the axis of the quadrupoles to be normal to the front face of the adapter flange. This can be done fairly easily using a machinists flat table and an indicator. Once this is initially aligned there are no alignment measurements needed to assemble the detector.

On the rear of the scintillator housing are two perpendicular scribed lines whose intersection defines the beam line of the detector. The height of the horizontal line is at the height of the beam plane when the apparatus is at atmospheric pressure. This line is used to set up the cathetometer on routine alignment procedures.

E. Parent Beam Alignment

The molecular beam uses two kinds of sources in terms of method of alignment. One is a source with a large slit such as a high temperature oven, and the other is a source with a small oriface behind a beam defining skimmer such as the hypersonic nozzle source. First the easier alignment of the oven type source will be outlined and then the more difficult

nozzle type source.

As mentioned previously, the collimating slits are mounted on the collimation chamber from the main chamber side. The hole in collimation chamber 1 is 0.722 inches wide and .987 inches high and the hole in collimation chamber 2 is .747 inches wide and .989 inches high. The holes serve two purposes. First, the size provides an adequate viewing area to make positioning of the rear slits easy. Second, by making a locating surface on the collimating slit holder to fit tightly into the collimation chamber the slits can be removed and replaced without necessitating realignment.

With the collimating slits out of the apparatus the oven type source is aligned as follows:

1. Set up the optical cathetometer facing the beam source that is to be aligned. Level the cathetometer using the two leveling bubbles on the cathetometer. This is important since the height of the beam will be determined by the cathetometer and the cathetometers height will be positioned from the horizontal scribe mark on the back of the scintillator housing.
2. Move the cathetometer to the correct angular position opposite the beam being aligned. This is done by moving the cathetometer into a position so that both the COR wire and the vertical scintillator housing scribe mark, when the rotating lid is at 0.0 or 90.0 degrees, are lined up on the vertical cross hair of the cathetometer.
3. Once the cathetometer is properly aligned, place the oven in its mount and position the oven slit so it lines up on the cross hair of

the cathetometer. For maximum deviation from perfect alignment see Table II-4.

4. To line up the collimating slits, loosely attach the slits in the collimating slit holder. Place the collimating slit holder in the collimating chamber hole and tighten the nuts to hold the collimator in place.

5. Gently move one of the collimating slits until the beam defining edge is lined up on the cross hair of the cathetometer. Tighten the screws that hold this slit side and remove the collimating slit holder from the collimating chamber.

6. Using a Graetner shadow machine, set the free slit side one half of the desired slit width from the fastened slit side. Tighten the newly aligned slit side and loosen the one on the center of the slit opening. Now set this slit the full slit width from the other and tighten all the screws. This should successfully align the collimating slits.

7. Replace the collimating slit holder in the hole of the collimating chamber and recheck the alignment with the cathetometer. The beam slits should now be perfectly lined up.

The following is the procedure for the alignment of the nozzle source:

1. Line up the cathetometer as in steps 1 and 2 of the previous procedure.

2. Using the cathetometer as a sight, position the oriface of the skimmer so that its center lines up perfectly with the intersection of the cathetometer cross hairs. Tighten down the skimmer.

3. Place a piece of paper on the wall opposite the beam chamber of

the beam being aligned. Put a mark on this paper so it falls on the cross hairs of the cathetometer.

4. Set up the He-Ne laser behind the inside source chamber of the nozzle being aligned. Adjust the He-Ne laser so it passes through the skimmer oriface and hits the mark on the paper.

5. Now place the nozzle in its support (see nozzle section of this chapter). Adjust the nozzle position until the laser light passes through the nozzle oriface. Now adjust the nozzle adjustment screws to try to get the laser light coming through the nozzle oriface to pass through the center of the skimmer oriface.

6. Shut off the laser and place a light bulb behind the gas inlet tube for the nozzle. Temporarily remove the paper. Look at the nozzle with the cathetometer and adjust the nozzle until the light from the oriface is centered in the skimmer oriface. This may take some patience.

7. Vary the distance between the nozzle and the skimmer and check to see that the nozzle oriface remains centered in the skimmer oriface.

8. Remove the light bulb, replace the paper, and turn on the laser. Move the nozzle close to the skimmer. A round diffraction pattern should appear on the paper. If this is so, the nozzle is lined up.

9. Align the collimating slits as in steps 4 through 7 of the previous alignment procedure. This concluded the alignment of the nozzle source.

This section has explained the various methods for aligning different

parts of the apparatus. It is imperative that these alignment procedures be rigorously followed since only slight misalignments, especially in the nozzle sources, can lead to extremely reduced signals. If any terms used in the alignment procedures are ambiguous, detailed explanations may be found in the assembly procedures in the Appendices of this chapter.

D. The Detector

The detection of scattered products in low energy neutral-neutral scattering, whether it be from elastic, inelastic, or reactive scattering, poses detection problems more difficult than found in beam experiments at higher energies or in ion-molecule scattering studies. At high energies it is relatively easy to discriminate against signal from low energy background gas, but for these low energy neutral-neutral scattering experiments the signal contribution from background gas is of paramount concern. Although surface ionization techniques have been used in neutral-neutral scattering and are to a large extent free of background problems, they are limited to a specific group of elements that can be studied. Therefore, it is necessary to use a detector that is non-specific in the products it ionizes, and to discriminate against unwanted products by use of a suitable mass filter.

An electron bombardment molecular beam detector was designed by Brink[6] in 1965. The Brink design consisted of an electron bombardment ionizer, which was able to ionize up to 0.1% of the particles passing through it, and a Paul mass filter[17] to discriminate against unwanted masses. This apparatus utilizes a detector similar to the Brink detector, but modified to enhance the signal. It also utilizes a scintillation ion detector system to help discriminate against noise other than background gas such

as photons and electrons.

The other detection technique employed in this apparatus, and already mentioned, is the use of beam modulation. This enables the background to be subtracted out unambiguously as long as careful selection of the beam modulation frequency is used.

The general design of the detector is such that detector components lie in the plane of the beam. The ionizer is in a separate chamber from the rest of the detector and utilizes a "fly-through" design to reduce the background gas in the ionization chamber. The ionization chamber is pumped by a noble gas ion pump and a liquid helium pump, plus extensive liquid nitrogen cooling to make the background pressure in the ionization chamber as low as possible. A schematic diagram of the detector and detector chamber electronics is shown in Fig. II-16.

1. The Ionizer

The electron bombardment ionizer for this apparatus is designed to be as efficient as possible. This has meant that parameters such as a well defined electron energy and ionizing region size had to be sacrificed in order to achieve a higher detection efficiency. A well defined electron energy could have been used to do appearance potential measurements in some experiments.

The response of an electron bombardment ionizer is dependent on the k, the "rate constant" for electron bombardment ionization. Assuming that the ion is produced from a electron-particle interaction and neglecting processes such as second ionization and electron attachment, then the probability that a particle will pass through the ionizer without being ionized is e^{-kt} if t is the amount of time spent passing through the ionizing region.

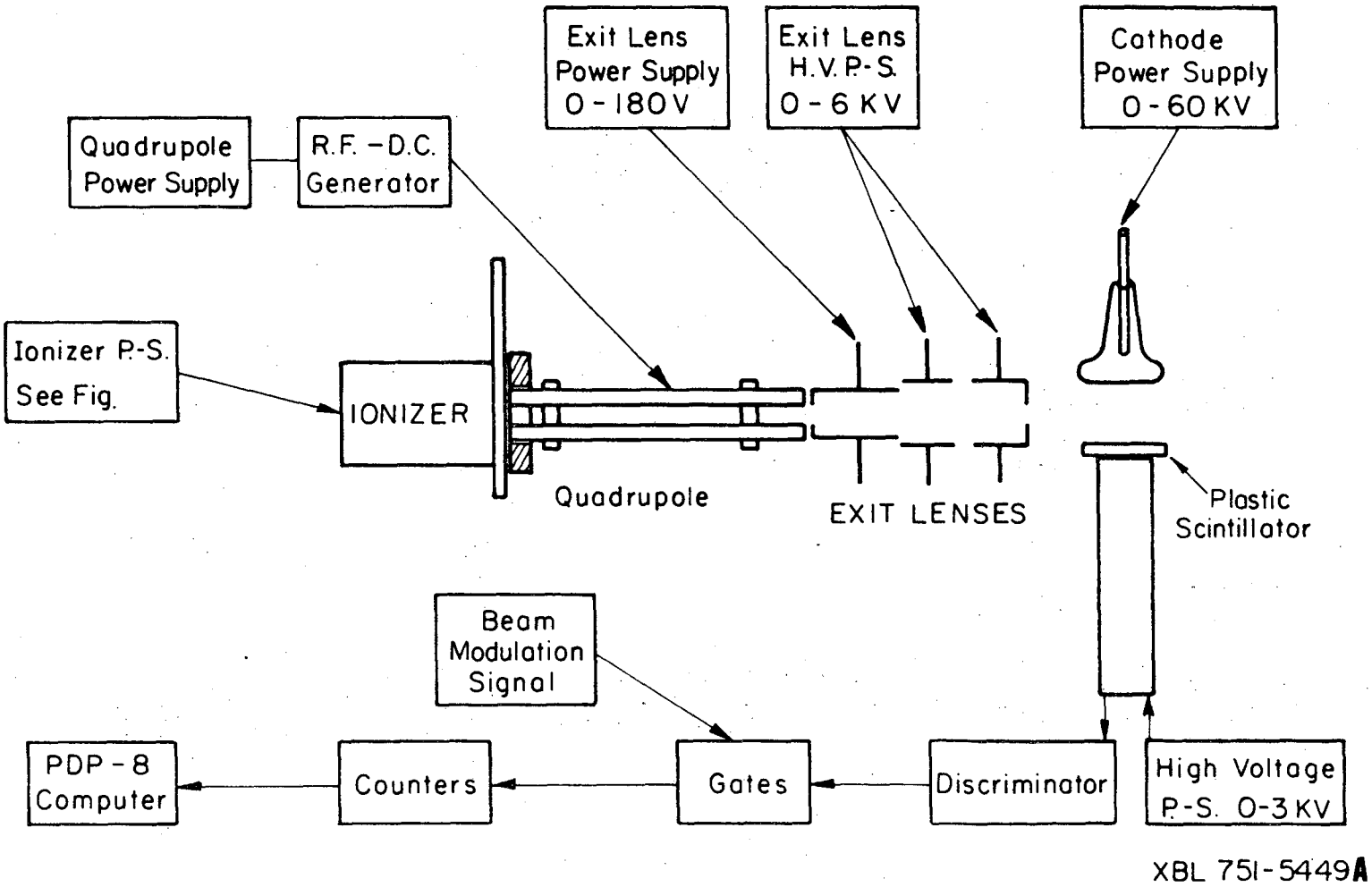

Fig. II-16. Schematic of detector and associated electronics.

The ionization efficienty (B) is given by $B = 1 - e^{-kt}$. If $kt \ll 1$, then $B \cong kt$ and is thus proportional to the residence time in the ionizer. Therefore, the detector response is inversely proportional to the velocity of the particle, and the detector detects a number density.

So the number of ions that are formed in an electron bombardment ionizer per second is given by

$$N = inlAQ(E) \tag{28}$$

where i is the electron flux in the region of the ionizer that the beam passes through, n is the number density of the species being ionized, l is the length of the ionizing region and A is the cross sectional area that the beam sweeps out through the ionizing region, and Q(E) is the ionization cross section. The number of ions per second from the ionizer can be increased by increasing the electron flux in the ionizing region or the volume of intersection between the scattered beam and the ionizing region. The difference between the ion signal from background gas and scattered signal, besides the number density of each in the detector, is the effective ionizing volume that contributes to each through the ionizer. Therefore, for the best signal to noise conditions the ionizing region of the ionizer should only be as large as the cross sectional area of the scattered beam that passes through it.

In order to achieve as high an electron density as possible, the ionizer has a design similar to Brink's. A schematic of the ionizer and electronics is shown in Fig. 17 and a detailed assembly drawing in Fig. 30. The ionizer essentially consists of a coaxial grid and cylinder with two filaments diametrically opposite between the grid and the cylinder. The filament floats at a negative potential with respect to the grid and a

positive potential with respect to the cylinder. The filaments are 1% thoriated tungsten ribbons (0.0005" × 0.025" cross section, Rembar Co. Inc., Dobbs Ferry, N.Y.) and are mounted as close as possible (0.050") to the grid. One end of the filaments is attached to the cylinder and the other end is attached to two separate metal connectors on a spring loaded alumina plate which keeps tension on the filaments to prevent sagging when heated.

After the filaments are first installed in the apparatus they must be activated. This entails heating the filaments above their usual operating temperature to bring the thorium to the surface, oxidizing the thorium on the surface and carburizing the filaments by heating in an atmosphere of butane to prolong their life. (See Rosebury, Handbook of Electron Tube and Vacuum Techniques, Addison-Wesley, 1965). When the filament is heated, electrons are drawn off the surface by the grid (made from 0.010" dia platinum wire wrapped around the grid structure) and accelerated through the axial part of the ionizer toward the other side of the cylinder where they are repelled back toward the center of the ionizer. The electrons thus make several passes through the ionizing region before they are finally collected by the grid. This high density of electrons creates a space charge effect which forms a potential well along the axis of the ionizer. This potential well traps ions along the axis of the ionizer. To collect the ions from the ionizing region a three lens focusing system was included in the ionizer.[18] The focusing system consists of three cylinder lenses. The first two lenses after the ionizing region are split in two halves so they can also act as ion deflectors if needed. The last lens is simply the hole through the ionizer support plate which is always at ground potential. The lenses are unable to focus the ions perfectly because the ions may be

"born" anywhere along the axial distance of the ionizer and at different potentials depending upon how far from the axis of the ionizer they were ionized. Because the quadrupole mass filter used in this detector could accept a fairly large ion entrance angle, and quadrupoles in general are not extremely sensitive to entrance energy, the ions were not color corrected. The typical operating conditions for the ionizer are listed in Table II-9. The grid potential will give the upper limit for the ion energy for the ionizer. The optimum ionizer conditions also depend on what mass is being detected. For proper quadrupole resolution of high masses lower ion energies must be used.

The ionizer is constructed from stainless steel and alumina. All of the ionizer elements are mounted coaxially on four alumina rods which are fastened to the ionizer support plate which bolts into the ionization chamber and locates the ionizer in the proper position. The ionizer elements are spaced by alumina spacers which slide over the alumina rods and the entire assembly is held together by spring tension. All the ionizer electrical connections come through eight metal to ceramic feedthroughs mounted on the ionizer plate. The assembly procedure for the ionizer is listed in Appendix II-3 of this chapter.

The power supplies for the ionizer are a Kepco SC-32-15A for the filament, a Lambda C-880-M for the cylinder shield, and a series of 45 volt B batteries with various high resistance potentiometers for the other ionizer elements.

The electron bombardment ionizer has presented problems when looking at high density signals, such as looking directly at a nozzle beam. The ionizer behaves in an extremely nonlinear fashion when a high density

Table II-9. Ionizer Operating Conditions

Element	
Grid (Ion Energy)	+60 V[a]
Electron Energy	-110 V[a]
Electron Emission	15 ma
Lens 1	
Side A	-92 V[a]
Side B	-84 V[a]
Lens 2	
Side A	-147 V[a]
Side B	-143 V[a]
Filament	
Voltage	9 V
Current	2.1 Amps

a Potential with respect to ground.

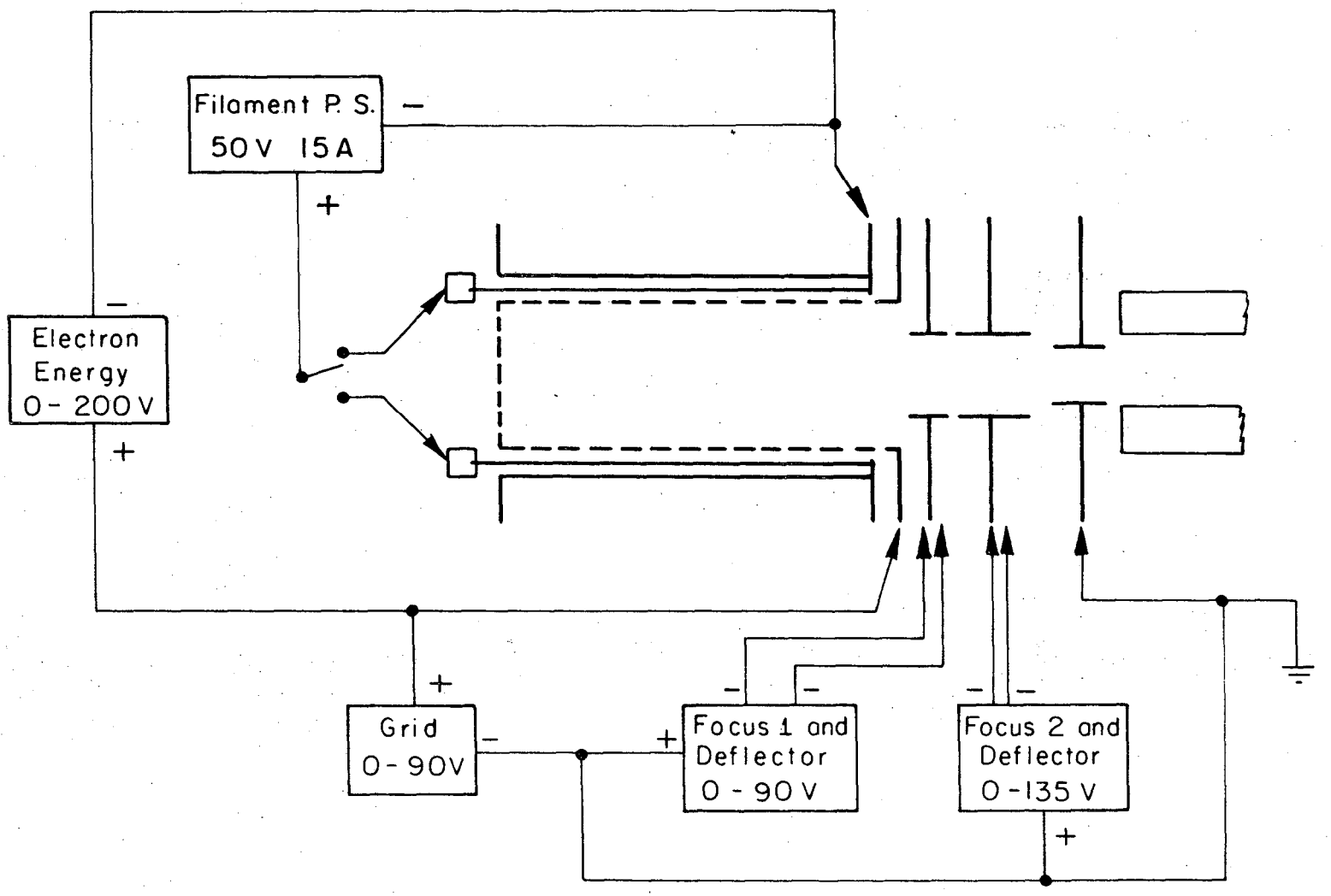

Fig. II-17. Cross section of ionizer and associated electronics.

signal is detected. This is illustrated in a time-of-flight distribution of an argon nozzle beam at various source pressures shown in Fig. II-18. These spectra were taken using a 1% transmitting time of flight chopping wheel with a slot period of 500 μsec, and observing the beam through the .003" diameter detector entrance hole. The combination of the narrow wheel slot and the special separate .003 of an inch hole on the gate valve gives a time of flight wheel gate function time of approximately 6 μsec which is small compared to the ionizer response function time of approximately 65 μsec. The ionizer response function time is just crudely calculated from the most probable velocity and the length of the ionizing region of the ionizer. This ionizer response time is close to the FWHM time on the time of flight distributions. The transition from a smooth distribution at an argon pressure of 50 torr to a bimodal distribution of 650 torr suggests that the ionizer acts in a nonlinear mode at high number densities in the ionizing region. The ionizer ion energy and electron emission were also varied but the distributions remained bimodal except that the relative heights of each peak would change. Only by reducing the argon nozzle pressure could the bimodal peak be eliminated for the case of argon. The time of flight distribution of an oxygen beam and a methane beam were also measured. The methane beam had no bimodal structure over ranges of both electron emmission and ion energy. The oxygen beam has a bimodal structure at low ion energies for the O_2^+ product but only one peak for the O^+ product at the same ion energy and electron emmission as shown in Fig. II-18. From these observed phonomena, it is possible that at a high number density a resonant charge transfer process is taking place between the newly formed

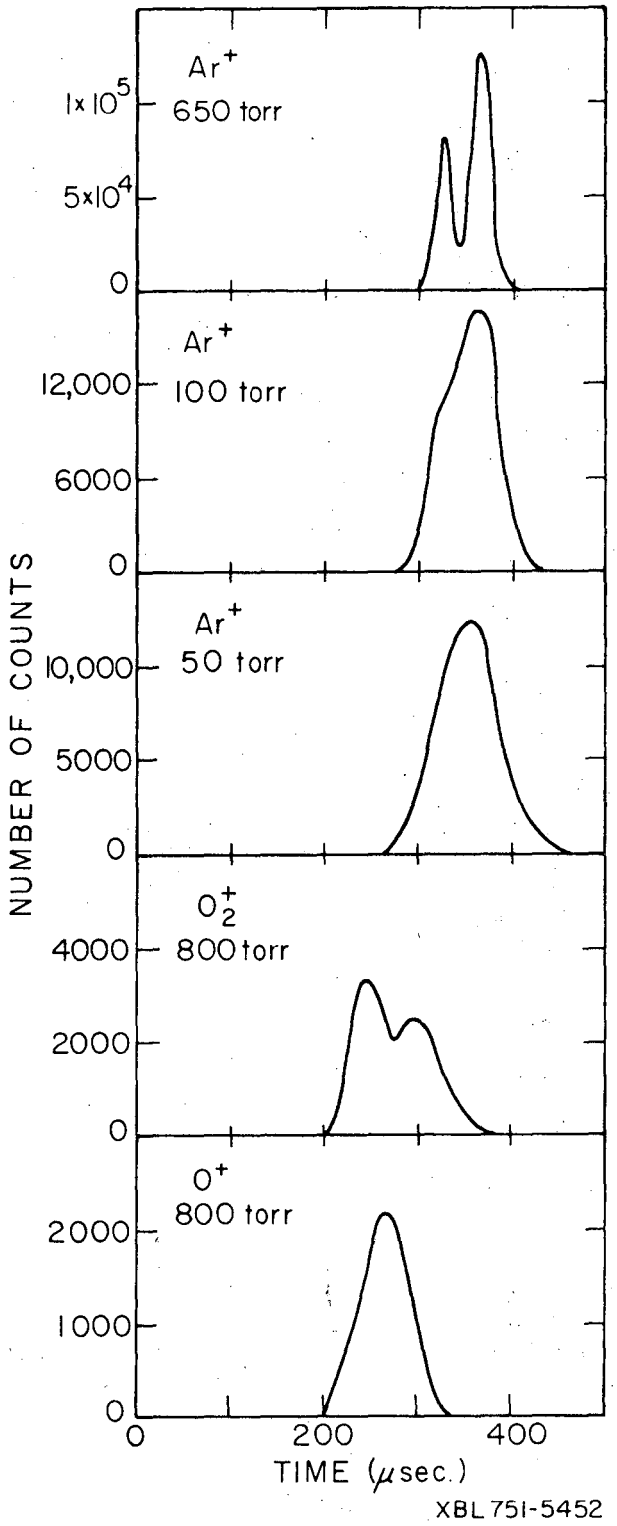

Fig. II-18. Time of flight distribution for nozzle sources at various pressures.

argon beam ion and a background argon atom traveling in a nonaxial direction, thus causing an ion signal attenuation at high densities. With this effect present for high number densities, extreme care must be taken when measuring beam profiles or parent beam velocity distributions. This effect has only been seen with this ionizer when a low transmission time of flight wheel and a small entrance aperture were used. This characteristic may be present in other electron bombardment ionizers but may go undetected since for large gate functions the effect would be a slight skewing of the time of flight distribution.

The ionizer is the one part of the apparatus that could stand substantial improvement. The electron bombardment ionizer can at best be called an inefficient detector. Improvement in detection efficiency of the electron bombardment ionizer may be enhanced by increasing the electron density in the ionizer and using a strong extraction lens system. Recent advances in thin film technology have led to the development of field emmission devices capable of supplying high current densities[19] (7.7 to 23 amps/cm^2) without destruction from ion bombardment. An electron source of this type may be useful in designing an ionizer with sharper electron energy and ion energy ranges and a shorter path length for a given ionizer efficiency.

Field ionization is another technique that has the potential of being a good ionizer but has seen limited application in the molecular beam field due to fabrication difficulties and ion collection problems due to ion formation at high potentials. Again, thin film technology has apparently advanced this field with the development of a multipoint grid structure to be used as a field ionization source.[20] The structure is a uniform array

of points spaced 25 microns apart with a grid structure 125 microns above the points. The potential between the grid and the points is approximately 3000 volts. The ionization efficiency at this ionizer is slightly better than 0.1%. Of course, this type of ionization process could not be used with a quadrupole mass filter since the former is a high voltage device and the latter is a low voltage device. Undoubtedly, if a more efficient field ionization source is made a magnetic mass spectrometer could be used as a mass filter.

An even more attractive ionization source would be a photoionization source. Although the ion intensity would be a step function of photon energy, this type of ionization was rejected since the light source would have to extend far down into the vacuum UV and be extremely intense. State of the art light sources are not intense enough to give an ionization efficiency near that of an electron bombardment ionizer.

2. Mass Filter

The mass filter used is an RF quadrupole type (Model EAI Quad 250) which was purchased from Electronics Associated, Inc., along with the RF-DC electronics power supplies. The main advantages of using this quadrupole mass filter are its ability to accept ions of large entrance angles, its variable resolution which allows the use of low resolution if there isn't a nearby interfering mass peak, and its compact size. The main advantage is the variable resolution. The transmission of the quadrupole can be substantially increased on the high mass range if the resolution can be lowered without having interference from an adjacent mass peak. An illustration of this is shown in Fig. II-19. The resolution is defined by EAI to be unity when two mass peaks of equal height one mass unit apart have a valley between them of 10% of the peak height.

Fig. II-19. The upper panel shows two scattered signals ICl^+ resolved from $BaCl^+$ at a resolution of 0.09 times the mass number. The lower panel shows a mass scan of $SnCl^+$ at a resolution of ~0.5 times the mass number. The transmission of a given ion peak at the setting in the upper panel is more than 10 times greater than at the setting in the lower panel.

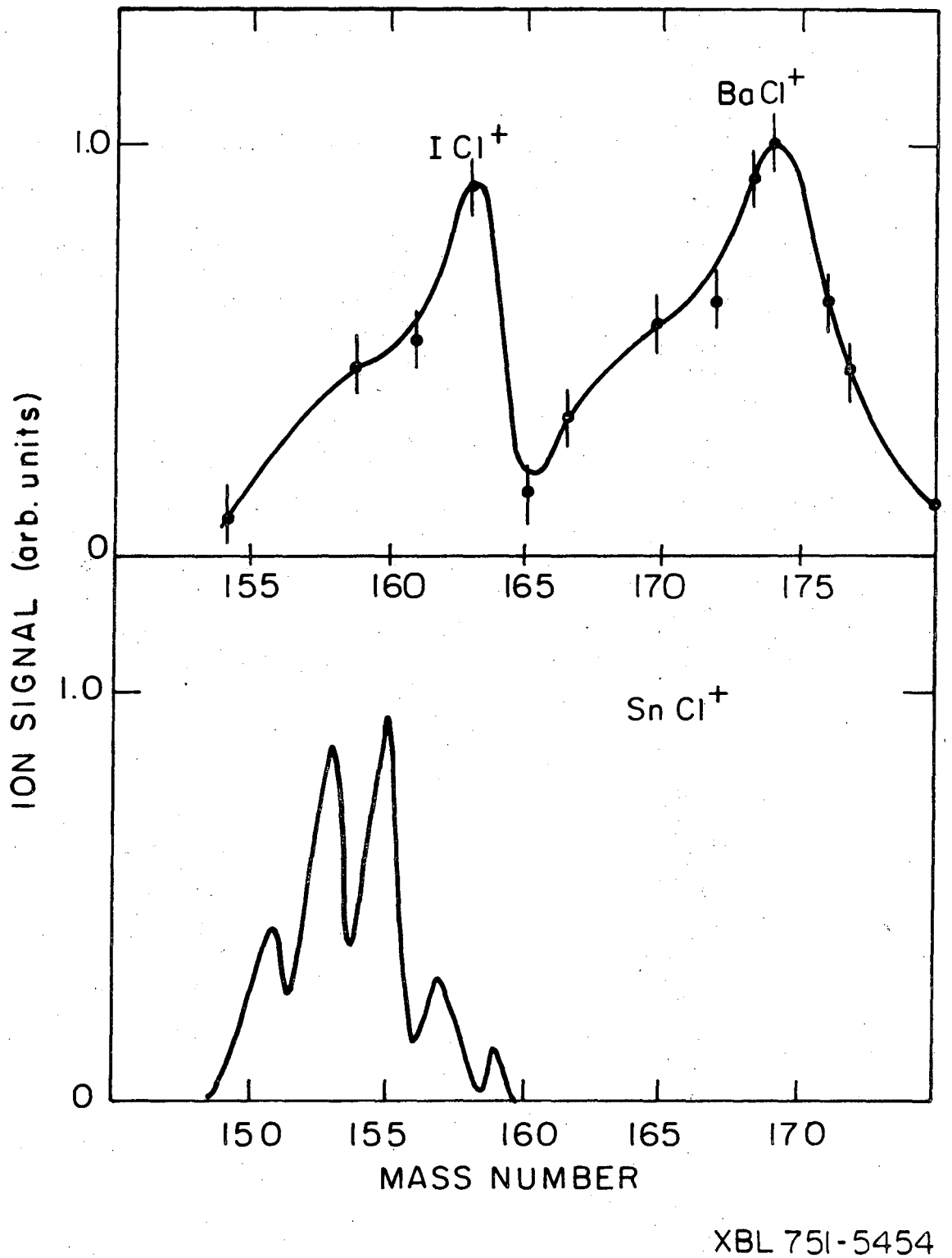

Fig. II-19.

The quadrupole filter is mounted on the rear of the ionizer support plate. The assembly and alignment procedures for this unit are given in the alignment section of this chapter. The background mass spectra after 1 year of running experiment is shown in Fig. II-20. Several of the higher mass background peaks are due to tungsten, thorium, and thorium oxide from the ionizer filament. There is also a background peak from iodine at 127.

3. Exit Lenses and Scintillation Counter

This apparatus utilizes a scintillation detection technique to count the ions that are passed through the mass filter. The scintillation technique was utilized rather than an electron multiplier for several reasons. First, the scintillation technique makes it easier to discriminate against background from other sources such as photons or electrons. Second, the photomultiplier tube that is used to count the light pulses is never subject to contamination as is an electron multiplier, or semiconducting detector. Third, the scintillation counter has a potentially faster counting rate than semiconducting[21] ion detectors.

The scintillation unit is similar to the one described by Daly.[22] A cross sectional detail view is shown in Figs. II-31 and II-32 and a schematic view with associated electronics is shown in Fig. II-16. Essentially the scintillation unit consists of a set of electrostatic lenses which extract the filtered ions from the mass filter and accelerate them toward a high voltage cathode. The ions strike the aluminum surface of the high voltage cathode and cause 2 to 6 secondary electrons[23] to be emitted from the cathode and accelerated into the Pilot B plastic scintillator. The plastic scintillator yields one photon per 2.5 kev of electron energy.

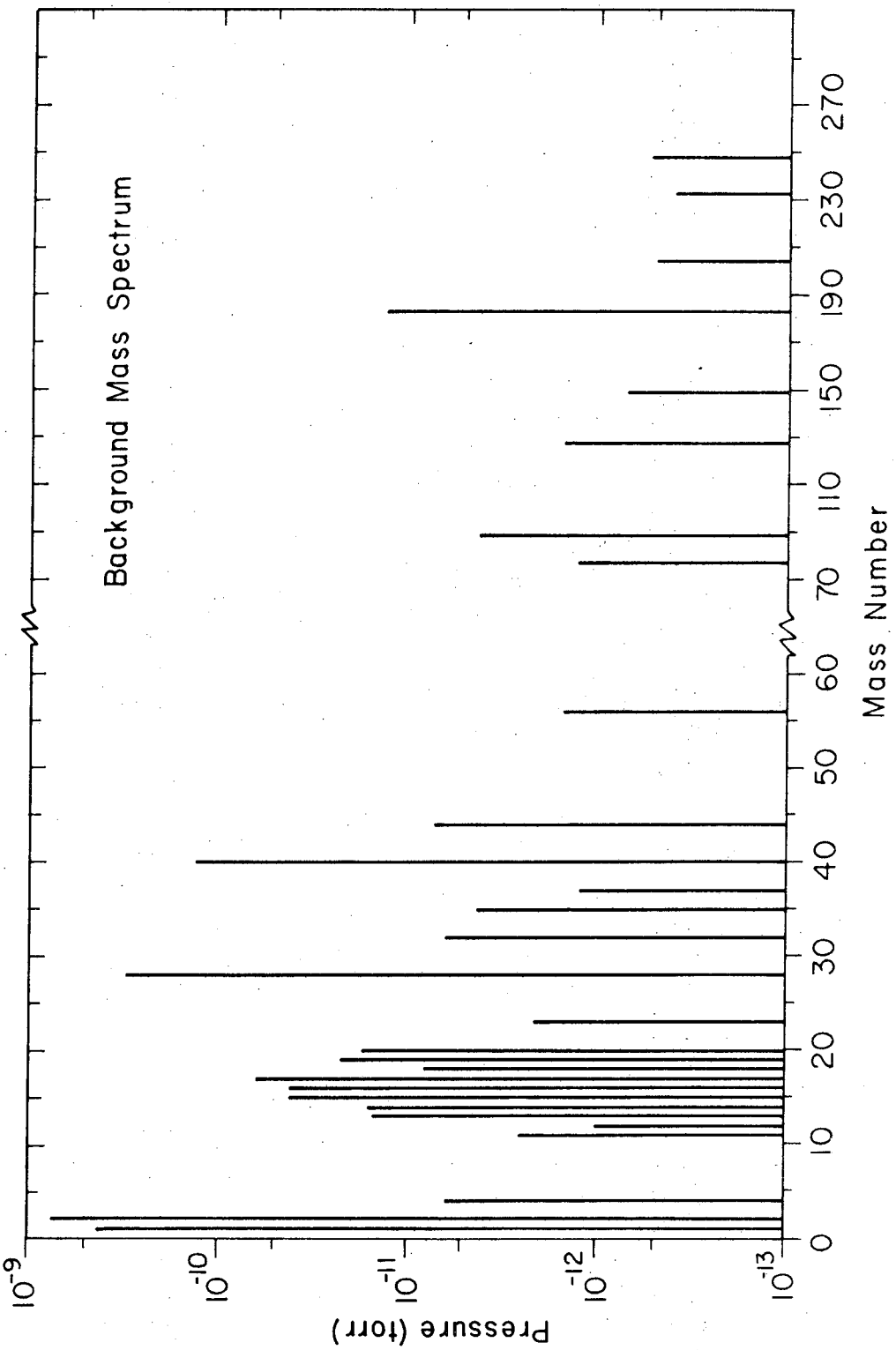

XBL751-5451

Fig. II-20.

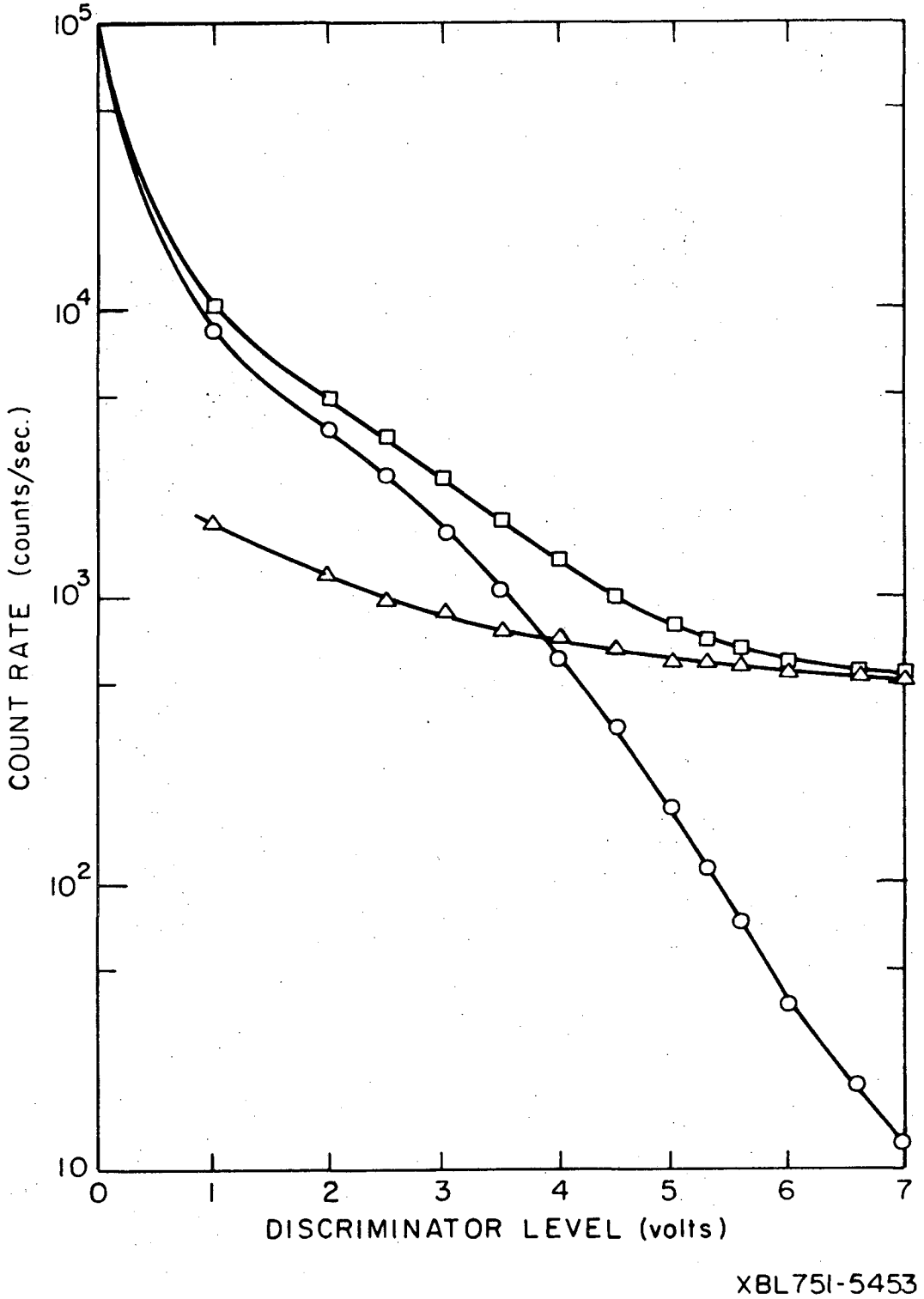

Fig. II-21. The detector count rate as a function of discriminator level. The detector has been set to filter out all ions. The total count rate with all detector electronic supplies on (squares), the single photon count rate (circles) and the difference between the two (triangles) are shown.

This light pulse from the plastic scintillator is then amplified by a photomultiplier tube (EMI 9524S).

All of the scintillator unit parts are made from stainless steel or alumina. The high voltage cathode is a highly polished stainless steel surface that has been coated with a .001 inch thick layer of aluminum by vacuum evaporation. The distance between the high voltage cathode surface and the plastic scintillator surface is variable which allows the position at which the electrons strike the plastic scintillator to be optimized. The plastic scintillator used in this apparatus is Pilot B scintillator material.[24,25] The surface of the scintillator is coated with a 1000 Å thick layer of vacuum deposited aluminum. This layer of aluminum reduces the background light that can enter the photomultiplier, keeps the face of the plastic scintillator at ground potential, and increases the collection efficiency of photons from the scintillator.[26] The 9524S photomultiplier tube is covered with an aluminum shield that floats at its cathode potential. Optical contact is made between the photomultiplier tube and the plastic scintillator with Dow Corning 705 silicon oil in order to lower reflection losses of small angle of incidence photons at the surfaces of the phosphor and photomultiplier tube. The photomultiplier tube can count at a rate of 10^7 counts/sec.

A Signetics NE 529K discriminator is used to discriminate against one photon pulses and electrical noise from the photomultiplier. Fig. II-21 shows the count rate as a function of the discriminator level. The count rates in this figure were taken with the quadrupole resolution as high as possible and the mass setting tuned to a mass where there should be no background peak. Count rates for two different operation modes were measured. In Fig. II-21 the count rate when all of the detector power supplies

are on is shown by the curve with the squares, and the count rate with the electron energy supply off, which reduces the electron emmission to virtually zero, is shown by the curve with the circles. The difference between these two values are shown on the curve with the triangles. The count rate with no electron emmission (circles) is due to the photon background from the ionizer filament. At low discriminator levels this is the predominate background, but as shown in the figure it can be effectively discriminated against and reduced to 10 counts/sec. The curve with all of the detector supplies on (squares) minus the photon background gives the curve shown by the triangles in Fig. 21. This count rate is due to ions and not single photons since any single photon source would be discriminated against at the higher discriminator settings. In order to ascertain where these ions are being formed, various detector conditions were changed. Even though these count rates were measured with a high resolution and not near a background mass peak, it was still possible that the same ions were still being passed through the quadrupole filter. To check this possibility the last two lens elements were set at a potential of + 1000 volts to prevent ions from reaching the scintillation detector chamber. This did not reduce the background ion signal at all, which means that these ions are being formed in the scintillation chamber. This is a very serious problem for reactive scattering, and has to this point hindered the collection of data. It has been necessary to count for much longer times in order to achieve a good signal to noise ratio for reactions that should be easy to collect data for in a short time. This problem must be rectified in order to make this machine operate as it was designed. The most likely source of this high ion background is from a photoionization process taking place

in the scintillation housing. The UV photons for this process can come from radiative relaxation of excited particles in the ionizer. Since this source of UV photons will be relatively weak and the number density of particles in the scintillator housing will be low the ions are most likely being on the back surface of the scintillator housing. The solution to this problem will be to either divert the ions from their axial path around an optical baffle before they reach the ionization chamber or to place a grid near the rear wall to prevent the ions that are being formed from getting to the high voltage cathode. Once this is satisfactorily done the apparatus should easily be able to perform reactive scattering experiments better than it can now.

Figure 22 shows the count rate for a background mass as a function of the high voltage cathode potential. The slight dip in the curve at 15 kilovolts is due to the potential at last exit lens being held constant causing the ions not to strike the optimum position on the high voltage cathode, thus causing the count rate to decrease. Another minor problem has been operating the high voltage cathode over 35KV. At potentials over 35 KV the high voltage supply arcs at some point and power supply shuts off. Since this makes running an experiment difficult the high voltage cathode has usually been run at a potential between 30 and 35 kilovolts.

The electronics for the scintillation unit are shown in Fig. II-16. The voltages for the three electrostatic lenses are supplied by a series of 45 volt "B" batteries and a Fluke model 408B 6KV high voltage power supply. The potential for the high voltage cathode is supplied by a Hipotronics model 850-10R/B188 60 KV power supply. A Fluke 415B 3KV power supply is used for the photomultiplier tube.

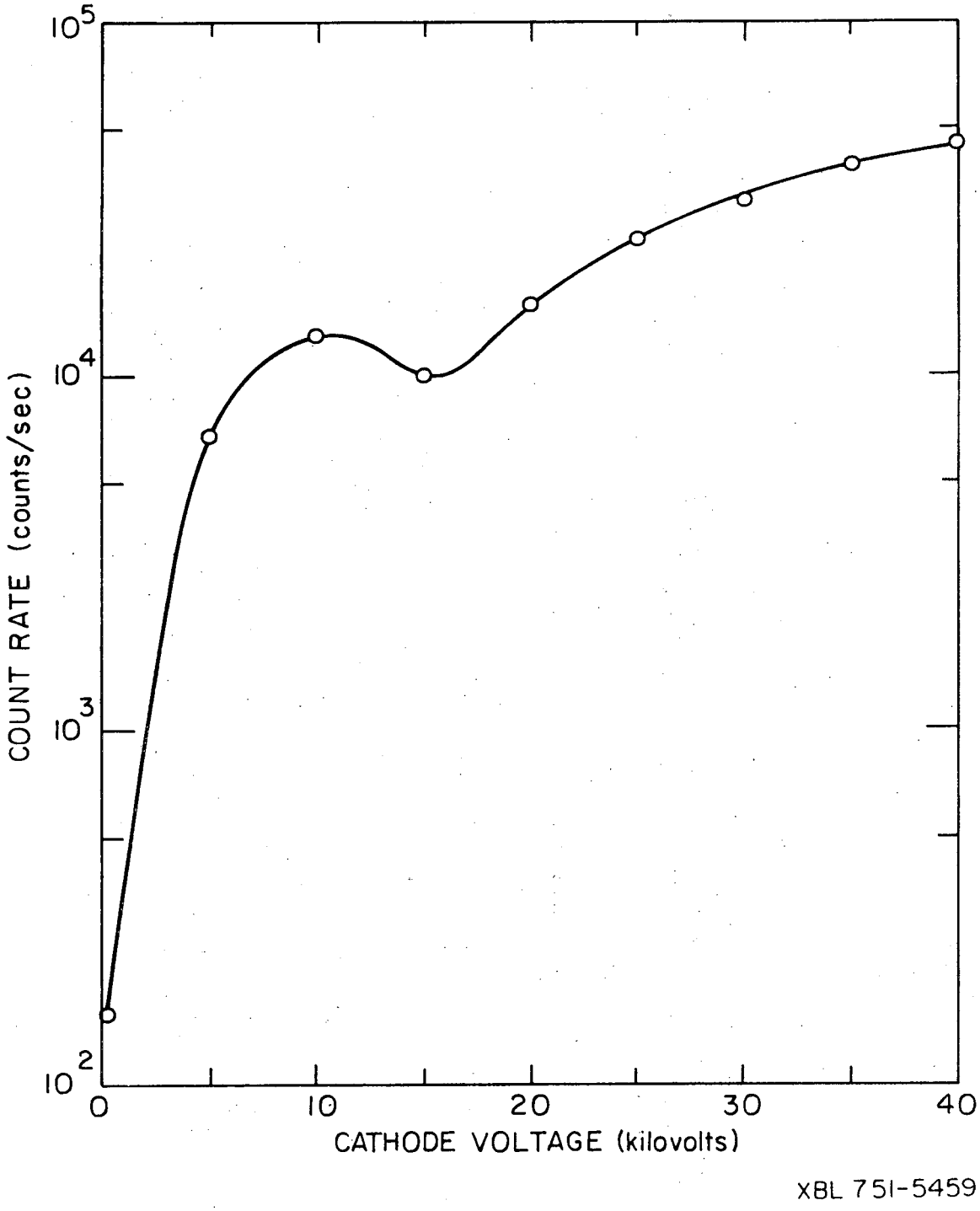

Fig. II-22. Count rate versus high voltage cathode potential for a background mass peak.

The output pulses from the discriminator can either be counted by a separate counter (T/I Model 1535) or directed to the computer to be counted there and then stored in different memory locations.

E. Nozzle Source

Ever since Kantrowitz and Gray[27] postulated the use of a supersonic gas expansion as an intense molecular beam source in 1951, extensive work has been done in construction and understanding these nozzles. The hypersonic nozzle has demonstrated its promise of 1) providing a source which is orders of magnitude more intense than effusive sources, 2) preparing a nearly monoenergetic velocity distribution in the beams and 3) providing a new source of unusual aggregates through condensation processes in the nozzle expansion. Much literature has postulated various methods and explanations of how to achieve as intense a nozzle source as possible and why they behave in the manner that they do - which unfortunately is not exactly the way that Kantrowitz and Grey had originally predicted.

To characterize the nozzles used in this apparatus the measured intensities and velocity distributions will be compared to the simple theory of nozzles.

If an isentropic expansion is assumed then

$$H + \frac{1}{2}mV^2 = H_o \tag{29}$$

where H is the enthalpy and V the local flow velocity and H_o is the enthalpy of the gas in the stagnation source. Therefore, the local flow velocity is given by

$$V^2 = \frac{2}{m}\int_T^{To} C_p \, dT \tag{30}$$

To obtain the functional form usually seen in nozzle papers the Mach number

must be introduced which is simply

$$M^2 = \frac{V^2}{C^2} \tag{31}$$

where C is the velocity sound in an ideal gas

$$C^2 = \frac{\gamma RT}{m} \tag{32}$$

and $\gamma = C_p/C_v$. Substituting equations 31 and 32 into equation 30 yields the equation derived by Kantrowitz and Grey for the relative temperature of the gas (T) in the expanded beam of

$$\frac{T}{T_o} = \frac{1}{\left[1+\frac{(\gamma-1)M^2}{2}\right]} \tag{33}$$

Thus, it is the lowered relative temperature (T) in the beam that leads to the expression supersonic nozzle. The actual energy enhancement over an effusive beam is small, but the Mach numbers are high because the flow velocity of the beam is compared to the local speed of sound in the beam which is low. Another question that arises when estimating the local flow velocity or the relative temperature of the beam, is what value to use for the heat capacities, C_p and C_v. For a monatomic gas only translation degrees of freedom are present and are thus the only ones that can relax. For diatomic or polyatomic molecules, rotational and vibrational degrees of freedom may also relax so the extent of relaxation of each must be considered when estimating the heat capacity to be used. For small molecules the rotational degrees of freedom are relaxed and the vibrational degrees of freedom are not relaxed, since the rotational energy level spacings are smaller than the vibrational energy level spacings, thus less collisions

are needed to relax rotational modes than vibrational modes. In general the relative vibrational, rotational, and translational temperatures in the beam are in the order

$$T_{vib} > T_{rot} > T_{trans}$$

The flow velocity of the beam also accounts, in part, for the higher intensities in nozzle beams than in effusive beams. The flow of the gas makes the intensity more directed along the axis of the flow and thus tends to increase the intensity of the nozzle source.

The intensity along the centerline of the nozzle, I(0,U) can be put in a form analogous to an effusive source.

$$\frac{dI(0,u)}{du} = \frac{N_s A_s}{\pi^{3/2}} \left(\frac{u}{\alpha_s}\right)^3 \exp\left(\frac{-(u-v)^2}{\alpha_s^2}\right) \qquad (34)$$

where n_s, A_s, α_s refer to the number density area, and most probable velocity of the skimmer oriface respectively, and v is the bulk gas or flow velocity and u is the molecular velocity. Anderson and Fenn[28] have shown that this reduces to

$$\frac{dI(0,u)}{du} = \frac{N_o A_s}{\pi 3/2}\left(\frac{u}{\alpha_o}\right)^3 \left[1 + \frac{(\gamma-1)M^2}{2}\right]^{3/2}$$

$$x \exp\left\{ -\left(\frac{u}{\alpha_o}\left[1 + \frac{(\gamma-1)M^2}{2}\right]^{1/2} - \frac{\gamma^{1/2}M}{\sqrt{2}}\right)^2 \right\} \qquad (35)$$

where n_o and α_o are the number density and most probable velocity in the nozzle chamber respectively. Equation 35 predicts an increasing intensity as long as the Mach number M keeps increasing toward infinity. In practice this does not happen since as the gas expands the number of collisions that

occur decrease until eventually the gas goes over to the free flow condition and the Mach number becomes "frozen in". Anderson and Fenn have shown that the terminal Mach number can be summarized by the equation

$$M_T = 1.17\left(\frac{\lambda_o}{D_n}\right)^{-0.4} \tag{36}$$

where λ_o is the viscosity based mean free path in the nozzle chamber and D_n is the diameter of the nozzle oriface. This effect of "freezing in" a terminal Mach number means that another expression for the intensity must be used which takes account of the fact that the isentropic expansion may be completed before the gas reaches the skimmer oriface. This has been accounted for by Anderson, Andres, and Fenn[29] by using the following expression for the intensity for Mach numbers above 4 of

$$I \cong n_s \left(\frac{l_s}{l_1}\right)^2 A_s\left(\frac{1}{\pi X^2}\right) V_1\left(\frac{1}{2}\gamma M_1^2 + \frac{3}{2}\right) \tag{37}$$

where n_s and l_s are the number density of the skimmer and distance from the nozzle to skimmer respectively, l_1 is the distance from the nozzle to the surface where the terminal Mach number occurs, V_1 is the flow velocity associated with the Mach number M_1 and X is the distance from the nozzle oriface to the point where the intensity is to be determined. If the distance between the nozzle and skimmer is less than the distance where the terminal Mach number occurs then $l_1 = l_s$, $V_1 = V_s$, and $M_1 = M_s$, the Mach number at the skimmer. One final relation is needed in order to be able to do this simple calculation and that is the relation between the nozzle chamber conditions and the parameters of the flow as it moves downstream.

This relation has been found by Sherman and Ashkenas [30] to be

$$M = A\left(\frac{X-X_o}{D}\right)^{\gamma-1} - \frac{1}{2}\left(\frac{\gamma+1}{\gamma-1}\right)\Big/ A\left(\frac{X-X_o}{D}\right)^{\gamma-1} \qquad (38)$$

where X_o is the distance downstream of the nozzle oriface where the streamline flow appears to radiate from, X is the distance downstream of the nozzle oriface, A is a value determined by the method of characteristics for a given X_o and M, and D is the nozzle oriface diameter. The value for A and X_o depend on the value of γ and their values found by Sherman and Ashkenas are listed in Table II-10.

Table II-10

γ	$\frac{Xo}{D}$	A	$\frac{Xo}{D}^{1}$
1.67	0.075	3.26	0.04
1.40	0.40	3.65	0.13
1.286	0.85	3.96	

Finally, to obtain the number density of the skimmer a modification of the Sherman and Ashkenas formula for pitot tube pressure measurements gives

$$\frac{n_x}{n_o} = \left(\frac{\gamma-1}{\gamma}\right)\left(\frac{\gamma+1}{\gamma-1}\right)^{\gamma/\gamma-1}\left(\frac{\gamma+1}{2\gamma}\right)^{1/\gamma-1} A^{-2/\gamma-1}\left(\frac{X-X_o}{D}'\right)^{-2} \qquad (39)$$

The configuration of the nozzle source used in this apparatus is shown in Fig. II-23. The skimmer is mounted on the front plate of the main support. The nozzle chamber is mounted at the end of a 3/16 inch diameter tube and is seated on the end of the fluid cooling support. The nozzle chamber is enclosed in insulated tantalum heating wires and the temperature is monitored with a chromel-alumel thermocouple placed in the thermocouple hole in the nozzle chamber. The oriface for the nozzle chamber is made from a round shim of either nickel or stainless steel and is sealed in place in the nozzle

Figure II-23. Nozzle Source

1. Nozzle slide support.
2. Nozzle slide.
3. Dovetail for vertical movement
4. Cooling chambers and nozzle support.
5. Alignment screws.
6. Nozzle feed.
7. Nozzle chamber.
8. Copper sealing gasket.
9. Nickel oriface.
10. Oriface cover.
11. Heating wire holder.
12. Skimmer
13. Gas inlet.

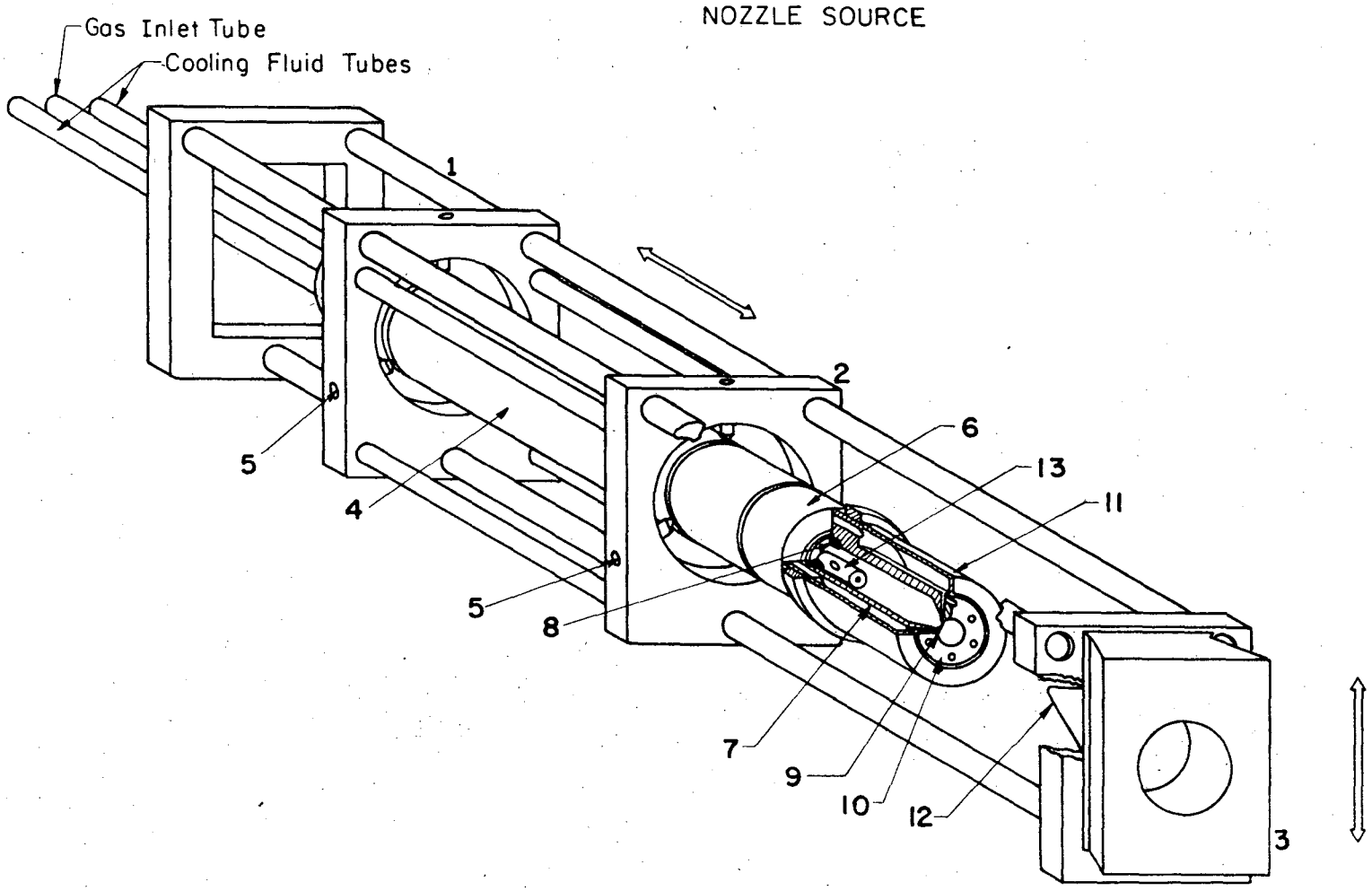

Fig. II-23.

XBL 751-5450

chamber with a knife edge seal. The nozzle chamber on the cooling chamber support is positioned in a slide on the main support and must be aligned with the skimmer oriface as described in the alignment section. Once aligned the nozzle skimmer distance can be varied from the outside by means of a mechanical feedthrough.

The performance of the nozzle source has been tested by measuring the velocity distributions at various nozzle skimmer distances, by measuring the change in intensity of a scattered signal at one angle as a function of the nozzle-skimmer distance, and by measuring the beam attenuation of the other beam being operated at a low intensity. This was done to avoid the nonlinear effects of the ionizer. The time-of-flight distributions of narrow angle elastic scattering were used to determine the velocity distributions in the beam so as to avoid the bimodel structure previously seen. The velocity distributions were obtained from the time of flight distributions by deconvoluting over the time of flight wheel and ionizer gate function as described in the time of flight section of this chapter. The nozzle oriface in this data is a .012 cm diameter hole with a .012 cm long throat. The Mach numbers from the velocity distributions occur at larger distances than predicted by Sherman and Ashkenas[29] and may be due to the relative nozzle diameter to throat length of the oriface.

The Mach numbers from the data taken for Fig. II-24 were used to calculate theoretical intensities for several nozzle skimmer distances using Equations 33, 37, and 39. The theoretical prediction is compared to the variation in intensity of an elastically scattered oxygen beam as a function of the argon nozzle skimmer distance and is shown in Fig. II-25. This simple model predicts the qualitative behavior fairly well as shown in the

Fig. II-24. Velocity distributions of an argon nozzle with a .005 inch diameter oriface and a .005 inch long throat. The various velocity distributions were deconvoluted from time-of-nozzle-skimmer distance (in nozzle diameters-L/D). The Mach number is also given for each distribution.

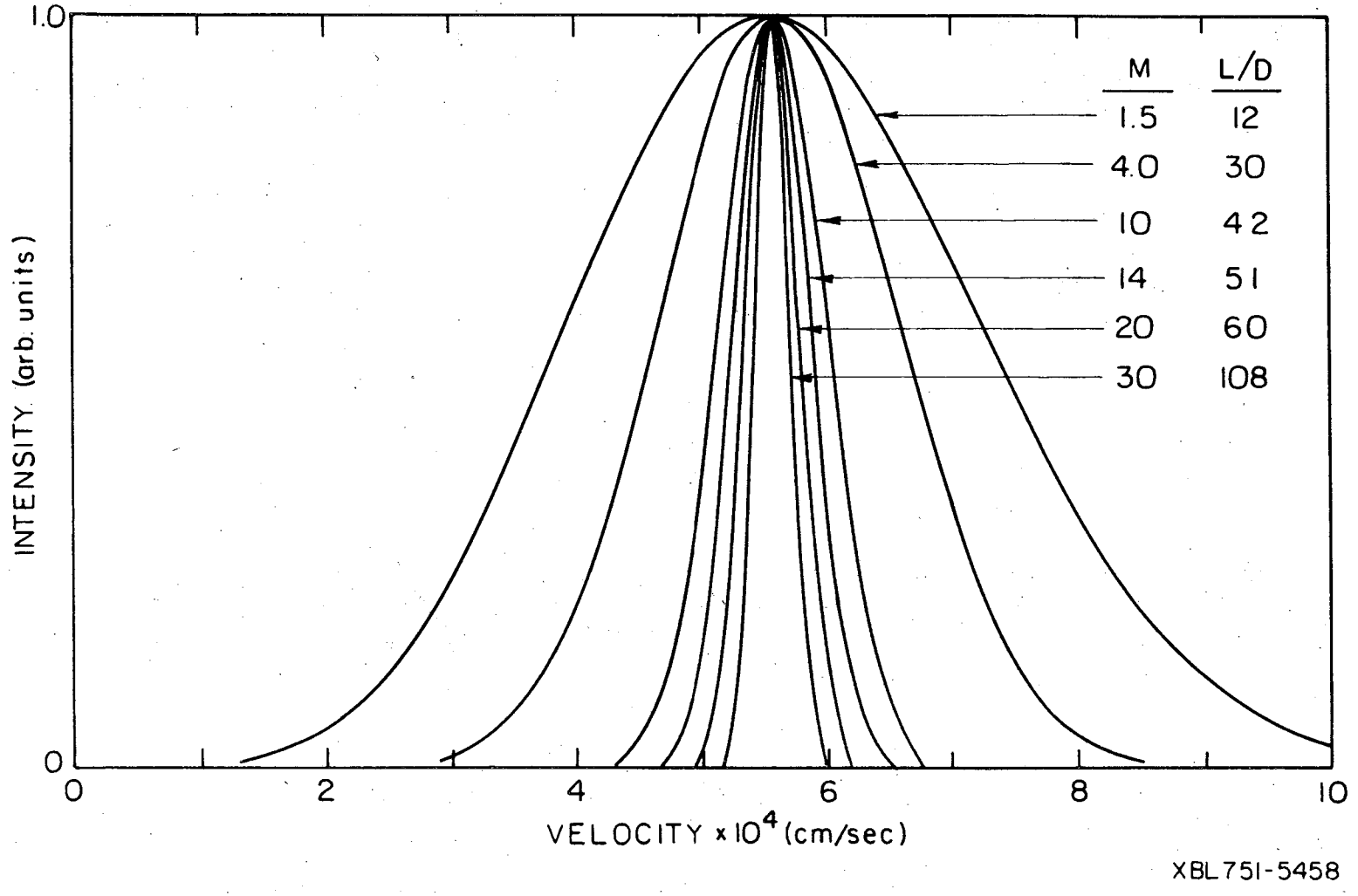
1.0
0
INTENSITY (arb. units)
0
2
4
6
8
10
VELOCITY x 10^4 (cm/sec)
M
L/D
1.5
12
4.0
30
10
42
14
51
20
60
30
108
XBL751-5458

Fig. II-24.

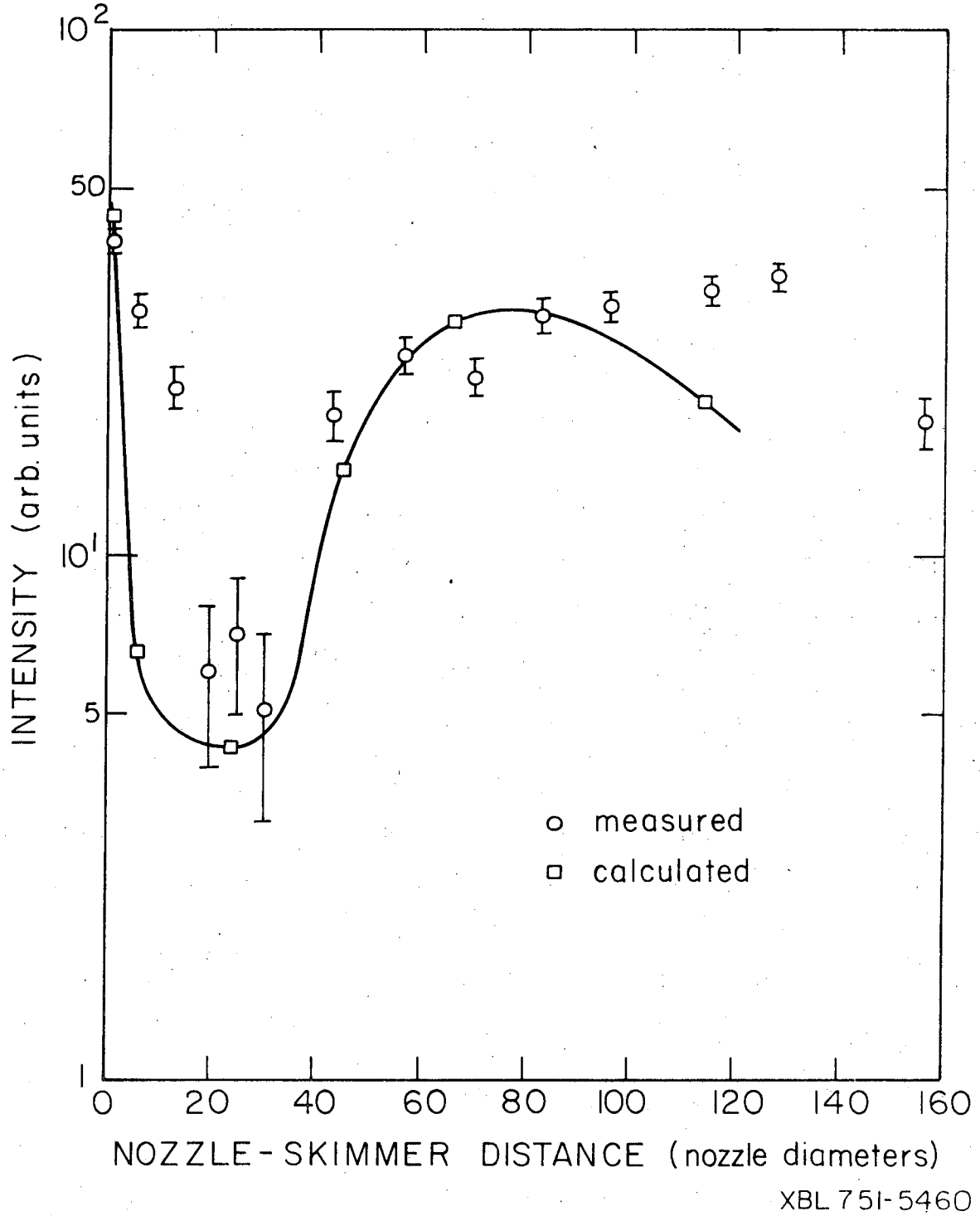

Fig. II-25. Nozzle intensity (in arbitrary units) versus nozzle skimmer distance. The circles represent the measured intensity of elastically scattered oxygen from the crossed beam for different nozzle-skimmer-distances. The curve is from a theoretical calculation using the Mach numbers measured at various nozzle skimmer distances shown by the squares.

figure but it does deviate from the measured valves at small and large nozzle skimmer distances. At nozzle skimmer distances of 10 nozzle diameters or less than Mach number is less than 4 which is in a region that is not accurately described by this model. The large increase in intensity at nozzle skimmer distance near zero is from the large angle of the flow subtended by the skimmer oriface. Although large intensities can be obtained in this region, sacrificing the narrow velocity distribution usually cannot be tolerated so the nozzle must normally be run at a large nozzle skimmer distance.

In order to estimate the intensity of the nozzle the attenuation of the other beam was measured. A typical measured beam attenuation for various beams was between 0.2 and 1.0 percent when the nozzle skimmer distance was set to give a narrow velocity distribution and maximum intensity. Unfortunately, this attenuation is smaller than what is expected from calculations for an isentropic expansion. A comparison of the theoretical and measured intensities is shown in Table II-11. Anderson, Andres, and Fenn[28] have also found that the measured nozzle intensity is less than the calculated nozzle intensity. They have found a good correlation between the ratio of the observed intensity to the calculated intensity and the Knudsen number Kn(mean free path divided by the oriface width) divided by the Mach number (M). For values of the Knudsen number divided by the Mach number of less than 0.1 the ratio of observed intensity to calculated intensity is equal to this number. For values above 0.1 the ratio does not continue to increase linearly with K_n/N_1 but rather, falls off faster as the nozzle is operated at higher pressures. Anderson and Fenn attribute this to an interaction between the nozzle flow and the

Table II-11. Comparison of theoretical intensities and measured intensities for Argon and Oxygen.

Parameter	Valve
Calculated total cross section*	500 $\mathring{A}^2$
Nozzle-skimmer distance	60 nozzle diameters
Width of collision zone	0.2 cm
Calculated number density of beam 1 at collision zone	5.15×10^{13} Molecules/$_{cm}^3$
Calculated beam attenuation	39%
Number density at skimmer	1.64×10^{15} Molecules/$_{cm}^3$
Knudsen # at skimmer	1.42
Measured beam attenuation	0.5%
Measured number density of beam 1 at collision zone	5×10^{11} Molecules/$_{cm}^3$
Beam Mach number	20

*Calculated from the dispersion force potential using values measured by Tully and Lee.[31]

skimmer oriface which causes a disturbance in the beam flow. If this is taken into account for the nozzle in this apparatus, a beam attenuation of approximately 2% should be seen. This is still about a factor of 5 higher than we measure. Since the Mach number continues to increase as the nozzle - skimmer distance is increased an attenuation of the nozzle flow in the source chamber is unlikely to be causing the attenuation. An explanation for this could be that the beam could be attenuated by a high pressure in the collimation chamber downstream of the skimmer. A pressure of 5×10^{-4} torr in the collimation chamber would cause a 50% beam attenuation on passing through the chamber. Each time the nozzle source was used in a different experiment the nozzle skimmer distance was adjusted so as to give a maximum elastically scattered signal from the other beam. The time-of-flight distributions were measured for the nozzle skimmer distance used in each experiment.

F. High Temperature Oven Source

The high temperature source in this apparatus used to generate salt or metal beams is capable of operating at temperatures of up to 1700°C. The oven essentially consists of a cylindrical molybdenum crucible approximately 25 cm high and 1.9 cm in diameter which can hold about 50 cm^3 of salt or metal. The crucible is encircled by two helical 3/16 inch diameter molybdenum rods which are attached to a water cooled copper block at each end. This is then heated by a 10 volt, 600 amp power supply which in turn radiatively heats the crucible. The heating coil and crucible are enclosed in a cylinder of Zircar[32] heat insulation which is in turn enclosed in a copper shroud which is attached to the top copper block. The crucible is supported on the bottom by two sapphire balls and on the top by a spring

loaded pressure plate pushing down on a sapphire ball. The vertical slit in the oven is 0.63 cm high and .025 cm wide. The temperature of the oven is measured by a Platinum - Platinum 13% Rhodium thermocouple placed next to the oven crucible and checked with an optical pyrometer. Figures of this source and further details will be described by A. Freedman.[33]

G. Time of Flight Measurements

The velocity distributions on this instrument are measured by a time of flight technique. A schematic description of the time of flight system is shown in Fig. II-26. The heart of the time of flight data acquisition system is a Digital Electronic Corporation PDP-8 computer with 4K of memory. As shown in the figure, two blocks of storage locations each with 256 locations are set aside to store data directly from the molecular beam apparatus. One block stores data when the system is in the beam on mode and the other block stores data from the beam off mode. One of the phototransistors on the beam modulation wheel initiates a pulse which controls a gate that directs the data to either the beam on or beam off storage locations. This line also contains a variable delay denoted by "variable throw out time" in the figure which allows a delay time to be set that stops the computer from collecting data when the beam is in a transient mode of turning on or off. The time of flight spectrum is obtained by chopping the signal with a slotted wheel that can be turned at various velocities. The wheel is located immediately before the first entrance to the detector chamber. As the slot in the wheel moves past the detector opening a segment of molecules start to fly through the detector chamber. At the same time that the molecules start to move into the detector a pulse is initiated from the photodiode on the time of flight wheel that causes the location counter to reset

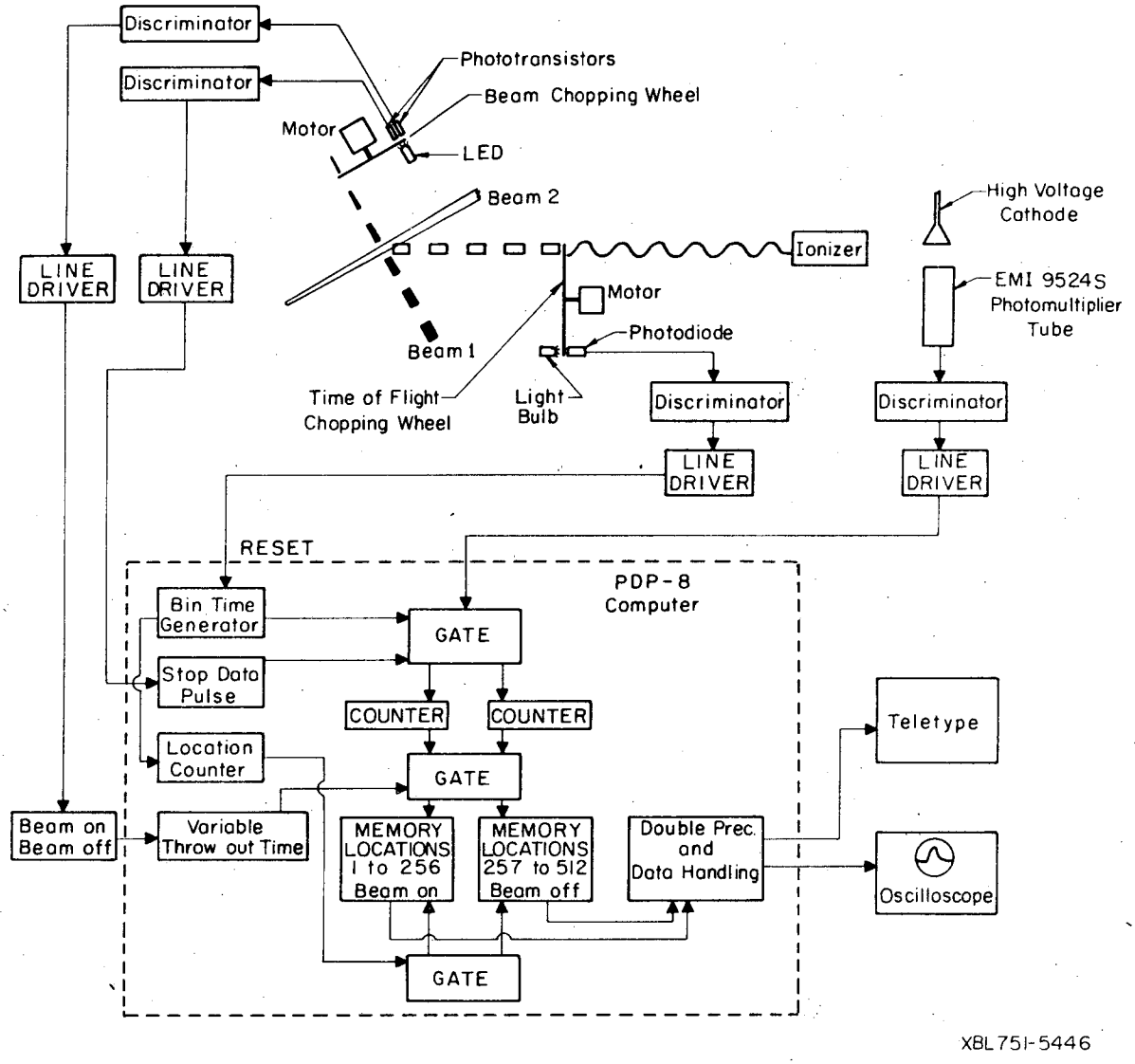

Fig. II-26. Schematic diagram of the time-of-flight data acquisition system. Blocks inside of dotted line are contained in the computer.

to zero. This then sets bin 1 (location 1) as the initial time slot for collecting data. As the molecules travel through the detector they are ionized somewhere in the ionizer and then accelerated toward the counting section of the detector where they are detected and formed into a pulse by the photomultiplier and discriminator. The pulse then goes through a gate and into one of two counters. Two counters are used so that as one counter is transferring information into a storage location the other is counting pulses from the detector. The time at which the gate switches the pulses from one counter to the other is controlled by the bin time generator. The bin time generator also controls the length of time that data will be collected in each bin. This allows the utilation of only 1 bin for each time of flight wheel pulse up to 256 bins per pulse. The limit on the smallest time allowed for a bin is 3 microseconds which is determined by the cycle time of the computer. To keep from counting only part of a time of flight pulse due to the beam chopping wheel turning on or off, an "about to turn off" pulse is generated from another phototransistortor on the beam chopping wheel which causes the computer to take a last time of flight measurement and then shut off until the next beam on or beam off signal comes.

When one of the data storage locations is filled at a value of 4096 an interrupt is generated and the data from all the direct access locations are stored in other double precision locations in the computer. While the computer is collecting data (actually during a lapse in one of the cycles), the time of flight distribution of either the beam on, beam off, or difference between the two can be stored on the oscilloscope. When enough data has been taken for a good time of flight distribution the number of counts

in each bin can be printed out on the teletype. The design of the counting and gating circuits and the interface with the computer has been done by Tim Parr and will be found in his thesis.[34]

The measured time of flight distribution could be transformed directly to a velocity distribution if the time of flight wheel slot open time (gate function) is small compared to the width of the time of flight distribution. In order to make the time of flight wheel gate function small the slots and detector entrance must be made very small which decreases the transmission of the wheel or the wheel must be turned very fast which means the number of slots on the wheel must be less or severe overlap between pulses will be encountered and correlation techniques must be used. The finite length of the ionizer compared to the flight path also causes difficulties in a direct transformation from a time of flight distribution to a velocity distribution.

This problem has been treated[33] by assuming a functional form for a velocity distribution and convoluting this with the gate function for the time of flight wheel and the ionizer and then comparing the calculated distribution with the measured time of flight distribution. The parameters of the velocity distribution are changed until a good fit is achieved between the calculated distribution and the measured time of flight distributions. The rate at which particles will be detected is given by

$$N_t(t) = N(v)\ G(L,\ v,\ t)\ dL\ dv \qquad (39)$$

where N(v) is the velocity distribution for either a flux or number density measurement and G(L,v,t) is the gate function for the detector. L is the distance downstream from the time of flight wheel, v is the velocity of the

particles and t is the time the particle is counted with t = 0 being when the first particles start through the detector. The gate function essentially gives the time dependence of the rate of arrivel at the detector of a monoenergetic beam of particles due to the spreading caused by the length of the open time at the time of flight wheel slot and the detector slit together with the different path lengths due to the length of the ionizing region. The effect of the time of flight wheel slot width and detector entrance width are shown in Fig. II-27. F is the width of the slot in the time of flight wheel and h is the width of the detector entrance slit. If w is the real time width of the time of flight wheel slot then the points on the trapezoid are a = 0, b = $\frac{h\omega}{f}$, c = ω, and d = $(f+h)\omega/f$. The time at which the particle is ionized in the ionizer is correlated with the time it passed through the chopping wheel by

$$t' = t - \frac{L}{V}$$

where t' is the time that it passed through the chopping wheel, t is the time at which the particle was ionized in the ionizer some length L from the chopping wheel and V is the velocity of the particle. The time of flight wheel expression is broken into four parts and integrated over L from the distance to the front of the ionizer, L_1, to the distance to the rear of the ionizer, L_2. This then given an expression than can be combined with equation 39 to give

$$N_t(t) = \int_0^\infty G(t,v)\ N(v)dv \qquad (40)$$

which is then numerically integrated to give the time of flight distribution $N_t(t)$.

Figure 27a. The figure at the left illustrates the relative time-of-flight wheel slot and detector entrance widths. The diagram at the right shows the time-of-flight wheel gate function. The top and bottom width of the trapezoid are shown where ω is the time width of the time-of-flight wheel slot. The time at the points on the trapezoid is $a = 0$, $b = h\omega/f$, $c = \omega$, $d = (1+h/f)\omega$.

Figure 27b. The gate function for two different particle velocities. For each gate function $h = 0.3$, $f = 0.44$, and $\omega = 74$ μsec. This illustrates how the ionizer length "smears" the time-of-flight wheel gate function. Time $t = 0$ is when the first particles start through the detector.

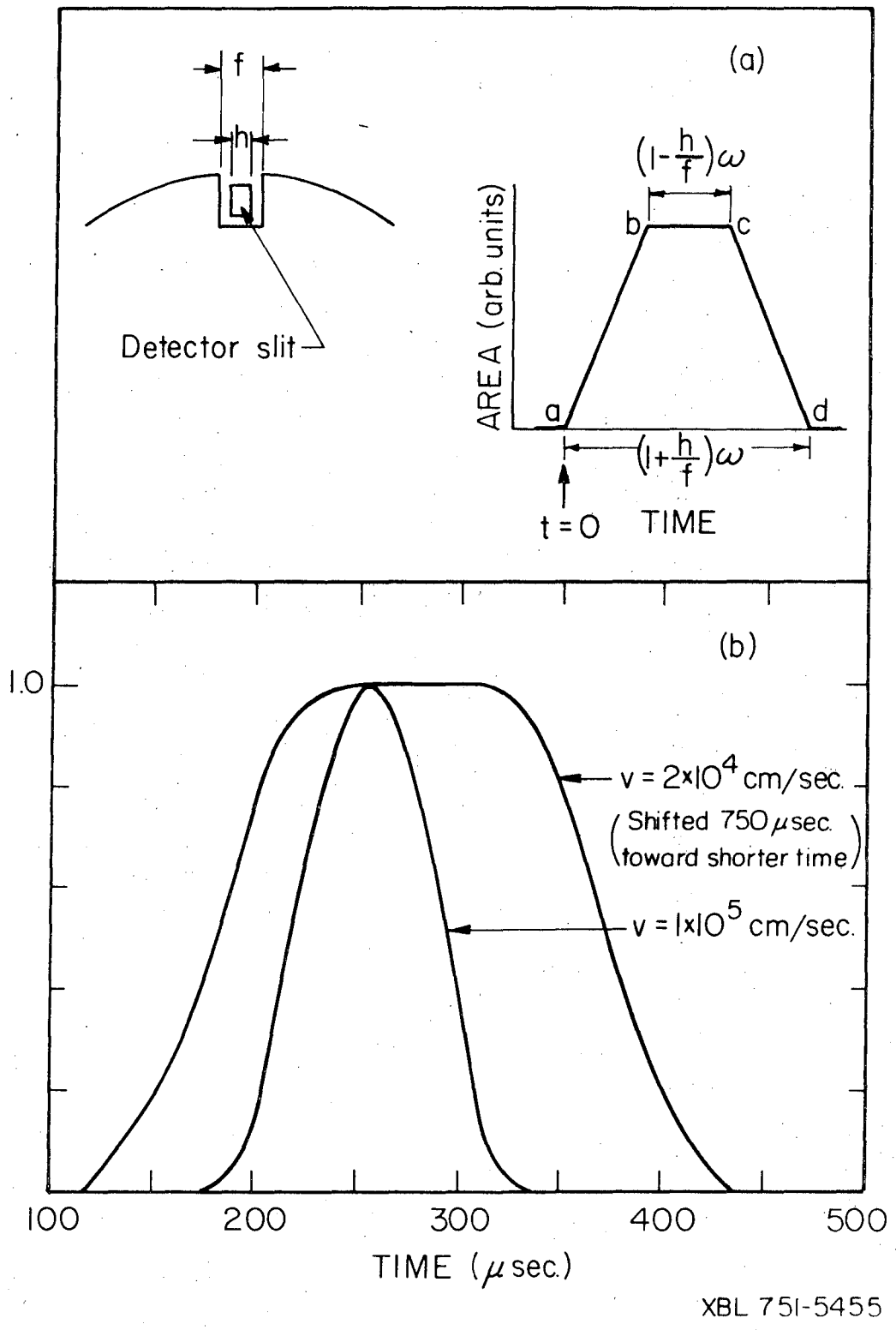

Fig. II-27 (a & b).

Various functional forms in terms of number density distributions such as a Maxwell Boltzman distribution or a nozzle distribution are used for N(v) and the results are then compared to the measured distribution.

APPENDIX 1

List of Apparatus Mechanical Drawings and LBL Numbers*

1. Vacuum Chambers

A. Source Chambers

outside side chamber	12N4294
side chamber stand	12N4304
inside side chamber #1	12N4316
inside side chamber #2	12N4326
side chamber #1 flange	12N4232
10-20 adapter flange	12N4823
side chamber flange	12N5263
side chamber feedthrough flange	12N5283
general side chamber feedthrough	12N5332
high current feedthrough	12N5352
side chamber ion gauge feedthrough	12N5362

B. Collimation Chambers

collimation chamber	12N4114

C. Collision Chamber

12" lip flange for cold shield	12N4062
6" lip flange for cold shield	12N4072
bottom lip of cold shield	12N4083
rotating ring	12N4093

*These drawings are filed at the Lawrence Berkeley Laboratory, copies of LBL drawings whose numbers are cited here may be obtained by writing to Lawrence Berkeley Laboratory, Technical Information, Building 90, Room 3118, Berkeley, California 94720.

main chamber stand	12N4104
main chamber	12N4126
cold shield	12N4136
bearing retainer ring	12N4283
side plate	12N4623
liquid nitrogen feed elbow	12N4633
side flange	12N4643
lid sprocket	12N4813
viewport holder	12N5273
main chamber ion gauge feedthrough	12N5372
ion gauge lead feedthrough	12N5382
main chamber assembly	12N6084
main chamber assembly top view	12N6043

D. Detector Chamber

detector rotating chamber	12N4146
gate holder	12N4182
gate valve parts	12N4192
valve slide	12N420A2
ionization chamber	12N4724
internal gear support	12N5161
counter swivel	12N5171
grip plate	12N5181
gate valve drive assembly	12N5192
counter support	12N5202
vernier support	12N5242

ring vernier	12N5252
liquid helium transfer tube	12N5654

2. Sources

A. Nozzles

dovetail	12N4212
gear support plate	12N4222
dovetail drive assembly	12N4243
nozzle source assembly	12N5413
slide rod support parts	12N5422
nozzle dovetail fixture	12N5432
nozzle slide	12N5442
cooling shield and support	12N5452
nozzle feed	12N5462
nozzle	12N5472
skimmer	12N5481
nozzle skimmers	12N6032
collar and gasket	12N5491
nozzle heater	12N5501
slide rod support front plate	12N6012
dovetail #3	12N6022
nozzle source	12N6073

B. Oven

bottom copper block	12N5511
top copper block	12N5562
molybdenum crucible	12N5532

Mo spiral heating mantle	12N5812
oven mount - top SS plate	12N5822
oven support - horizontal motion	12N5863
oven mount - vertical motion	12N5853

C. General

beam flag	12N4252
beam flag holder	12N4263
beam flag assembly	12N4273
beam chopping wheel	12N5581
solenoid support	12N5211
beam flag support	12N5221
beam flag 2	12N5231
deflector wedge	12N5661
beam deflector flange	12N5672

3. Detector

A. Ionizer

alumina support rods	12N4831
alumina rod holder	12N4841
lens #2	12N4851
lens #1	12N4861
filament tension support	12N4871
filament holder 1	12N4881
filament holder 2	12N4891
alumina spacers	12N4901
electrical connector	12N4911
ionizer grid	12N4922

ionizer shield	12N4932
ionizer support plate	12N4943
ionizer assembly	12N4953
B. Quadrupole	
quadrupole support flange	12N5612
UHV - quadrupole feedthrough	12N5402
C. Scintillation Unit	
scintillator feedthrough	12N4963
high voltage cathode	12N4972
high voltage insulator	12N4982
plastic scintillator	12N4991
support insert	12N5001
inserting tool	12N5011
exit lens #1	12N5021
exit lens #2	12N5031
exit lens #3	12N5041
exit lens support rod	12N5051
support nut	12N5061
alumina spacers	12N5071
alumina spacers 2	12N5081
alumina spacers 3	12N5091
support plate	12N5101
support nut 2	12N5111
corona ball	12N5121
photomultiplier holder	12N5133
scintillator housing	12N5144

ion detector assembly	12N5156
high voltage feedthrough	12N5342
photomultiplier & photodiode feedthrough	12N5392

4. Time of Flight

time of flight wheel support #1	12N5632
time of flight wheel support #2	12N5622
time of flight wheel	12N5642
time of flight guide	12N5711
slide cover plate	12N5721
time of flight slide	12N5731
photodiode holder	12N5741
photodiode cover plate	12N5751
P. C. board support	12N5761
LED - holder	12N5771
LED - support	12N5781
time of flight holder	12N5792

5. Alignment

ionization chamber entrance slit	12N5602
detector chamber #2 slit	12N5591
collimation slit #1	12N5682
collimation slits electrical connector	12N5692
collimating slit #2	12N5702
double collimation slits #1	12N5832
double collimation slit #2	12N5842

APPENDIX 2

List of Apparatus Electronic Diagrams and LBL Numbers

System wiring diagram MIBA - Kathy	8S3175
Single vacuum interlock	8S2803 - 1
NRC interlock	8S9993
Dual vacuum interlock	8S5754
Dual liquid nitrogen trap filler	8S7252
Ion gauge 5 position switch panel	8S7392
High temperature oven power supply	8S7351
PM17AY Relay Panel	8S9012
NRC noninterlock gauge	8S3102

APPENDIX 3

Assembly Procedures

This appendix is divided into subsections for the assembly of various parts of this molecular beam apparatus. When assembling or disassembling a particular part of the apparatus, the entire assembly procedure should be read before proceeding. Failure to do this may cause extensive damage to expensive parts. The assembly procedures are listed in a sequential form and in most instances references will be made to an assembly figure in this chapter or an LBL blueprint.

The following is a list of the assembly procedures covered in this appendix:

1. General assembly sequence.
2. Main chamber leveling
3. Diffusion and mechanical pump installation
4. Collimating chamber installation
5. Rotating ring assembly
6. Detector chamber installation
7. Cold Shield installation
8. Detector pump installation
9. Detector assembly
    a. Ionizer
    b. Quadrupole
    c. Scintillation unit
    d. Overall detector assembly

10. Side chamber and source wiring
11. Nozzle assembly
12. Beam chopper & beam flags assemblies
13. Time-of-flight wheel assembly

1. General Assembly Sequence

When this molecular beam apparatus is assembled from its totally unassembled condition a certain sequence of procedures is necessary for proper installation. The following assembly procedures must be done in the order listed. All other assemblies may be done in any order.

1. The main collision chamber once on its stand must be leveled.
2. The liquid nitrogen baffles, diffusion pumps and mechanical pumps that fit on the bottom of the main chamber must be installed.
3. The collimation chamber must be installed.
4. The rotating ring must be installed.
5. The detector chamber lid must be put in place.

2. Main Chamber Leveling

1. Move the main chamber, on its stand, to the desired location.
2. Using a machine level (e.g. Pratt & Whitney) placed on the rotating lid bearing surface of the main chamber, adjust the four leveling screws on the main chamber stand until the main chamber is level in all directions.

3. Diffusion Pump and Mechanical Pump Installation

1. Clean the liquid nitrogen baffles, the diffusion pumps and the mechanical pumps according to the procedures listed in the appropriate instruction manual.

2. Refer to the rough outline sketch in Fig. II-28 for the relative position of the baffles and pumps under the main chamber.
3. Place Kinney KC-15 mechanical pumps 1 and 3 in position as shown.
4. Bolt NRC 6" liquid nitrogen baffle into place.
5. Bolt the CVC 6" diffusion pump onto the NRC 6" LN_2 baffle with the exhaust flange in the position shown in Fig. II-28.
6. Bolt the NRC VHS-6 6" diffusion pump onto the port hole for collimation chamber 1 with the exhaust flange in a position as shown in Fig. II-28.
7. Bolt the other NRC 6" diffusion pump onto the porthole for collimation chamber #2 with the exhaust flange in the position shown in Fig. II-28.
8. Bolt the CVC 10" liquid nitrogen baffle onto the 10" porthole for the main chamber aligning the fill and vent ports as shown.
9. Bolt the 10" CVC diffusion pump onto the 10" liquid nitrogen baffle and align the exhaust flange as shown.
10. Place the Kinney KC-15 mechanical pump in position as shown.
11. Fill the four diffusion pumps with Dow Corning 705 diffusion pump oil.
12. Connect the exhaust from the diffusion pumps to the intake of the mechanical pumps as follows:

    NRC 6" D.P. 1 to Mechanical pump 1.

    NRC 6" D.P. 2 to Mechanical pump 2.

    The CVC 6" and 10" diffusion pump to Mechanical pump 3.
13. Connect the cooling water to the four diffusion pumps. Then connect the drain of each diffusion pump to the proper water

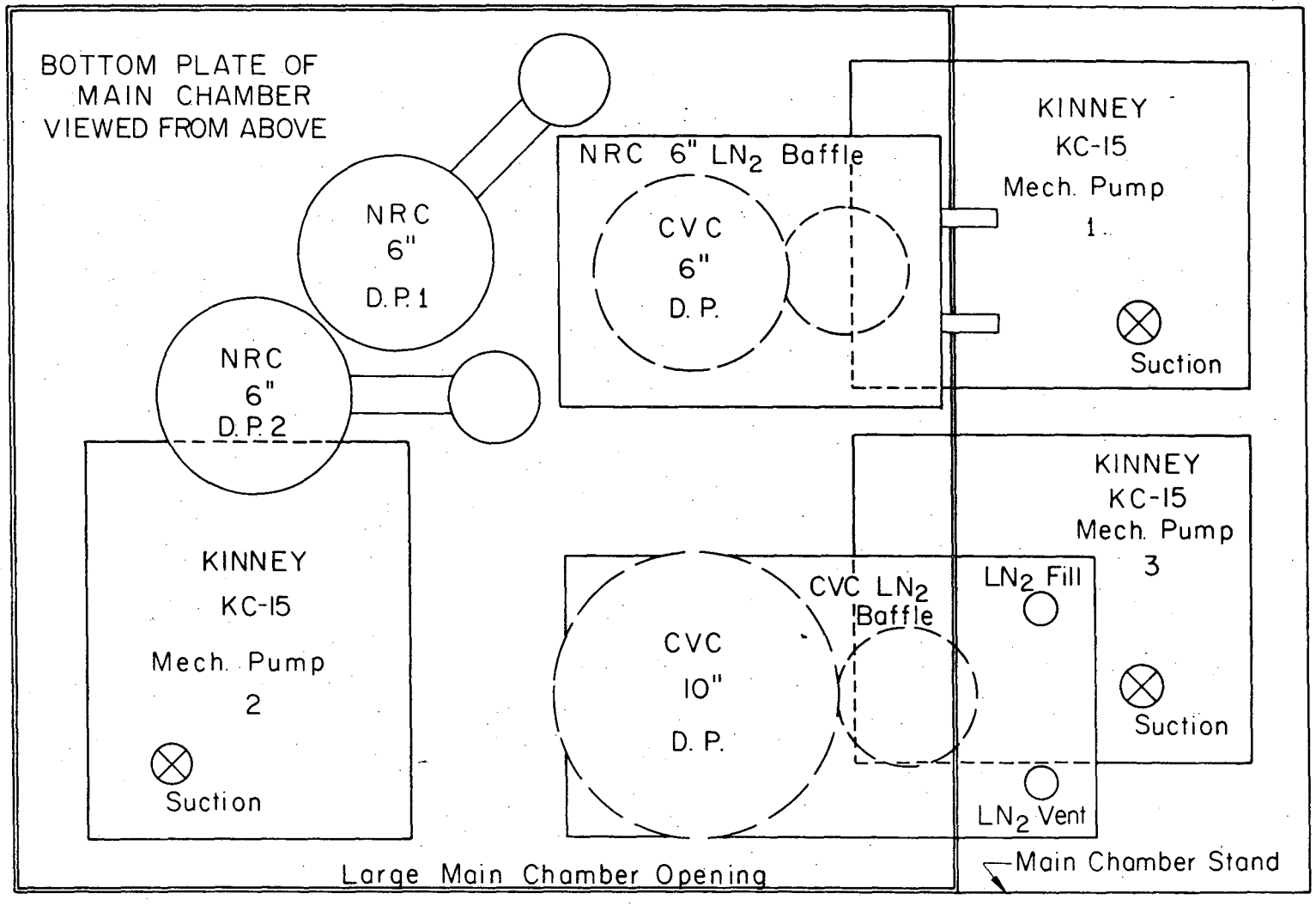

XBL 751-5443

Fig. II-28. Pump location.

interlock and connect the interlock to the water drain.

14. Referring to System Wiring Diagram MBA - KATHY (blueprint 8S3175) wire the 4 diffusion pumps and the three mechanical pumps. Referring to the same blueprint connect the appropriate wires to the water and temperature interlocks on each diffusion pump. Also connect the NRC thermocouple vacuum gauge tube to the proper vacuum interlock.

4. Collimating Chamber Installation

The collimating chamber has four flanges that must bolt to three different surfaces so patience is needed to install the collimation chamber.

1. Place the collimation chamber into the main chamber.
2. Shims must be placed between the flanges that connect each chamber to its diffusion pump and between 20 inch flange of collimation chamber 2.
3. Cover the diffusion pumps so bolts or screws won't fall in.
4. Gently maneuver the collimation chamber into place and start putting a few 1/4-28 socket head screws in the holes of all four flanges.
5. After several screws in each flange are started, put in as many screws as possible. Now start tightening all of the screws until all four flanges are snug against the respective main chamber surface.
6. Careful attention should be paid to make sure that the shim on the 20 inch flange does not block the 20 inch hole in the main chamber since this will make it impossible to put the source chamber in place.

5. Rotating Ring Assembly

1. Clean the O-ring grooves and the surrounding parts of the main chamber so that all surfaces are free of dust and lint etc. Rinse all of the surfaces with acetone and reagent grade methanol.
2. Refer to Figs. II-1 and II-10 for the location and position of the various rotating ring parts.
3. Turn the rotating ring upside down and lay it on a clean flat surface. With extreme care, place the Kaydon bearing on the rotating ring. The bearing ball spacer should be positioned so that the solid part of the brass spacer is facing upward when the assembly is placed in the apparatus.
4. Once the bearing is in place, a .005 inch thick brass shim stock must be inserted all around the rotating ring between the bearing and the rotating ring as shown in Fig. II-10. THIS MUST BE DONE TO PREVENT THE ROTATING RING FROM ROTATING OFF CENTER AND SCRATCHING THE MAIN CHAMBER SURFACE AND RUINING THE O-RINGS.
5. Clean the rotating ring and bearing surfaces thoroughly with acetone and reagent grade methanol.
6. Place the scraper O-ring in the groove on the rotating ring as shown in Fig. II-10. Grease should not be necessary since there is only light contact between the O-ring and the main chamber surface.
7. Carefully place the TEC-RINGS (No. A01926) in the two main chamber grooves. Extreme care must be taken not to scratch any of the Tec-ring surfaces. Note the orientation of the Tec-rings in the grooves in Fig. II-10. It may be helpful to heat the Tec-rings slightly to.

facilitate their installation.

8. Place the rotating ring and bearing in the proper position (such that the detector chamber can be inserted without having to rotate the rotating ring) over the main chamber. Gently lower the rotating ring into the hole. If the assembly does not seat with gentle tapping, use 4 "C" clamps evenly spaced around the ring and clamp between the top of the rotating ring and the bottom side of the top main chamber plate. Gradually tighten the four "C" clamps until the bearing seats on its outside race. Make certain that as the rotating ring starts to pass over each Tec-ring that the top of the Tec-ring is against the side of the rotating ring and not underneath the bottom of the rotating ring.
9. Place the bearing retainer ring in place and secure with the proper bolts.

6. Detector Chamber Installation

1. The rotating lid, ionization chamber, 26 pin electrical feedthrough, the quadrupole feedthrough, and the 1 1/2 inch Ultek blank flange should all be chemically cleaned and passivated, rinsed with water and finally reagent grade acetone.
2. Extreme care must be used in handling these clean parts in order to prevent getting body oils on them. The parts should only be handled using clean cloth gloves.
3. Clean the face sealing O-ring groove on the rotating ring so that it is free of dirt and dust particles. Rinse the O-ring groove with acetone and reagent grade methanol.

4. Clean the Viton O-ring and coat it with Apiezon L vacuum grease. Place the O-ring in the O-ring groove.
5. Check to see that the rotating ring is in the proper position.
6. Attach the wire rope cables to the lift holes and attach the hoist hook making certain that it is not more than 10 inches above the top of the detector chamber.
7. Lift the detector off the ground. Check to see that the detector is suspended in a horizontal plane. Remove the support legs from the detector.
8. Lift the detector over the top of the main chamber and position the two slots along the perimeter of the detector over the two pins in the rotating ring.
9. Gently lower the detector through the hole taking care not to bump any surfaces. Once the slots reach the pins lower the detector slowly the rest of the distance while always making certain that the detector is level.
10. Once the detector is seated cover the detector chamber holes to prevent dirt from entering.
11. Remove the hoisting feet from the detector chamber and place the large gear in place on top of the rotating ring. Position the gear so that the missing teeth will not come in contact with the chain when the detector is rotated to its two extremes.
12. After the gear is on the rotating ring place the 3/4 inch chain in place and tighten the drive gear assembly.
13. For the installation of the ionization chamber see the alignment section of this chapter.

7. Cold Shield Installation

    1. Thoroughly clean the inside main chamber walls.
    2. Make a sling from the polypropylene rope and using the crane place the cold shield in the main chamber.
    3. Align the port holes in the cold shield with the holes in the main chamber.
    4. Raise the cold shield on its three stainless steel feet until the top edge is as close as possible to the main chamber wall without touching it.
    5. Put the liquid nitrogen feedthrough elbow in place. Connect the gas venting tube to the metal gas vent tube which protrudes from the Ultek flange on the 4 inch copper tube.
    6. Connect the UHV flanges using a 2 inch copper gasket. All the bolts must be put in to connect these flanges or the seal will leak.
    7. Connect the liquid nitrogen elbow flange (O-ring 2-364).

8. Detector Pump Installation

    1. Refer to Fig. II-29 for the relative orientation of the various detector pumps.
    2. Clean off all of the ultra high vacuum flange surfaces. Wear cloth gloves while doing all ultra high vacuum assemblies.
    3. Use 6 inch copper gaskets to make vacuum seals on the three ion pumps.
    4. Hoist the Veeco 225 1/sec ion pump (2) and place it in the correct position over the port hole for detector chamber #2. With the copper gasket in place, lower the ion pump and bolt it into position.

Figure II-29. Top View of Detector Rotating Lid with Pumps and Feedthroughs.

1. Ultek 150 1/sec differential ion pump.
2. Veeco 225 1/sec Mag Ion pump.
3. Veeco 100 1/sec Noble gas pump.
4. Ultek titanium sublimation pump with cryoshroud.
5. Veeco E-beam titanium sublimation pump with cryoshroud.
6. Janis liquid helium pump.
7. 10 liter liquid nitrogen dewar (2).
8. Quadrupole electrical feedthrough.
9. 26 - pin electrical feedthrough.
10. Photodiode feedthrough.
11. Blank flange.
12. 26 - pin electrical feedthrough.
13. High voltage feedthrough.
14. Photomultiplier feedthrough.
15. Gate valve control feedthrough.
16. Blank flange.

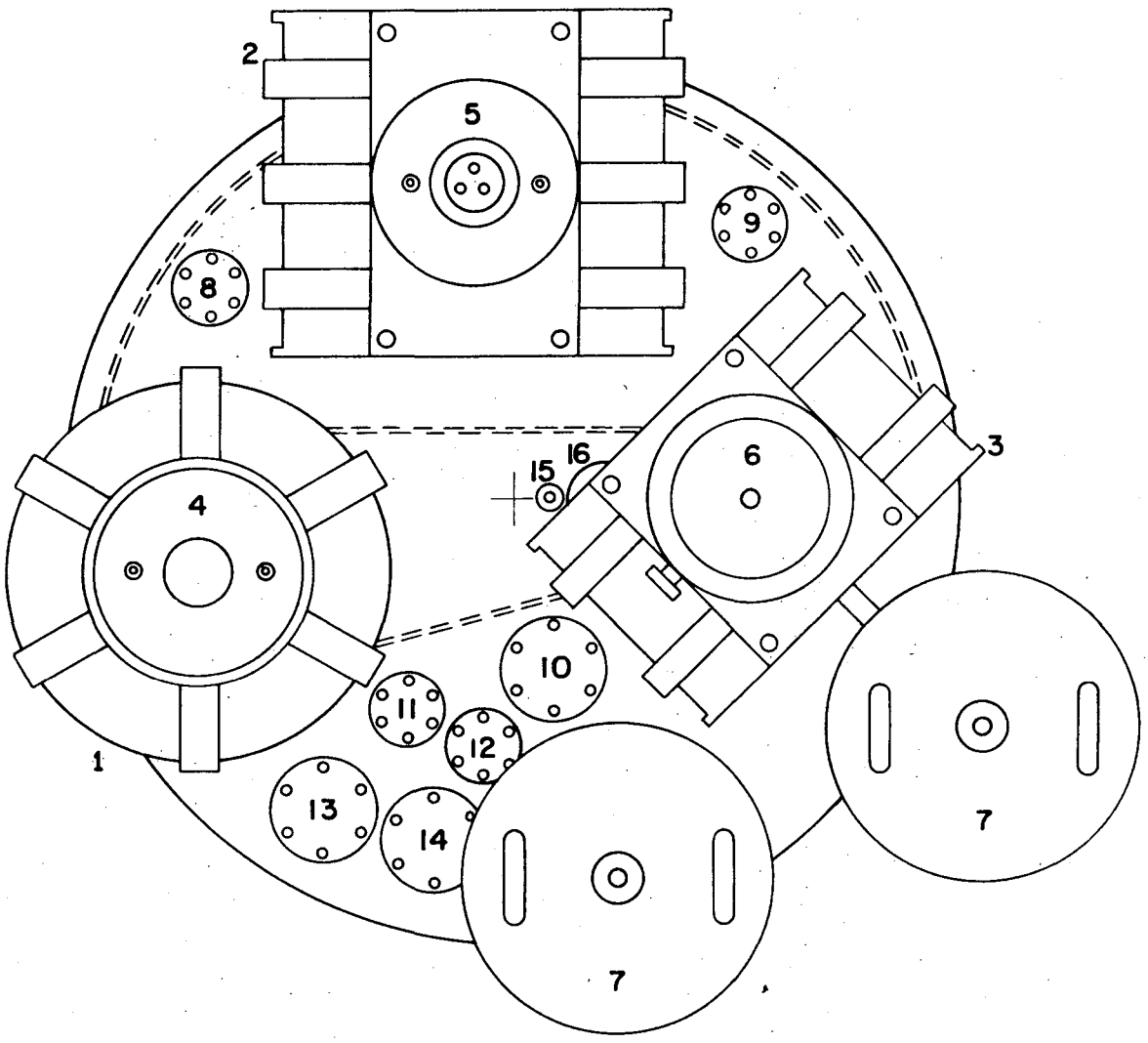

Fig. II-29.

5. Assemble the Veeco E-beam titanium sublimator (refer to operation manual) and insert unit with cryoshroud into the ion pump and tighten the ultra high vacuum flange.
6. Hoist the Ultek 150 l/sec ion pump(1) and place it in the correct position over the port hole for detector chamber #1. With the copper gasket in place, lower the ion pump and bolt it into position.
7. Assemble the Ultek titanium sublimator (refer to operation manual) and insert the unit with the cryoshroud into the Ultek ion pump and tighten the ultra high vacuum flange.
8. Hoist the Veeco 100 l/sec ion pump (3) and place it in the correct position over the ionization chamber flange. With the copper gasket in place lower the ion pump into place and bolt it into position.
9. Place a copper gasket on the top flange of the Veeco 100 l/sec ion pump (3). Lift the Janis liquid helium pump (6) to the top of the apparatus. Carefully place the liquid helium pump on top of the 100 l/sec ion pump and tighten the bolts to make a vacuum seal.
10. Place the Ultek UHV 1 1/2 blank flange over the hole above detector chamber #1 (16).
11. Connect the copper wires for the quadrupole (2) and the high voltage exit lens to the proper feedthrough and bolt into place (8).
12. Connect the wires for the ionizer and exit lenses to the correct positions on the 26 pin feedthrough as shown in the ionizer assembly section. Place the 26 - pin connector in the correct position, check for shorts, and bolt into place.

13. Connect the wires from the respective power supplies to each of the three ion pumps and two titanium sublimation pumps.
14. Bolt on the photodiode feedthrough (10), the blank flange (11), the 26 pin feedthrough (12), the high voltage feedthrough (13), and the photomultiplier feedthrough.
15. Place the 10 liter liquid nitrogen dewars in position and bolt down.

9a. Detector Assembly - Ionizer

1. In assembling the ionizer refer to Fig. II-30 or blueprint #12N4953.
2. The detector parts should be chemically cleaned. The metal parts should be cleaned by cleaning procedure 2 and the alumina parts by cleaning procedure 3. The quadrupole and scintillator parts should be cleaned at the same time if they need cleaning.
3. Referring to Fig. II-30 arrange all of the parts needed in the ionizer assembly. Separate the different size alumina spacers.
4. If the grid support is not wrapped with wire this should be done now. Use .010" platinum wire. Spot weld the wire to the end of the grid support and then wind the wire around the grid so the wire lies in the bottom of the V-notches. When the wire is all wound spot weld the other end.
5. Take the four alumina rod holders (2) and screw them into the ionizer support plate (14). Insert the four alumina rods (1) into each of the alumina rod holders and tighten the set screws. The alumina rod holders must fit flush against the ionizer support plate.
6. Place one 0.143 inch long alumina spacer (6) on each alumina rod.
7. Connect the two halves of lens #2 (3) using the two alumina pins. Gently slide lens 2 over the four alumina rods and down onto the alumina spacers as shown in Fig. II-30.

Figure II-30. Ionizer Assembly

1. Alumina Support Rods (4)
2. Alumina Rod Holder (4)
3. Lens 2a and 2b.
4. Lens 1a and 1b.
5. Filament Tension Plate
6. Alumina Spacer - 0.143 inch long (4).
7. Alumina Spacer - 0.214 inch long (4).
8. Alumina Spacer - 0.073 inch long (4).
9. Alumina Spacer - 0.083 inch long (4).
10. Alumina Spacer - 0.125 inch long (4).
11. Alumina Ring (5).
12. Ionizer Grid.
13. Ionizer Shield.
14. Ionizer Support Plate.
15. Ceramaseal Electrical Feedthrough.
16. Assorted Springs.
51. Filament Holder Nut.
52. Filament Holder Screw.

IONIZER ASSEMBLY

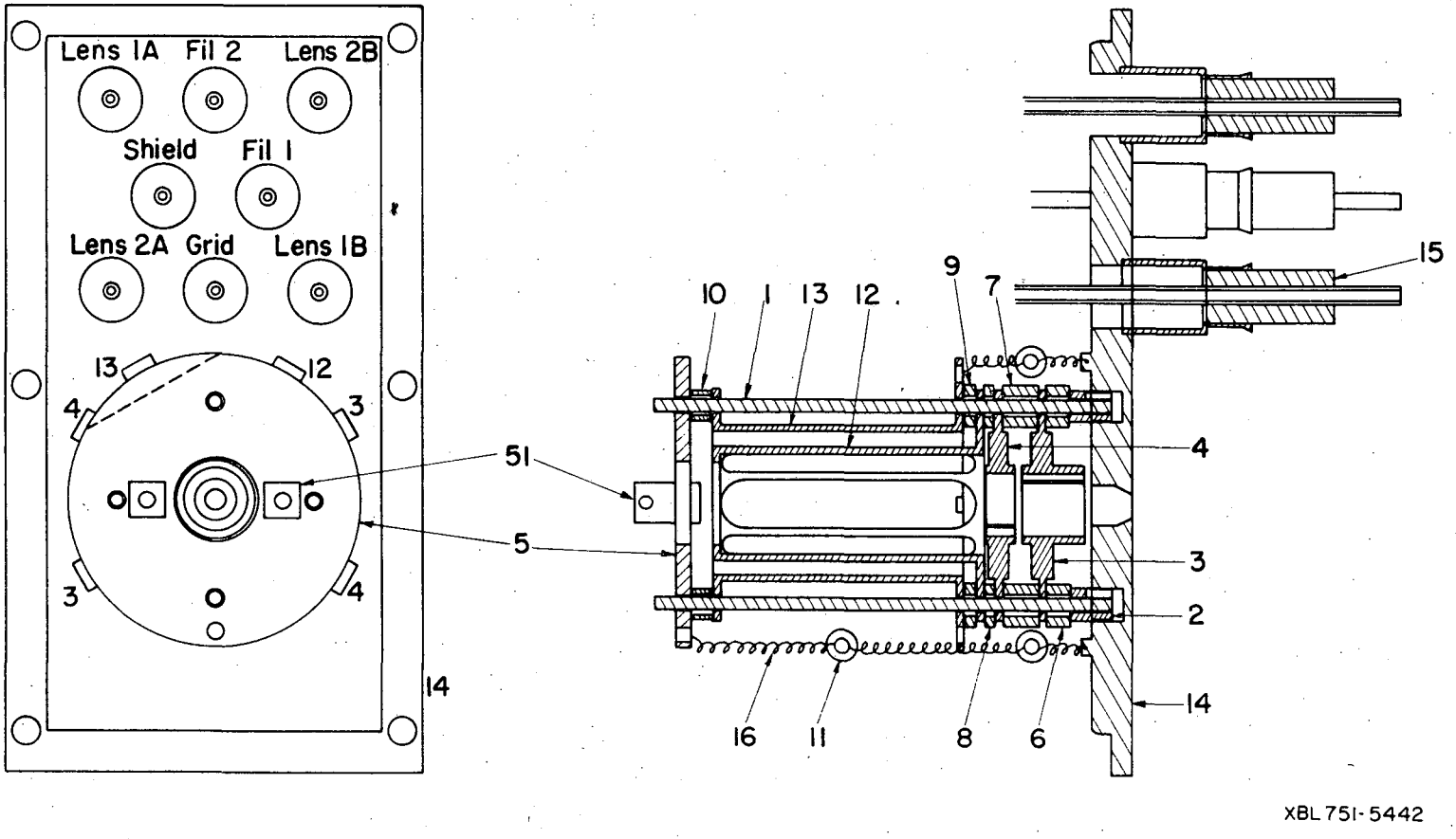

Fig. II-30.

8. Place one 0.214 inch long alumina spacer (7) on each alumina rod.
9. Connect the two halves of lens #1 (4) using the two alumina pins. Gently slide lens 1 over the alumina rods in the position shown in Fig. II-30. This should leave the slits in each lens perpendicular to each other.
10. Place one 0.073 inch long alumina spacer (8) on each alumina rod.
11. Carefully slide the grid (12) over the four alumina rods making sure not to damage the grid wiring.
12. Place one 0.083 inch long alumina spacer on each of the alumina rods.
13. Cut two ribbons of .0005 X .025 1% thoriated tungsten ribbon about 3 to 3 1/2 inches long. Pass the ribbon through the hole on each tab of the shield and spot weld the end of the ribbon to rear of the shield. Make certain that each spot weld is strong since the assembly steps from here on will have to be repeated if a ribbon breaks.
14. With the two ribbons passing through the inside of the shield start to slide the shield onto the four alumina rods as shown in the figure. The rods will pass through the holes in the rear plate of the shield fairly easily. It may be difficult to get the rods to pass through the holes in the front plate of the ionizer. By trying different orientations of the shield the holes may line up. If this doesn't work hold the shield in one hand and try to move the alumina rods by rotating the pieces already assembled.

15. Assemble the two filament holders(51 & 52) on the filament tension support plate (5).
16. Attach the four short spring sets with alumina rings (11) between the shield and the ionizer support plate. Attach the long spring to the shield as shown in Fig. II-30.
17. Place one alumina spacer 0.125 inch long (10) on each alumina rod.
18. Slide the two filaments through the filament holders in the filament tension plate. Check to see that the filaments are not twisted. Place the filament tension plate over the four alumina rods.
19. This step must be done at one time to get equal tension on both filaments. Connect the long spring from the shield to the filament tension plate. Hold down the filament tension plate so there is tension in the spring. Now pull each filament taut and spot weld it to the filament holder. After both filaments are spot welded, gently release the filament tension plate.
20. Using the stainless steel two set screw couplings connect the respective ionizer elements to the proper feedthrough shown in Fig. II-30. The final connection to the filaments on the front of the ionizer should be made with a flexible nickel wire.

9b. Detector Assembly - Quadrupole

1. The quadrupole alignment on the quadrupole adapter flange was described in the alignment section of this chapter. Briefly, the axis of the four poles must be orthogonal to the front face of the adapter flange.
2. The assembly procedure of the quadrupole itself is listed in the EAI quadrupole manual.

9c. Detector Assembly - Scintillation Unit

1. Refer to Figs. II-31 and II-32 for the top view and cross section view of the scintillation unit.
2. All of the detector parts should be cleaned before starting the assembly.
3. Arrange all of the parts on a clean surface and wear cloth gloves while assembling the parts.
4. First assemble the exit lens unit. Insert the 3 support rods (15) into the support plate (28) and fasten with nuts on the other side of the support plate. When looking from the entrance to the exit lens system the clockwise order of the rods will be denoted 3KV, 150 V, and ground. Blueprint 12N5156 shows the position of the various support rod in relation to the rest of the unit.
5. With the support plate end resting on a flat surface place the 2.080 inch long spacer (26) on the 3KV rod, the 1.075 inch long spacer (23) on the 150V rod and the 3.450 inch long spacer (27) on the ground rod. Also place the 1.183 inch long spacer (24) on the 3KV rod.
6. Slide exit lens #1 over the rods and spacers and into position.
7. Place the 0.870 inch long spacer (21) on the 3KV rod the 2.233 inch long and the 0.980 inch long spacer on the 150V rod, and the .980 inch long spacer on the ground rod.
8. Slide exit lens #2 into place and assemble the rest of the spacers and exit lens #3 as shown in Figs. II-31 and II-32.
9. Secure the assembly by screwing the support nuts (16) onto the end of each support rod.

Figures II-31 and II-32. Side View and Top View of the Scintillator Unit.

1. Scintillator Housing.
2. Photomultiplier Holder.
3. Plastic Scintillator (Pilot B).
4. Support Insert.
5. Parker Viton O-ring #2-25.
6. EMI 9524S Photomultiplier Tube.
7. Scintillator Feedthrough.
8. High Voltage Cathode.
9. High Voltage Insulator.
10. Support Nut.
11. Corona Ball.
12. Exit Lens #1.
13. Exit Lens #2.
14. Exit Lens #3.
15. Exit Lens Support Rod.
16. Support Nut.
17. Alumina Insulator (.125 long, 3KV).
18. Alumina Insulator (.125 long, 150V, gnd.).
19. Alumina Insulator (.950 long, 3KV).
20. Alumina Insulator (1.060 long, 150V, gnd.).
21. Alumina Insulator (0.870 long, 3KV).
22. Alumina Insulator (0.980 long, 150V, gnd.).
23. Alumina Insulator (1.075 long, 150V).
24. Alumina Insulator (1.183 long, 3KV, gnd.).

25. Alumina Spacer (2.233 long, 150V).
26. Alumina Spacer (2.080 long, 3KV).
27. Alumina Spacer (3.450 long, gnd.).
28. Support Plate.
29. Locating Pin.
30. 10-32 X 3/8 Allen Head Screw.
31. 5/16 - 18 X 2 Bolt.

ION DETECTOR ASSEMBLY
Side View

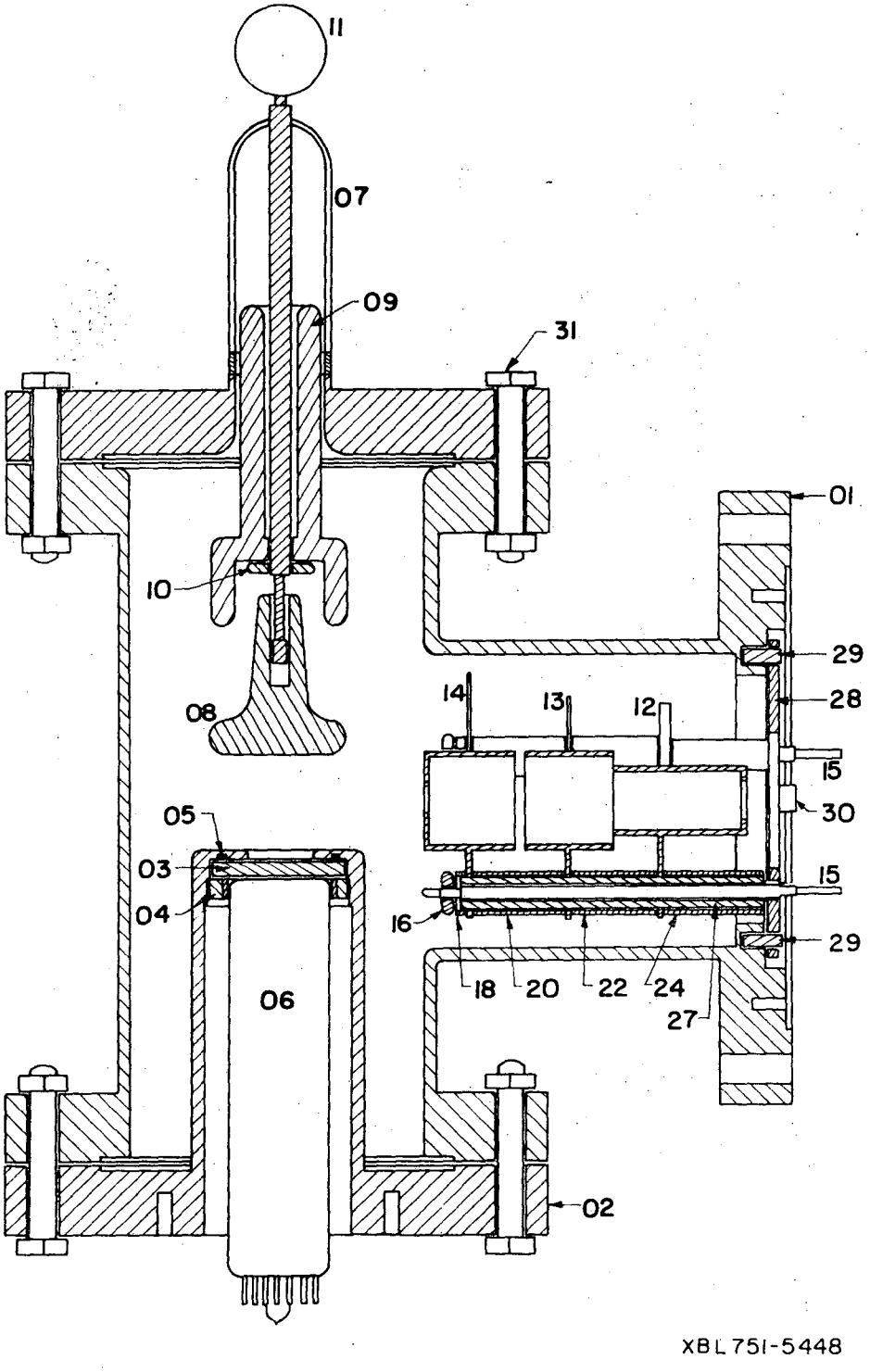

Fig. II-31.

Top View

ION DETECTOR ASSEMBLY

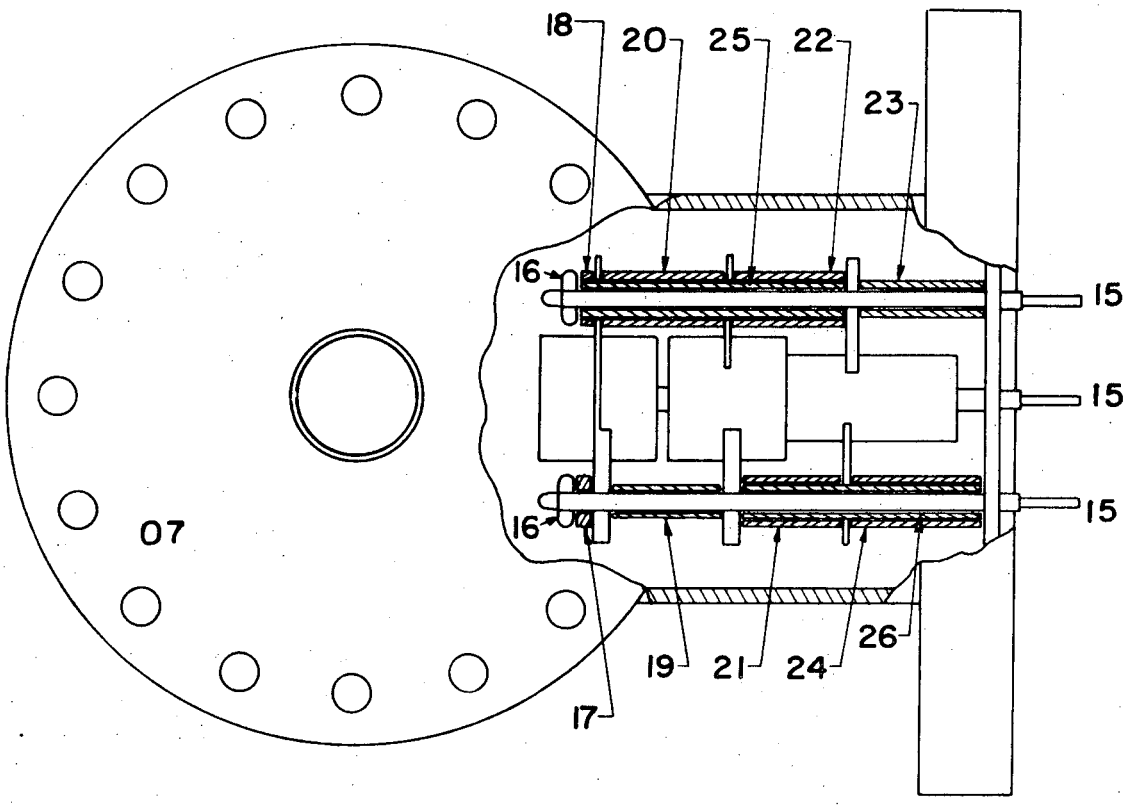

XBL751-5447

Fig. II-32.

10. Carefully place the assembly into the scintillator housing (1) and position the support plate over the two locating pins. Use two 10 - 32 X 3/8 allen head screws to fasten the exit lens assembly in place.
11. Place the high voltage insulator (9) on the high voltage feedthrough rod of the scintillator feedthrough (7) as shown. Screw the support nut (10) onto the rod. Carefully take the aluminum coated high voltage cathode (8) and screw it onto the high voltage rod.
12. Carefully put the high voltage assembly in an upright position and gently lower it into the scintillator housing after placing the 4 inch copper gasket in place. Tighten the two flanges to make a seal.
13. Place the Viton O-ring (5) in the photomultiplier holder (2).
14. Support the plastic scintillator (3) on a 5 inch long rod with the aluminumized side facing up. Slide the photomultiplier holder (2) over the plastic scintillator until the scintillator seats in the proper position. Make sure that the Viton O-ring remains in place. Turn the photomultiplier unit over so the plastic will remain in place.
15. Insert the support insert with the special tool and tighten the insert until the aluminized surface makes contact with the photomultiplier holder housing.
16. Place a copper gasket in the flange groove and bolt the photomultiplier holder into the scintillator housing.
17. This completes the assembly of the scintillation unit. Put

aluminum foil over the entrance flange to keep dirt out.

9d. Detector Assembly - General

1. This assembly assumes that the detector chambers have already been aligned. For alignment procedure see the alignment section of this chapter.
2. Place the assembled ionizer in the ionization chamber with the electrical feedthrough on the upper portion of the support plate. Be careful not to bump the ionizer against the ionization chamber when inserting it. The ionizer plate will locate the ionizer in the correct position. Fasten the support plate to the ionization chamber using six socket head screws which have a hole drilled through the center and which have been chemically cleaned.
3. Using the figure of the ionizer connect the appropriate wire from the 26 pin feedthrough (given in Table II-12) to respective feedthrough. Remember the figure is looking from the inside of the ionization chamber not the outside. The wires from the feedthrough are bare copper and they are spaced by alumina spacers.
4. Place the quadrupole filter in its proper position over the locating pins on the rear of the ionizer support plate. Using the four appropriate screws fasten it in place.
5. Connect the two quadrupole leads to the quadrupole mass filter.
6. Mount the assembled scintillator unit on a lab jack and align the detector chamber flange with the scintillation unit flange. Place a 5 inch copper gasket in place. Now make the two final electrical connections to the low voltage exit lens element and the high voltage lens element. Move the scintillation unit onto the locating

Table II-12. 26 Pin Feedthrough Connections for Detector.

Pin	Element
B	Low voltage exit lens.
C	Filament supply remote sensitivity - neg.
D	Shield.
E	Grid.
F	Filament #2.
G	Focus 1 A.
W	Focus 2 B.
X	Filament #1.
Y	Filament supply remote sensitivity - pos.
Z	Focus 1 B.
d	Focus 2 A.

pins and up against the copper gasket. After making sure the copper gasket is in place tighten the flange bolts. Check for shorts.

7. Bolt the blank flange in place on the bottom of the detector chamber.
8. Connect the quartz insulated high voltage wire to the high voltage cathode feedthrough securing it with the corona ball.

10. Side Chamber and Source Wiring

1. The configuration of the outside source chambers is shown in Fig. II-3. All the large seals are made with Parker 2 - 390 O-rings.
2. The inside source chamber bolts into place using 12 3/8 - 16 socket head screws. The seal is made between the inside source chamber and the main chamber.
3. The outside source chamber can be rolled up to and away from the inside source chamber. It is fastened with 12 1/2 - 13 cap screws which pass through the inside side chamber and into the main chamber. The seal here is made between the outside source chamber and the inside source chamber.
4. The electrical connections and gas and mechanical connections must be disconnected before rolling the source chamber back.
5. After the source is aligned the outside source chamber is rolled up and bolted on.
6. The configuration of the feedthroughs for each source chamber is shown in Fig. II-33.
7. After the chamber is bolted on the gas inlet tube and the cooling or heating fluid tubes should be connected using the appropriate Gyroloks.

Figure II-33. Feedthrough Location on Source Chamber Feedthrough Flanges

1. TG - 75 Ion Gauge Tube
2. Nozzle Skimmer Distance Drive
3. Nozzle Source Vertical Control
4. 26 - Pin Electrical Feedthrough
5. Gas Inlet
6. Nickel Thermocouple Feedthrough Tubes
7. High Current and Cooling Water Feedthroughs for High Temperature Oven
8. Chromel - Alumel Thermocouple Feedthroughs
9. Nozzle Fluid Temperature Control Inlet and Outlet
10. Main Source Chamber Feedthrough Flange

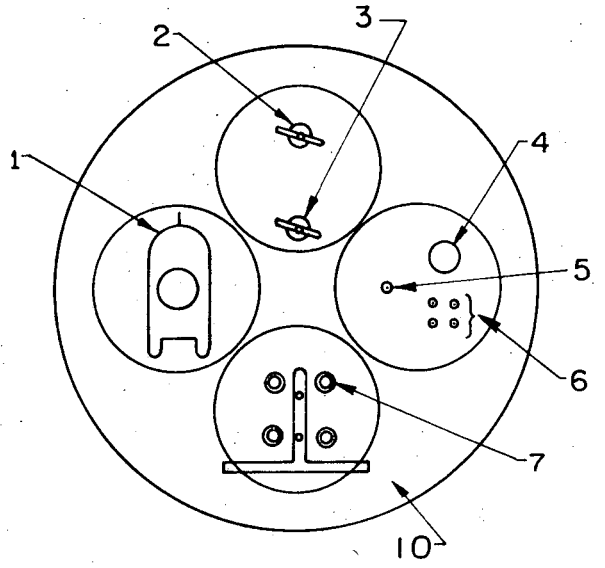

Source Chamber 2 Feedthrough Flange

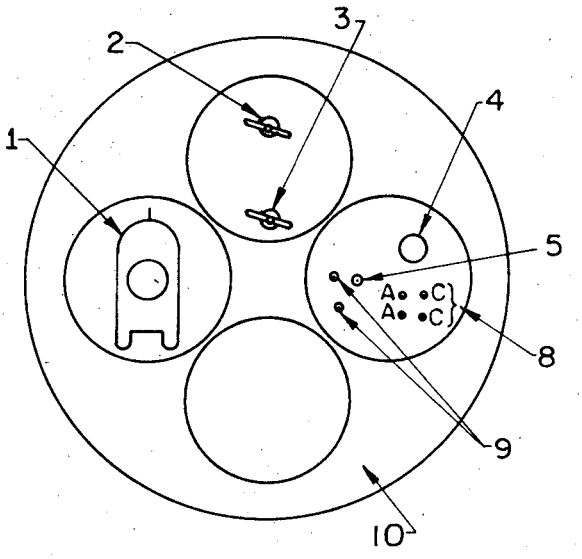

To Main Chamber

Source Chamber 1 Feedthrough Flange

XBL 751-5473

Fig. II-33.

8. The mechanical feedthroughs for nozzle adjustments must be made.
9. Connect the source chamber electrical connections to the appropriate position on the terminal strip as shown in Fig. II-34.

11. Nozzle Source Assembly
    1. For assembly of the nozzle source refer to Fig. II-23 and blueprint #12N5413. The alignment of the nozzle source is covered in the alignment section of this chapter.
    2. Assemble the nozzle slide (2) and place it on the nozzle slide support (1).
    3. Screw the skimmer (12) to be used onto the front plate of the nozzle slide support. Bolt the dovetail (3) in place on the source chamber inside face. Bolt the nozzle slide support (1) onto the dovetail. The skimmer oriface must now be aligned by moving the dovetail. When the skimmer oriface is aligned properly, tighten the dovetail slides so the dovetail will not slide.
    4. The nozzle has three main pieces - the cooling chambers and nozzle support (4), the nozzle feed (6), and nozzle chamber (7). The nozzle chambers are interchangeable and a set of 8 nozzle chambers with different oriface diameters are made. The oriface for most is in a .001 thick nickel shim (9) which is sealed with a fine knife edge seal. These seals should not be broken since the oriface shim may not reseal again. An indicator should be used when tightening the oriface cover (10) over a shim (9).
    5. The nozzle feed tube (6) slides through nozzle support (4) to allow the nozzle chamber (7) to be bolted on to the nozzle feed. The seal between the nozzle chamber and the nozzle feed is a knife edge

Figure II-34. Source Chambers Electrical Connections

All numbers refer to location when looking at the connection side of the terminal strips.

Chamber 1

A3	To alumel thermocouple feedthrough 1
A4	To chromel thermocouple feedthrough 1
A5	To alumel thermocouple feedthrough 2
A6	To chromel thermocouple feedthrough 2
B1	Phototransistor #1
B2	Phototransistor #2
B3	One return leg for hysterysis motor
B4	Blank
B5	Heater
B6	Heater
C1	To one pole of motor
C2	One return leg for hysterysis motor
C3	To other pole of motor
C4	Beam flag
C5	Beam flag
C6	LED power

Figure II-34 (cont'd.)

Chamber 2

A3→A6	To nickel thermocouple feedthroughs
B1	Beam flag
B2	Beam flag
B3	Collimating slits
B4	Collimating slits
B5	Heater
B6	Heater

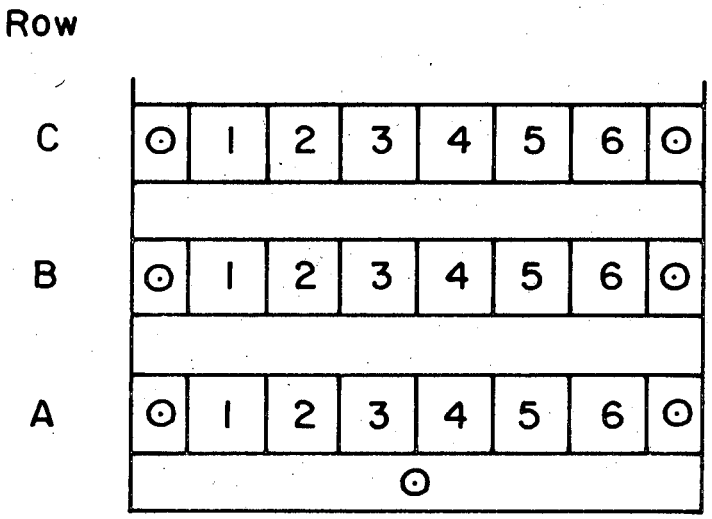

Chamber 1

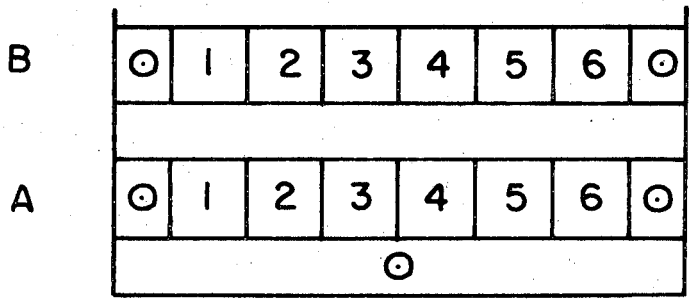

Chamber 2

XBL 751-5464

Fig. II-34.

seal utilizing either a nickel or copper gasket. The screws pass through the rear of the nozzle feed and screw into the nozzle chamber. After the nozzle chamber is fastened, the nozzle feed is pulled back until its located pins seal in the holes of the nozzle support. A retainer ring in the pack of the nozzle support is tightened to hold the nozzle feed in place.

6. The assembly is now placed in the nozzle slide and the adjusting screws tightened. See the alignment section for how to position the nozzle oriface.
7. After the nozzle has been aligned the heater (11) with .020 inch diameter tantalum wire insulated with .110 inch diameter ceramic beads is slid over the nozzle chamber and fastened in place with its set screw.
8. Place the thermocouple into the thermocouple hole in the front of the nozzle chamber. Secure the thermocouple leads with copper wire so the thermocouple does not come out of the hole.
9. Assemble the rear nozzle support on the cross bar in the inside source chamber.

12. Beam Chopper and Beam Flag Assemblies

1. The beam chopper and beam flag for beam 1 are in one unit shown in blueprint 12N4273. The entire unit must be assembled and the electrical sensing unit put in place and then attached to the front of inside source chamber #1 before inside source chamber #1 is installed in the apparatus.
2. To assemble the unit place the four roller bearings (PIC E4-8) in place. Put the upper and lower shafts through the bearing in the

back plate. On the lower shaft put on a spacer, a gear with hub toward rear plate, the chopping wheel with hub toward rear plate, a shaft lock ring and a spacer. On the upper shaft put on a spacer, a gear, a shaft lock ring and a spacer. Now place the top plate with the two bearings over the end of each shaft and fasten the plate down. Align the gears and the chopping wheel and then secure the set screws in gears, chopping wheel and shaft lock rings. Spin the upper shaft. The assembly should spin freely and coast for 15 to 30 seconds.

3. Now insert the beam flag and attach it to the solenoid (Deltrol type D-30). Attach the solenoid to the rear plate.
4. Screw the LED onto the rear plate and place the printed circuit board with the two phototransistors on front plate. Adjust the phototransistors so the bottom one will turn on or off when the beam turns off or on.
5. Connect the wires from the solenoid, the LED, and phototransistors to the feedthroughs on the source chamber feedthrough flange.
6. On the source side of the inside side chamber hook up the hysterysis motor to the upper beam chopper shaft. Use one universal coupling and one coupling that will allow the shaft to expand in the coupling.
7. Test the beam chopper, the phototransistor signals, and the beam flag.
8. To assemble the beam flag for beam 2 screw the solenoid onto the solenoid plate and the plate onto inside source chamber #2. Screw the beam flag and beam flag guide onto the front of the inside

source chamber. Connect the solenoid to the beam flag using nylon string.

13. Time of Flight Assembly

    1. Bolt the time-of-flight motor into place as shown in Fig. II-1.
    2. Carefully put time-of-flight wheel on the motor shaft.
    3. Referring to Fig. II-35 assemble the holder for the light bulb, the photodiode and the discriminator. The photodiode should be placed in the photodiode holder (7) and then the leads of the photodiode should be passed through printed circuit board holder (8) and these two parts and the photodiode cover plate screwed together. The printed circuit board with the discriminator is then mounted on the back and the photodiode leads soldered to the P.C. board.
    4. Bolt the time-of-flight slide guide (10) to the bottom of the motor support fork. Slide the photodiode assembly into the guide.
    5. To adjust the parts position the time-of-flight wheel as close as possible to the detector without touching it. Then adjust the time-of-flight slide guide so the time-of-flight wheel will pass between the light bulb and the photodiode. Move the photodiode assembly to the proper height on the wheel.
    6. Connect the discriminator output to the proper feedthrough. Connect the discriminator power supply, the time-of-flight motor and the light bulb to the proper pin on the 26 pin feedthrough as shown in Table II-13.

14. Gate Valve and Gate Valve Drive Assembly

    1. Clean the gate valve slide groove and O-ring groove on the detector, the valve slide, and the valve cover plate.

Figure II-35. Time-of-flight Assembly

1. Time-of-flight holder.
2. Slide cover plate.
3. Time-of-flight slide.
4. Photodiode Holder.
5. Photodiode cover plate.
6. Light bulb holder.
7. Photodiode.
8. Printed Circuit Support.
9. Printed Circuit - discriminator.
10. Time-of-flight slide guide.

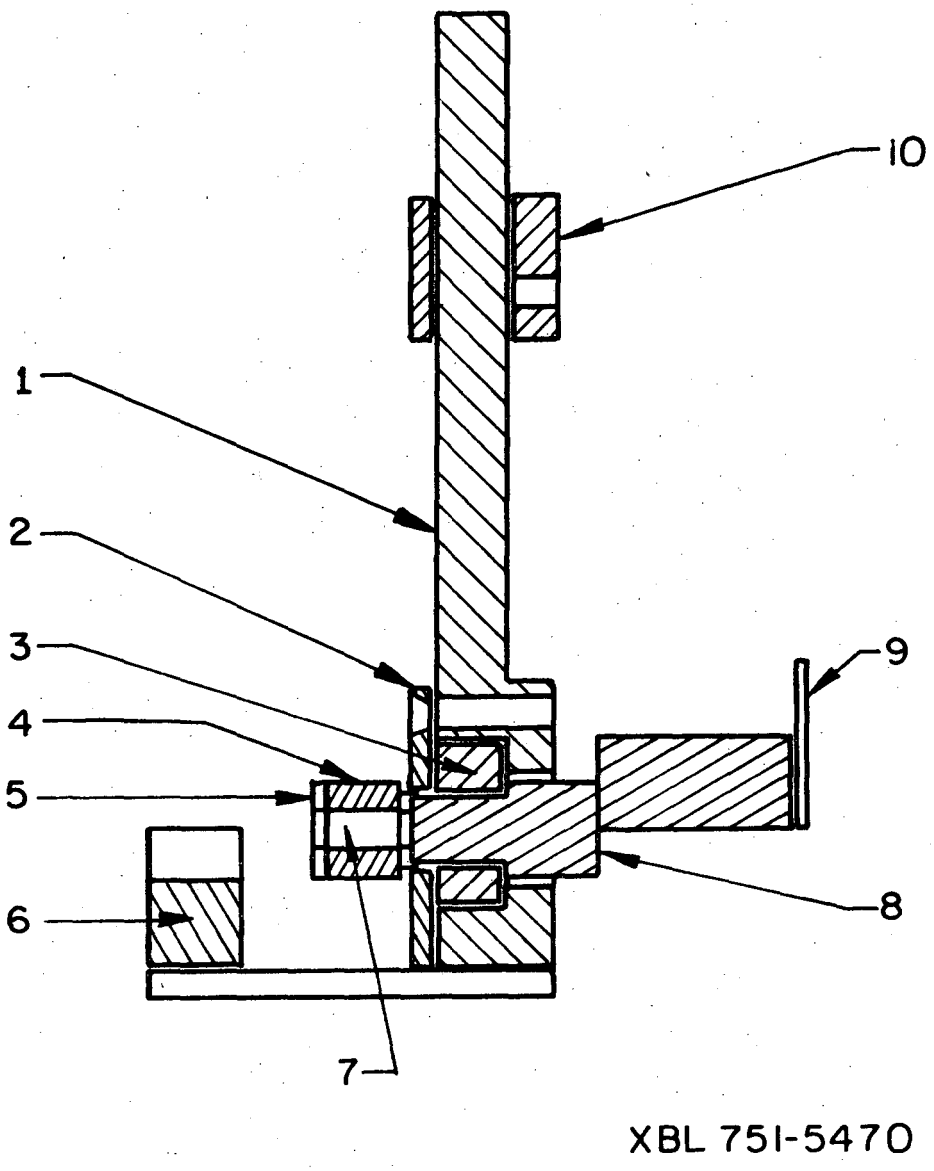

Fig. II-35.

Table II-13. Time-of-Flight Electrical Connections

Motor Drive Supply Location	Terminal Strip #	Feedthrough Pin	Time-of-Flight Connection
U	1	E	TOF Motor - Yellow
Y	2	D	TOF Motor - Green
V	3	F	TOF Motor - Black
X	4	Y	TOF Motor - White
Z	5	X	TOF Motor - blue
W	6	C	TOF Motor - red
D	7	G	Photodiode (-6.7) - purple
E	8	Z	Photodiode (+5) - orange
F	9	d	Light bulb (brown)
M	10	W	Ground
aa	11	B	Discriminator trigger level (Yellow)

Low

High

2. Insert the Tec-ring (#CR-012-CS-OF) into the O-ring groove in the detector, place the gate valve slide in the groove, and screw the gate valve cover plate into place.
3. Slide the gate valve drive rod through the Cajon fitting on the lid. Screw the drive rod through the valve slide and seat the bottom of the shaft in the hole of the valve cover. Secure the shaft with the cover plate.
4. Using Fig. II-36 for reference assemble the gate valve drive and indicator assembly.
5. When the gate valve opening is aligned (see alignment section of this chapter), set the counter at a given valve and tighten down the counter so the spur gear (2) and the internal gear mesh. Move the gate valve until the small diameter hole is aligned and note this number. These two numbers will be used to align the detector entrance hole so care must be taken that the gears will not slip.

Cleaning Procedures

I. See F. Rosebury, Handbook of Electron Tubes and Vacuum Techniques, Addison Wesley Publishing Co., 1965. See page 15, procedure SS-1.

II. For cleaning procedure see page 3-17 of the EAI Quad 250 Residual Gas Analyser Manual. The acid solution is:

80% Deionized water

10% Hydrogen peroxide

10% Formic acid.

III. For alumina parts use a chromic acid cleaning solution. See F. Rosebury, Handbook of Electron Tube and Vacuum Techniques, Addison Wesley Publishing Co, 1965. Refer to page 5.

Figure II-36. Gate Valve Drive and Indicator Assembly

1. Veeder Root small counter series 1141 - 10 counts/rev.
2. 20° spur gear, 12 teeth.
3. 20° internal gear, 48 teeth.
4. Internal gear support.
5. Pinion, 32 pitch.
6. Collar.
7. Gear, 32 pitch 1.00 P.D.
8. Counter support.
9. Grip plate.
10. Counter swivel.
11. Cajon fitting.

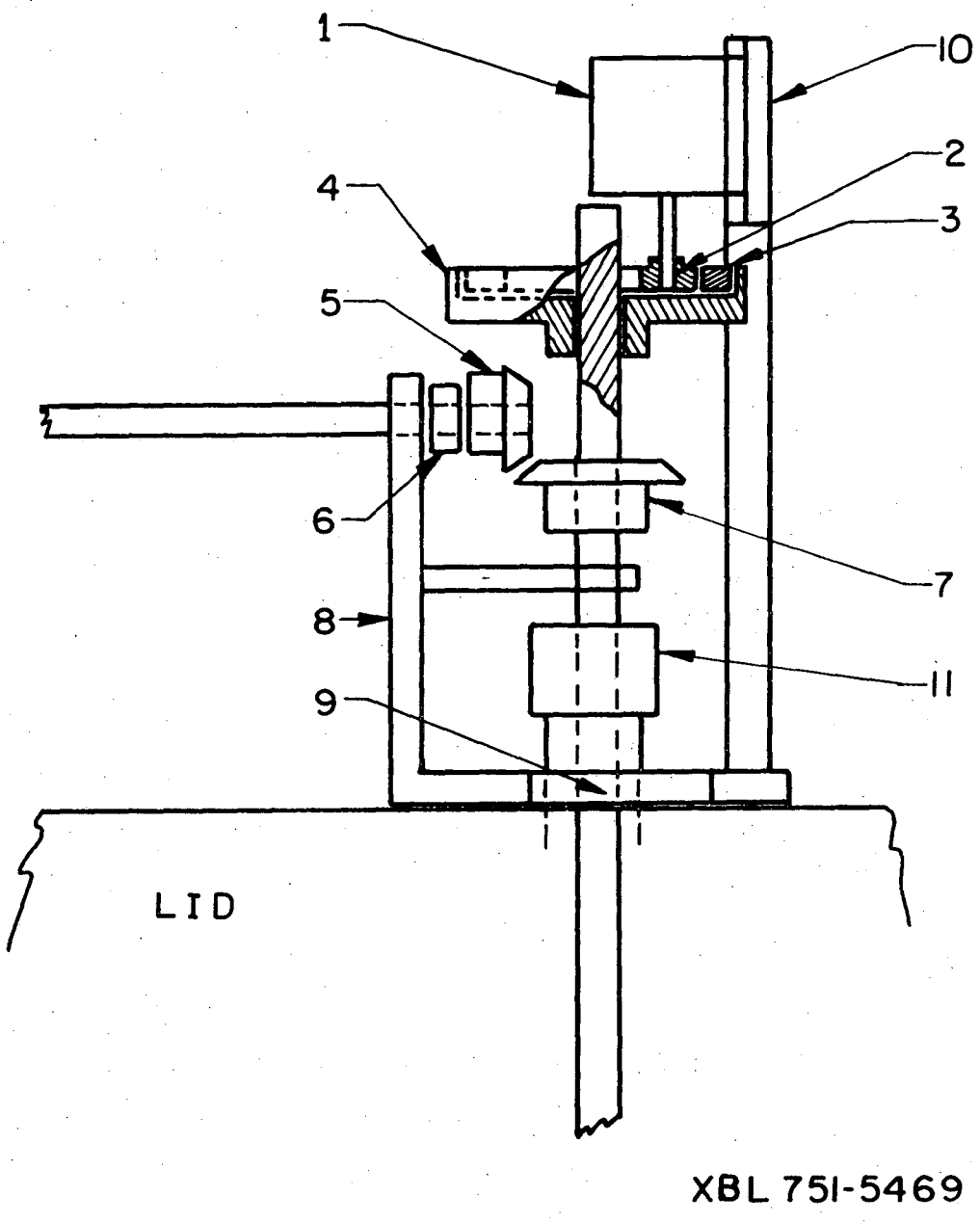

Fig. II-36

References

1. Y.T. Lee, J.D. McDonald, P.R. LeBrenton, D.R. Herschbach, Rev. Sci. Inst. 40, 1402 (1969).

2. C.F. Carter, M.R. Levy, R. Grice, Faraday Discussions, 55, 357 (1973).

3. D.L. McFadden, E.A. McCullough, Jr., F. Kalos, J. Ross, J. Chem. Phys., 59, 121 (1973).

4. R.W. Bickes, Jr., and R.B. Bernstein, Rev. Sci. Inst. 41, 759 (1970).

5. R. Weiss, Rev. Sci. Inst. 32, 397 (1961).

6. G.O. Brink, Rev. Sci. Inst. 37, 857 (1966).

7. N.C. Blaiss and J.B. Cross, J. Chem. Phys. 52, 3580 (1970).

8. J.B. Cross and N.C. Blaiss, J. Chem. Phys. 55, 3970 (1971).

9. J. Grosser, H. Haberland, Chem. Phys., 2, 342 (1973).

10. J. Geddes, H.F. Krause, W.L. Fite, J. Chem. Phys. 56, 3298 (1972).

11. P.L. Moore, P.N. Clough, J. Geddes, Chem. Phys. Letters, 17, 608 (1972).

12. Copies of LBL drawings whose numbers are cited here may be obtained by writing to Lawrence Berkeley Laboratory, Technical Information, Building 90, Room 3118, Berkeley, California 94720.

13. Keene Corp., Kaydon Bearing Division, 2860 McCracken, Muskegon, Michigan 49433.

14. Fluorocarbon Company, 22624 Avalon Blvd. Carson California 90745.

15. a. D.D. Parrish and R.R. Herm, J. Chem. Phys. 51, 5467 (1969).

    b. D.D. Parrish and R.R. Herm, J. Chem. Phys. 54, 2518 (1971).

16. C.A. Mims, Ph.D. thesis, Univ. of California, Berkeley (1973).

17. W. Paul and M. Raether, Z. Physik, 140, 262, (1955).

18. K.R. Spangenberg, Vacuum Tubes, (McGraw Hill, New York, 1948) Chapter 13.

19. C.A. Spindt, Thin Film Field Emmission Devices, 1973 IEEE Conference on Electron Device Techniques, New York. (Information available from Stanford Research Institute, Menlo Park, California.)

20. W.H. Aberth, C.A. Spindt, M.E. Scolnick, R.A. Sperry, M. Amber, Sixth International Mass Spectrometry Conference, Edinburgh, Scotland (September, 1973).

21. F.S. Goulding, Nucl. Instrum. Methods 43, 1 (1966).

22. N.R. Daly, Rev. Sci. Inst. 31, 264 (1960).

23. H.M. Gibbs, E.D. Commins, Rev. Sci. Inst. 37, 1385 (1966).

24. Pilot B plastic scintillator is available from Pilot Chemical Inc., 36 Pleasant Street, Watertown, Massachusetts.

25. R.J. Potter, Rev. Sci. Inst., 32, 286 (1961).

26. J.R. Young, J. Applied Phys., 27, 1,(1955).

27. A. Kantrowitz and J. Grey, Rev. Sci. Inst., 22 328 (1951)

28. J.B. Anderson and J.B. Fenn, Phys. Fluids, 8 780 (1965).

29. J.B. Anderson, R.P. Andres, J.B. Fenn, Molecular Beams ed. J. Ross.

30. H. Ashkenas and F.S. Sherman, Rarefied Gas Dynamics, Vol. II, 84 (1966).

31. F.P. Tully and Y.T. Lee, J. Chem. Phys., 57 866 (1972).

32. Zircar - a Union Carbide trademark.

33. A. Freedman, Ph.D. thesis, Univ. of California, Berkeley, to be written.

34. T. Parr, Ph.D. thesis, Univ. of California, Berkeley, to be written.

III. INTERMOLECULAR POTENTIALS OF CH_4 + ARGON AND NH_3 + ARGON FROM ELASTIC SCATTERING MEASUREMENTS

A. Introduction

Since the advent of modern chemistry, the study, measurement and use of intermolecular potentials have always been at the foundation of the understanding of chemical properties and the dynamics of chemical systems. Much of the statistical theory on the properties and behavior of gases and liquids is predicated on atom or molecule pair interactions. So in order to test, and ultimately utilize, these statistical theories it is necessary to obtain intermolecular potentials as accurately as possible. These intermolecular potentials can then be used in the statistical theories to predict observable values which can then be compared with experimental values. Accurately known intermolecular potentials also are of interest in the area of chemical physics. Here accurately measured intermolecular potentials can be compared to calculated potentials, thus, allowing the scientist to feel confident that he is gaining more insight into the workings of nature.

The problem of determining the intermolecular potential of pair interactions has been the concern of the experimentalist for many years. Many of the experimental values in the literature for a wide range of atomic or molecular pairs have come from transport phenomena of dilute gases, second virial coefficient measurements, and spectroscopic measurements. When spectroscopy can be done on a bound pair, very accurate intermolecular potentials can be obtained in the

region of the bound states. By measuring the temperature dependence of transport properties such as self-diffusion, thermal diffusion, and viscosity, and the temperature dependence of the second virial coefficient, values for different forms of intermolecular potential on a large number of systems have also been obtained. These measurements have provided potential parameters on many systems but the accuracy of the measured values and the agreement of potential parameters for a particular system were not always in good agreement when measured by different transport properties (although there is little reason to expect there to be exact agreement). Since the interpretation of transport properties of a gas are based on bimolecular collision dynamics at low pressure it is reasonable to expect that a good method of measuring the intermolecular potential would be by observing the scattering of the individual molecular pairs. Crossed molecular beams thus provide an excellent means for obtaining very accurate intermolecular potentials.

Several different features of scattering yield information on different parts of the intermolecular potential. Classically, the measurement of the total cross section vs. the collision energy at low energies will give information on the long range part of the potential. Measurement of the differential cross section in arbitrary units at small scattering angles gives the exponential behavior of r, in the long range potential term and the wide angle scattering gives the form of the repulsive wall. A reasonable estimate of the well depth, ϵ, can be obtained from the position of the rainbow, classically.

Semiclassically the presence of interference terms from different branches of the deflection function which produce undulations in the differential cross section are very sensitive to the intermolecular potential. The glory undulations in the total cross section measurements are also very sensitive to the potential.

Very accurate intermolecular potentials have been obtained by many different molecular beam groups. The first extensive studies of elastic scattering systems were done on the alkali metals with a wide variety of different gases. A review of this work is given by Bernstein and Muckerman.[2] Another group of atom-atom pairs that has been successfully and extensively studied are the rare gas elements.[3-7] The resolution of quantum oscillations in these systems has yielded highly accurate intermolecular potentials. A further extension of elastic scattering work in recent years has been into the field of atom-molecule pairs and molecule-molecule pairs. Differential cross sections have been measured on several diatomic-rare gas systems.[8-11] Generally, only the rainbow angle has been resolved in most of these measurements. This has given reasonable estimates of the well depth, ε, of the potentials but not very accurate values for the range parameter, r_m. Differential and integral cross sections have also been measured on polyatomic-atom[7,12-16] and molecule-molecule pairs.[17,18] In some cases[12,15,16,17] the rainbow angle was measured and in another[12] only the slope of the narrow angle fall off. Oscillations in the H_2, and D_2 with polyatomic molecules have been reported.[18] Several difficulties are encountered when attempting to study the elastic scattering of molecule-atom or molecule-molecule pairs which tend to

average out some of the extrema definition of the angular distribution, thus, substantially decreasing the accuracy of the information that can be extracted. The two important averaging effects in systems which do not undergo chemical reaction are (1) a variation of the intermolecular potential for separate collisions due to the anisotropy of the potential of the molecule and (2) the possibility that the molecule may undergo rotational transitions due to the collision.

In order to study those effects it was decided to measure both the elastic and rotationally inelastic scattering of a series of hydride molecules - CH_4, NH_3, and HF. These molecules have several properties which, if effectively studied, would give information regarding the effect of anisotropy and rotational transitions on the scattering. These three molecules provide a varying degree of symmetry and a variation in the dipole moment. They also have relatively large rotational energy level spacings so that at least the higher rotational energy transitions can be studied with time-of-flight analysis. One problem with studying these molecules is that the mass of each (HF to a lesser extent) lies in the region of the mass spectrum where background is moderately high, making it some what more difficult to collect data.

The systems to be run first were CH_4-A, NH_3-A and HF-A. While at Berkeley only the elastic scattering of the first two, CH_4-A and NH_3-A, were completed before the apparatus had to be disassembled and moved. This chapter presents the results of these two interactions.

These elastic scattering measurements have also demonstrated the high resolution of the apparatus and have shown that there are no systematic errors due to viewing factor effects (see Chapter II).

B. Experimental

The experimental arrangement of the apparatus for these measurements is the same as described in chapter 2. The primary beam, which is the species being detected after scattering, is formed in source chamber 2 and the crossed beam, argon for these experiments, is formed in source chamber 1. Both beams are nozzle sources with the Mach numbers for the primary beam (NH_3 or CH_4) between 7 and 10 and a much number of 20 for the crossed argon beam. The Mach numbers were measured by the fitting technique described in chapter II and the relative collision energy, g, is calculated using the velocity at the peak of the calculated nozzle distribution for each beam. The beam conditions for the different experiments are given in Table III-1. The double set of collimating slits were used to form the primary beam and the single collimating slits were used to form the crossed beam (the different slits are described in chapter II). The argon beam was chopped at 55 Hz and the signal was recorded by dual counters and stored in the PDP-8E computer.

Each experiment was run two or three thimes. Counting times for each angle between 3 and 10 degrees were 40 seconds of which 20 seconds were with both beams on and 20 seconds were with the argon beam flag on (argon beam off). For angles between 10 degrees

Table III-1. Elastic Scattering Beam Conditions

System Primary-Crossed	Temperature Primary Crossed (°K)		Pressure Primary-Crossed (Torr)		Beam Width (FWHM) Primary-Crossed		Mach # Primary-Crossed		Relative Collision-Energy (10^{-14}ergs)
CH_4-Ar	295	295	760	760	1.3	1.5	8.0	20	14.0
CH_4-Ar	295	220	480	750	0.6	1.5	10.0	15	13.4
NH_3-Ar	295	295	400	750	0.6	1.5	7.2	20	13.8

and 30 degrees the counting time was either 80 or 120 seconds half of which was beam flagged. After taking measurements at 2 to 4 different angles, the signal at the reference angle, 10 degrees, was measured so that all the data could be time normalized to this value to correct for drift in beam intensities and detector sensitivity. The standard deviation of the reference angle at room temperature (295°K measured with a thermocouple) was 4.1% for the CH_4-argon system and 5.4% for the NH_3-argon system.

Since the intermolecular potential is essentially independent of the relative collision energy, an excellent method for proving the uniqueness of a particular intermolecular potential is to measure angular distributions at two different collision energies. The particular intermolecular potential should give the best fit to both angular distributions.

In order to change the relative collision energies of the systems the crossed beam argon nozzle was cooled by passing chilled nitrogen gas through the cooling chambers on the nozzle. The nitrogen gas was cooled by flowing it through copper coils immersed in liquid nitrogen outside of the apparatus. The temperature of the nozzle could be regulated, but not very well, by controlling the rate of flow of the gas through the system. The temperature was measured by a thermocouple in the wall of the nozzle chamber. Since regulation of the chilled gas was not precise the temperature of the argon nozzle varied ±15 degrees over the course of the experiment. There was also

a decrease by a factor of 5 in the scattered signal of the lower temperature. With these problems, the standard deviation of the low temperature (220°K) CH_4-argon reference point is 21%.

The detector was operated with the same slit dimensions and ionizer conditions listed in chapter II.

C. Data Analysis and Results

The analysis of crossed molecular beam angular distributions from elastic scattering has been treated extensively in many places (for example see reference 19). The following is just a brief summary of the methods used to analyze molecular beam angular distributions to obtain intermolecular potentials.

The binary collision can be reduced to the one body central potential problem. Figure III-1a shows a collision of this type where the mass of the one particle is the reduced mass $\mu = m_1m_2/m_1+m_2$, b is the impact parameter, r is the intermolecular distance, Θ_m is the orientation at the distance of closest approach, and χ is the angle which the particle is scattered through. The velocity vector or Newton diagram for a typical crossed molecular beam experiment is shown in Fig. III-1b where $\vec{V}_1$ and $\vec{V}_2$ are the velocities of each beam, $\vec{C}$ and θ_{cm} are the center-of-mass velocity vector and angle respectively, U_1 and U_2 are the center-of-mass velocities of each beam, U_3 is the center-of-mass velocity vector of the molecule scattered through a center-of-mass angle χ. Θ and V_3 are the laboratory angle and velocity vector for a particle scattered through an angle

Fig. III-1. a) A bimolecular elastic collision reduced to the one body central force interaction. The particle of reduced mass μ approaches at an impact parameter b with a velocity $\vec{g}$. The particle has a closer approach of r_m and is scattered through an angle χ and leaves with an impact parameter b.

b) A velocity vector or Newton diagram representing the collision of two particles (beams) at an intersection angle of 90° with velocities of $\vec{V}$, and $\vec{V}_2$. $\vec{C}$ is the center-of-mass velocity and θ_{cm} is the center-of-mass angle. The center-of-mass velocities of each incident particle are $\vec{u}$, and $\vec{u}_2$. The particle is scattered through the center-of-mass angle χ and the product has a final center-of-mass velocity $\vec{U}_3$ ($U_3=U_1$ for elastic scattering). The measured scattering angle in the laboratory system is H and the velocity is $\vec{V}_3$.

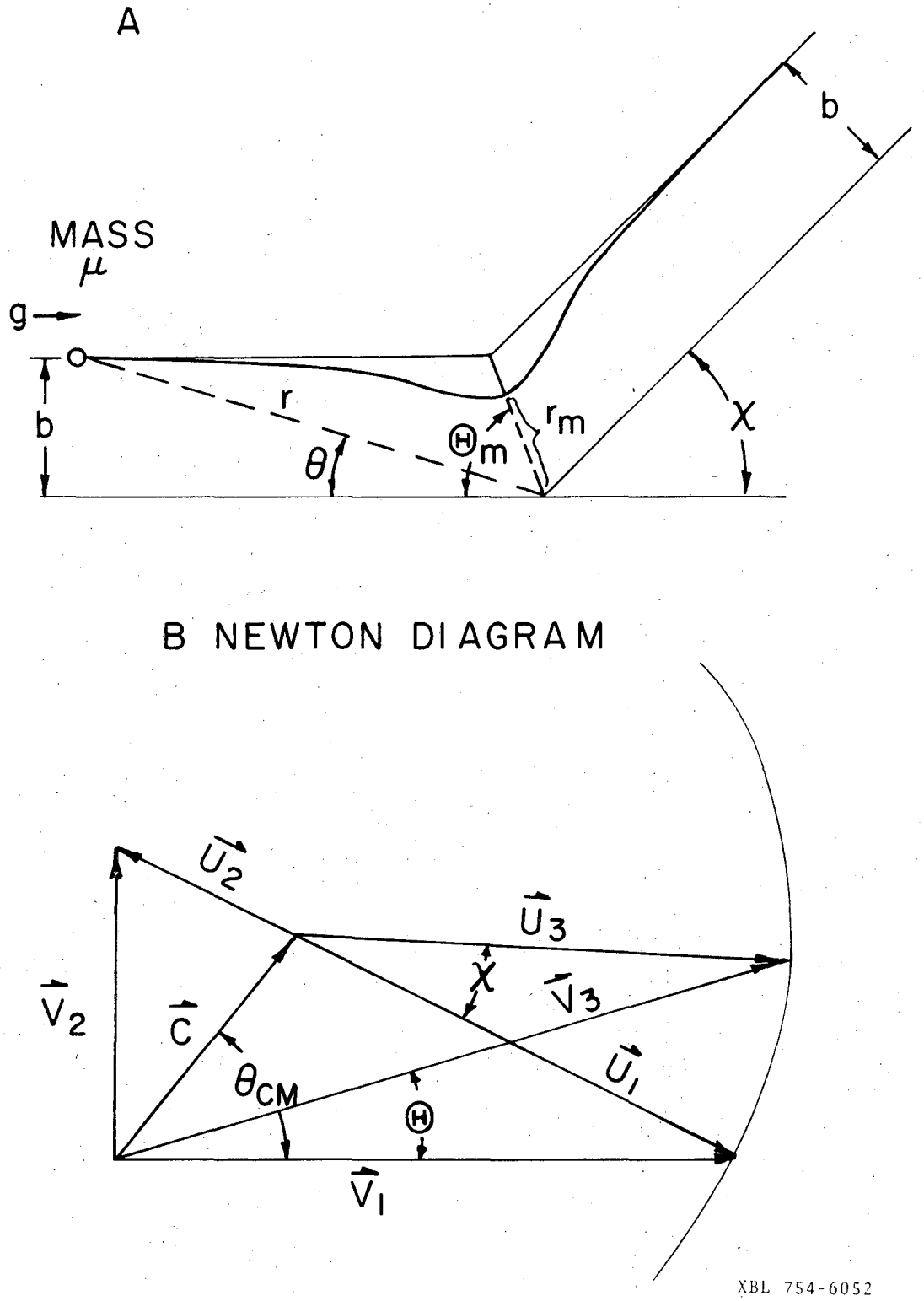
A
MASS
μ
g
b
r
θ
⊕m
rm
χ
B NEWTON DIAGRAM
U2
U3
V2
C
χ
V3
θCM
U1
⊕
V1
XBL 754-6052

Fig. III-1.

χ in the center-of-mass. For elastic scattering $U_3=U_1$ and the scattered intensity versus lab angle Θ is measured. Figure III-2 shows the angular distribution for CH_4 + Ar at a collision energy of 14.0×10^{-14} ergs and Fig. III-3 shows the angular distribution for NH_3+Ar at a collision energy of 13.8×10^{-14} ergs. The error bars indicate the reproducibility of the results.

In Figs. III-2 and III-3 the angular distribution is actually a plot of the laboratory number density $N_L(\Theta)$ against the lab angle (Θ). To determine the intermolecular potential from this data, the angular distributions will have to be calculated for a given intermolecular potential and then compared to the measured angular distribution. This is then repeated for other intermolecular potentials until a best fit is found. To compare the measured laboratory data with the calculated data, it is necessary to use the Jacobian of transformation from the center-of-mass to laboratory coordinate system. With the LAB number density $N_L(\Theta)$, the LAB flux, $I_L(\Theta)$, and the center-of-mass flux $I_{cm}(\chi)$ the relation is[20]

$$N_L(\Theta) = V_3^{-1} I_L(\Theta) = V_3^{-1} [V_3^2/U_3^2 \cos(U_3,V_3)] I_{cm}(\chi) \qquad (1)$$

where V_3 and U_3 are the scattered velocity vectors shown in Fig. III-1b and (U_3,V_3) is the included angle between $\vec{U}_3$ and $\vec{V}_3$. So in order to calculate an angular distribution to fit the data the center of mass flux must be calculated.

Fig. III-2. The measured angular distribution of CH_4 + Ar with the CH_4 product being detected. The error bars indicate one standard deviation calculated from the background counts of the measurement. Points with no error bars have standard deviations smaller than the symbol. The collision energy is 14.0×10^{-14} ergs, r_m = 3.82 Å, and B = 7.05.

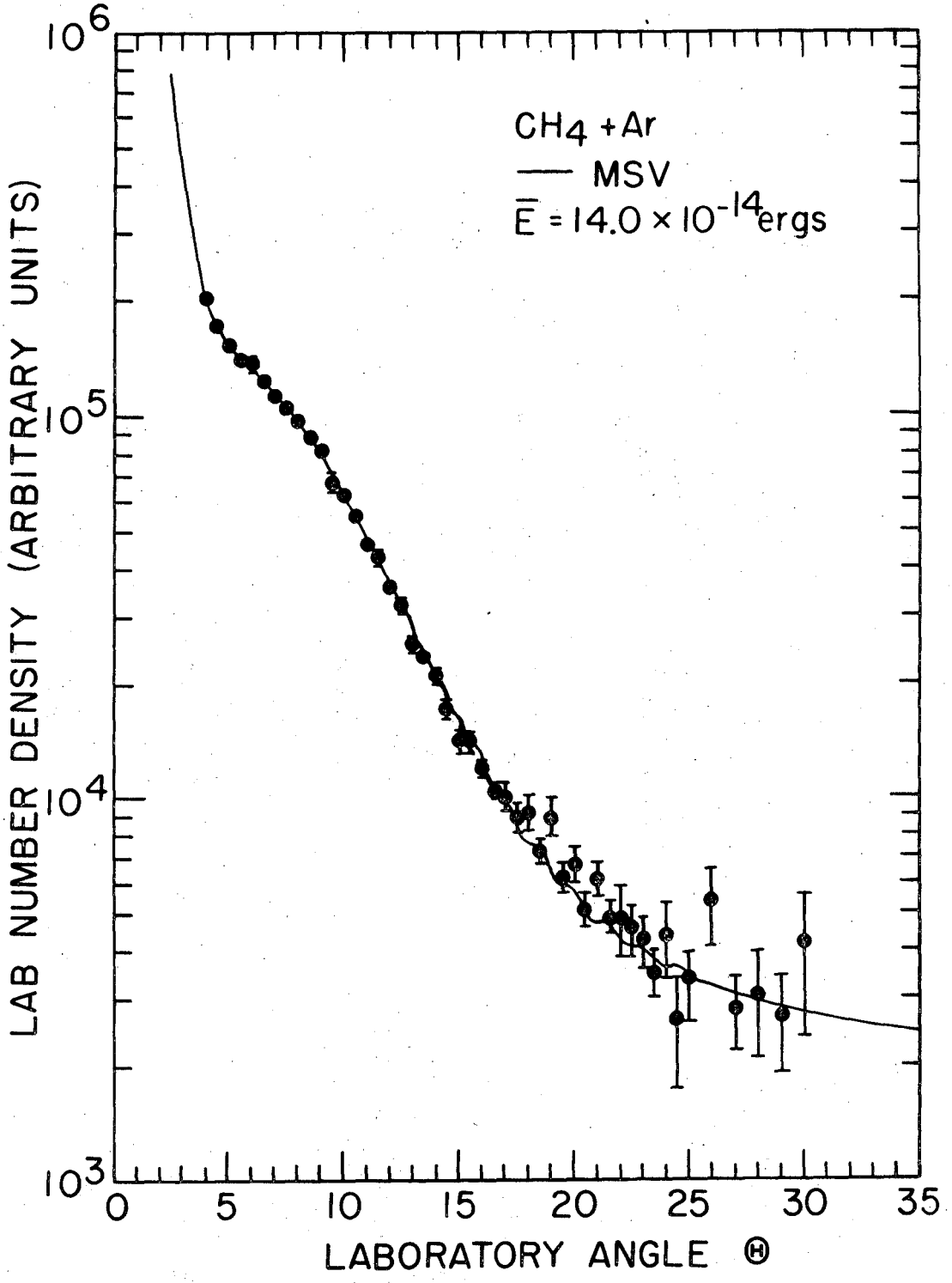

XBL 754-6062

Fig. III-2.

Fig. III-3. The measured angular distribution of NH_3 + Ar with the NH_3 product being detected. The error bars indicate either one standard deviation calculated from the background counts or the standard deviation of several points measured at one angle whichever is larger. Points with no error bars have standard deviations smaller than the symbol. The collision energy is 13.8×10^{-14} ergs. The solid line is the best calculated distribution using an MSV potential with $\varepsilon = 2.21\times10^{-14}$ ergs, $r_m = 3.93$ Å, and $B = 8.45$.

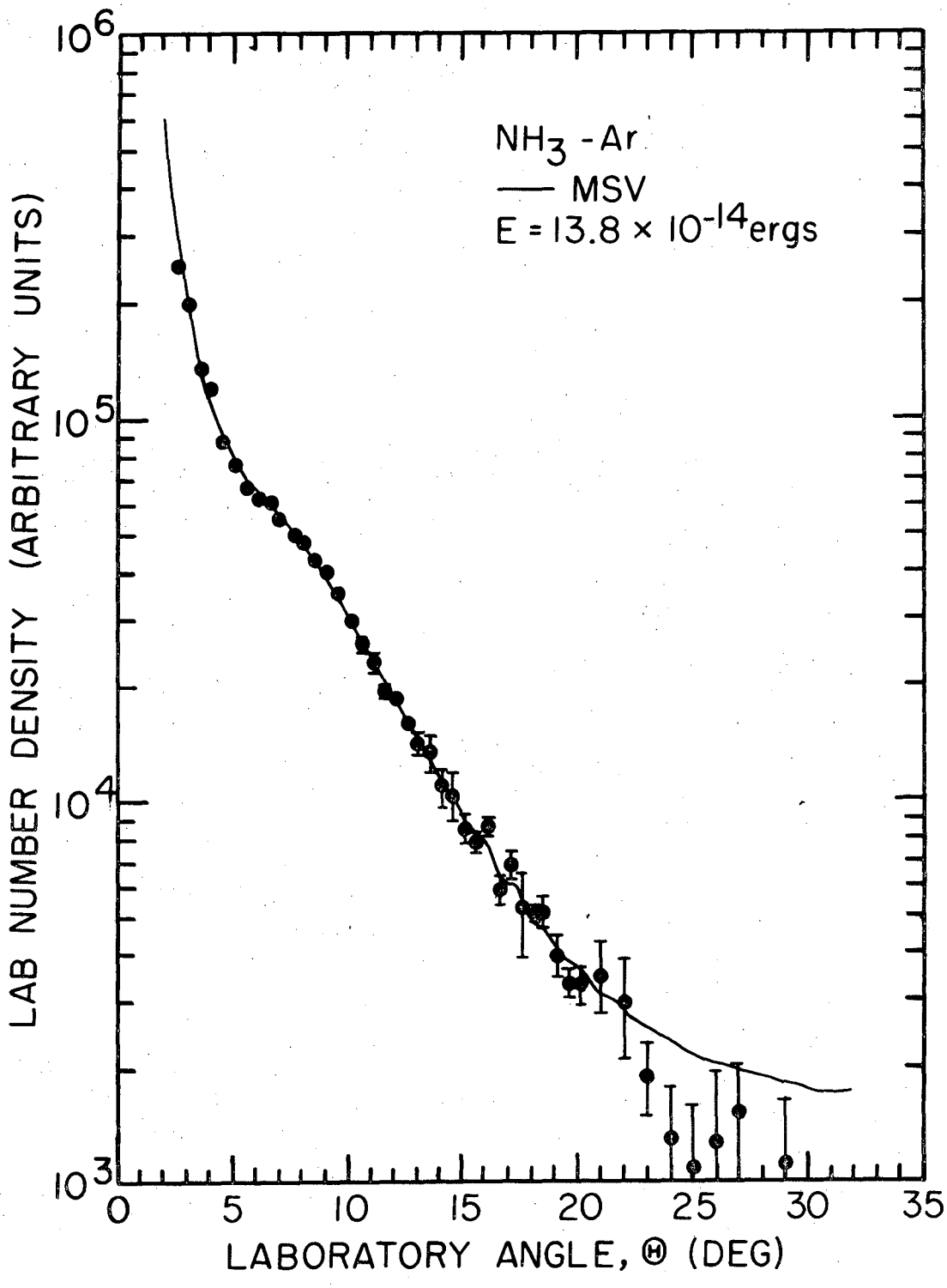

XBL 754-6061

Fig. III-3.

The differential cross section may be calculated either classically or quantum mechanically. The expression for the angle of deflection χ is classically given by

$$\chi(E,b) = \pi - 2b \int_{r_c}^{\infty} \frac{dr}{r^2\left[1 - \frac{V(r)}{E} - \frac{b^2}{r^2}\right]^{1/2}} \qquad (2)$$

where b is the impact parameter, r_c is the distance of closest approach, V(r) is the potential energy, $E = \frac{1}{2}\mu g^2$, and r is the intermolecular separation. Introducing reduced variables in terms of the well depth of the potential ε and the position of the bottom of the well r_m we have

$$\chi = r/r_m; \qquad \beta = b/r_m \qquad f(\chi) = V(r)/\varepsilon$$
$$K = E/\varepsilon$$

and the angle of deflection can be written as

$$\chi(K,\beta) = \pi - 2\beta \int_{\chi_c}^{\infty} \frac{d\chi}{\chi^2\left[1 - \frac{f(\chi)}{K} - \frac{\beta^2}{\chi^2}\right]^{1/2}}$$

The deflection angle as a function of reduced impact parameter for a Lennard-Jones^{12,6} potential is shown in Fig. III-4. The differential cross in classical mechanics is given by

$$I(\chi) = \sum_i \frac{b_i}{\sin\chi \left| \frac{d\chi}{db_i} \right|} \quad . \qquad (4)$$

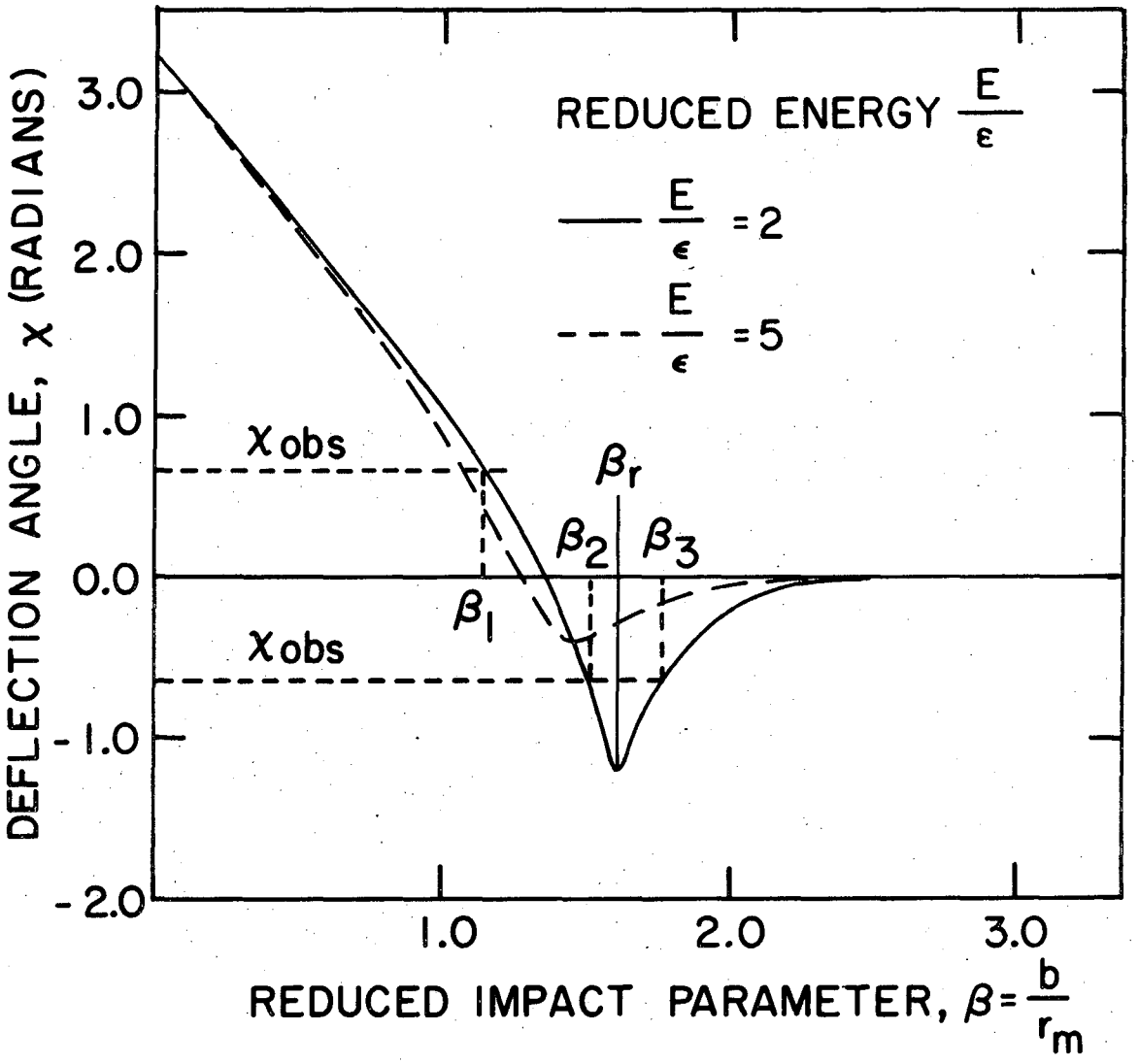

XBL 754-6050

Fig. III-4. The center-of-mass deflection angle, χ, is shown as a function of the reduced impact parameter, β, for two different reduced energies, K. Since positive and negative angles cannot be distinguished in these measurements, χ_{Obs} illustrates how the intensity measured at a particular angle can come from contributions at different impact parameters. The rainbow angle comes from scattering in the region of β_r.

This illustrates two effects seen in scattering: one where χ goes to zero and the cross section has a discontinuity classically which is glory scattering and the other more commonly seen rainbow scattering where $|d\chi/db|$ goes to zero. The impact parameters that correspond to rainbow scattering are at β_r in Fig. III-4. Classically the total differential cross section at a particular angle is the sum of differential cross sections for each branch which contribute to the scattering at a particular angle. This makes it classically impossible to obtain a unique $V(r)$ from $I(\chi)$. For the differential cross section at the angle shown in Fig. III-4 the total differential cross section at that angle would be

$$I_{total}(\chi) = I_1(\chi) + I_2(\chi) + I_3(\chi) \tag{5}$$

So classical mechanics predicts discontinuities at the glory angle ($0, \pm\pi, \pm 2\pi \ldots$) and at the rainbow angle. It also does not allow for interference effects between different contributing branches at each angle. To treat these problems it is necessary to use a quantum mechanical treatment.

In the quantum mechanical treatment of the scattering problem the scattering is represented by a wave function of the form

$$\psi = e^{ikz} + \frac{f(\chi)e^{ikr}}{r} \tag{6}$$

where e^{ikz} represents the incoming plane wave traveling in the z direction and $f(\chi)e^{ikr}/r$ represents the outgoing scattered wave. The differential cross section in this case is given by

$$I_{cm}(\chi) = |f(\chi)|^2 \tag{7}$$

The scattering amplitude for this problem has been shown[21] to be

$$f(\chi) = \frac{1}{2ik} \sum_{\ell=0}^{\infty} (2\ell + 1)\ (\exp(2i\eta_\ell)-1)\ P_\ell(\cos\chi) \tag{8}$$

where ℓ is the angular momentum quantum number, k is the wave number ($k = mV/\hbar$, $P_\ell(\cos\chi)$ are the Legendre polynomials for each ℓ, and η_ℓ is the phase shift. In practice the summation is performed up to some value of ℓ, ℓ_{max}, which is the value of ℓ for which the phase shift is less than .001 radians. The differential cross-section can then be written as

$$I_{cm}(\chi) = \frac{1}{k^2} \left| \sum_{\ell=0}^{\infty} (2\ell+1)\exp(i\eta_\ell)\sin\eta_\ell\ P_\ell(\cos\chi) \right|^2 . \tag{9}$$

It is therefore only necessary to calculate the phase shifts in order to obtain the differential cross section and finally the angular distribution. To calculate the phase shifts η_ℓ for each quantum angular momentum number ℓ, the semiclassical JWKB phase shift method was used. This approximation uses less computer time than the numerical integration of the Schrodinger equation. The two systems studied have de Broglie wavelengths of approximately 0.2Å so the JWKB approximation is valid for these systems. The JWKB phase shifts were calculated by the Gaussian integration method of Munn and Smith.[22] The quantum mechanical formulation now gives rise to interference effects between the different branches, β_1, β_2, and β_3 in Fig. III-4. This gives

a differential cross section of

$$I_{cm}(\chi) = |f_1(\chi) + f_2(\chi) + f_3(\chi)|^2 \quad .$$

This effect has been solved by stationary phase[19] to give expressions for the interference patterns.

Before proceeding to the determination of the intermolecular potentials, the velocity and angular resolution averaging should be outlined. The experimental angular distribution is measured with beams that have a distribution in velocities and a detector that does not have infinite resolution. Basically, the measured data can be represented by[3]

$$N_L(\Theta) = \int d\Theta' h(\Theta - \Theta') \int dv_1 \int dv_2 n_1(v_1) n_2(v_2) V \times [v_3/u_3^2 \cos(u_3, v_3)] I_{cm}(\chi, V) \qquad (10)$$

where $I_{cm}(\chi,V)$ is the cross section for a relative velocity V from Eq. (9), n(v) are the number density velocity distributions which for nozzle beams have the form $n \propto v^2 \exp(-(v-v_f)^2/\alpha_o^2)$ where v_f is the flow velocity and α_o is a measure of the local temperature of the beam, and u_3 and v_3 are the vectors shown in Fig. III-1b. The function h(X) is a trapezoid of variable half width given by

$$h(X) = 1, \qquad |X| \leq X_o$$

$$h(X) = 1 - \tfrac{1}{2}(|X| - X_o)/(X_1 - X_o) \qquad X_o < |X| < 2X_1 - X_o$$

$$h(X) = 0 \qquad |X| \geq 2X_1 - X_o$$

where X_o is fixed at 0.47 and is the half angle subtended by the ionization slit of the detector assuming a point source at the scattering zone and X_1 is variable with Θ and accounts for the finite volume of the scattering zone. It has been found[3] that for an experiment of this arrangement the contribution from a spread in the angle of intersection of the beams and the out-of-plane scattering is negligible.

To summarize, the data is fit by calculating the differential cross section for center-of-mass angles with a chosen interval using the JWKB approximation to calculate the phase shift for each ℓ. These contributions are then averaged over the velocities of the beams and the angular resolution of the apparatus along with the Jacobian factor to give a calculated angular distribution in terms of number density $N_L(\Theta)$.

1. The Potential Form

Many of measurements on atom-atom, atom-molecule, and molecule-molecule pairs are interpreted with either a Lennard-Jone (12,6) potential or a Lennard-Jones (n,6) potential where in terms of the reduced parameters $X = r/r_m$, $f(X) = V(r)/\varepsilon$, the potential is given by

$$f(X) = \frac{n}{(n-6)} \left[\frac{6}{nX^n} - \frac{1}{X^6} \right] \qquad (11)$$

This LJ(n,6) potential is used extensively in low energy scattering because the potential gives the correct R^{-6} asymptotic behavior. One of the main drawbacks of this potential is that the well depth ϵ and the location at the bottom of the well r_m are coupled with the van der Waal C_6 constant [$= n\epsilon r_m^6/(n-6)$]. These coupled parameters increase the difficulty of obtaining a potential that will fit an angular distribution. A more versatile potential has been used by Lee et al.[3] which allows the intermolecular potential to be represented by different functions for different ranges of interaction. This is the "exponential-spline-morse-spline-van der Waals" (ESMSV) potential, and is given by

$$
\begin{aligned}
f(x) &= A \exp[-\alpha(x-1)] && 0 < x \leqslant x_1 \\
f(x) &= \exp(a_1 + (x-x_1)\{a_2 + (x-x_2)[a_3 + (x-x_1)a_4]\}) && x_1 < x < x_2 \\
f(x) &= \exp[-2\beta(x-1)] - 2\exp[-\beta(x-1)] && x_2 \leqslant x \leqslant x_3 \\
f(x) &= b_1 + (x-x_3)\{b_2 + (x-x_4)[b_3 + (x-x_3)b_4]\} && x_3 < x < x_4 \\
f(x) &= -C_b x^{-6} - C_8 x^{-8} - C_{10} x^{-10} && x_4 \leqslant x < \infty
\end{aligned}
\qquad (12)
$$

The potential function has 12 free parameters ϵ, r_m, A, α, β, C_6, C_8, C_{10}, x_1, x_2, x_3, x_4 of which as many as possible are determined from other sources when they are accurately known and are left at a fixed value while the others are varied. For the CH_4 and NH_3 experiments little is known about the repulsive wall so x_1 and x_2 are set equal to zero and the morse function is allowed to represent the repulsive wall at the potential which is fine for these experiments since the particles do not sample far up the potential wall. The function is

now a "Morse-Spline-van der Waals" (MSV) potential with 8 variables ε, r_m, β, C_6, C_8, C_{10}, x_3, and x_4.

These two intermolecular potentials, the Lennard Jones (n,6) and the MSV, were both used to fit the data. To obtain a fit to the measured data a least squares fit was performed between each calculated angular distribution and the measured distribution. In the Lennard Jones potential the values for ε, r_m, and n were varied to obtain the best fit and for the MSV potential the values for ε, r_m, and β were varied to obtain the best fit. For MSV the van der Waals constant for the CH_4-Ar interaction was that suggested by Kramer and Herschbach[24] [$C_6 = 1.97\times10^{-10}$ erg Å^6], and C_8 and C_{10} were set equal to zero since the data did not extend into narrow angles where these two terms would be important. The two nodes x_3 and x_4 for the cubic spline function were set so x_3 would be the value of x where value of the Mose potential was $f(x) = -0.75$ and x_4 was set at 1.4.

2. Results

The measured angular distributions for collisions of CH_4 and argon at two different collision energies, 14.0×10^{-14} ergs and 13.4×10^{-14} ergs are shown in Figs. III-2 and III-5, respectively. The angular distribution for the collision of NH_3 and argon at a collision energy of 13.8×10^{-14} ergs in shown in Fig. III-3. The error bars on each data point are either one standard deviation calculated from the total number of counts at the particular angle or the standard deviation of the points measured at a given angle

Figure III-5. The measured angular distribution for CH_4 + Ar at a relative collision energy of 13.4×10^{-14} ergs. The error bars indicate the larger of either one standard deviation calculated from the number of background counts or the standard deviation of several points measured at the given angle. The solid line is the MSV potential with $\varepsilon = 2.14 \times 10^{-14}$ergs, $r_m = 3.82$ Å and $\beta = 7.05$.

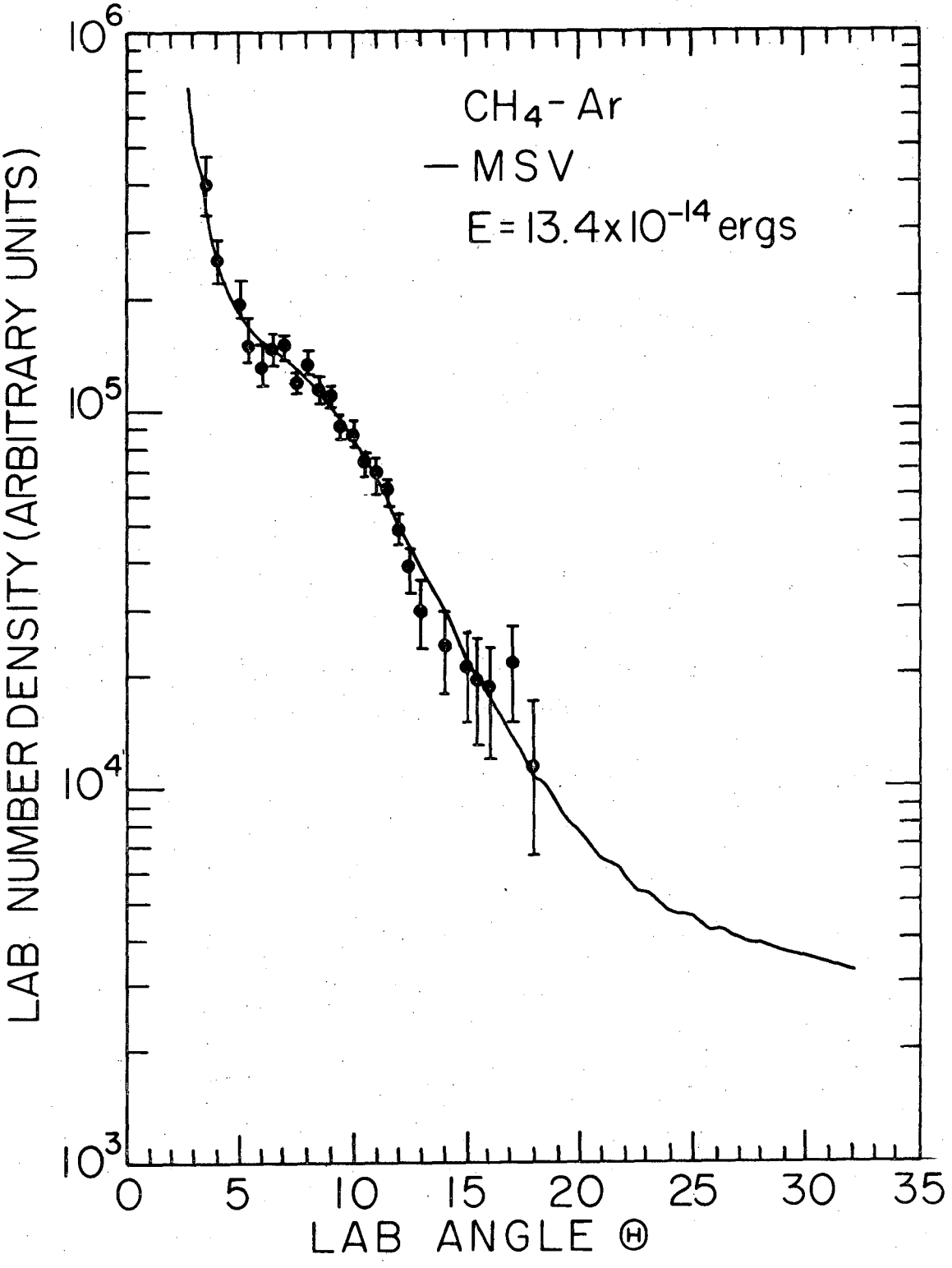

XBL 754-6053

Fig. III-5.

whichever is larger. In order to be convinced that the apparatus was working properly the O_2 + Ar system was run briefly to see if it reproduced published results. The O_2 + Ar angular distribution is shown in Fig. III-6 along with the calculated angular distribution using a Lennard-Jones (12,6) potential and the values for the potential as measured by Tully and Lee[10] of $\varepsilon = 2.03\times10^{-14}$ ergs and $r_m = 3.90$ Å. The fit is good and provides confidence that the measurements from the apparatus are not in disagreement with measurements of other groups. Unfortunately, very few of the molecular beam experiments have ever been reproduced by different groups-one exception being the Ar-N_2 interaction.

The CH_4-Ar data has been analyzed using two potentials--the Lennard-Jones (N,6) and the MSV. The angular distributions are calculated as previously described with averaging over angular resolution for beam parameters given in Table III-1 and averaging over three velocities in the CH_4 beam and one velocity in the argon beam. The monoenergetic approximation for the argon beam is valid since the velocity distribution is narrow (FWHM ~5%) and the averaging effect from the crossed beam is smaller. The C_6 constant for the MSV potential for a collision of two different species has been calculated using the combining rule of Kramer and Herschbach[24]

$$C_{ab} = \frac{2C_{aa}C_{bb}}{\left[\left(\frac{\alpha_b}{\alpha_a}\right) C_{aa} + \left(\frac{\alpha_a}{\alpha_b}\right) C_{bb}\right]} \qquad (13)$$

Figure III-6. The angular distribution of O_2 + Ar with the O_2^+ signal being detected. The solid line is the calculated angular distribution using the values of Tully and Lee[10], $\varepsilon = 2.03 \times 10^{-14}$ ergs and $r_m = 3.90$ Å, in a LJ (12,6) potential.

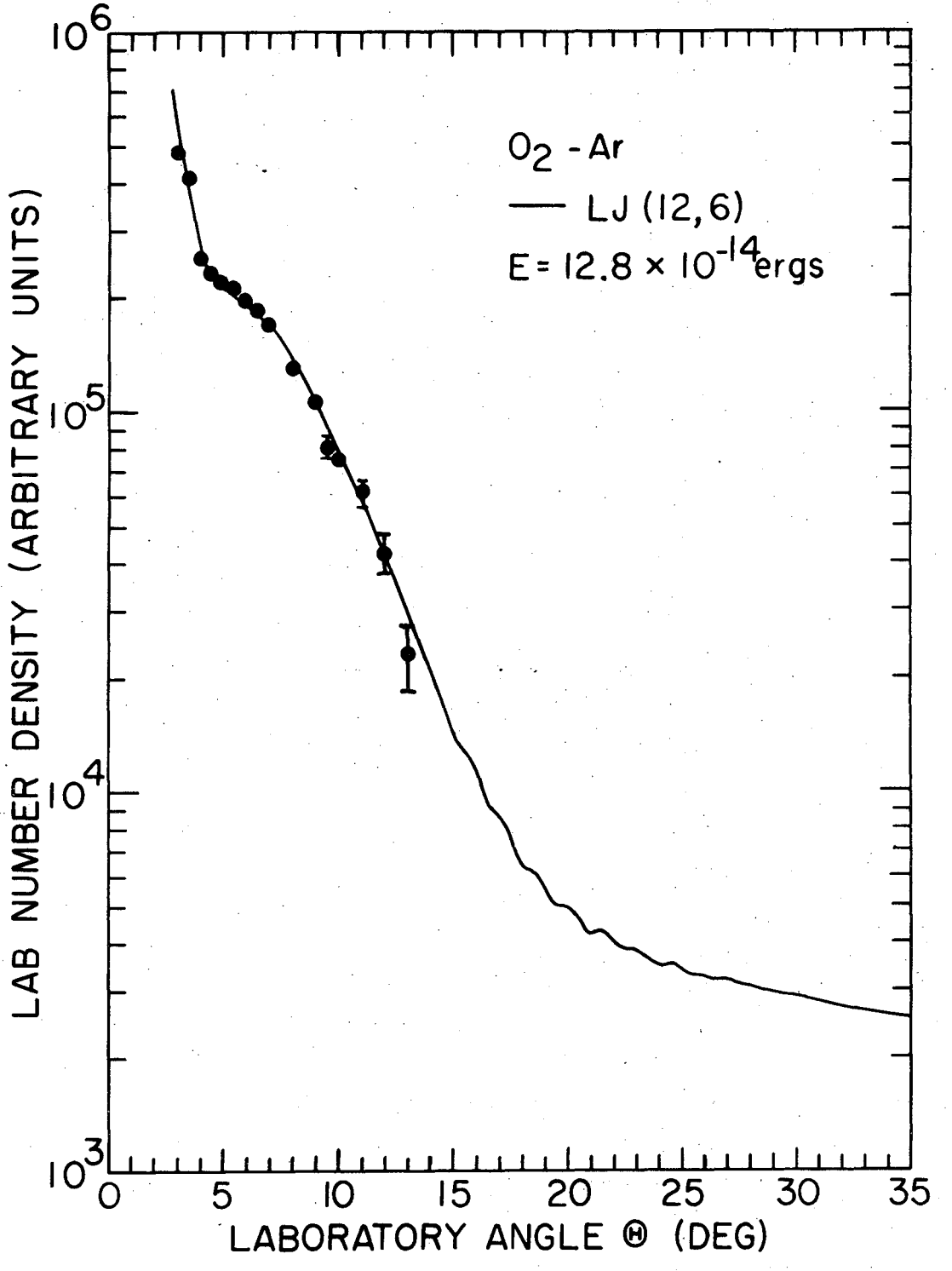

XBL 754-6056

Fig. III-6.

where C_{aa} and C_{bb} are the C_6 constants for the interaction of identical species and α_a and α_b are the polarizabilities for a particular particle. The values for C_6 from Dalgarno[25] are 6.22×10^{-11} erg $Å^6$ for Ar-Ar and 1.43×10^{-10} erg $Å^6$ for CH_4-CH_4. The polarizability of CH_4 is 17.6 $Å^3$ from reference (1) and the polarizability of Ar is 11.1 from reference (26). The value for the CH_4-Ar C_6 value is then 9.42×10^{-11} erg $Å^6$. The best fit using the MSV potential is shown in Fig. III-2 for the CH_4-Ar pair. Two interesting features of Fig. III-2 are the good fit to the distribution in the rainbow region around 10 degrees and the appearance of shoulders on the dark side of the rainbow between 10 and 25 degrees. In Fig. III-5 the parameters for the best fit of the higher energy data are shown for the low energy data. These potential parameters fit the data to within experimental error but because of the poor quality of this data these potential parameters are obviously not a unique fit to the data. Therefore the potential parameters must be obtained from the better high energy data.

As a better illustration of the features of the angular distribution Fig. III-7 shows the distribution plotted in the center-of-mass system. The intensity in the center-of-mass $I(\chi)$ times the $\sin\chi$ is plotted vs. χ, the center-of-mass angle. The $\sin\chi$ factor removes the geometrical weighting by large impact parameter collisions. The solid curve is that calculated for the best fit parameters using the MSV potential. The circles are the data points nominally transformed from the laboratory to the center-of-mass coordinate system.

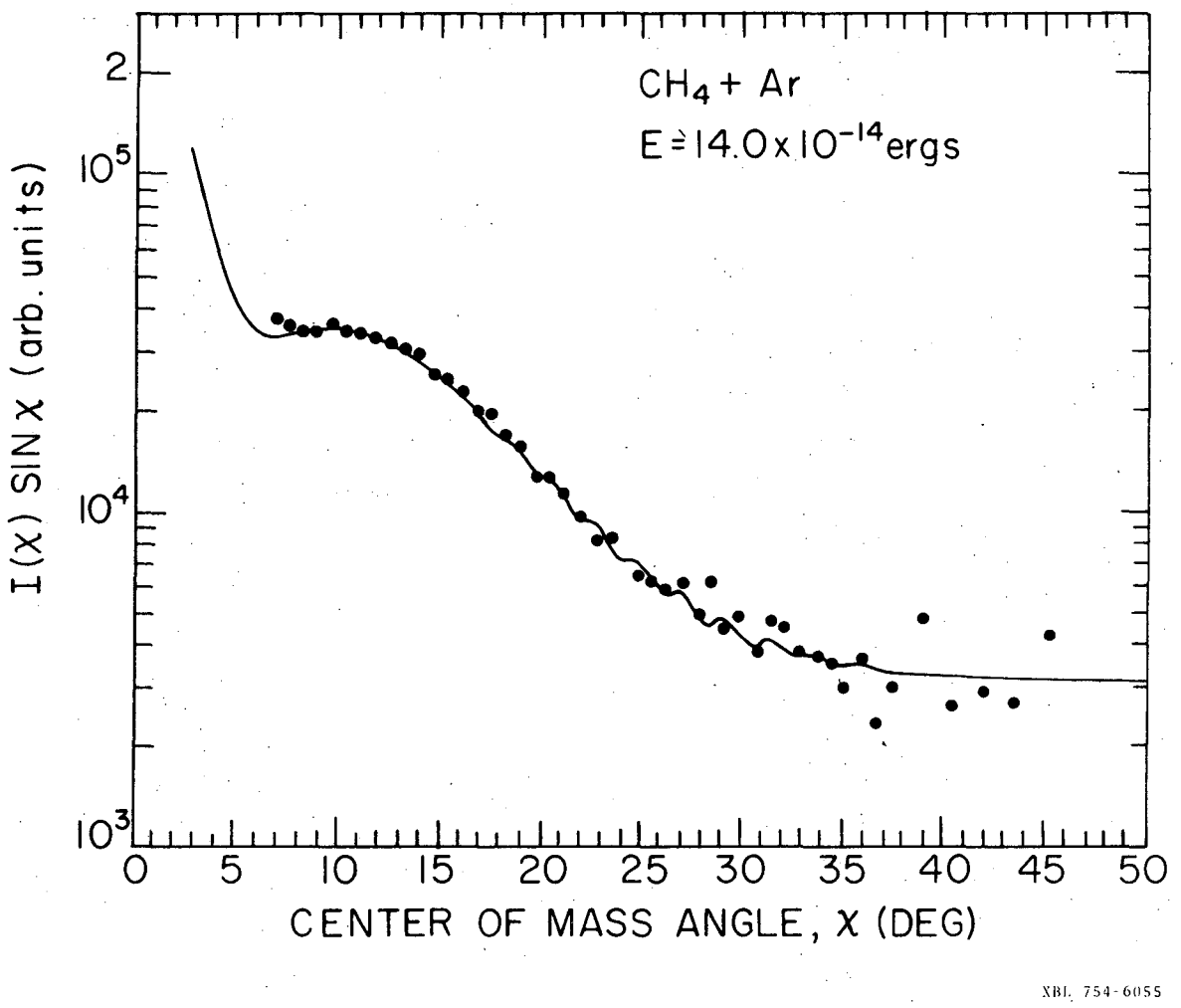

Fig. III-7. The center-of-mass angular distribution for CH_4 + Ar. The data points were transformed using a nominal LAB → CM1 transformation.

These points are not accurate since the velocity averaged beams can not be taken into account. The figure does make the rainbow angle more pronounced.

In order to illustrate the scattering better, the narrow angle scattering is factored out by plotting $N_L(\Theta)\ \Theta^{4/3}\ \sin\Theta$ vs. Θ where $N_L(\Theta)$ is the LAB number density. A plot of this is shown in Fig. III-8. The rainbow angle is now very apparent, peaking at 10°, and the oscillations are also more pronounced. The presence of these oscillations has permitted a more accurate determination of the potential parameters since the location of the rainbow is predominently determined by the depth of the potential well, ϵ, and the frequency of the oscillations is dependent on r_m. These oscillations in molecular systems have been seen before for H_2+H_2[5] and for H_2+O_2, SF_6, NH_3, CO and CH_4 and D_2+O_2, SF_6, and NH_3.[18] These results seem to contradict the semi-classical calculation of Cross[27] which predicts a damping of the oscillations due to the anisotropy in the potential, but as pointed out by Gordon, Coggiola and Kupperman[18] the oscillations for the H_2 scattering arise from diffraction effects from the steep repulsive wall of the potential. Since CH_4 is a relatively light molecule, the observed oscillations in the data may arise from these diffraction effects. To test this hypothesis an angular distribution was calculated for a purely repulsive potential on both the CH_4-Ar and H_2-Ar systems. The angular distributions for each are shown in Fig. III-9. Both calculations use the same angular and velocity averaging as used in analysing the data. It is apparent that the

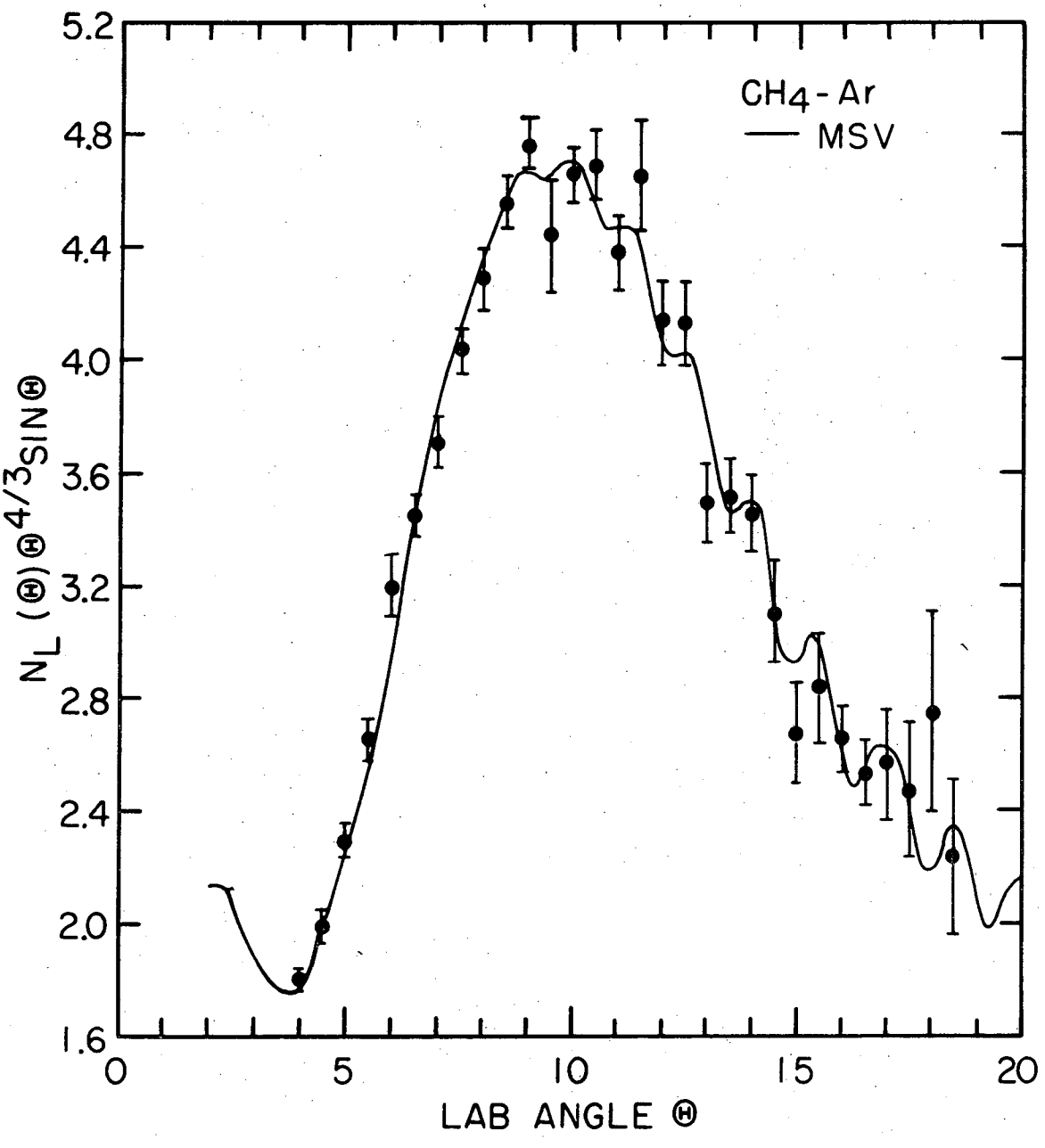

XBL 754-6057

Fig. III-8. A N_L (Θ) $\Theta^{4/3}$ SIN Θ vs. Θ plot showing the pronounced rainbow angle centered about 10 degrees along with the interference oscillations with a period of 1.4 degrees.

Fig. III-9. The calculated angular distribution for (- - -) H_2 + Ar and (——) CH_4 + Ar for the repulsive potential shown in the insert. The potential is of the form $f(\chi) = A \exp \alpha(1-\chi)$.

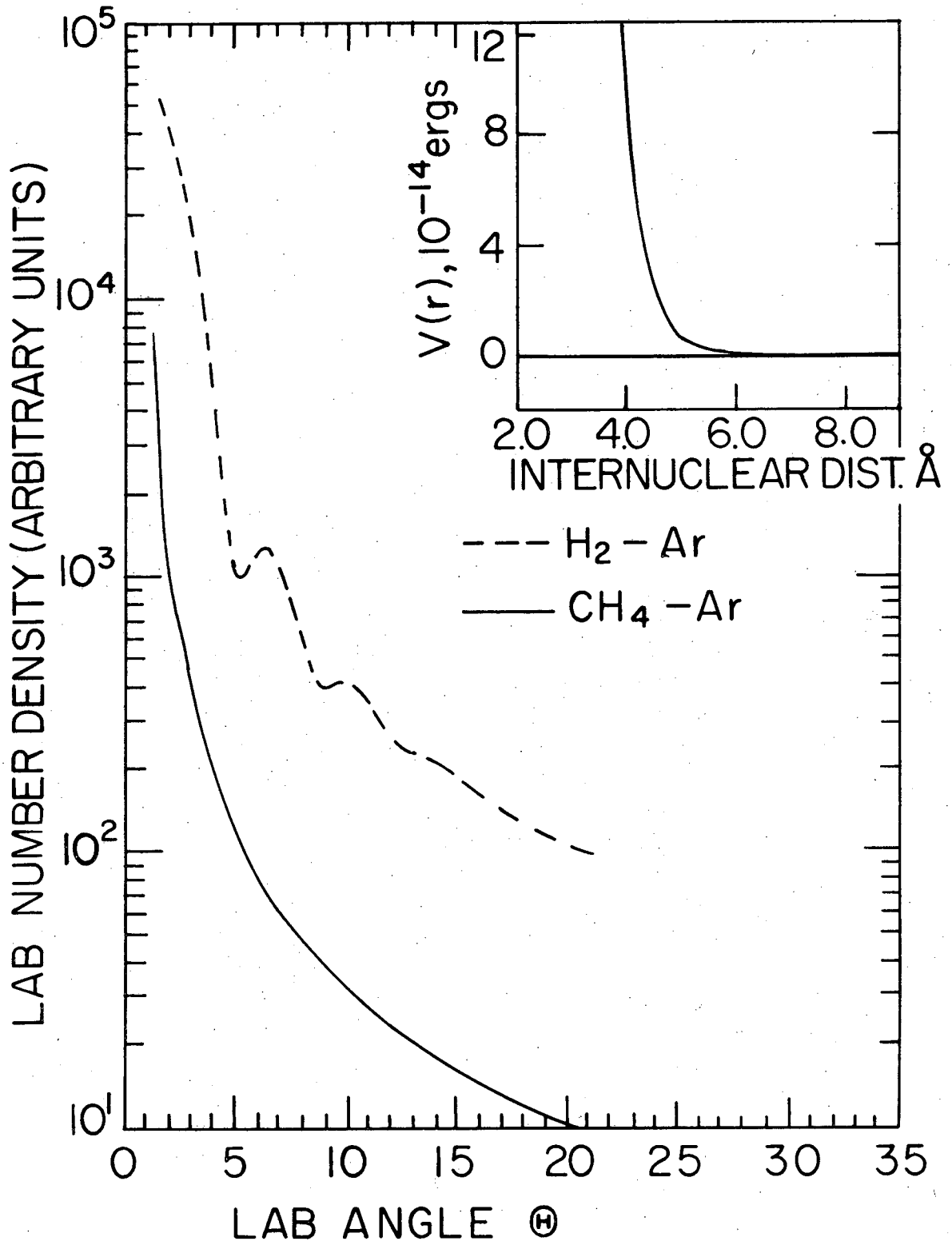

XBL 754-6054

Fig. III-9.

the diffraction effects do not survive for the CH_4-Ar system whereas they are quite pronounced for the H_2-Ar pair. This leads to the conclusion that for CH_4-Ar the oscillations must arise from interferences between different branches of the potential. Methane must therefore not have a substantial anisotropic potential. This is consistent with the model of rigid tetrahedral molecules used by Verlin, Cooper, and Hoffman[28] to fit transport coefficients in a magnetic field which finds that methane is only slightly anisotropic.

To determine the range of parameters for the MSV potential that would give a good fit to the data the computer program was used to calculate the standard deviation of the data for a range of potential parameters. The calculated angular distributions were averaged over angle and velocity as described before, prior to calculating the standard deviation. The results for these calculations are shown in Table III-2 and contour diagrams using values from the table for each value of β are shown in Fig. III-10. The best values for the parameters of the MSV potential are listed in Table III-3. The best values for the three varied parameters in the potential are: $\varepsilon = 2.20(\pm.04)\times10^{-14}$ ergs, $r_m = 3.82(\pm.04)$Å, and $\beta = 7.05\pm.20$. The values of the parameters ε, r_m, and β which fit the data have the errors given above but consistent with the shaded area in Fig. III-10 for $\beta = 7.05$. The limits on r_m were ultimately determined when the frequency of the oscillations in the calculated distribution varied from the frequency of the oscillations in the data.

Table III-2. Standard Deviations of the CH_4-Ar Data from the MSV Potential

$\beta = 6.70$ $\epsilon(X10^{-14}$ ergs); r_m (Å)

r_m / ϵ	2.050	2.064	2.071	2.099	2.106	2.113	2.120	2.154	2.189	2.196	2.203	2.217	2.224	2.238	2.252	2.259	2.280	2.293	2.300	2.307	2.314	2.332	2.362	2.370	2.397	2.419
3.59																							.156			
3.62																										.0624
3.65																					.116		.0663		.0631	
3.67																								.0623		.113
3.68																										
3.70															.116			.0712				.0590				
3.73																			.0591							
3.735															.0729											
3.75									.123											.0845						
3.77												.0710														
3.775															.0572											
3.80					.165			.100					.0557			.0981		.138								
3.825										.0584				.0975												
3.85				.110			.0910																			
3.855								.0559																		
3.86											.100															
3.88	.149																.238									
3.89						.0631																				
3.90				.0696				.0902	.135																	
3.93		.0797					.0858																			
3.95	.0891			.0851				.152					.254													
4.00			.1034																							

Table III-2 (Cont'd)

$\beta = 7.05$

r_m \ ϵ	2.105	2.130	2.154	2.161	2.168	2.175	2.189	2.203	2.210	2.217	2.224	2.241	2.248	2.259	2.269	2.280	2.297	2.314	2.328	2.335	2.346	2.356	2.363	2.370	2.397
3.63																									.0879
3.66																	.158			.106				.0760	
3.70																.113				.0626					
3.705																		.0713			.0585				
3.710																						.0628			
3.73														.0951				.0548							
3.74																	.0542								
3.75																.0545									
3.76									.110					.0584											
3.77																.0527			.0998			.145			
3.79											.0567				.0585	.0681									
3.80							.0810												.143						
3.805												.0491													
3.81				.102												.0924									
3.82													.0664				.120								
3.825		.121								.0472															
3.835								.0471																	
3.84											.0639														
3.845						.0520																			
3.85			.0649													.136									
3.86	.112																								
3.873			.0519																.262						
3.865					.0597		.0768					.163													
3.90	.0703																								
3.91				.0759																					
3.93	.0607																								

Table III-2 (Cont'd.)

$\beta = 7.40$

r_m \ ξ	2.015	2.036	2.050	2.064	2.085	2.099	2.106	2.113	2.127	2.134	2.148	2.168	2.175	2.189	2.210	2.224	2.238	2.252	2.259	2.273	2.280	2.293	2.314	2.328	2.363
3.67																								.139	
3.69																									.0829
3.70																						.132			
3.725																								.0735	
3.75															.155										.0904
3.76																			.0889			.0649			
3.78																				.0608			.0744		
3.80																.0746		.0583			.0642	.0740		.111	
3.815																			.0621						
3.825													.0952												.188
3.83															.0605										
3.85					.170									.0612			.0703				.118				
3.86									.110																
3.88												.0599			.0757										
3.90						.101		.0744			.0597														
3.91									.0681							.127									
3.92			.139																						
3.93												.0634													
3.94							.0673			.0663															
3.95		.124			.0746																				
3.97						.0669																			
3.98				.0764					.0894			.137													
3.99		.0932																							
4.00					.0730																				
4.025	.0913																								
4.05			.0782		.106																				
4.07	.0774																								

Figure III-10. The contours show the lines of standard deviation of the CH_4 - Ar data obtained from values listed in Table III-2. The standard deviation is listed on each contour line. The shaded area on the center contour is the region of ε and r_m values which fit the data. The β value of 7.05 for the center contour is the best fit to the data.

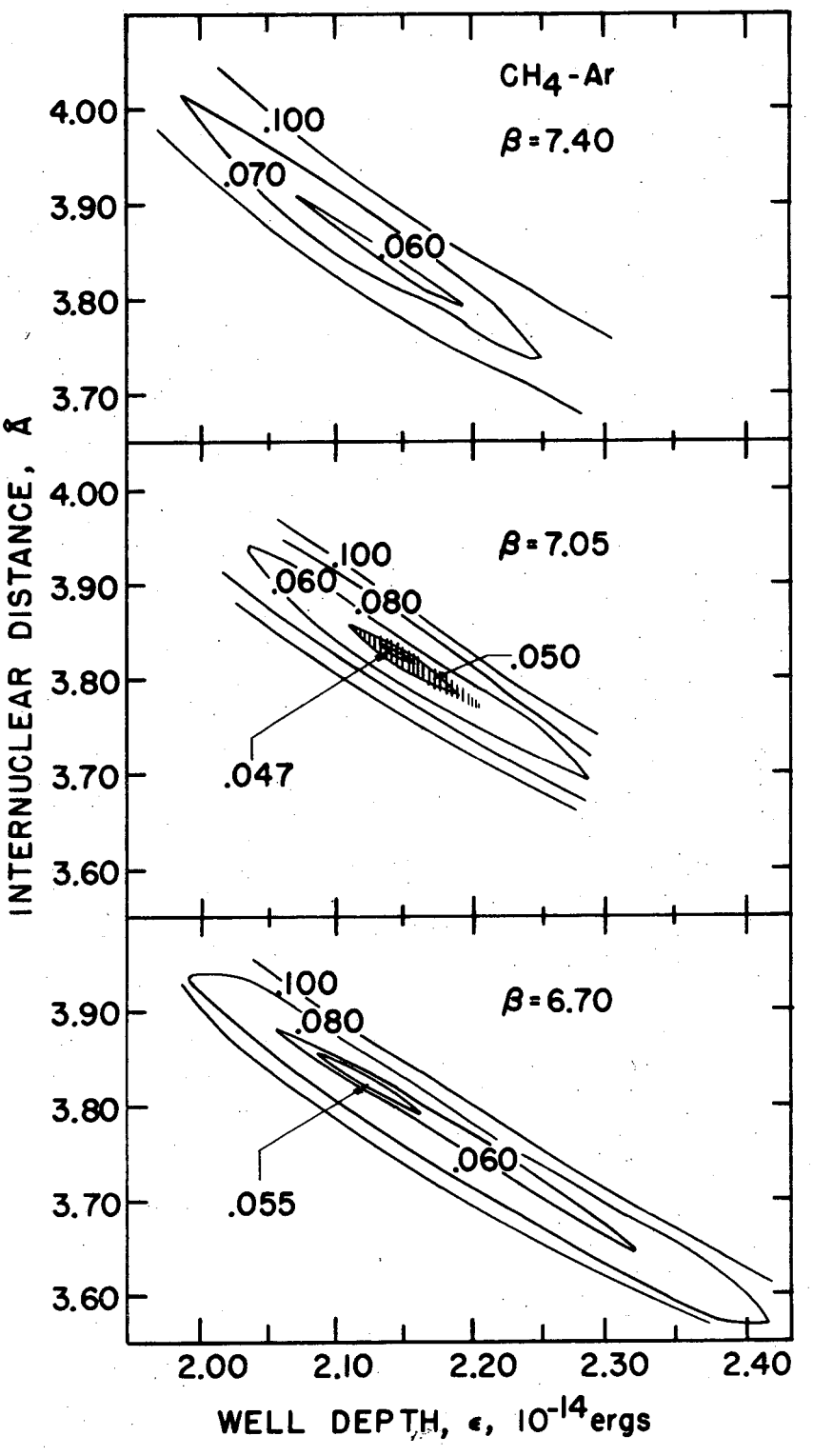
CH4 - Ar
β = 7.40
.100
.070
.060
β = 7.05
.100
.060
.080
.050
.047
β = 6.70
.100
.080
.060
.055
INTERNUCLEAR DISTANCE, Å
4.00
3.90
3.80
3.70
3.60
2.00
2.10
2.20
2.30
2.40
WELL DEPTH, ε, 10-14ergs
XBL 754-6060

Fig. III-10.

Table III-3. MSV Potential Parameters

Parameter	CH_4 - Ar	NH_3 - Ar
ε	$2.20(\pm.04)\times10^{-14}$ ergs	$2.21(\pm.04)\times10^{-14}$ ergs
r_m	3.82(±.04) Å	3.93(±.05) Å
β	7.05 ±.20	8.45 ±.30
C_6	9.416×10^{-11} erg Å^6	8.999×10^{-11} erg Å^6
χ_3	1.098	1.082
χ_4	1.40	1.40
b_1	-0.75	-0.75
b_2	1.894	1.886
b_3	-5.405	-7.355
b_4	5.502	1.084

The data was also fit using a Lennard-Jones (n,6) potential. The best fit parameters for the Lennard-Jones potential were: $\varepsilon = 2.27\times10^{-14}$ ergs, $r_m = 3.77$ Å, and n = 18. Both the Lennard-Jones (n,6) and the MSV for CH_4-Ar are shown in Fig. III-11. The agreement between the two curves is good with the greatest differences being in the region of the potential well.

The NH_3-Ar angular distribution is shown in Fig. III-3. This data was first analyzed using a Lennard-Jones (n,6) potential. The best fit to the data was found using potential parameters of $\varepsilon = 2.43\times10^{-14}$ ergs, $r_m = 3.50$ Å, and n = 30. When the data is plotted in the $N_L(\Theta)\ \Theta^{4/3}\ \sin\Theta$ vs. Θ form, the oscillations of the calculated distribution do not fit the oscillations of the data points as shown in the lower half of Fig. III-12. This placed a certain degree of uncertainly on the reality of oscillations in the measured data. Since the Lennard-Jones (n,6) potential has its parameters coupled as mentioned previously, the MSV potential was used instead to try to fit the data.

Since experimental values for C_6 do not exist for NH_3-Ar it was necessary to calculate the C_6 constant to use in the MSV potential. A combination of the Slater-Kirkwood approximation along with the Kramer and Herschbach combining formula was used for the calculation. The approximate value for the C_6 constant for like interactions is

$$C_{aa} = \frac{3}{4}\ \alpha_a^2\ \bar{\omega}_a \qquad (14)$$

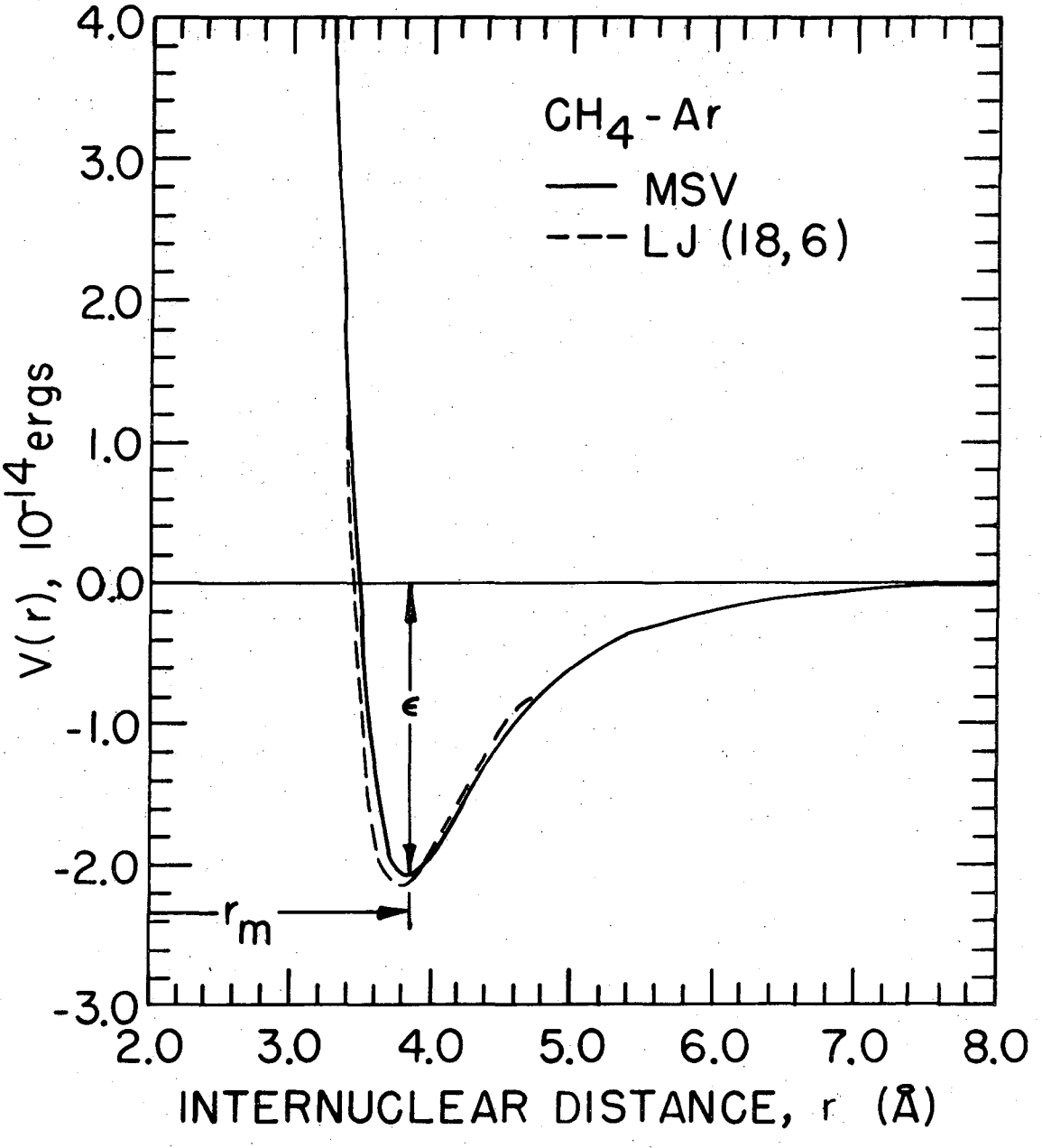

XBL 754-6051

Fig. III-11. The CH_4 - Ar intermolecular potentials. The solid line is the best MSV potential and the dashed line is the best Lennard Jones potential.

Figure III-12. Two plots of N_L (H) $H^{4/3}$ SIN H vs. H are shown for the NH_3 - Ar data. The solid curve in the upper distribution is the calculated fit for the best MSV potential. The dashed line in the lower distribution shows the best fit for the LJ (30,6) potential.

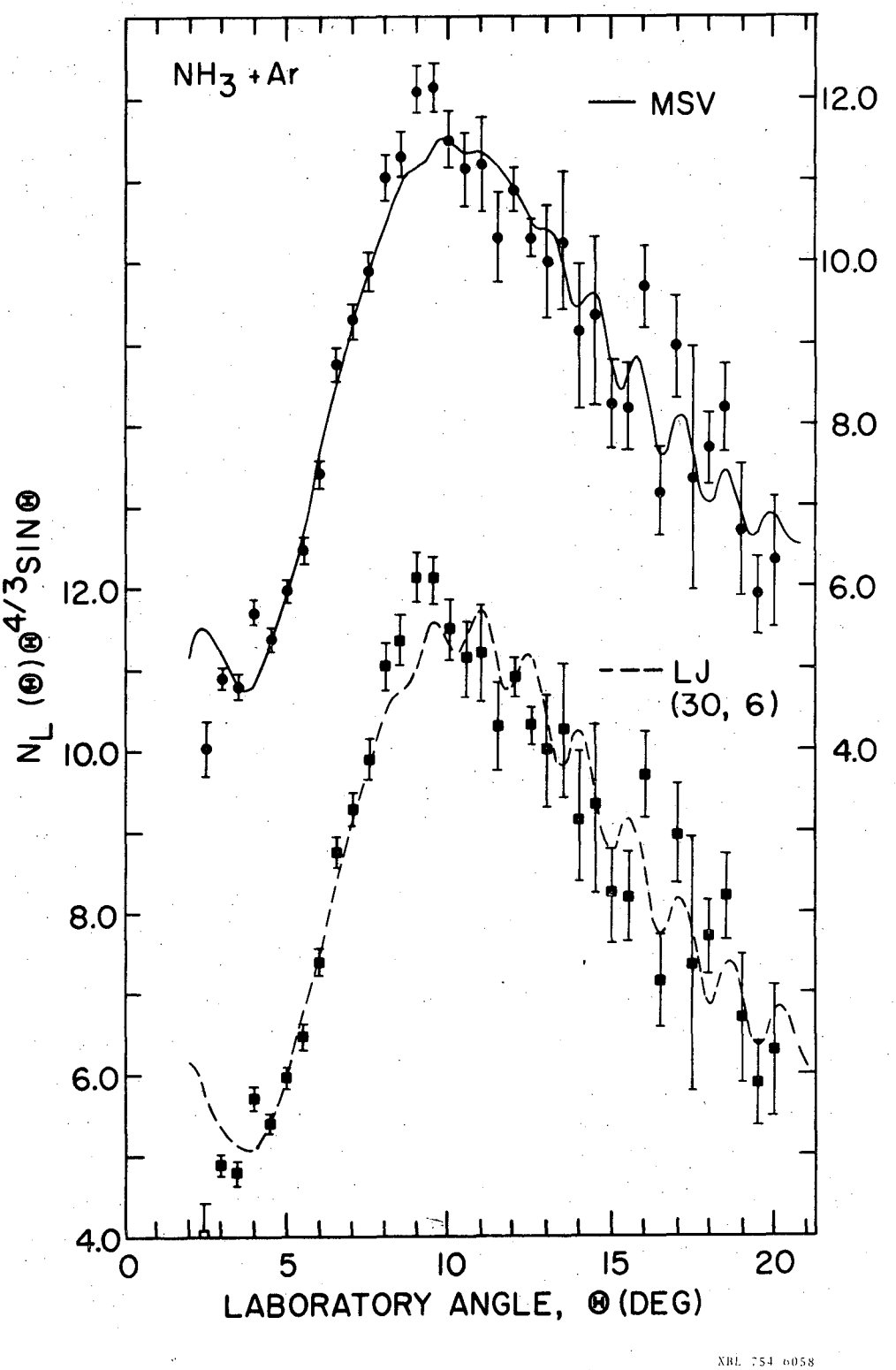

Fig. III-12.

where α_a is the polarizability and $\bar{\omega}_a$ is some average energy for transitions from the initial state. In the Slater-Kirkwood approximation

$$\bar{\omega}_a = (N_a/\alpha_a)^{1/2} \quad , \tag{15}$$

where N_a is the number of electrons in the outer shell of a. Using a value of 8 for N_a, $C_{NH_3-NH_3} = 1.203\times10^{-10}$ erg Å^6. This is probably a good approximation since for CH_4 a value of 7.4 for N_a in the Slater-Kirkwood approximation would give the same $C_{CH_4-CH_4}$ constant as calculated by Dalgarno.[25] This calculated value for $C_{NH_3-NH_3}$ was then used in the Kramer-Herschbach formula (Eq. 13) to calculate the C_6 constant for NH_3-Ar.

The use of the Slater-Kirkwood approximation for the NH_3-Ar C_6 constant would be poor compared to the Kramer-Herschbach method because the Slater-Kirkwood gives a very poor approximation to the Ar-Ar C_6 constant. So the value for C_{Ar-Ar} ($=6.22\times10^{-11}$ ergs) is again from Dalgarno, $\alpha_{NH_3} = 2.26$ Å^3[1], and $\alpha_{Ar} = 1.64$ Å^3. The value of C_6 for NH_3-Ar is 8.64×10^{-11} erg Å^6. The value of C_6 to be used in the MSV potential should also have the dipole-induced dipole term included in it even though it is a small contribution. The contribution to the potential from the dipole-induced dipole is

$$V_{\text{dipole-induced dipole}} = -\frac{\mu_{NH_3}^2 \alpha_{Ar}}{r^6} [g(\theta)] \quad , \tag{16}$$

where μ_{NH_3} is the dipole moment of ammonia (=1.47 Debye), and $g(\theta)$ is the orientation term which for a geometrical average is 1. The $1/r^6$ coefficient for the dipole-induced dipole term is then 3.52×10^{-12} erg $Å^6$. This gives a final value of 8.99×10^{-11} erg $Å^6$ to be used for C_6 in the MSV potential.

The MSV best fit to the angular distribution is shown in Fig. III-3, and $N_L(\Theta)\ \Theta^{4/3}\ \sin\Theta$ vs. Θ plot is shown in the upper half of Fig. III-12. The oscillations of the calculated distribution have the same frequency and phase as the measured data for these MSV parameters. The three varied parameters for this fit have values of $\varepsilon = 2.21(\pm.04)\times10^{-14}$ ergs, $r_m = 3.93(\pm.05)$ Å, and $\beta = 8.45\pm.30$. Three contour diagrams representing the stardard deviation of the measured data from the calculated values for three different values of β are shown in Fig. III-13 and the associated standard deviations are listed in Table III-4. The values of ε and r_m again must fall within the shaded area shown on the β=8.45 contour of Fig. III-13. The values for all of the MSV parameters are listed in Table III-3. The potential energy curve for the MSV potential and the Lennard-Jones (30,6) potential are shown in Fig. III-14. The difference between the two potential energy curves is very pronounced. One difference to be noted in the LJ(30,6) potential is the less rapid descent at the larger internuclear distances. This is due to the value of C_6 being 5.58×10^{-11} erg $Å^6$ which is 38% lower than the calculated value of 8.99×10^{-11} erg $Å^6$. The shape of both potential wells is approximately the same with respect to the width at different energies. This difference of the LJ curve from the MSV

Figure III-13. The contours show the lines of standard deviation of the NH_3-Ar data obtained from values in Table III-4. The standard deviation is listed on each contour line. The shaded area on the center contour is the region of ϵ and r_m values which fit the data. The β value of 8.45 for the center contour is the best fit to the data.

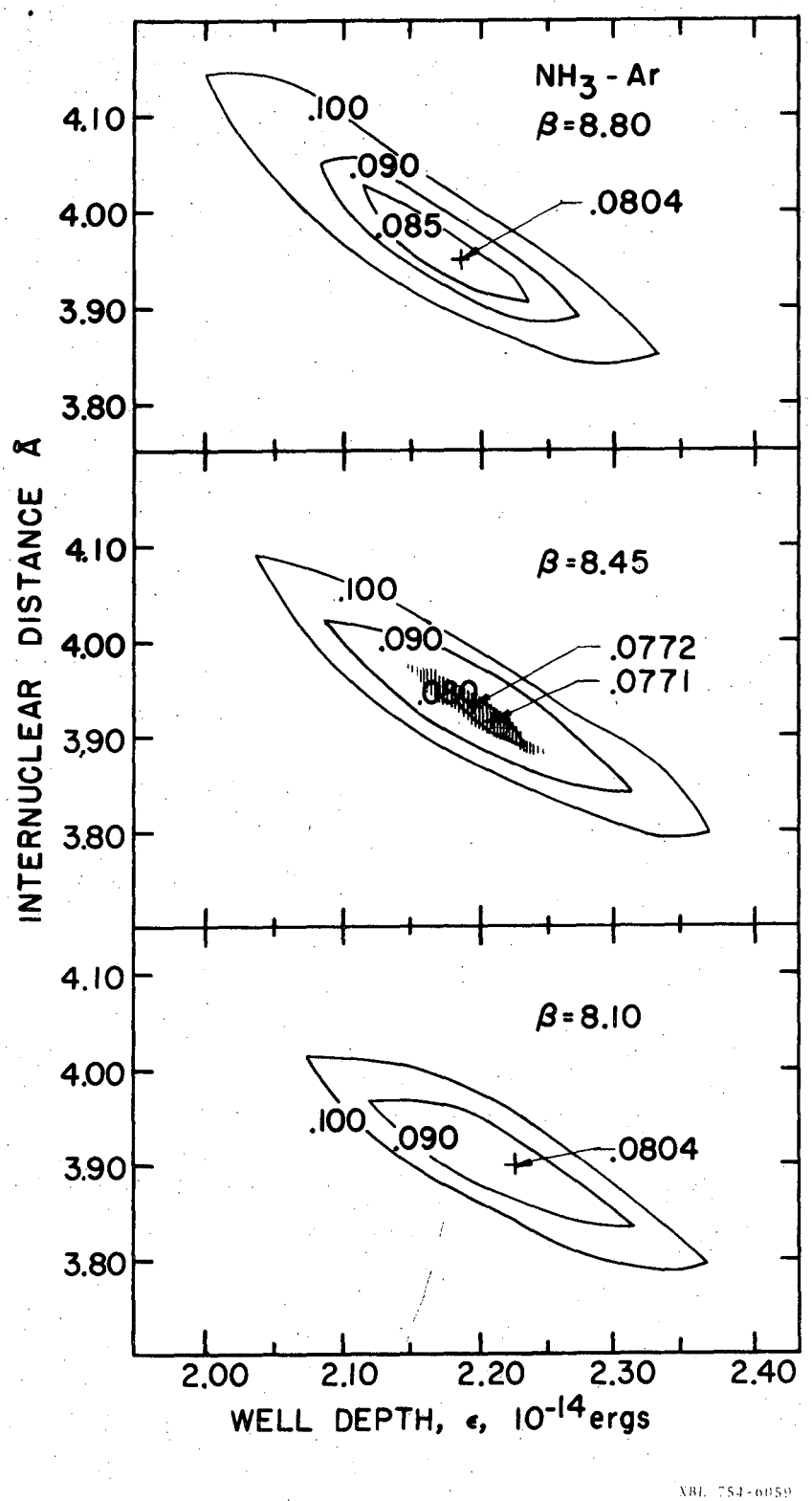

XBL 754-6059

Fig. III-13.

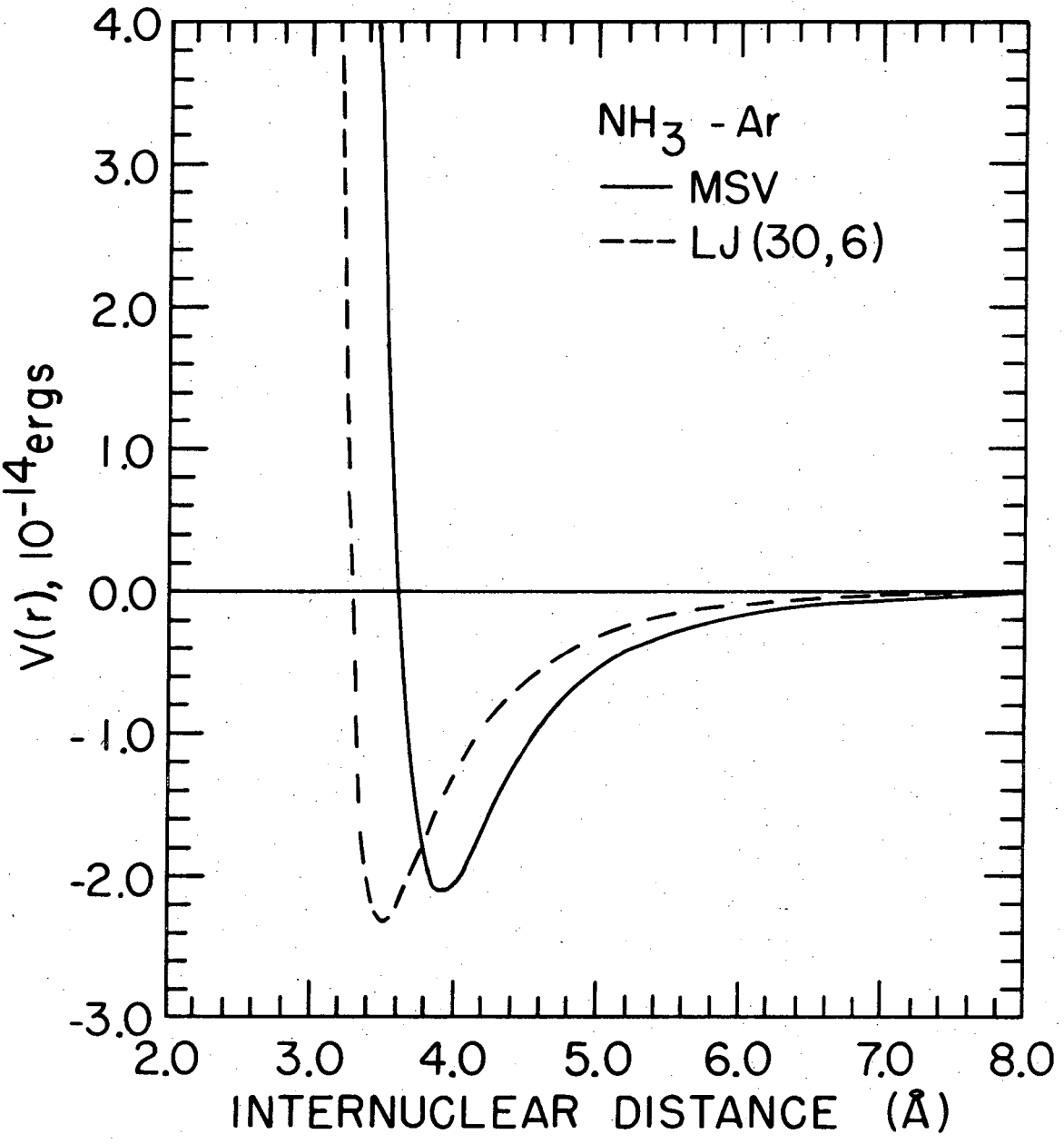

XBL 754-6049

Fig. III-14. The intermolecular potentials for NH_3-Ar. The best potential is the MSV potential shown by the solid line. The LJ (30,6) potential is shown as a comparison to illustrate the difficulty in fitting with a Lennard-Jones potential.

Table III-4. Standard Deviations for NH_3-Ar $\varepsilon(\times 10^{-14}$ergs) r_m(Å) β = 8.10

r_m \ ε	2.015	2.050	2.085	2.120	2.154	2.189	2.224	2.259	2.293	2.328	2.363
3.60	-	-	-	-	-	-	.294	-	.258	-	.220
3.65	-	-	-	-	-	-	-	-	-	-	.175
3.70	-	-	.290	-	.253	-	.212	-	.171	-	.134
3.75	-	-	-	-	-	-	-	-	-	-	.107
3.80	.257	-	.216	-	.171	-	.128	-	.0968	.0941	.100
3.85	-	-	-	-	-	-	.0927	.0849	.0883	.102	-
3.90	.187	-	.139	-	.0962	.0828	.0804	.0908	.110	.132	-
3.95	-	-	-	.0932	.0838	.0869	.0995	.119	.147	-	-
4.00	.133	-	.0981	.0947	.0984	.1138	.135	.161	-	-	-
4.05	-	.109	.105	.112	.127	.1475	-	-	-	-	-
4.10	-	.115	.123	.137	-	-	-	-	-	-	-

Table III-4 (Cont'd.)

$\beta = 8.45$

r_m \ ε	2.015	2.050	2.085	2.120	2.154	2.189	2.203	2.224	2.238	2.259	2.273	2.293	2.307	2.328	2.342	2.363
3.65																.190
3.70												.183		.165		.148
3.75								.180		.160		.142		.126		.116
3.76															.115	
3.80								.137		.119		.105	.102	.0986		.101
3.85						.115		.100		.0882		.0869		.0964		.114
3.87											.0833					
3.88									.0815							
3.90					.100	.0845		.0783		.0835		.0992				
3.915							.0772									
3.94						.0771										
3.95				.0933	.0798			.0895		.109						
3.98					.0821	.100										
4.00		.112	.0945	.0857	.0875			.121								
4.05	.119	.100	.0943	.0982	.112											
4.10	.108	.101	.107	.120												
4.15	.105	.112														

Table III-4 (Cont'd.)

$\beta = 8.80$

r_m \ ϵ	2.015	2.050	2.085	2.120	2.154	2.189	2.224	2.259	2.293	2.328	2.363	2.398	2.432
3.60													.213
3.70											.163		.139
3.75									.156	.141	.129	.122	.123
3.80					.188		.150	.133	.119	.111	.110	.115	.129
3.85						.128	.110	.0987	.0954	.0999	.113	.132	
3.90			.153		.110	.0940	.0837	.0864	.0980	.118	.139		.190
3.95				.0991	.0842	.0804	.0867	.103					
4.00	.136	.115	.0979	.0843	.0839	.0945	.1120		.155		.214		.265
4.05		.0981	.0900	.0896	.102								
4.10	.0994	.0920	.0949		.129		.179		.232		.284		
4.20					.187		.241		.293				

curve just points out that the Lennard-Jones potential is a very inflexible potential and it is difficult if not in some instances almost impossible for it to give the proper potential energy curve.

D. Discussion

Through the resolution of the rainbow and the interference undulations, the potential for CH_4-Ar has accurately been determined. Two other studies have been done on the CH_4-Ar pair interaction. One is a velocity dependent total cross section measurement by Eckelt, Schimpke, and Schügerl[7] in which they determined the potential parameters by fitting the slope of the higher velocity data. They were unable to resolve the glory undulations at lower velocities due to thermal averaging by the gas in the scattering cell. The other measurements on this system are thermal diffusion measurements by Stevens and de Vries.[29] They have studied the thermal diffusion rates for mixtures of various hydrogen isotopes of methane with methane and also with argon. A comparison of the measured values of these two studies and ours is shown in Table III-5.

Table III-5. Potential Parameters for the CH_4-Ar Interaction.

Work	Potential Form	ε ergs(10^{-14})	r_m(Å)
Eckelt et al.	LJ(12,6)	1.81	2.67
Stevens & de Vries	LJ(12,6)	2.04	-
Present	MSV	2.20	3.82

The work by Eckelt et al. is in disagreement with our measured values for both ϵ and r_m. They have expressed their doubts as to the validity of the values and they believe that their values may be low. They also measured the velocity dependent cross sections for the Ar-Ar pair interaction along with CH_4-Ar, and obtain values of $\epsilon = 1.70\times10^{-14}$ ergs and $r_m = 2.89$Å. These values are also low when compared to those obtained from differential cross section measurements by Parson, Siska, and Lee[4] of $\epsilon = 1.994\times10^{-14}$ ergs and $r_m = 3.715$Å. This tends to confirm that their values are low. The value of ϵ obtained by thermal diffusion is in fairly good agreement with ours.

The ammonia-argon pair interaction has previously been measured by Brooks and Grosser.[16] They have fit their data with three different potentials--a Lennard-Jones(n,6), a Kihara-Stockmayer, and a Maitland-Smith. A list of their ϵ, and r_m values for the different potentials are shown in Table III-6. The Brooks and Grosser data cannot be directly compared to our data since the relative collision energies of each are different. Even if the angular distributions of the two experiments were run at the same collision energy they still could not be easily compared since the data for each was taken under different beam conditions.

As can be seen from Table III-6, the Brooks and Grosser LJ(12,6) ϵ and r_m parameters are close to our ϵ and r_m parameters for a LJ(30,6) potential, but the large difference in the value of n makes these two potential curves quite dissimilar. Since the value for C_6 in our Lennard-Jones (30,6) potential differs substantially from the calculated

Table III-6. Potential Parameters for the NH_3-Ar Interation.

Work	Potential	$\varepsilon_{ergs}(\times 10^{-14})$	r_m (Å)	
Brooks & Grosser	LJ(12,6)	2.45	3.65	
	LJ(18,6)	2.32	4.11	
	K-S*($\bar{g}$=1.0)	2.25	4.00	$2a/r_m = 0.143$
	K-S*(g=1.25)	2.23	4.02	$2a/r_m = 0.143$
Present	LJ(30,6)	2.43	3.50	
	MSV	2.21	3.93	$\beta = 8.45$

*Kihara-Stockmayer

$$V(r) = 4\varepsilon\left[\left(\frac{\sigma}{r-2a}\right)^{12} - \left(\frac{\sigma}{r-2a}\right)^{6}\right] - \frac{\mu_p \alpha_n}{r_6}\ [g(\theta)]$$

a is the Kihara core size, μ_p and α_n are the dipole moment and the polarizability of the polar and non-polar species, respectively.

value, the LJ(30,6) potential just again illustrates the difficulty in fitting scattering data with a coupled potential. The best potential curve to fit the data is the MSV potential, with $\varepsilon = 2.21\times10^{-14}$ ergs; $r_m = 3.93$ Å, and $\beta = 8.45$. This ε value is in good agreement with Brooks and Grosser for the LJ(18,6) and the K-S potential. The agreement between the r_m values is not as good. Our potential gives a lower r_m value than the other potentials, although there is better agreement between the MSV and the K-S r_m values. The Brooks-Grosser value for C_6 from their LJ(18,6) potential is 1.67×10^{-10} erg Å^6 which is 85% larger than the value of 8.999×10^{-11} erg Å^6 calculated from the Slater-Kirkwood approximation as described previously and using a value of 8 for the number of electrons in the outer shell of the NH_3 molecule. This calculation together with the contribution from the dipole-induced dipole term should give an upper limit which is accurate to within 10% to the C_6 value, which for the Brooks-Grosser data is exceeded by 85%. The r_m value for the best fit to our MSV potential also gives a good fit to the period of the oscillations seen in the data. The period of the oscillations is strongly dependent on the value of r_m and thus restricts the range of r_m that will fit the angular distribution. Therefore, by using a calculated value for C_6 which is accurate to within 10% and also fitting the period of the oscillations in the angular distribution our best fit parameters in the MSV potential should provide the better potential for the NH_3-Ar interaction.

Once potential parameters are known for two pair interactions for three different species, combining rules have been used to predict the third pair interaction. This is very useful for calculating the unknown pair interaction, but caution must be exercised in using the combining formula because as pointed out and experimentally shown by Chen, Siska, and Lee the use of the combining formulas are unreliable when the potentials of the two like pair interactions differ substantially. The use of the combining formulas are predicated on the potentials for each interaction having the same reduced form. Since not only ϵ and r_m but also the shape at the curve may change making the use of simple combining rules inaccurate. But if accuracy is not needed then the simple combining rule could be used and values for the CH_4-CH_4 and the NH_3-NH_3 pair interactions could be calculated since the Ar-Ar interaction potential is well known.[4]

The presence of oscillations in the angular distributions for both methane and ammonia leads to the conclusion that both must have a fairly symmetric potential so as to be consistent with the averaging effects of anisotropic potentials an angular distributions, as discussed by Cross.[27] In the total cross section measurements of Li plus a large number of gases by Rothe and Helbing[30,31] only a very small amount of quenching of the glory undulations was seen for the Li + CH_4 interaction and a moderate amount of quenching was seen for the Li + NH_3 interaction. For the CH_4-Ar interaction this long range dispersion interaction for the C_6 term is symmetric since $\alpha_{\parallel}$ and $\alpha_{\perp}$,

the polarizabilities parallel and perpendicular to the interaction axis, are equal for CH_4. The first asymmetric long range term will be the quadrupole-induced dipole term which will be small. For the short range interaction it has been shown[28] that for a rigid model assumption the potential for CH_4 is highly symmetric. The long range interaction between NH_3 and Ar is somewhat different from CH_4. First there is a dipole-induced dipole force which is a small effect since it is only about 5% as strong as the dispersion term. The anisotropy introduced in the dispersion term should be small for NH_3 since $\alpha_{\parallel} = 2.42$ Å^3 and $\alpha_{\perp} = 2.18$ Å^1 where $\alpha_{\parallel}$ is along the symmetry axis of NH_3. These estimates of the anisotropy on these two systems are in agreement with the quenching seen by Rothe and Helbing for Li plus NH_3 and CH_4 and for the CH_4-Ar and NH_3-Ar interactions. Thus, the survival of the undulations in the angular distribution is not unreasonable if only the anisotropy of the potential is considered.

The interference effect seen in the angular distributions arises from the interference between the repulsive branch of the deflection function and attractive branch around the rainbow region. Therefore, the angular distribution is sampling the region of "hard collisons" which contribute to the positive angles of deflection. Rotationally inelastic collisions would be expected to occur in this region of moderately hard collisions. Consequently, since there is very little damping in the undulations for both NH_3 and CH_4 interacting with argon in this region the cross section for rotational inelastic scattering should be small.

In conclusion, it is apparent that the hydride molecules are well suited for the study of elastic and rotationally inelastic scattering. With the large rotational energy level spacings in CH_4, NH_3, and HF, the rotationally inelastic processes can be studied using the time-of-flight technique. This study would provide much more information on the anisotropy of the hydride's potential. Also, an elastic scattering study of larger molecules such as CF_4, SF_6, C_2H_6 and C_2H_4 may provide more information on the relative anisotropies of these molecules. This molecular beam apparatus has proved its capabilities by resolving the interference undulations on these hydride systems, but the inelastic scattering studies, being more difficult, will undoubtedly take much more work, so thought must be given to pursuing these studies or some other chemical questions that molecular beams are suited to answering.

Chapter III. References

1. See J.O. Hirschfelder, C.F. Curtiss, R.B. Bird, Molecular Theory of Gases and Liquids, 1954.
2. R. B. Bernstein and J. T. Muckermann, 1967 Adv. Chem. Phys. 12, 389-486 ed J.O. Hirschfelder (New York: Interscience).
3. P. E. Siska, J. M. Parson, T. P. Schafer, and Y. T. Lee, J. Chem. Phys. 55, 5762 (1971)
4. J. M. Parson, P. E. Siska, Y. T. Lee, J. Chem. Phys. 56, 1511 (1972).
5. J. M. Farrar and Y. T. Lee, J. Chem. Phys. 56, 5801 (1972).
6. C. H. Chen, P. E. Siska, and Y. T. Lee, J. Chem. Phys. 59, 601 (1973).
7. W. R. Eckelt, B. Schimpke, and K. Schügerl, Z. Physik Chem. (Frankfurt) 68, 266 (1969).
8. R. W. Bickes, Jr. and R. B. Bernstein, Chem. Phys. Letters 4, 111 (1969).
9. F. Kalos and A. E. Grosser, Chem. Phys. Letters 6, 537 (1970).
10. F. P. Tully and Y. T. Lee, J. Chem. Phys. 57, 866 (1972).
11. J. M. Farrar and Y. T. Lee, Chem. Phys. Letters 26, 428 (1974).
12. B. Schimpke and K. Schügerl, Z. Physik, Chem. (Frankfurt) 75, 32 (1971).
13. H. Hose, U. Koller, and K. Schügerl, Z. Physik Chem. (Frankfurt) 82, 97 (1972).
14. R. Düren, A. Frick, and C. Schlier, J. Phys. B 5, 1744 (1972).

15. R. Brooks, F. Kalos, and A. E. Grosser, Molec. Phys. 27, 1071 (1974).

16. R. Brooks and A. E. Grosser, Molec. Phys. 28, 593 (1974).

17. M. J. Cardillo, M. S. Chou, E. F. Greene, and D. B. Sheen, J. Chem. Phys. 54, 3054 (1971).

18. R. J. Gordon, M. J. Coggiola, and A. Kuppermann, Chem. Phys. Letters 20, 493 (1973).

19. R. B. Bernstein, 1966 Adv. Chem. Phys. 12, 75-134 ed. J. Ross (New York: Interscience).

20. F. A. Morse and R. B. Bernstein, J. Chem. Phys. 37, 2019 (1962).

21. N.F. Mott and H. S. W. Massey, The Theory of Atomic Collisions, Clarendon Press, Oxford, 3rd ed. 1965.

22. R. J. Munn and F. J. Smith, Mol. Phys. 10, 163 (1966).

23. A. Kantrowitz and J. Grey, Rev. Sci. Instr. 22, 328 (1951).

24. H. L. Kramer and D. R. Herschbach, J. Chem. Phys. 53, 2792 (1970).

25. A. Dalgarno, 1967 Adv. Chem. Phys. 12, 143 (1967)

26. A. Dalgarno and A. E. Kingston, Proc. Roy. Soc. (London) A259, 424 (1960).

27. R. J. Cross, J. Chem. Phys. 52, 5703 (1970).

28. J. D. Verlin, E. R. Cooper, and D. K. Hoffman, J. Chem. Phys. 56, 3740 (1972).

29. G. A. Stevens and A. E. de Vries, Physica 39, 346 (1968).

30. E. W. Rothe and R.K.B. Helbing, J. Chem. Phys. 53, 1555 (1970).

31. E. W. Rothe and R.K.B. Helbing, J. Chem. Phys. 53, 2501 (1970).

IV. VAN DER WAALS MOLECULES: WEAK INTERACTIVE CHEMISTRY

A. Introduction

The use of supersonic nozzle sources to form weakly bound dimers and higher polymers has initiated the study of more sophisticated experiments on weak interactive chemistry. Due to the relaxation of translational, rotational, and vibrational energy plus a relaxation toward chemical equilibrium in an isentropic nozzle expansion, new aggregates can be formed in sufficiently high concentration[1-6] to enable them to be studied by molecular beam techniques. In the original design of this molecular beam apparatus, one of our objectives was the study of these weak interactive reactions. One of the first interesting experiments would be a reaction governed by only dispersion forces. The rare gas-rare gas dimer reactions such as

$$Ar_2 + Xe \rightarrow ArXe + Ar \qquad (1)$$

or

$$Ar + Xe_2 \rightarrow ArXe + Xe \qquad (2)$$

would be a group of such reactions. The $ArXe^+$ product signal or the Ar^+ or Xe^+ product signal with time-of-flight analyses can be measured to study these reactions. This type of reaction would give valuable information on the dispersion force effect on Van der Waals molecule reactions.

Crossed molecular beams have categorically been used to study bimolecular collision processes. Recently, Lee et al.[7] have formed a complex with a fluorine atom and various olefin molecules and observed the unimolecular decay. Now with the ability to form unusual Van der Waals molecules, such as ArHCl and ArHF, as shown in electric resonance beam experiments,[8-11] termolecular reaction kinetics can be studied by crossed molecular beams. For example, if ArCl can be formed from Ar + Cl· where the Cl· is made in a gas discharge, then atomic recombination process such as

$$ArCl\cdot + Cl\cdot \rightarrow Ar + Cl_2 \qquad (3)$$

could be studied. This termolecular process may be important in these recombination reactions. Also of interest would be the study of highly exothermic reactions via a termolecular process such as possibly

$$\begin{aligned} ArF_2 + HI &\rightarrow F_2HI^* + Ar \\ F_2HI^* &\rightarrow HF + IF \qquad \Delta H = -93 \text{ kcal.} \end{aligned} \qquad (4)$$

The study of nucleation effects can also be studied by the crossed molecular beam technique with reactions such as

$$ArNH_3 + HCl \rightarrow NH_4Cl + Ar \ . \qquad (5)$$

Beams of larger size cluster species where the cluster is comprised of greater than 100 atoms or molecules have been formed[12-16] and the structure of several have been elucidated by electron scattering measurements. It therefore appears promising to look for reactive scattering of these species.

Most of the studies of reactive scattering of Van der Waals molecules have been made on diatomic alkali molecules.[19-25] However, the most astounding reactions studied so far in this field of weakly bound molecules are the facile six-centered reactions

$$(Cl_2)_2 + Br_2 \rightarrow 2BrCl + Cl_2 \qquad (6)$$

and

$$(Cl_2)_2 + HI \rightarrow Cl_2 + HCl + ICl \qquad (7)$$

by King, Dixon, and Herschbach.[26] In these reactions they have described a model for the mechanism in which the Cl_2 dimer forms a six-centered ring complex with the Br_2 and subsequently the reaction proceeds by sequentially breaking the Br-Br bond, and two of the Cl-Cl bonds, thus, giving two BrCl molecules which recoil in opposite directions in the center-of-mass system. The beauty of this reaction is that it conserves orbital symmetry throughout the reaction whereas the direct reaction $Br_2 + Cl_2 \rightarrow 2BrCl$ does not. They have estimated the cross section for the six-center reaction to be 50Å^2 or greater. The prospect of studying the kinetics of a large variety of these weakly bound Van der Waals molecules was enhanced by the large cross sections and unusual kinetics found for reactions (6) and (7).

A study of the Van der Waals molecule reactions was initiated by trying to reproduce the results of King, Dixon, and Herschbach. Unfortunately, even after varying the pressure of the chlorine in the nozzle stagnation chamber (in effect varying the intensity of the dimers and higher polymers) the reaction of $Br_2 + (Cl_2)_2$ as described in the literature was not observed. Instead, ion mass peaks corresponding to $BrCl^+$, $Br_2Cl_2^+$, $Br_2Cl_6^+$, $Br_2Cl_8^+$, and $Br_2Cl_{10}^+$ were observed in the detector only in the region of laboratory angles within ~15° of the Cl_2 beam. A measured angular distribution for the $BrCl^+$ ion signal is shown in Fig. IV-1. The dominant feature of this angular distribution is the one very narrow peak near the Cl_2 beam. This is the only peak observed in this angular distribution, unlike the data for the six centered reaction[26] which has another peak in the proximity of the Br_2 beam. The peak seen in Fig. IV-1 could be the observation of condensation of a Br_2 molecule on a heavy chlorine cluster, $(Cl_2)_x$, to form a long lived complex which either lives long enough to reach the detector or fragments with the resulting particules having very small recoil velocities which are then ionized in the detector. To further analyze a condensation phenomena, formation of the clusters from a lighter gas such as H_2 would move the centroid angle for a given cluster size, x, further from the beam. Thus, permitting a more detailed analysis by having larger angles between cluster centroids. Since a low cryogenic temperature (~30°K) is needed to form a beam of hydrogen clusters and could not be accomplished with the present nozzle configuration, ammonia was used instead in a similar

Fig. IV-1. The measured angular distribution for the $BrCl^+$ signal from the data collected on 3/26/74. The total number of counts in 30 seconds is plotted for each angle. The error bars represent one standard deviation based on the statisical deviation from the total number of counts at each angle.

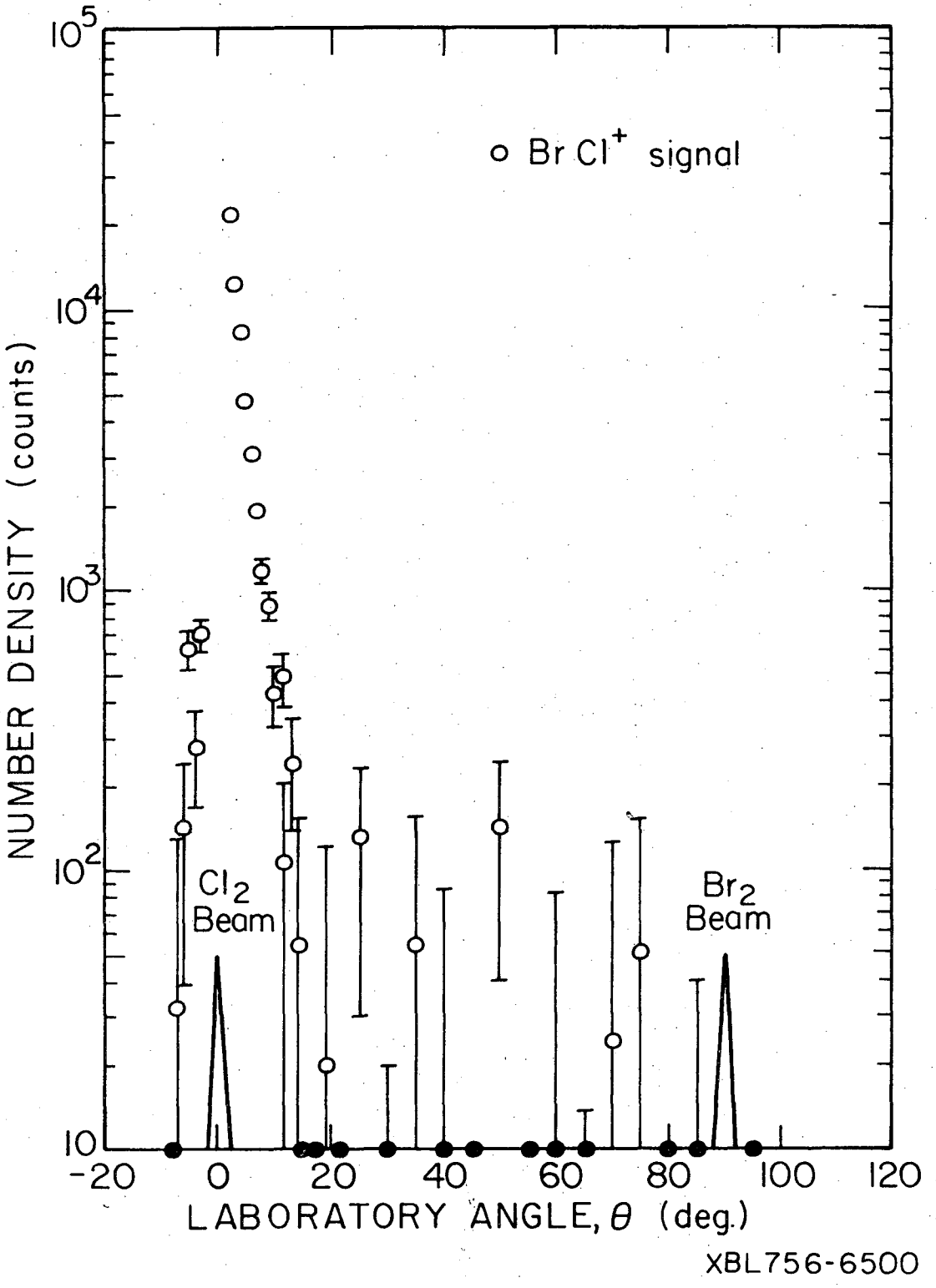
10^5
10^4
10^3
10^2
10
NUMBER DENSITY (counts)
o Br Cl$^+$ signal
Cl_2 Beam
Br_2 Beam
-20
0
20
40
60
80
100
120
LABORATORY ANGLE, θ (deg.)
XBL756-6500

Fig. IV-1.

reaction of $Br_2 + (NH_3)_x$. The angular distribution for this reaction was similar to that of $Br_2 + (Cl_2)_x$ with a very sharp peak near the NH_3 beam, indicating that a complex was also being formed between Br_2 and NH_3 clusters. These are two of the first observations of this type of a complex being formed in a crossed molecular beam experiment. Although recently, a similar phenomena was also seen in the reaction of alkali atoms with $(CH_3I)_x$ as reported by Ureña, Bernstein, and Phillips.[27] The two reactions studied here are

$$(Cl_2)_x + Br_2 \rightarrow Br_2(Cl_2)_x^* \xrightarrow{?} \quad (8)$$

and

$$(NH_3)_x + Br \rightarrow Br_2(NH_3)_x^* \xrightarrow{?} \quad (9)$$

Both appear to form a long lived complex. The experimental conditions, the measured data, and interpretation of the measurements will be discussed in sections 2 and 3 of this chapter. Implications of the data and possible improvement in the measurements and further experiments will be discussed in section 4.

B. Experimental

The apparatus used for these experiments is the "supermachine" described in chapter II. The experiments were run using the two nozzle sources described in chapter II with the nozzle for beam 1 having a 0.01 cm diameter oriface with an oriface channel length of .0125 cm and a skimmer with an external angle of 64° and a hole diameter of .050 cm. The nozzle for beam 2 has a 0.01 cm diameter oriface and a

oriface channel length of .0025 cm and a skimmer with an external angle of 86° and a hole diameter of .062 cm. The operating conditions for each nozzle for different experiments and different runs are listed in Table IV-1. The velocity distribution parameters for the nozzles are in a slightly different form from that used in previous chapters in order to be able to fit the velocity distributions of the higher polymers which generally travelled at a slightly slower velocity than that predicted for a simple nozzle expansion. A theoretically based distribution function for the clusters would be an entire study in itself since it would have to include condensation processes in the expansion and seeding effects (i.e. where the velocity of the species in lower concentration approaches the velocity of the higher concentration species through collisions during the expansion). Although a good model for the formation of clusters in the expansion would be instructive, it is only necessary here to be able to characterize the velocity distributions of the clusters. The number density velocity distribution is of the form.

$$N(V) = K\, V^2 \alpha_1^{-3} \exp\left[-\frac{(V-V_f)^2}{\alpha_1^2}\right] \tag{10}$$

where V is the velocity, V_f is the flow velocity, α_1 is the width parameter and K is a normalization constant. For a standard nozzle expansion

$$\alpha_1^2 = \alpha_o^2 \left[1 + \frac{(\alpha-1)M^2}{2}\right]^{-1} \tag{11}$$

$$V_f = 1.225\, \alpha_o M \left[\frac{\gamma}{3 + 1.5(\gamma-1)M^2}\right]^{1/2} \tag{12}$$

where $\alpha_o^2 = 2kT_o/m$, T_o is the stagnation chamber temperature, m is the mass of the monomer, M is the Mach number, and $\gamma = C_p/C_v$. Of the two reactions studied, $(Cl_2)_\chi + Br_2$ and $(NH_3)_\chi + Br_2$, the velocity distribution of the Br_2 beam could always be fit using a Mach number, and the velocity distributions of the Cl_2 and NH_3 clusters were fit by varying V_f and α_1 independently. Figure IV-2 shows the measured time-of-flight spectra for several different size chlorine clusters. The velocity distribution obtained from the deconvolution of the time-of-flight spectra for the heaviest cluster measured was used for averaging over the beam velocities in calculations. This should be a good approximation since for increasing cluster size the decrease in the measured flow velocity gets smaller.

The velocity distributions from the $(Cl_2)_\chi$ beam for a range of detected Cl^+ ions from Cl_2^+ to Cl_{14}^+ are shown in Fig. IV-3. The figure shows that the velocity distributions of the ions are the same for odd-even pairs (Cl_3^+ and Cl_4^+, Cl_5^+, and Cl_6^+ etc). The relative intensities of the chlorine ions that were measured at the same detector resolution setting are shown in Fig. IV-4. Here again there is a correspondence between the even and odd size cluster ions with the even cluster ion always being more intense than the odd cluster ion by the same factor over the range of pairs measured. The solid line through the data points of the Cl_2^+ ion distribution in Fig. IV-3 represents the theoretical nozzle velocity distribution calculation, assuming rotational relaxation, for a Cl_2 stagnation temperature of 298°K and a Mach number of 14, convoluted over the time-of-flight gate function.

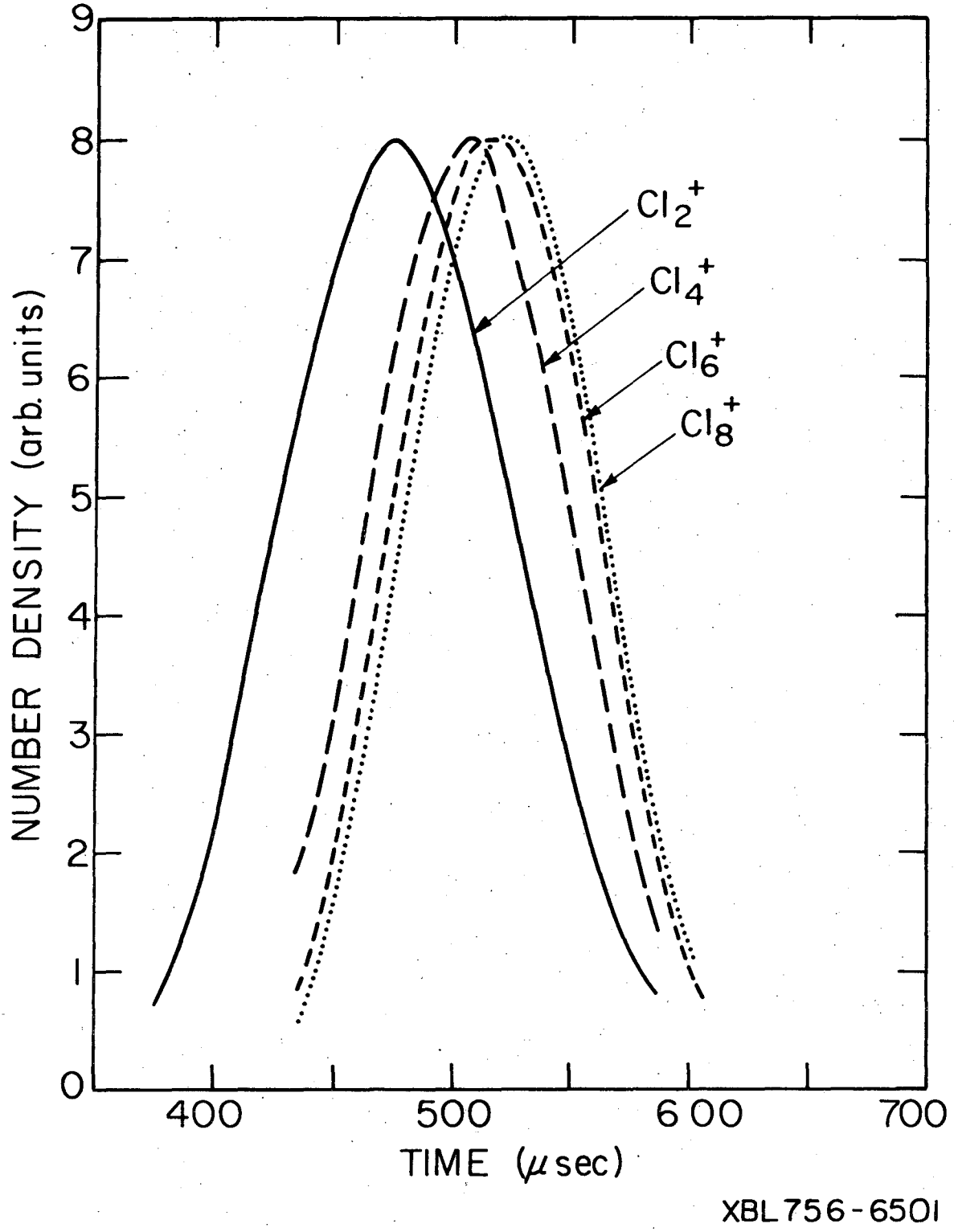

Fig. IV-2. The measured time-of-flight distributions of the chlorine beam for the data taken on 8/12/74. The four curves are for the different chlorine cluster fragments measured in the detector.

Fig. IV-3. The time-of-flight distributions are shown for eleven different chlorine ion sizes. The even size ions are represented by circles and the odd size ion by squares. The solid line through the Cl_2^+ distribution is the time-of-flight distribution for a theoretical Cl_2 nozzle distribution assuming rotational relaxation. Each chlorine ion distribution is on an arbitrary scale with the scales adjusted to show the similarity of odd-even pairs.

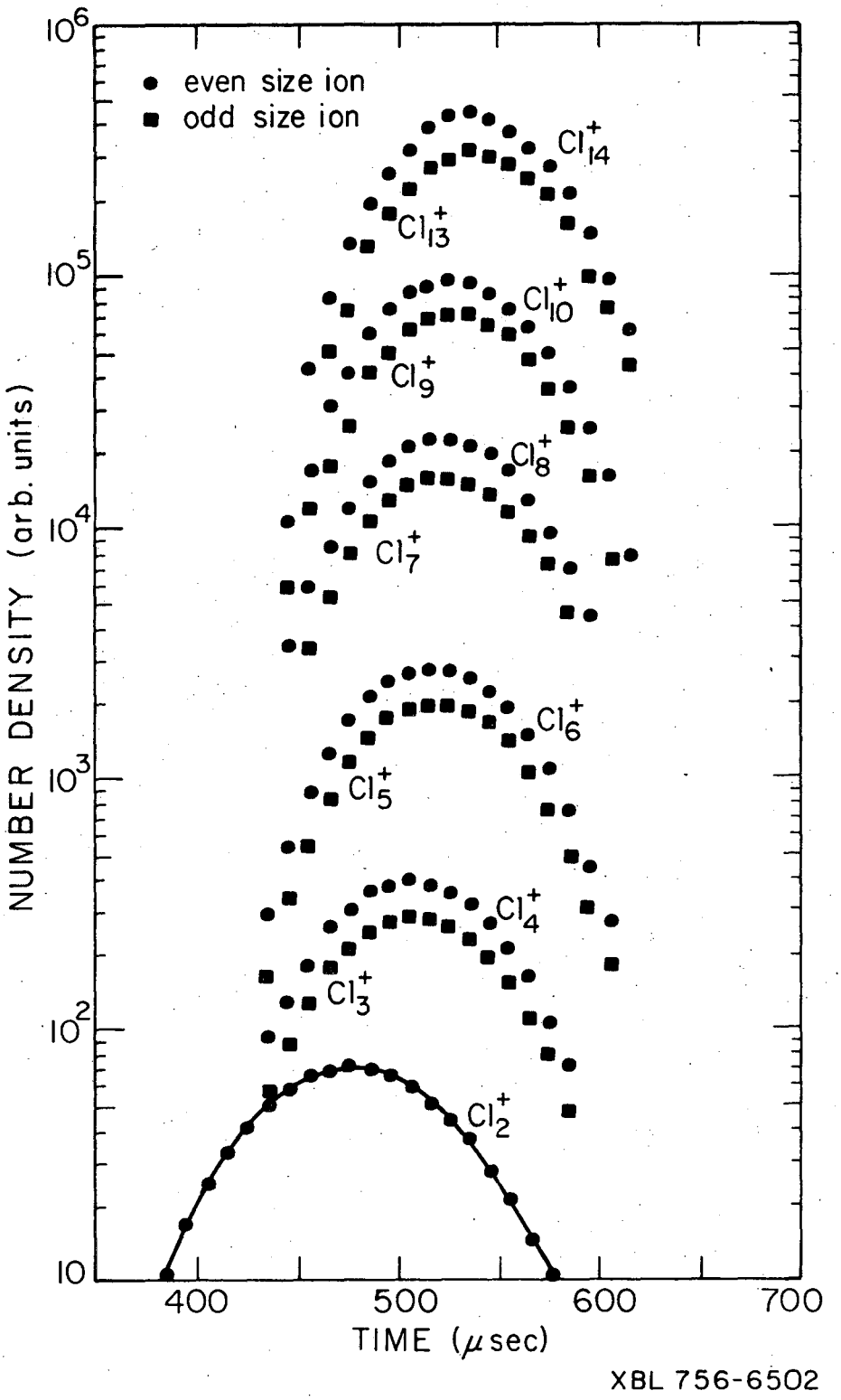
even size ion
odd size ion
Cl_{14}^+
Cl_{13}^+
Cl_{10}^+
Cl_9^+
Cl_8^+
Cl_7^+
Cl_6^+
Cl_5^+
Cl_4^+
Cl_3^+
Cl_2^+
NUMBER DENSITY (arb. units)
10^6
10^5
10^4
10^3
10^2
10
400
500
600
700
TIME (μsec)
XBL 756-6502

Fig. IV-3.

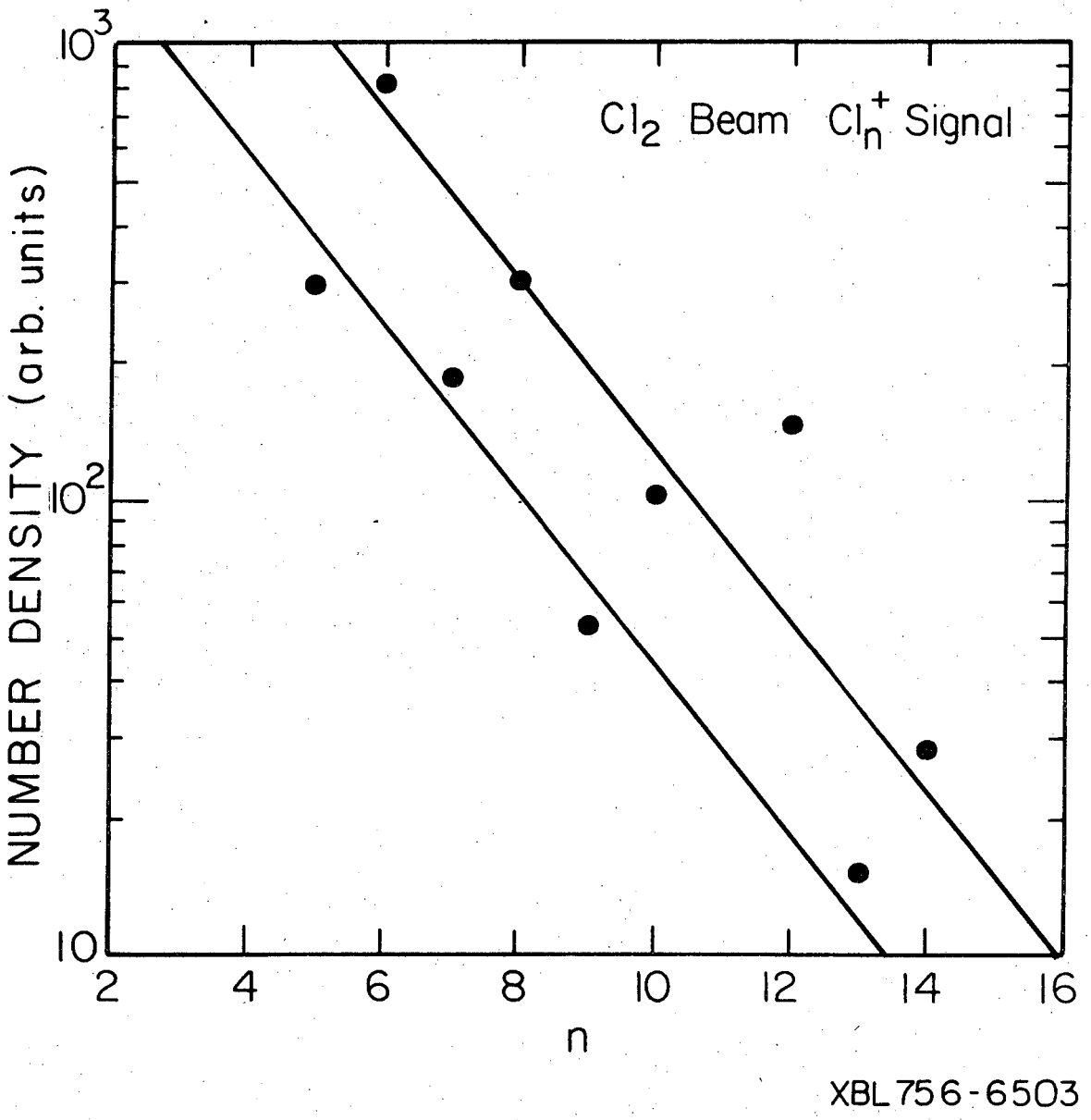

Fig. IV-4. The relative intensities of different size chlorine cluster ions measured at one quadrupole resolution setting are shown. The two lines are drawn through the even and odd cluster sizes.

The $Br_2 + (Cl_2)_x$ reaction was run five times. For the first three runs the $(Cl_2)_x$ beam was modulated and the $Br_2(Cl_2)_n^+$ products were detected. Since the products were detected within 10° of the $(Cl_2)_x$ beam, the possibility existed that the signal was from background $(Cl_2)_x$ or a background modulation effect in the detector (both of which are unlikely since a mass filter was used and a heavy product was detected). To circumvent this possible ambiguity the last two runs of the $Br_2 + (Cl_2)_x$ reaction and the $(NH_3)_x + Br_2$ reaction were done with the Br_2 beam modulated. The results from the modulation of different beams were virtually the same.

The detector configuration and the detector aperture dimensions were the same as described in chapter II. The detector was run with the resolution set so as to transmit the largest amount of product without having contributions from the elastically scattered chlorine clusters which were the other predominate mass peaks at high masses. Most of the data was collected with the 12.9% transmission time-of-flight wheel in the apparatus. The count times for angular distributions were between 20 and 50 seconds at each angle and the count times for the time-of-flight distributions ranged from 100 seconds to 300 seconds. The time-of-flight distributions were deconvoluted as described in chapter II.

C. Data and Analysis

In light of the sharp peak indicating condensation, shown in Fig. IV-1, plus similar data for larger ion clusters, an examination of how the condensation of molecules on clusters can be analyzed will verify that, indeed, condensation on clusters is being observed. It will also allow the extraction of as much information as possible from the experiments already performed and will provide some ideas for future experiments. First, the general analysis of the angular distributions will be presented and second, the analysis of the velocity or time-of-flight distributions.

In the analysis of the data from cluster experiments two problems are present which are not present in the usual molecular beam experiment. First, since all of the clusters are formed in an isentropic nozzle expansion there is a distribution in the size of the clusters which is not well characterized. This means the relative concentrations of various size clusters in the beam are unknown which implies that the distribution of the center-of-mass velocity vectors are unknown. Second, the cracking patterns of clusters from electron bombardment are not known. Therefore, difficulty in determining the origin of the parent of a particular detected ion can lead to ambiguities in the analysis of the data. The general reaction of clusters considered here is

$$A + B_x \rightarrow AB_x^* \quad , \tag{13}$$

where A is an atom or molecule and x is the number of monomer units of B in a particular cluster. AB_x^* represents the activated cluster complex formed by A sticking on the cluster B_x.

The formation of clusters in the beam will be examined first. If F_x' represents the flux of B_x in the main beam in particles/cm^2-sec at the ionizer, v_x is the velocity of B_x in the main beam, V is the volume of the ionizing region, i is the electron current density, and $Q_i(B_x)$ is the total cross section for ionization of B_x then the total number of ions formed per second from the cluster of size B_x in the beam is

$$I_x = VQ_i(B_x)i\ F_x'/v_x \quad . \tag{14}$$

After x equals 3 or 4 the velocity of the clusters is essentially independent of x and will be represented by v. Letting $G_{n,x}$ be the probability that B_x, upon ionization, will appear as the ion B_n^+ where n is the number of B monomers in the fragmented ion, then the number of counts per second of B_n^+ in the main beam I_n is given by

$$I_n = \frac{Vi}{v} \sum_{x \geq n}^{x_{max}} T(nm_B)\ Q_i(B_x)\ G_{n,x}\ F_x' \quad . \tag{15}$$

where $T(nm_B)$ is the transmission of the quadrupole mass filter and the ion optics which are only dependent on mass. The relative fluxes of different size clusters can be estimated by comparing the ratios of different ion intensities, I_n, if $T(nm_B)$, $Q_i(B_x)$, and $G_{n,x}$ are known.

$T(nm_B)$ can be determined for the detector and the ionization cross section, $Q_i(B_x)$, can be estimated[28] from the polarizabilities. Unfortunately, the cracking pattern, $G_{n,x}$, of these small size clusters is not known. Thus the relative intensities of different size clusters can not be calculated until values for $G_{n,x}$ are obtained.

A qualitative understanding of the measured angular distributions like the one shown in Fig. IV-1 can be gleaned by comparing them with the calculated centroid distributions for the different size clusters with the monomer beam. The general velocity vector diagram for calculating the centroid distribution is shown in Fig. IV-5. The centroid angle, θ_c, for a particular cluster size, x, is given by

$$\theta_c = \arctan\left(\frac{\gamma}{x}\right) \tag{16}$$

$$\gamma = \frac{m_A v_A}{m_B v_x}$$

where m_A and m_B are the masses of the monomer for each beam (i.e. Ar, Cl_2, NH_3, or Br_2), v_A is the velocity of the monomer beam A, and v_x is the velocity of a particular cluster size. Now assuming infinitely good angular resolution in the detector and monoenergetic beams so only one cluster size will contribute to the scattering at a particular angle, then the number of AB_x complexes formed per second, N_{AB_x}, is given by

$$N_{AB_x} = \tau \bar{g}\, Q_c(AB_x)\, \frac{F_A}{v_A}\, \frac{F_x}{v_x} \tag{17}$$

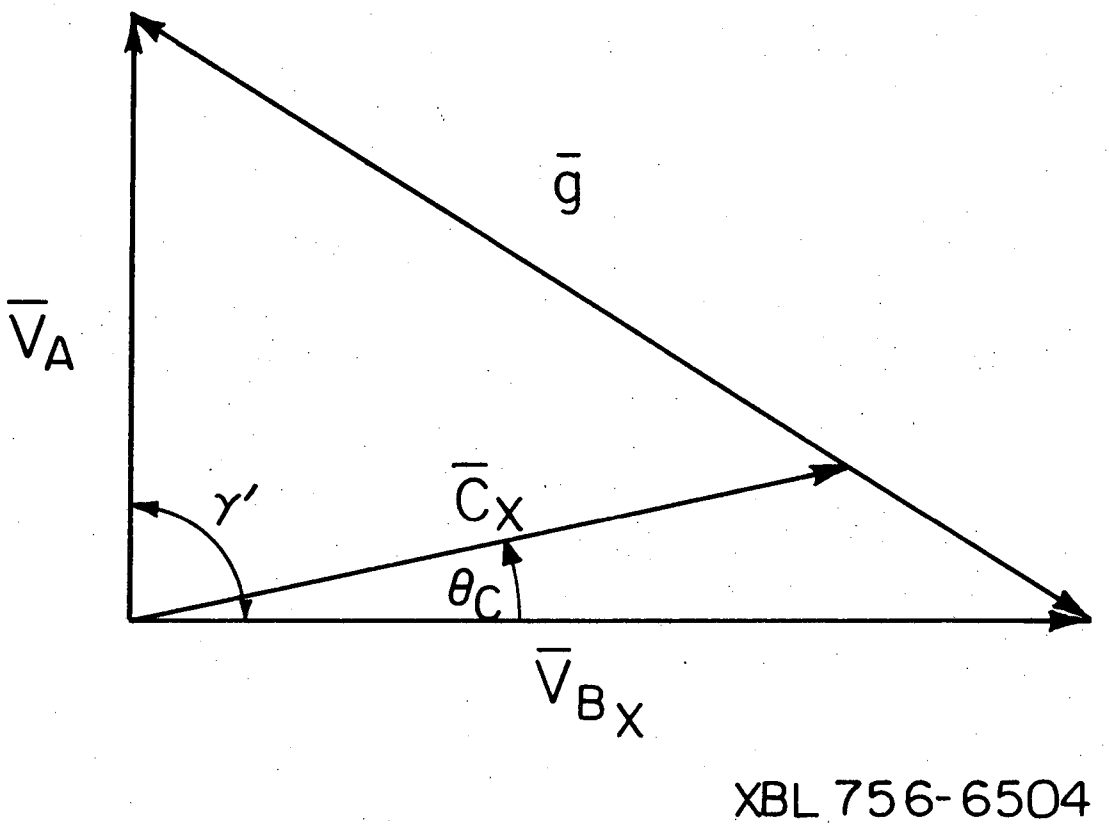

Fig. IV-5. A Newton diagram for the kinematics of the A + B_x collision. $\bar{V}_A$ and $\bar{V}_{B_x}$ are the velocities for the monomer beam A and the cluster beam B_x. $\bar{C}_x$ is the centroid velocity vector corresponding to a cluster size, x. θ_c is centroid angle and $\bar{g}$ is the relative velocity vector.

where τ is the volume of the collision zone defined by the two beams, $\bar{g}$ is the relative velocity vector (see Fig. IV-5), $Q_c(AB_x)$ is the cross section for the formation of AB_x from $A + B_x$, and F_A and F_x are fluxes of A and B_x respectively in particles/cm^2-sec at the collision zone. The flux of AB_x complexes, $\mathcal{F}_A(x)$, away from the collision zone assuming that the complexes do not decompose is given by

$$\mathcal{F}_A(x) = \frac{\tau \bar{g}\, Q_c(AB_x)}{D} \frac{F_A}{v_A} \frac{F_x}{v_x} \tag{18}$$

where D is the cross sectional area of the collision zone normal to the center-of-mass velocity vector at the angle θ_c, and the other terms are previously defined. Therefore, at an angle $\theta=\theta(x)$ the detected signal, S_n, would be

$$S_n = VT(nm_B + m_A)\, Q_i(AB_x)\, H_{n,x} \frac{\mathcal{F}_A(x)}{C_x} \tag{19}$$

$$C_x = \frac{1}{M} \left(m_A^2 v_A^2 + x^2 m_B^2 v_x^2\right)^{1/2} . \tag{19a}$$

C_x is the center-of-mass velocity vector for a cluster size x, $T(nm_B + m_A)$ is the transmission of the quadrupole mass filter and ion optics, $Q_i(AB_x)$ is the ionization cross section for AB_x, $H_{n,x}$ is the probability that ionization of AB_x gives the ion AB_n^+, and V is the volume of the ionizing region. If it is assumed that the complex lives long enough to reach the ionizer and the ionizer "sees" all of the collision zone, then the ionizing volume, $V = D\ell$, where ℓ is the length of the ionizer and D is defined in Eq. (18). The detected ion

signal S_n at an angle $\theta=\theta(x)$ is then given by

$$S_n = \frac{\tau \ell i}{C_x} \; T(nm_B + m_A) \; Q_i(AB_x) H_{n,x} \; \bar{g} \; Q_c(AB_x) \; \frac{F_A}{v_A} \; \frac{F_x}{v_x} \qquad (20)$$

The value that one would like to obtain from this expression is obviously $Q_c(AB_x)$, the cross section for condensation on a cluster, but again lack of values for several of the parameters leads to difficulties. Again, assuming that the detector has infinite resolution such that only one cluster size will contribute to the ions being detected at a given angle, then information can be extracted on the ratios of $T(nm_B + m_A) \; H_{n,x}$ by simply looking at the ratios of S_n for different ion sizes, n, at one angle. The relative condensation cross sections for different size clusters can be found if the relative fluxes $F_x/F_{x'}$ for different size clusters are known. The absolute cross section can also be obtained if F_A, the flux of the crossed beam is known. This assumes that it is possible to estimate values for $Q_i(AB_x)$.

Now in the actual experiments the beams are not monoenergetic and the detector does not have infinite angular resolution. Therefore, the angular distribution will not have discrete undulations corresponding to the centroids for individual cluster sizes, so θ_c must be treated as a continuous variable. Treating θ_c as a continuous variable implies treating x as a continuous variable. For this case the signal, $S_n(\theta_c)$, is given by

$$S_n(\theta_c)d\theta_c = \frac{\tau \ell i}{C_x} T(nm_B + m_A)\, Q_i(AB_x) H_{n,x} \bar{g}\, Q_c(AB_x) \frac{F_A}{v_A} \frac{F_x}{v_x}\, dx \qquad (21)$$

where all the terms have been defined in Eq. (20) except for the new Jacobian $dx/d\theta_c$. As shown previously θ_c = arctan γ/χ so the Jacobian $dx/d\theta_c = -\gamma/\sin^2\theta_c$. This Jacobian predicts that the measured angular distribution should be strongly peaked near the cluster beam. This effect comes from fact that as the clusters increase in size the centroid velocity vectors keep approaching the cluster beam in smaller increments, thus causing the number of centroids that contribute in a given angular interval to increase as the centroid angle approaches the cluster beam direction.

The measured angular distributions for the $Br_2 + (Cl_2)_x$ system are shown in Figs. IV-6, IV-7, and IV-8 for the data collected on three different runs (3/26, 8/12, and 8/30, respectively). The measured angular distribution for $Br_2 + (NH_3)_x$ is shown in Fig. IV-9. Of all the $Br_2 + (Cl_2)_x$ runs only the run on 3/26 has measurements on both sides of the cluster beam since all the other runs were taken with the time-of-flight wheel in the apparatus. The significant point to be made about the angular distributions of 3/26 is that the measured intensities on the negative angle side of the cluster beam are about one order of magnitude less intense than on the positive side of the beam. This was another observation that indicated condensation on clusters was taking place. Further measurements with a time-of-flight arrangement corroborate these initial observations.

Fig. IV-6. The measured angular distributions for four different detected ions are shown for the data taken on 3/26/74. The number of counts in 30 seconds is shown for each angle. The error bar represents one standard deviation based on the statistical deviation of the total counts. The arrows on the error bars indicate the error bar extends further but is omitted for clarity and the solid points indicate that the measured valve was below this point but was left there for clarity. The scales alternate from the left to right starting with the top left for the first distribution.

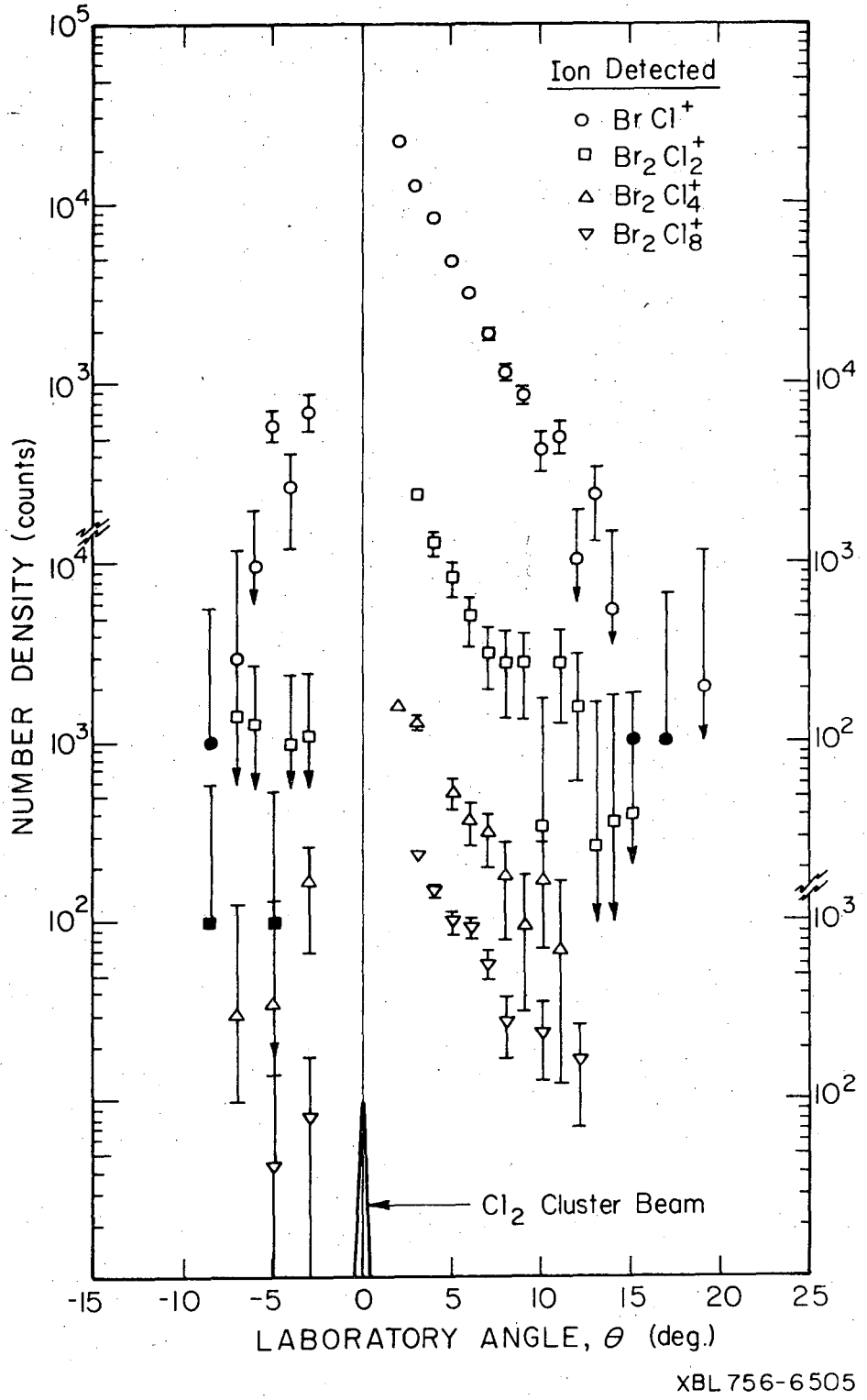

Fig. IV-6.

Fig. IV-7. The measured distributions for five different detected ions are shown for the data taken on 8/12/74. The number densities are in arbitrary units but can be scaled with the number of counts in 30 seconds being as follows at 5°: $BrCl^+$ = 2500, $Br_2Cl_4^+$ = 6400, $Br_2Cl_6^+$ = 4300, $Br_2Cl_8^+$ = 1320, and $Br_2Cl_{10}^+$ = 1480. The error bars and symbols are the same as described in Fig. IV-3.

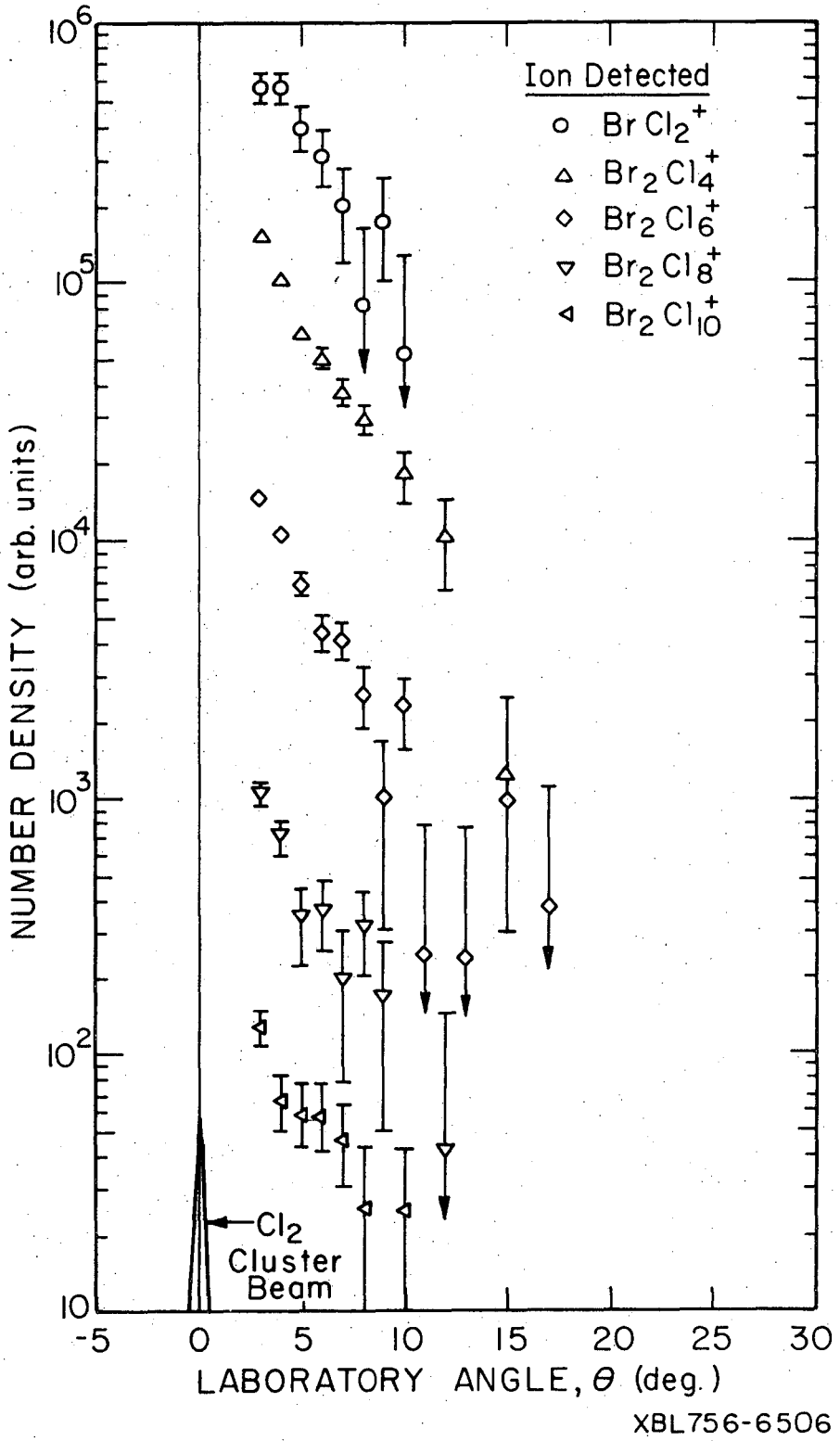

Fig. IV-7.

Fig. IV-8. The measured angular distributions for four different detected ions are shown for the $Br_2 + (Cl_2)_x$ data taken on 8/30. The error bars represent one standard deviation based on the statistical deviation of the total number of counts. The number of counts in 30 seconds is shown at each angle. The scales are the same as in Fig. IV-6.

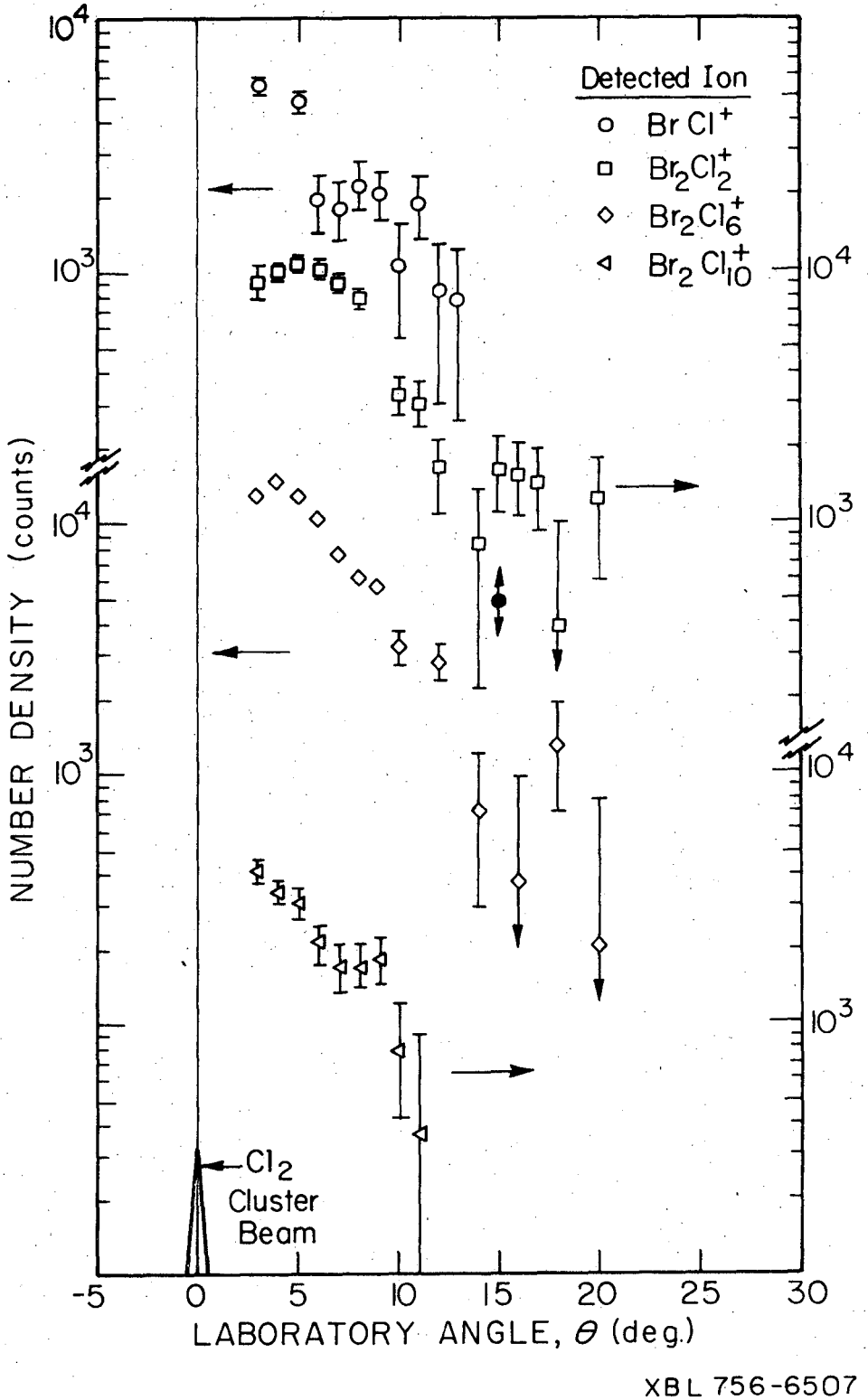

Fig. IV-8

Fig. IV-9. The measured angular distributions for four different detected ions are shown for the $Br_2 + (NH_3)_x$ data taken on 8/31/74. The total number of counts in 30 seconds is shown at each angle. The error bars represent one standard deviation based on the statistical deviation for the total number of counts. The scales alternate from left to right with the top left for the first distribution.

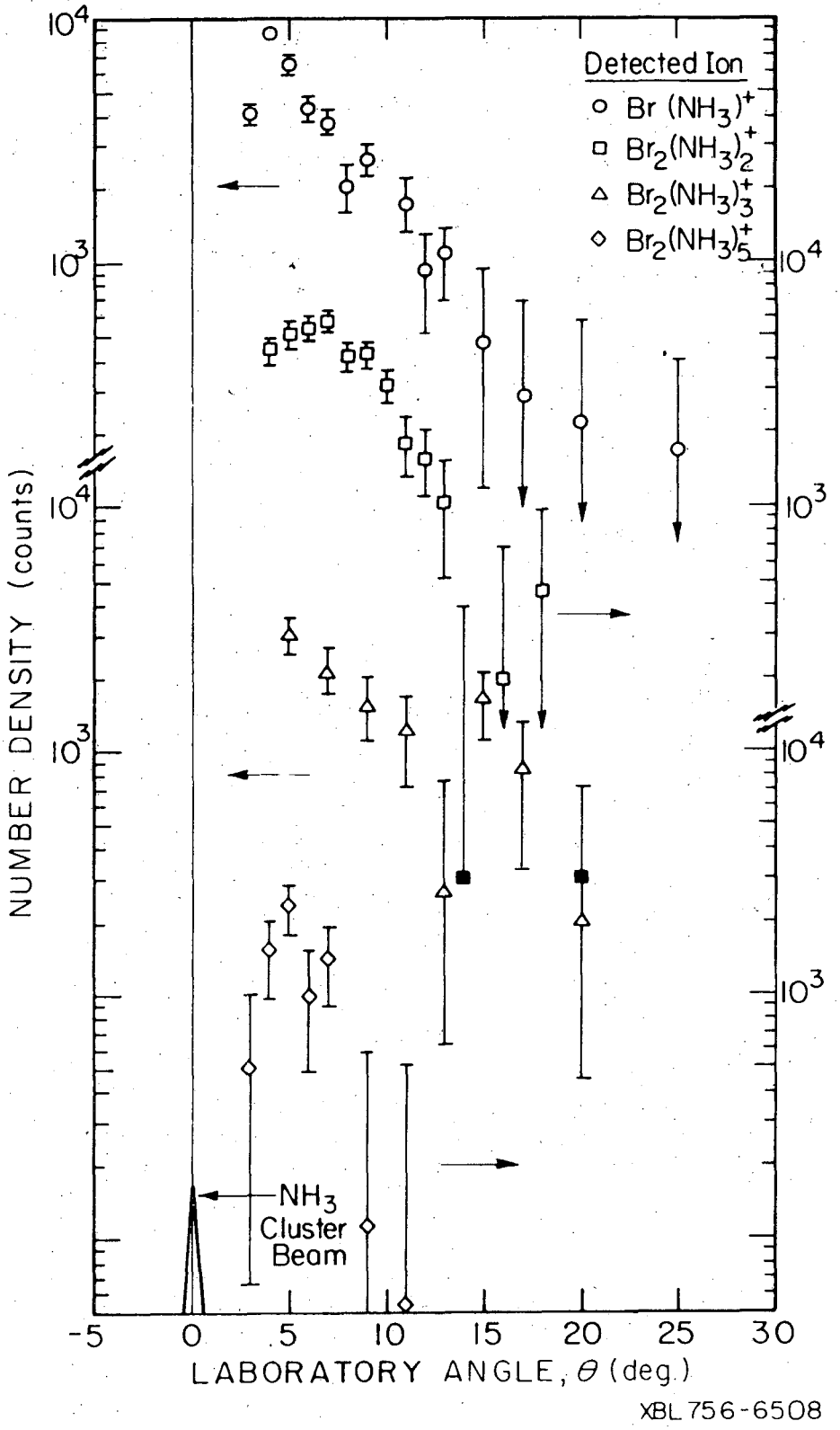

Fig. IV-9.

The ratio of the factors of the quadrupole and ion optic transmission times the probability of ion formation from a given neutral parent ($T(nm_B + m_A)H_{n,x}$) can be obtained by comparing the number of counts of various ions at one angle since

$$R_{n',n} \equiv \frac{S_{n'}(\theta_c)}{S_n(\theta_c)} = \frac{T(n'm_B + m_A)H_{n',x}}{T(nm_B + m_A)H_{n,x}} \qquad (22)$$

Comparisons of these measurements and $R_{n',n}$ for the $Br_2 + (Cl_2)_x$ and $Br_2 + (NH_3)_x$ data are shown in Tables IV-2 and IV-3. One trend that can be observed from the $R_{n',n}$ factors in Tables IV-2 and IV-3 is that as the number of cluster monomer units in the ion decreases the intensity of the ion increases. This is reasonable since upon severe fragmentation where several small ions are formed there is a higher probability to form a small ion since there can be more small fragments than large fragments formed from a given parent. It should be noted here that there appears to be severe fragmentation of medium size clusters (up to $x \simeq 60$ for NH_3) whereas it appears that larger hydrogen clusters[12] ($x \simeq 2000$) do not fragment. For example, a cluster size of n=40 for $Br_2 + (NH_3)_x$ will have a centroid at an angle $\theta_c = 5°$. In the $Br_2 + NH_3$ systems no fragments of a mass higher than $Br_2(NH_3)_5$ could be detected that would give statistically meaningful values in a reasonable counting time ($\sim$ 60 sec). Since it was not possible at the time to collect more data on larger size ions and the transmission of the quadrupole was not absolutely linear over the mass range studied it is impossible to obtain an exact functional dependence of $R_{n',n}$

from the present data. Therefore, from the measured angular distributions a crude trend for the cracking pattern can be seen along with the fact that large clusters undergo severe cracking in the electron bombardment ionizer.

Some more insight into which range of cluster sizes contribute most heavily to the angular distribution can be gained by removing the $1/\sin^2\theta_c$ of the Jacobian factor from the angular distribution. The angular distributions for the $Br_2 + (Cl_2)_x$ data on 8/30 and the $Br_2 + (NH_3)_x$ data are shown with the $1/\sin^{-2}\theta_c$ term removed in Figs. IV-10 and IV-11, respectively. The distributions for $Br_2 + (Cl_2)_x$ in Fig. IV-10 peak between 8° and 10° which corresponds to a Cl_2 cluster size of x=11 to 14. For the $Br_2 + (NH_3)_x$ reaction distributions shown in Fig. IV-11, the peak appears in the vicinity of 9 or 10 degrees which corresponds to a NH_3 cluster size of x=20 to 22. The location of the peak of the distributions with and without the $1/\sin^2\theta_c$ term illustrates how powerful a weighting factor the Jacobian is for looking at condensation on these clusters.

From here it is not too difficult to make a rough estimate of the product of the flux, F_x, and the cracking pattern, $H_{n,x}$, by using Eq. (21) and some rough estimates for the condensation and ionization cross sections. The product of the flux and the cracking pattern is

$$H_{n,x} F_x = \frac{S_n \sin^2\theta_c}{Q_i(AB_x) Q_c(AB_x) K} \qquad (22)$$

Fig. IV-10. The angular distributions for four different detected ions are shown with the $1/\sin^2\theta_c$ Jacobian factor removed for the $Br_2 + (Cl_2)_x$ data collected on 8/30. The error bars are one standard deviation based on the statistical deviation of the total number of counts. The centroid angles where the peaks in the distributions occur correspond to cluster sizes of x=11 to 14. The scaling for the distributions are independent of each other.

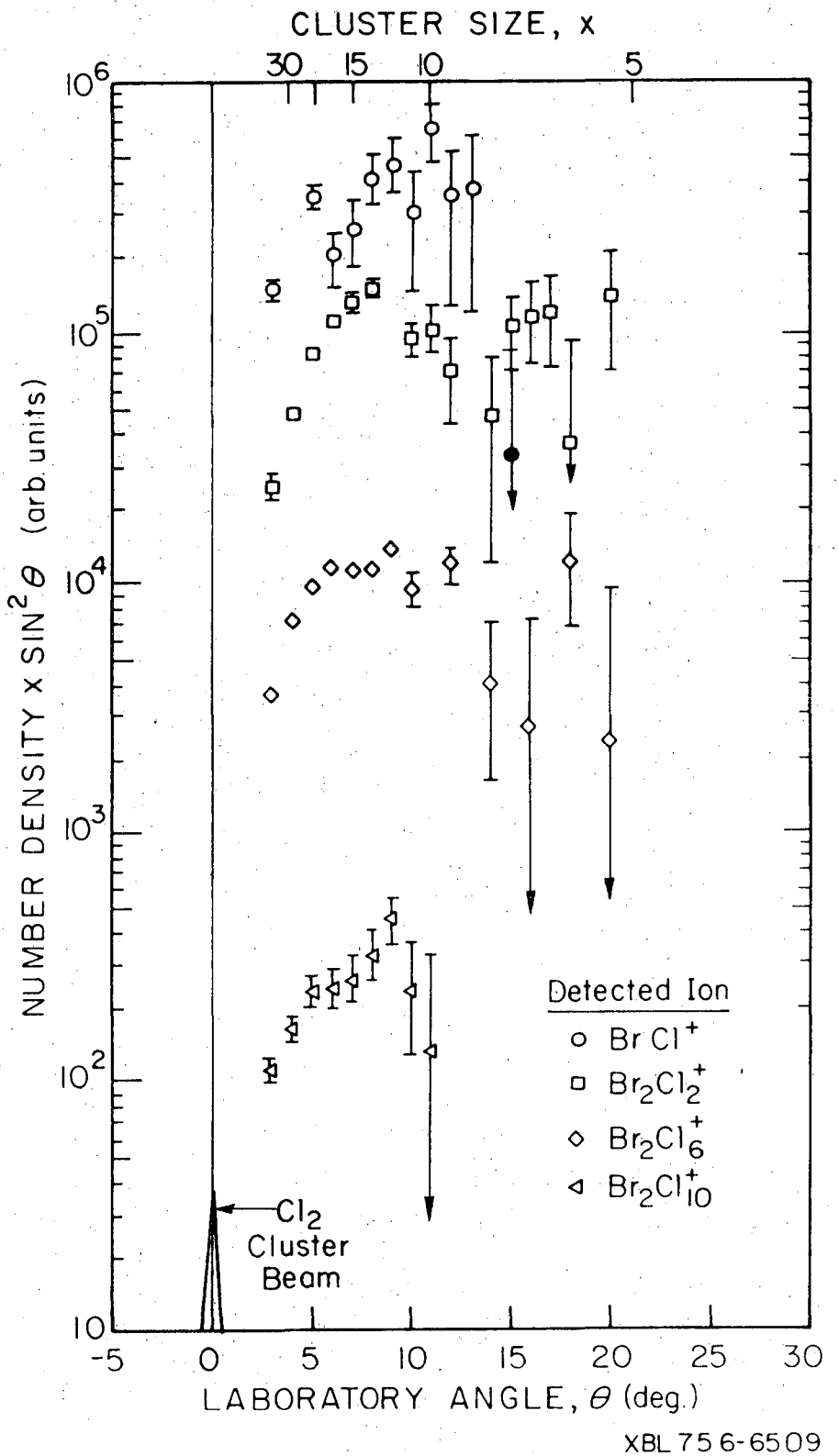

Fig. IV-10.

Fig. IV-11. The angular distributions for four different detected ions are shown with the $1/\sin^{-2}\theta_c$ Jacobian factor removed for the $Br_2 + (NH_3)_x$ data collected on 8/31. The error bars are one standard deviation based on the statistical deviation of the total number of counts and the arrows on the error bars indicate a termination of the error bar for clarity. The centroid angles where the peaks in the distributions occur correspond to cluster sizes of x=20 to 22. The scaling for the distributions are independent of each other.

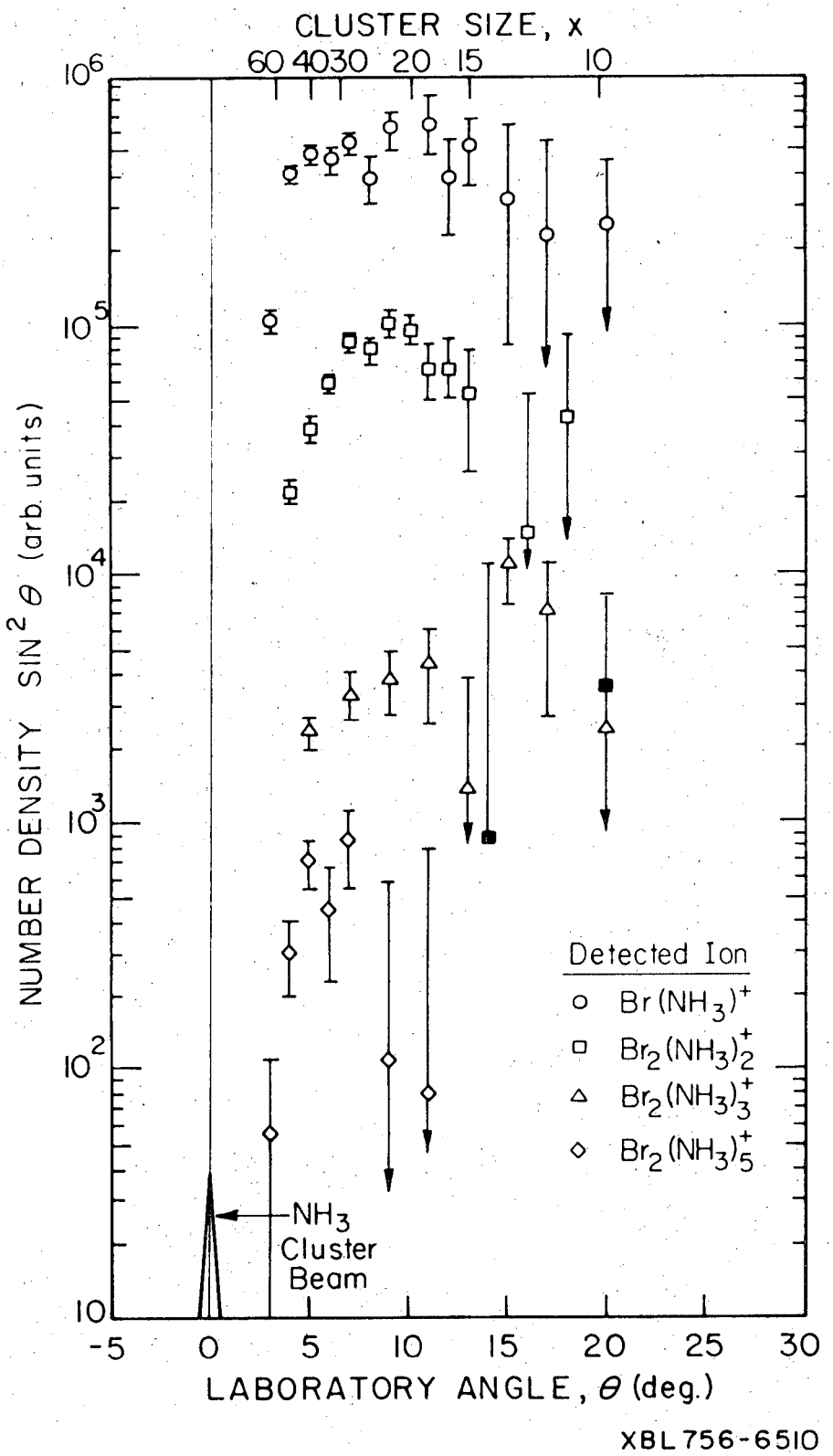

Fig. IV-11.

where the constant K which is valid for large X is

$$K = \frac{\tau \ell i T (n m_B + m_A) \bar{g} F_A}{C_x v_A v_X} \quad . \tag{23}$$

Assuming that the condensation cross section is proportional to the area swept out by the cluster and thus varies as $X^{2/3}$ and the ionization cross section varies linearly with the polarizability[28] and is thus proportional to X, then the product, $H_{n,x} F_x$, can easily be calculated for a measured S_n. Plots of $H_{n,x}F_x$ as a function of x are shown for the 8/30 $Br_2 + (Cl_2)_x$ and the $Br_2 + (NH_3)_x$ data in Fig. IV-12. The linear dependence of $H_{n,x}F_x$ on x when plotted on a semi-log scale indicated the expected exponential behavior for the formation of the cluster. The linearity of the data is quite good for higher clusters sizes where the above approximation is valid and where the detected signal had less noise. The change in the slope of the line that fits the different size cluster ions for the $Br_2 + (Cl_2)_x$ data arises from the different probabilities of the cluster, AB_x, fragmenting into different ions. It appears that the probability of forming different fragments from a parent becomes equally likely as the fragments become larger.

The last interesting observations in the angular distributions are the effects of varying the nozzle stagnation pressure and the nozzle oriface geometry on the location of the peak in the angular distribution. The three angular distributions for the $Br_2Cl_6^+$ ion are shown in Fig. IV-13 for three different nozzle conditions. The

Fig. IV-12. The two graphs show the product of the cracking pattern and the flux of B_x, $H_{n,x}F_x$, versus the cluster size, x. The upper graph shows the $Br_2(NH_3)_2^+$ ion from the $Br_2 + (NH_3)_x$ data. The lower graph shows the data for three ions $Br_2Cl_2^+$, $Br_2Cl_6^+$, and $Br_2Cl_{10}^+$ from the $Br_2 + (Cl_2)_x$ data taken on 8/30/74.

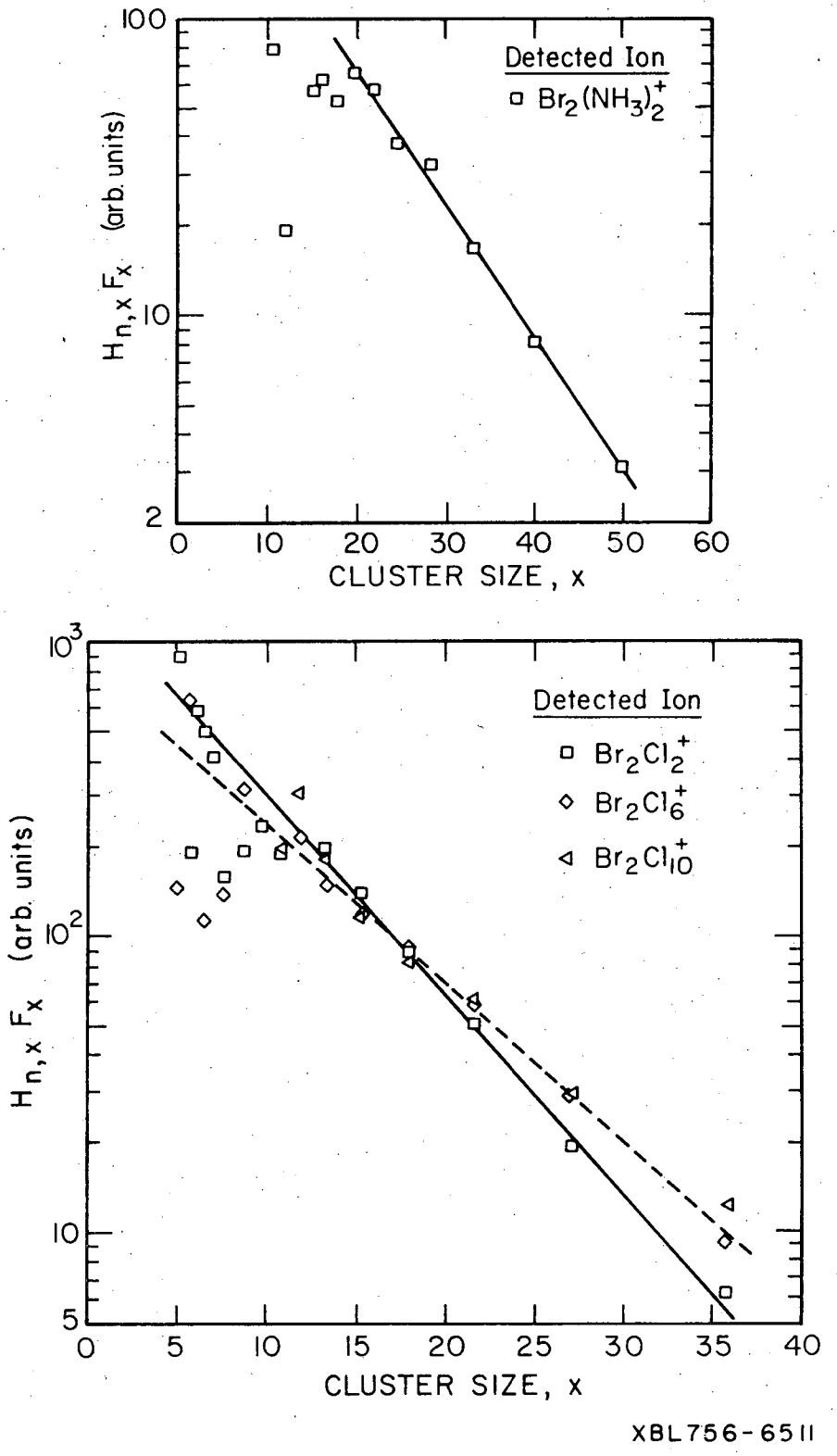
100
10
2
$H_{n,x}\,F_x$ (arb. units)
Detected Ion
$Br_2(NH_3)_2^+$
0
10
20
30
40
50
60
CLUSTER SIZE, x
10^3
10^2
10
5
$H_{n,x}\,F_x$ (arb. units)
Detected Ion
$Br_2Cl_2^+$
$Br_2Cl_6^+$
$Br_2Cl_{10}^+$
0
5
10
15
20
25
30
35
40
CLUSTER SIZE, x
XBL756-6511

Fig. IV-12.

Fig. IV-13. The measured angular distributions with the $1/\sin^2\theta_c$ Jacobian factor removed are shown for the $Br_2 + (Cl_2)_x$ data taken on several different runs. The top distribution is the $BrCl^+$ signal for a Cl_2 cluster nozzle operating at 450 Torr taken from the data on 8/12/74. The two following distributions show the $Br_2Cl_6^+$ data, both taken on the same run (8/12/74), but with the upper one having a 400 Torr Cl_2 nozzle stagnation pressure and the lower one having a 700 Torr Cl_2 nozzle stagnation pressure. The lower two distributions are taken at the same stagnation pressure of 700 Torr but with different nozzle geometries. The upper one has a channel length equal to the diameter of the oriface and the lower one has a channel length 1/5 the diameter of the oriface. The scales for each curve are independent of each other.

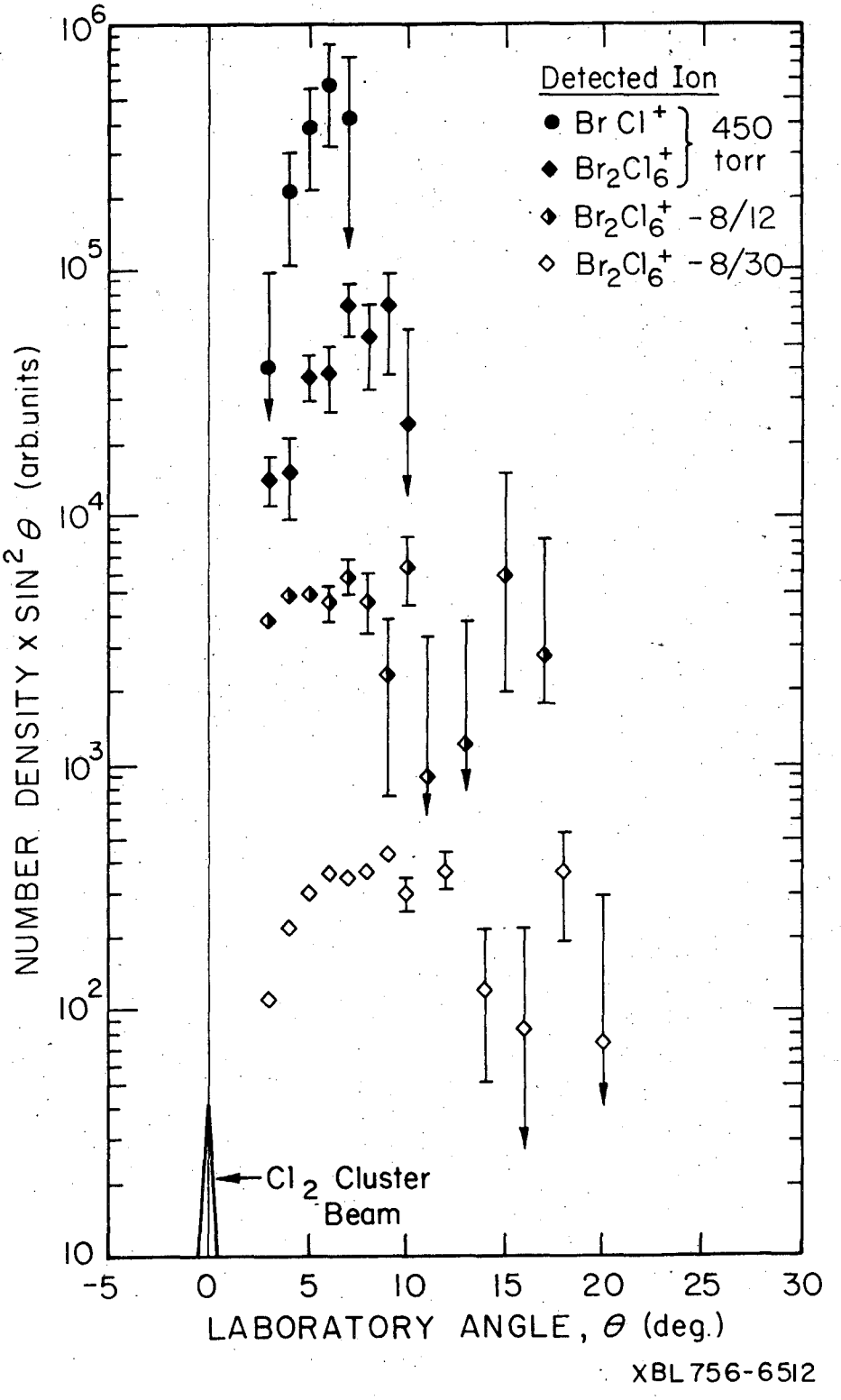
Detected Ion
Br Cl+
Br2Cl6+
450 torr
Br2Cl6+ - 8/12
Br2Cl6+ - 8/30
Cl2 Cluster Beam
NUMBER DENSITY x SIN2θ (arb.units)
LABORATORY ANGLE, θ (deg.)
XBL756-6512

Fig. IV-13.

first two angular distributions for $Br_2Cl_6^+$ are taken with the same nozzle oriface geometry but at two different pressures, 450 torr and 700 torr of Cl_2, respectively. The result, as expected, shows a lower relative concentration of the higher cluster species for the lower pressure than for the higher pressure as indicated by the location of the peak in each distribution. Slightly more interesting is the effect of the nozzle geometry on the relative concentration of the clusters. The lower two angular distributions for the $Br_2Cl_6^+$ ion shown in Fig. IV-13 show this effect. The $(Cl_2)_x$ clusters for the first distributions were formed through an oriface with a .0127 cm diameter and a channel length of .0127. The $(Cl_2)_x$ clusters for the second distribution were formed through an orifice with a .0127 cm diameter and a channel length of .0025 cm. Both distributions were taken with a Cl_2 stagnation pressure of 700 torr. The two distributions indicate that the nozzle with the longer channel forms a higher relative concentration of larger clusters. If one assumes that the nozzle oriface with a channel length equal to its diameter starts to approximate a Laval nozzle and that the oriface with the channel length less than the diameter is a sonic nozzle then the findings here are in agreement with those of Hagena and Obert[6] for cluster formation in Ar and CO_2. They find that to produce a given cluster size the sonic nozzle must be operated at a higher pressure than the Laval nozzle. This is also true for these experiments. Also shown in the top angular distribution of Fig. IV-13 is the angular distribution for the $BrCl^+$ ion taken with a Cl_2 stagnation pressure of 450 Torr.

It is presented here to show that there is no apparent change in the shape of the distribution which might be expected if the $BrCl^+$ signal was coming from a different reaction at lower pressures such as a product from the $Br_2 + Cl_4$ reaction. Along with the data shown in Fig. IV-1, an attempt was made to measure a $BrCl^+$ signal in the vicinity of the Br_2 beam on 8/12/74 by counting for 300 seconds at an angle 4° from the Br_2 beam. After 300 seconds no statistically meaningful signal was observed. This along with the data shown Fig. IV-1 indicate that no $BrCl^+$ signal could be observed near the Br_2 beam.

Further information on this newly observed condensation phenomenon was obtained by comparing the measured time-of-flight distributions with calculated distributions. The data was first compared to convoluted centroid velocity distributions. The number density centroid distributions for the clusters were calculated by extending previously used methods.[29,30] Two beams of particles of masses M_A and XM_B, where XM_B is the mass of a cluster of size X, are assumed to cross at an angle γ' (=90° for these experiments) defining a volume of intersection, τ. The relative velocity, $\bar{g}$, relative collision energy, E, and the center-of-mass velocity for a particular cluster size x, $\bar{C}_x$, can be defined in terms of the velocities of the particles in beams A and B_x, $\bar{v}_A$ and $\bar{v}_{B_x}$, by:

$$\bar{g} = \bar{v}_{B_x} - \bar{v}_A \tag{23a}$$

$$M\bar{C}_x = xM_B \bar{v}_{B_x} + M_A \bar{v}_A \tag{23b}$$

$$E = \frac{\mu g^2}{2} \tag{23c}$$

where the mass factors M and μ are given by

$$M = xM_B + M_A \tag{24a}$$

and

$$\mu = xM_BM_A/M \quad . \tag{24b}$$

The velocities used here are illustrated in the velocity vector diagram in Fig. IV-5. The number of reactive events per second, N, can be expressed in terms of the number densities at the collision zone, n_A and n_{B_x}, as

$$N = n_A n_{B_x} \tau Q_c(AB_x) \int_o^\infty \int_o^\infty \bar{g}\, \rho_A(v_A)\rho_{B_x}(v_{B_x})\, dv_A\, dv_{B_x} \tag{25}$$

where ρ_A and ρ_{B_x} are the number density probability density speed distribution functions for beams A and B_x. This may also be written as

$$N = \int_o^{\gamma'}\int_o^\infty P_x(\theta,C_x)\, dC_x\, d\theta \tag{26}$$

where $P_x(\theta,C_x)\, dC_x d\theta$ is the number of reactive collisions per second with a center-of-mass speed for a given cluster size x between C_x and $C_x + dC_x$ and direction between θ and θ + dθ. Equating Eqs. (25) and (26), $P_x(\theta,C_x)$ is written as

$$P_x(\theta,C_x) = n_A n_{B_x} \tau Q_c(AB_x)\, \bar{g}\rho_A(v_A)\rho_{B_x}(v_{B_x})M^2C_x/xM_AM_B\, \sin\gamma' \tag{27}$$

This equation is useful for a flux detector but the electron bombardment ionizer is a number density detector so that the corresponding centroid distribution for a given cluster size becomes

$$J_x(\theta,C_x) = \frac{\delta P_x(\theta,C_x)}{C_x} \tag{28}$$

where δ is a constant characterizing the detector sensitivity. Since the measured data collected at a particular angle is a sum from different size clusters, the appropriate centroid distribution is

$$J(\theta,C) = \sum_{x=1}^{\infty} J_x(\theta,C_x) \quad . \tag{29}$$

Assuming that the beams intersect at 90°, letting $K = n_A n_{B_x} \tau\delta$, and using the following relations for g, v_A, and v_{B_x} as a function of θ and C_x as given in Ref. 29:

$$v_A = MC_x \sin\theta / M_A \tag{30a}$$

$$v_{B_x} = MC_x \sin(90-\theta) / xM_B \tag{30b}$$

$$\bar{g} = MC_x/m \tag{30c}$$

where

$$m^2 = \left[\frac{\sin^2(90-\theta)}{M_A^2} + \frac{\sin^2\theta}{(xM_B)^2} \right]^{-1} \tag{30d}$$

the final centroid distribution can be expressed as

$$J(\theta,C) = \sum_{x=1}^{\infty} KQ_C(AB_x)\rho_A(\theta,C_x)\rho_{B_x}(\theta,C_x)\, M^3 C_x / mxM_A M_B \quad . \tag{31}$$

The number density probability density speed distributions ρ_A and ρ_{B_x} used in Eq. (31) are the nozzle number density distribution

$$\rho(v) = kv^2 \alpha_S^{-3} \exp[-(v-v_S)^2/\alpha_S^2] \tag{32}$$

with v expressed as a function of θ and C_x. The expressions used for ρ_A and ρ_{B_x} become

$$\rho_A(\theta,C_x) = k\alpha_{SA}^{-3} \frac{M^2C_x^2 \sin^2\theta}{M_A^2} \exp\left[-\left(\frac{MC_x \sin(\theta)}{M_A} - V_{SA}\right)^2 /\alpha_{SA}^2\right] \tag{33a}$$

and

$$\rho_{B_x}(\theta,C_x) = k\alpha_{SB}^{-3} \frac{M^2C_x^2 \sin^2(90-\theta)}{x^2M_B^2} \exp\left[-\left(\frac{MC_x \sin(90-\theta)}{xM_B} - v_{SB}\right)^2 /\alpha_{SB}^2\right] \tag{33b}$$

where α_{SA}, v_{SA} and α_{SB}, v_{SB} are the width parameters and flow velocities respectively for each beam as described in the experimental section of this chapter and k is a constant.

The centroid velocity distributions needed to compare to the measured data were calculated using Eqs. (31) and (33a,b). A computer program, CLUSTER, was written that calculates $J(\theta,C)$ at a given angle by first summing over a set of C_x velocities for a given angle and then summing over the cluster sizes x for each C_x up to a value of x that is sufficiently larger than the cluster size that is dominant at the smallest LAB angle to be calculated. The calculated centroid velocity distribution is then convoluted with the time-of-flight wheel and ionizer parameters to obtain a time-of-flight distribution. This

distribution is then compared with the measured data. The time-of-flight distributions to be presented are the actual measured LAB data with the ion transit time through the mass filter subtracted out. The ion transit time through the mass filter is simply calculated for the particular ion mass traveling the length of the quadrupole at an energy defined by the nominal ion energy for the ionizer.

The time-of-flight spectra for the $Br_2 + (Cl_2)_x$ and the $Br_2 + (NH_3)_x$ systems are shown in Figs. IV-14, IV-15, and IV-16A,B. Each figure shows the time-of-flight distribution that was measured for different ions during one run. The beam conditions and velocity distribution parameters for each run are listed in Table IV-1. Figure IV-14 shows the $Br_2 + (Cl_2)_x$ data collected on 8/12, Fig. IV-15 shows the $Br_2 + (Cl_2)_x$ data collected on 8/30, and Fig. IV-16A,B shows the $Br_2 + (NH_3)_x$ data collected on 8/31. The solid lines on all the figures are the calculated centroid time-of-flight distributions. For these calculations the cross section for condensation, $Q_c(AB_x)$, and the relative fluxes, F_x, were assumed to be equal for all cluster sizes and the constant K was set equal to unity. The equal cross section equal flux approximation should be reasonable for this calculation since the only interest is to fit the velocity (time-of-flight) distribution at a given angle. Since only a small range of cluster sizes (≤ 4) contribute to the major fraction of the intensity at a given angle, the variation of the cross section over this range is probably small. However, a comparison of intensities at different angles using this approximation is liable to be inaccurate especially

Fig. IV-14. The measured time-of-flight spectra for two different laboratory angles and several different detected ions are shown for the $Br_2 + (Cl_2)_x$ data collected on 8/12/74. The error bars represent one standard deviation based on the statistical deviation for the total number of counts at each time. The solid curves are the calculated time-of-flight distributions for the centroids at the particular angle. Two measured distributions are also shown for $BrCl^+$ and $Br_2Cl_6^+$ signals for data taken with the Cl_2 stagnation pressure at 450 Torr.

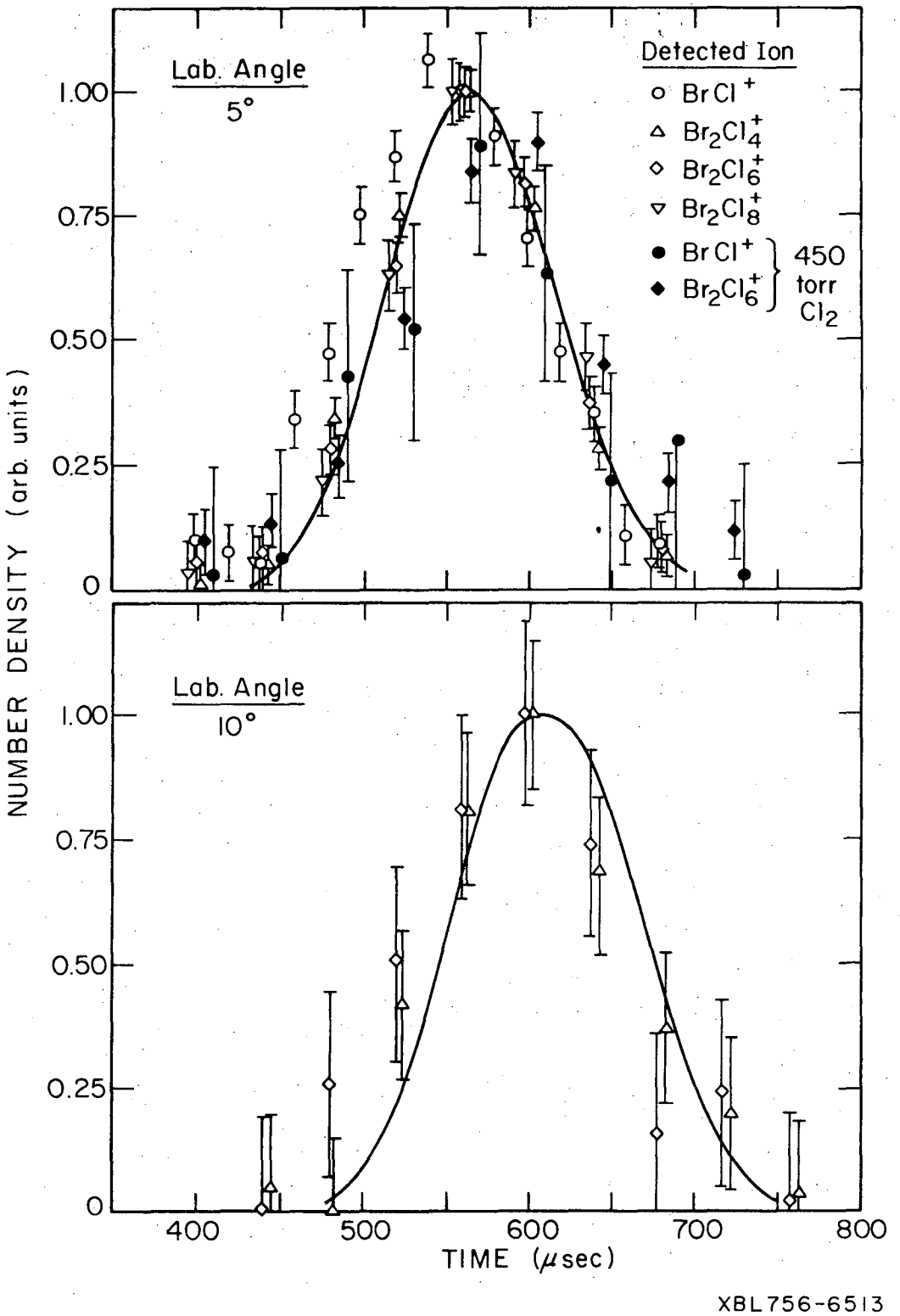
Lab. Angle
5°
Detected Ion
BrCl+
Br2Cl4+
Br2Cl6+
Br2Cl8+
BrCl+
Br2Cl6+
450 torr Cl2
Lab. Angle
10°
NUMBER DENSITY (arb. units)
TIME (μsec)
1.00
0.75
0.50
0.25
0
400
500
600
700
800
XBL756-6513

Fig. IV-14.

Fig. IV-15. The measured time-of-flight spectra for two different laboratory angles and two different detected ions are shown for the $Br_2 + (Cl_2)_x$ data collected on 8/30/74. The error bars represent one standard deviation based on the statistical deviation for the total number of counts at each time. The solid curves are the calculated time-of-flight distributions for the centroids at the particular angle.

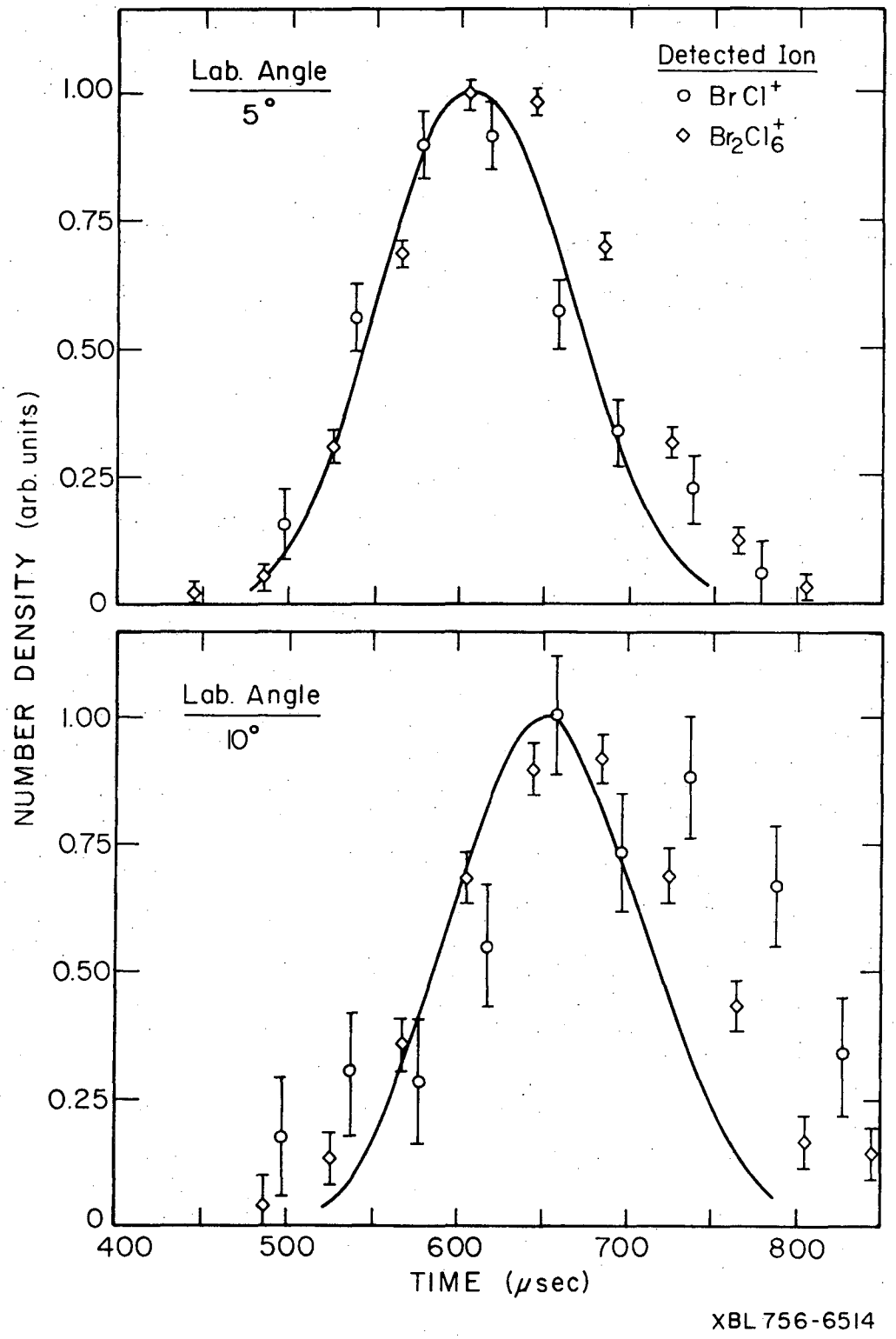
Lab. Angle
5°
Detected Ion
○ BrCl+
◇ Br2Cl6+
1.00
0.75
0.50
0.25
0
Lab. Angle
10°
1.00
0.75
0.50
0.25
0
NUMBER DENSITY (arb. units)
400
500
600
700
800
TIME (μsec)
XBL 756-6514

Fig. IV-15.

Fig. IV-16. A&B. The measured time-of-flight spectra for three different laboratory angles and several different detected ions are shown for the $Br_2 + (NH_3)_x$ data collected on 8/31/74. The error bars represent one standard deviation based on the statistical deviation for the total number of counts at each time. The solid curve are the calculated time-of-flight distributions for the centroids at the particular angle.

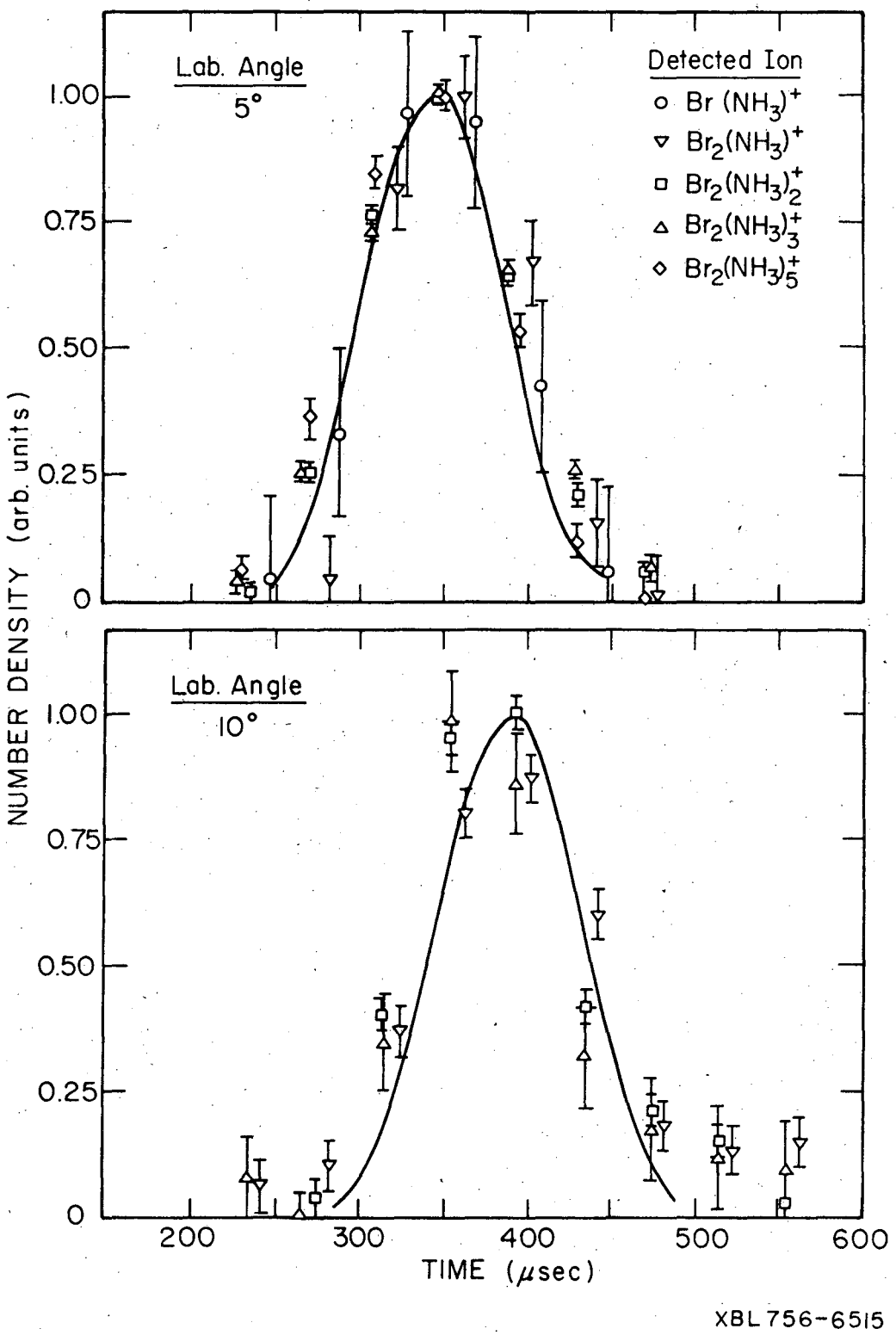
Lab. Angle
5°
Detected Ion
Br $(NH_3)^+$
$Br_2(NH_3)^+$
$Br_2(NH_3)_2^+$
$Br_2(NH_3)_3^+$
$Br_2(NH_3)_5^+$
Lab. Angle
10°
NUMBER DENSITY (arb. units)
1.00
0.75
0.50
0.25
0
200
300
400
500
600
TIME (μsec)
XBL 756-6515

Fig. IV-16 A

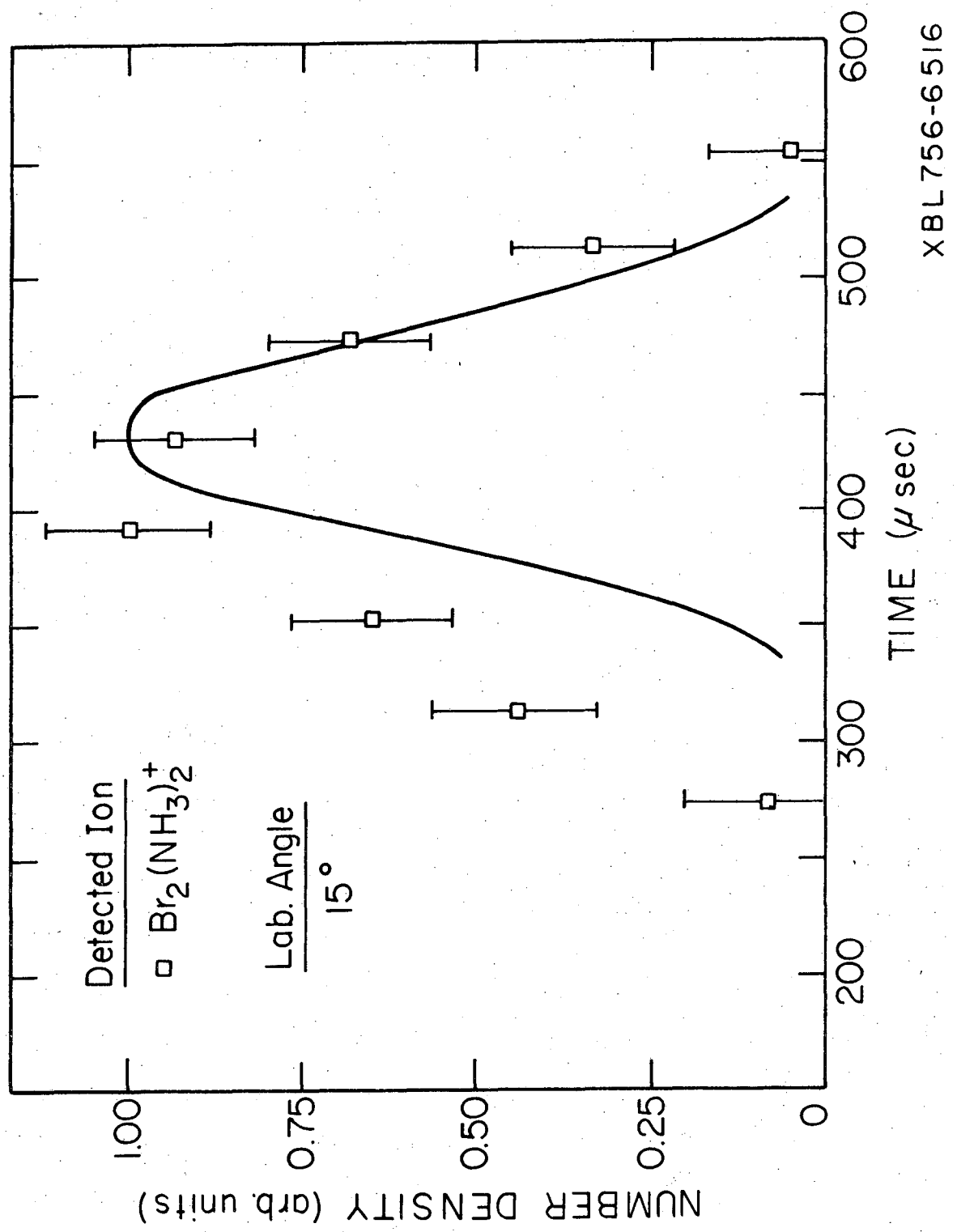
NUMBER DENSITY (arb. units)
1.00
0.75
0.50
0.25
0
200
300
400
500
600
TIME (μ sec)
Detected Ion
□ $Br_2(NH_3)_2^+$
Lab. Angle
15°
XBL756-6516

Fig. IV-16 B

at larger θ values where the centroid cluster size is smaller.

The first apparent observation after looking at all of the distributions is that the peak of the calculated distribution coincides with the peaks of the measured distributions to within 10 μsec. This is a very pleasing result since it is further evidence that condensation of a molecule on a cluster is being observed. On further examination of the data for $Br_2 + (Cl_2)_x$ in Figs. IV-14 and IV-15, there appears to be broadening of the measured speed distributions with respect to the calculated centroid distributions as the laboratory scattering angle increases. This can most likely be attributed to a small fraction of the excited complex, AB_x^*, decomposing before it reaches the detector. There appears to be an apparent discrepancy between the distribution for $Br_2 + (Cl_2)_x$ shown in Figs. IV-14 and IV-15. For example, at a LAB angle of 10° the measured data in Fig. IV-14 appears at shorter times than the centroid calculation and in Fig. IV-15 the measured data appears at longer times than the centroid calculation. The $Br_2 + (Cl_2)_x$ data shown in each figure was taken on different runs using two different nozzle oriface geometries. As discussed previously, the different nozzle geometries determine the relative concentrations of different clusters, with a long channel oriface producing more larger clusters than a short channel oriface. This effect can now be seen in the time-of-flight spectra. The data presented in Fig. IV-14 corresponds to the data collected using the longer channel and having a higher relative concentration of larger clusters. Referring to the Newton diagram for $Br_2 + (Cl_2)_x$ shown in Fig. IV-17, a fragmentation

of the cluster with a resulting small recoil velocity would lead to faster products appearing at 10° which is exactly what is seen in Fig. IV-14. With the distribution of cluster sizes moving toward smaller clusters as is the case for the data presented in Fig. IV-15, then the wider angle centroids will have a larger number of complexes and upon fragmentation will contribute to smaller angles. This will appear as particles with a slower laboratory velocity at a given angle which consequently appears at longer times in the time-of-flight distributions. This is observed at angles of 5 and 10 degrees for the 8/30/74 $Br_2 + (Cl_2)_x$ data shown in Fig. IV-15. So there is further evidence that nozzle geometry does play an important rule in determing the relative concentrations of the different size clusters in the beam. The same trend in the data can also be seen in Fig. IV-16A,B for the $Br_2 + (NH_3)_x$ system. In this system the deviation of the measured distribution from the calculated one becomes quite apparent at θ=15° where the measured data is approximately 100 μsec wider at FWHM.

Ultimately one would like to be able to predict the approximate lifetime of the cluster complex, AB_x^*, for different cluster sizes by determining whether the complex lives long enough to reach the detector. Also information on the channel or channels by which the complex decomposes would be interesting. Unfortunately, this would require the knowledge of many more variables than are known at the present time. The relative cluster concentrations in the beam, the relative condensation cross sections for all the different size clusters, and

the cracking patterns for the complex must be known in order to do a detailed calculation. What can be gleaned from the present data, though, is a qualitative picture of the possible reaction channels. The velocity vector diagrams with superimposed calculated centroid velocity distributions for different centroid angles are shown for the two different reactions in Fig. IV-17. A regular plot of the calculated centroid velocity distributions are shown in Fig. IV-18. It should be noted here that a large fraction of the breadth in the time-of-flight distributions comes from the time-of-flight gate functions and not the width of the velocity distributions. Looking at the velocity vector diagrams, it is apparent that interpretation of the velocity distribution at a given angle will be increasingly more difficult when the velocity of the recoiling particle increases because there will be more "cross-talk" between clusters of a larger range in size. Qualitatively one would expect to see more slow velocity praticles at smaller angles and more higher velocity particles at larger angles, if particles are allowed to recoil out of the cluster. This is observed for all of the measured velocity distributions except for 10° on the 8/30 Br_2 + $(Cl_2)_x$ run. To obtain a crude estimate of the upper limit for the recoil velocity from the cluster, a computer program that transforms an assumed center-of-mass distribution into a laboratory distribution[31,32] was used to calculate velocity distributions at laboratory angles for which there was data. The resulting velocity distribution was then convoluted over the time-of-flight wheel and ionizer gate functions to give a time-of-flight spectra.

Fig. IV-17. The Newton diagrams for the $Br_2 + (Cl_2)_x$ and the $Br_2 + (NH_3)_x$ reactions with the velocity vectors indicating the actual most probable beam velocity used in the experiments. The C values on each angle denote the cluster size that contributes most at the particular centroid angle. The velocity distributions superimposed on each angle are the centroid velocity distributions that were convoluted over the detector gate function to give the time-of-flight spectra shown in Fig. IV-15 and IV-16.

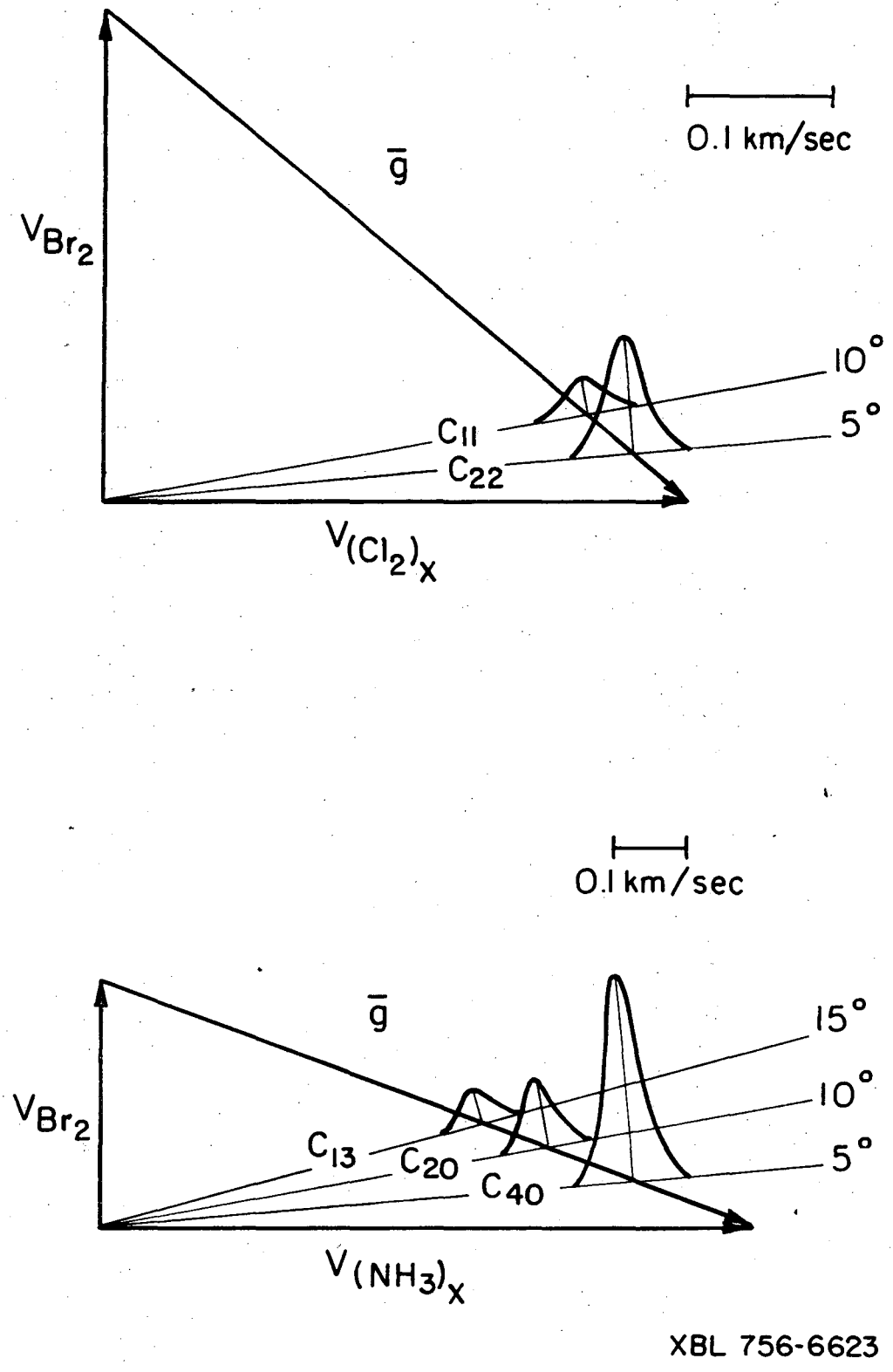
0.1 km/sec
$\bar{g}$
V_{Br_2}
10°
5°
C_{11}
C_{22}
$V_{(Cl_2)_x}$
0.1 km/sec
$\bar{g}$
15°
10°
5°
V_{Br_2}
C_{13}
C_{20}
C_{40}
$V_{(NH_3)_x}$
XBL 756-6623

Fig. IV-17.

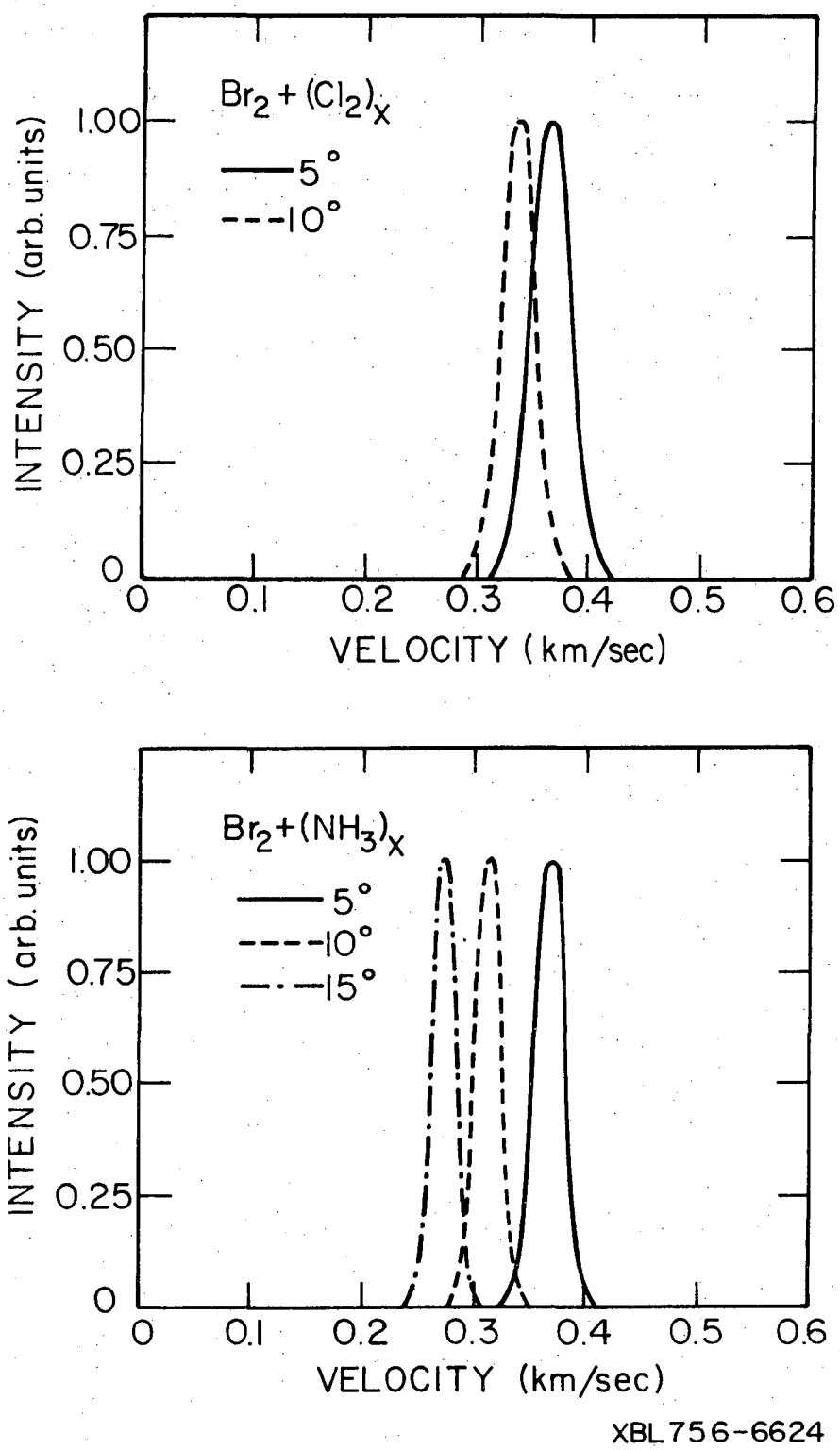

Fig. IV-18. The calculated centroid velocity distributions that were convoluted over the detector gate function to produce the time-of-flight spectra shown in Fig. IV-15 and IV-16 are shown.

The center-of-mass distribution used in the calculations was isotropic, with the recoil velocity represented by a Maxwell-Boltzman distribution whose peak velocity could be varied. Several distributions were calculated for different recoil velocities from the most probable cluster corresponding to centroid angles of 5, 10, and 15 degrees for the $Br_2 + (NH_3)_x$ system. Again, the cross sections were assumed to be equal for all cluster sizes and the relative cluster concentrations were assumed to be equal. A recoil velocity of 1×10^4 cm/sec is the upper limit where the calculated distribution will be wider than the measured one. This velocity corresponds to a relative recoil energy of approximately 0.5 kcal/mole for a small product (i.e. $Br_2(NH_3)_x$; where x = 1,2,3,4) up to 1.0 kcal/mole if the heaviest cluster splits evenly. This energy is less than 7% of the relative collision energy of the particles which is 14.2 kcal/mole for a cluster of x=40 and 10.2 kcal/mole for a cluster with x=13. It should be mentioned again that these numbers come from a very crude calculation that includes only three cluster sizes and does not take into account, the condensation cross section, relative intensities of different cluster sizes, cracking patterns, or the dependence of the complex lifetime on the cluster size.

The data collected so far on the two systems studied has definitely shown that a new phenomena of condensation on a cluster to form a complex which has a long lifetime or fragments into particles with very small recoil velocity has been seen. From the angular distributions the largest concentration of cluster sizes for $(Cl_2)_x$ is 11 to 14 and for

$(NH_3)_x$ is 20 to 22. It also appears that the cluster is able to absorb up to 14 kcal/mole of energy in its internal modes for clusters where x=40.

D. Discussion

Like most unexpected observations, these experiments with clusters have asked more questions than they have answered. The main conclusions from the experiments performed so far are that condensation of molecules on clusters to form a long lived complex ($\tau \geq 10^{-4}$ sec, assuming the complex lives to the detector) can definitely be seen in crossed molecular beam experiments and severe cracking of the cluster complexes has also been seen in the mass spectrometer. These are the two definite conclusions from the presently collected data. From the broader width of the measured velocity distributions, it appears that a small fraction of the complexes are decomposing before reaching the detector. This can either be a small part of the cluster "boiling off" or the splitting of the cluster into two equal size fragments. A lack of knowledge of the cluster cracking patterns and the relative concentration of the incident clusters as described in the previous section does not permit the two decomposition channels to be distinguished.

The questions that arise from these experiments are many. First, to extract much more information from experiments of this type the cracking patterns of these clusters must be determined or an ionizer must be developed that will predominately give the parent ion. How to accomplish this is one of the more difficult experimental problems. The second question that arises is how to determine the relative concentrations of clusters in the beam. This again is a difficult problem and could itself be an entire study of nucleation processes in the nozzle expansion. If these two problems can be solved or

circumvented more interesting questions about the complexes themselves can be studied. Determination of properties such as the condensation cross section dependence and the decomposition channel of the complex on cluster size would be very interesting. The mode of decomposition of the cluster complex could be determined by a standard molecular beam analysis if it were possible to prepare a beam of clusters that contained only one size cluster or a very small range in cluster sizes. It does not seen unreasonable that it may be possible to form a source of this type which utilizes the phenomena already observed. If two nozzles can be mounted at 90 degrees to one another behind one skimmer in such a way that intersection of the axis of the skimmer and the axis of the primary nozzle can be set at various angles, it should be possible to "skim off" a small range of cluster sizes. These can then pass through to the collision chamber where they are crossed with the other beam. Forming cluster substrates with another type of molecule on the surface may also be prepared by this technique. Experiments of this type may give qualitative insight into the structure of different size clusters. The structure of large clusters of Ar, Co_2, and H_2O where x is greater than 500 has been found to be crystalline as observed by electron diffraction of clusters in a nozzle expansion.[17,18] Due to a lack of sensitivity this technique has not yet been able to measure an electron diffraction pattern of smaller clusters where the structure becomes non-crystalline. It seems that much work is to be done before there will be a thorough understanding of nucleation of neutral clusters of sizes between 5 and 100. Experiments

of ion nucleation seem to be more promising at the present time since the severe problem of cracking patterns is not present with ions as it is with neutrals. Some interesting experiments on the condensation of water on hydrated protons have been done by Searcy and Fenn.[33] Use of a heavy ion rather than a heavy neutral, such as Br_2 used in these experiments, may prove to be a better way of probing the clusters formed in the nozzle expansion since this would again eliminate the problem of the ionizer cracking patterns.

These interesting effects observed in these experiments along with the many possible future experiments on cluster properties have not dealt with the discordant results for the $Br_2 + (Cl_2)_2$ and $Br_2 + (Cl_2)_x$ systems obtained by the Harvard and present groups. The reaction of $Br_2 + Cl_4$ observed by King, Dixon, and Herschbach[26] shows very pronounced forward and backward scattering symmetric about 90° in the center-of-mass system, whereas, the observations of these experiments indicated no BrCl product was forward or backward scattered but only a condensation complex of Br_2 on $(Cl_2)_x$ was formed. Our experiments were performed at Cl_2 nozzle stagnation pressures down to 400 Torr and at a temperature of 298°K as shown in Fig. IV-13. At a Cl_2 stagnation pressure of 450 Torr, only a decrease in the count rate was observed for the velocity distributions but no apparent change in the shape of the distribution was observed as shown in Fig. IV-14 that would indicate that anything besides a complex was being observed. The angular distributions taken at a Cl_2 a nozzle stagnation pressure of 400 Torr as shown in Fig. IV-13 also do not appear to change shape

on varying the pressure. In addition to the data shown in Fig. IV-1, $BrCl^+$ signal was also looked for in the vicinity of the Br_2 beam with the Cl_2 pressure of 400 Torr and even after counting for 300 seconds of an angle 4 degrees from the Br_2 beam no statistically meaningful signal was observed. The only phenomena observed in the data collected in these experiments has been that of condensation. There was no indication that the $Br_2 + Cl_4$ reaction was being observed. The Harvard group was also unable to reproduce our results. This apparent experimental disagreement may still be arising from very subtle effects in the operating characteristics of the nozzle sources which appear to be very sensitive to the temperature, pressure, and geometry parameters.[34]

The observation of this condensation on clusters in crossed molecular beams is peculiar to experiments using supersonic nozzles for sources. We have also observed this condensation phenomenon in reactions of alkaline-earth halides with chlorine. In particular, the reaction

$$BaI_2 + Cl_2 \rightarrow BaICl + ICl$$

had a sharp peak near the chlorine beam superimposed on the angular distribution for the reaction. This again can be attributed to condensation on the clusters. So care must be taken in interpreting data from experiment performed using supersonic nozzle sources.

In conclusion there seems to be many interesting experiments to be performed both for the simpler Van der Waals molecule and also the larger clusters. One important experiment that should be reexamined

is the effect of nozzle conditions on the formation of clusters in the beam so the apparent discrepancy between dimer reactions and the Br_2 condensation on the Cl_2 clusters can be resolved since both of these phenomena can lead to many more exciting experiments.

Table IV-1. Beam Conditions for Different Cluster Experiments.

Run (Date)	Source[1] Chamber	Molecule	Temperature[3] (°K)	Pressure (Torr)	Flow Velocity (V_f) α_1 (m/sec)	Width Parameter α_1 (m/sec)	Beam Width (FWHM)
3/26/74	1	$(Cl_2)_x$	298.	780.	n.m.[2]	n.m.	1.1°
3/26/74	2	Br_2	298.	250.	n.m.	n.m.	1.5°
8/12/74	1	$(Cl_2)_x$	298.	700.	440.	29.5	1.1°
8/12/74	2	Br_2	323.	260.	331.	49.4	1.5°
8/14/74	1	$(Cl_2)_x$	298.	710.	440.	29.5	1.1°
8/14/74	2	Br_2	318.	260.	331.	49.4	1.5°
8/30/74	1	Br_2	323	260.	336.	36.6	1.1°
8/30/74	2	$(Cl_2)_x$	298.	700.	400.	29.5	1.5°
8/31/74	1	Br_2	323.	260.	336.	36.6	1.1°
8/31/74	2	$(Cl_2)_x$	298.	700.	900.	72.8	1.5°

1. Source chamber 1 is the modulated beam.
2. Not measured.
3. Thermocouple readings

Table IV-2. $R_{n',n}$ Factors† for $Br_2 + (Cl_2)_x$††

	$R_{n',n}$		
n',n θ_c	5°	7°	10°
2, 2	1.0	1.0	1.0
2, 3	.67	.69	.78
4, 2	.21	.20	-
5, 2	.23	.31	.33

†$R_{n',n} = S_{n'}(\theta_c)/S_n(\theta_c)$; see Eq. (22)

††The detector resolution is the same for the different ions Table IV-3 $R_{n',n}$ Factors† for $Br_2 + (NH_3)_x$††

	$R_{n',n}$			
n',n θ_c	5°	7°	9°	11°
1, 1*	1.0	1.0	1.0	1.0
2, 1	.78	1.52	1.59	1.11
3, 1	.47	.55	.59	.70
5, 1	.36	.40	.037	.035

†$R_{n',n} = S_{n'}(\theta_c)/S_n(\theta_c)$; see Eq. (22)

*n=1 is for $BrNH_3$

††The detector resolution is the same for different ions.

Chapter IV References

1. R. E. Lecken, E. J. Robbins, and P. A. Trevalion, Proc. R. Soc. A280, 409 (1964).
2. T. A. Milne and F. T. Greene, J. Chem. Phys. 47, 4095 (1967).
3. T. A. Milne, A. E. Vandegrift, and F. T. Greene, J. Chem. Phys. 52, 1552 (1970).
4. D. Golomb, R. E. Good, R. F. Brown, J. Chem. Phys. 52, 1545 (1970).
5. D. Golomb, R. E. Good, A. B. Bailey, M. R. Busby, and R. Dawbarn, J. Chem. Phys. 57, 3844 (1972).
6. O. F. Hagena and W. Obert, J. Chem. Phys. 56, 1793 (1972).

7a. J. M. Parson, K. Shobatake, Y. T. Lee, and S. A. Rice, J. Chem. Phys. 59, 1402 (1973).

b. K. Shobatake, J. M. Parson, Y. T. Lee, and S. A. Rice, J. Chem. Phys. 59, 1416 (1973).

c. K. Shobatake, J. M. Parson, Y. T. Lee, and S. A. Rice, J. Chem. Phys. 59, 1427 (1973).

d. K. Shobatake, Y.T. Lee, and S. A. Rice, J. chem. Phys. 59, 1435 (1973).

8. S. E. Novick, P. B. Davies, T. R. Dyke, and W. Klemperer, J. Am. Chem. Soc. 95, 8547 (1973).
9. T. R. Dyke, G. R. Tomasevich, W. Klemperer, and W. E. Falconer, J. Chem. Phys. 57, 2277 (1972).

10a. S. E. Novick, P. Davies, S. J. Harris, and W. Klemperer, J. Chem. Phys. 59, 2273 (1973).

b. S. J. Harris, S. E. Novick, and W. Klemperer, J. Chem. Phys. 60, 3208 (1974).

c. S. J. Harris, S. E. Novick, and W. Klemperer, J. Chem. Phys. 61, 193 (1974).

11. S. J. Harris, S. E. Novick, J. S. Winn, W. Klemperer, J. Chem. Phys. 61, 3866 (1974).

12. H. Falter, O. F. Hagena, W. Henkes, and H. V. Wedel, Int. J. Mass Spectrom. Ion Phys. 4, 145 (1970).

13. R. Klingelhöfer and H. O. Moser, J. Appl. Phys. 43, 4575 (1972).

14. J. Gspann and K. Körting, J. Chem. Phys. 59, 5726 (1973).

15. A. Van Deursen and J. Reuss, Int. J. Mass Spectrom. Ion Phys. 11, 483 (1973).

16. W. Henkes and F. Mikosch, Int. J. Mass Spectrom. Ion Phys. 13, 151 (1974).

17. G. D. Stein and J. A. Armstrong, J. Chem. Phys. 58, 1999 (1973).

18. J. Farges, B. Raoult, G. Torchet, J. Chem. Phys. 59, 3454 (1973).

19. R. J. Gordon, Y. T. Lee, and D. R. Herschbach, J. Chem. Phys. 54, 2393 (1971).

20. D. R. Hardin and R. Grice, Mol. Phys. 26, 1321 (1973).

21. J. C. Whitehead, D. R. Hardin, and R. Grice, Chem. Phys. Lett. 13, 319 (1972).

22. J. C. Whitehead, D. R. Hardin, and R. Grice, Mol. Phys. 25, 515 (1973).

23. P. B. Foreman, G. M. Kendall, R. Grice, Mol. Phys. 23, 117 (1972).

24. D. R. Hardin, K. B. Woodall, and R. Grice, Mol. Phys. 26, 1057 (1973).

25. J. C. Whitehead and R. Grice, Chem. Soc. Faraday Disc. 55, 320 (1973).

26. D. L. King, D. A. Dixon, and D. R. Herschbach, J. Am. Chem. Soc. 96, 3328 (1974).

27. A. G. Ureña, R. B. Bernstein, and G. R. Phillips, J. Chem. Phys. 62, 1818 (1975).

28. F. W. Lampe, J. L. Franklin, and F. H. Field, J. Am. Chem. Soc. 79, 6129 (1957).

29. S. Datz, D. R. Herschbach, and E. H. Taylor, J. Chem. Phys. 35, 1549 (1961).

30. C. A. Mims, S. M. Lin, R. R. Herm, J. Chem. Phys. 57, 3099 (1972).

31. E. A. Entemann, Ph.D. thesis, Harvard University, Cambridge, Massachusetts 1967.

32. C. A. Mims, Ph.D. thesis, University of California, Berkeley, Berkeley, California 1973.

33. J. G. Searcy and J. B. Fenn, J. Chem. Phys. 61, 5282 (1974).

34. D. R. Herschbach, Harvard University, private communication.

APPENDIX II-4.

Calibration of the Time-of-Flight Apparatus

This appendix explains a procedure for determining the delay time arising from the photodiode reference signal from the time-of-wheel turning on at a different time from the actual time that the beam turns on. The experimental arrangement is shown in Fig. II- looking from the time-of-flight wheel toward the detector for the wheel turning in both directions. PD represents the location of the photodiode and x=0 is defined by the line passing through the center of the detector hole and the center of the time-of-flight wheel. Letting F represent the width of the detector hole, H represent the width of the time-of-flight wheel slot, and x_{PD} the distance of the photodiode from x=0, then the distance x_{PD} can be determined by looking at the signals from a beam for the time-of-flight wheel turning in opposite directions. Once x_{PD} is determined the delay time can be calculated for any speed of the wheel. If T is the true turn on time of the beam of molecules defined as that point where the leading time-of-flight slit passes over the first detector slit and TA is the apparent turn on time of the reference signal presently defined as when the trailing edge of the time-of-flight slit passes over the photodiode causing it to send the reference signal to the computer, and V_w is the velocity of the wheel at the photodiode, then for case 1 where the wheel is turning in a clockwise direction.

$$TA1 = T + (\frac{F}{2} + H - x_{PD})/V_w$$

For case 2 with the wheel rotating in the CCW direction

$$TA2 = T + (-\frac{F}{2} - H - X_{PD})/(-V_w)$$

So by comparing a reference point on a measured time-of-flight distribution for the wheel turning in each direction and comparing the apparent times of the reference point one obtains

$$TA2 - TA1 = (-\frac{F}{2} - H - X_{PD})/(-V_w) - (\frac{F}{2} + H - X_{PD})/(V_w)$$

or

$$X_{PD} = \frac{V_w(TA2 - TA1)}{2}$$

where V_w is simply the circumference of the wheel at the photodiode divided by the period of rotation.

Since there may be an uncertainty in the triggering level of the discriminator from the photodiode pulse, care must be taken to set the level to obtain a pulse width that corresponds to the width of the slot on the wheel turning at its set frequency. The frequency is simply obtained from the period between pulses thus enabling the trigger level to be set to give the theoretical pulse width. However, only the ratio of the actual pulse width to the theoretical pulse width needs to be known.

Fig. II-37. The relation between the time-of-flight wheel with slot H, the detector entrance slit of width F and the location of the photodiode PD are shown for the wheel turning in the clockwise and counter-clockwise direction. The figure is viewed assuming the time-of-flight wheel is in front of the detector entrance.

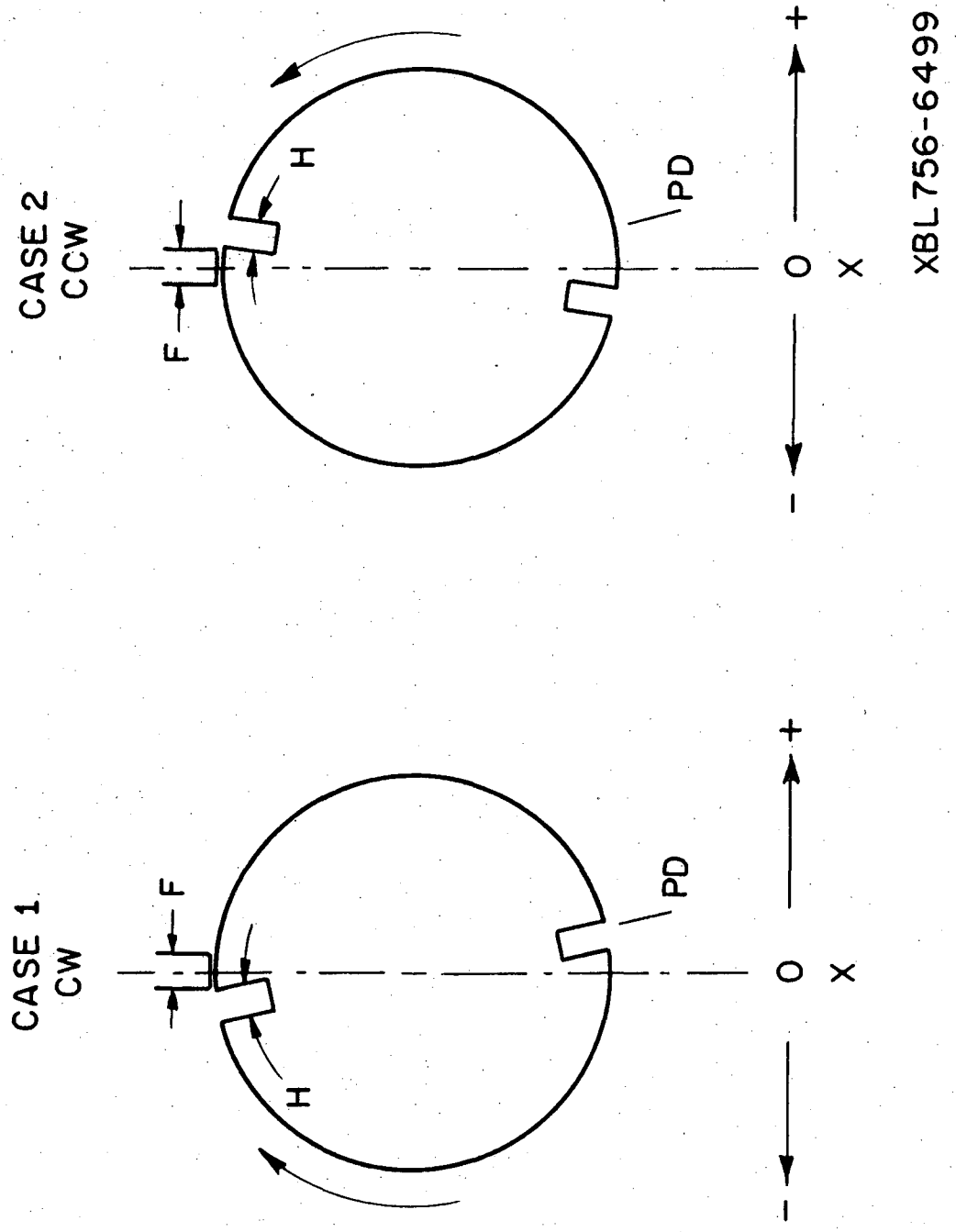

XBL756-6499

ACKNOWLEDGEMENTS

First, I would like to thank Professor Ronald Herm for his valuable insight, patience, and teaching abilities during my years as a graduate student. His sense of when to let a student make his own decisions has helped to build confidence in experimental abilities while his presence to answer many difficult questions concerning both experimental problems and chemistry in general was of utmost value.

The construction of this apparatus would not have been possible without the work of many skilled people at both LBL and the Berkeley Chemistry Department. The construction of virtually all the mechanical parts was done at the Chemistry Department machine shop by some highly competent craftsmen. The largest portion of the machining was done by Clay Taylor with much help from Frank Lopez, Ron Talbot, and Chuck Saunders. The beautiful welding on the apparatus was done by Bob Waite. After the apparatus was assembled and running, Carl Baugh and Slim Bohac facilitated those quick repairs and minor changes that are always needed during the course of running experiments. I would also like to thank everyone in the machine shop for those many early morning cups of coffee and many friendships which made the construction and assembly of this apparatus so pleasurable.

I would also like to thank Steve Smiriga and Tom Merrick for the early design work and the assembly of the interface for the computer for the time-of-flight analysis.

At IMRD, special thanks must go to Sandy Stewart who expedited ordering the multitude of parts and equipment for the apparatus and to Dan Curtis and Del Peterson who helped in constructing all of the electrical wiring while funds were running low. Thanks must also go to Alice Ramirez for typing and compiling this thesis and to Gloria Pelatowski for the beautiful work on the figures.

I would like to thank Y. T. Lee for his program to analyze the elastic scattering data.

Throughout a large portion of this work I have had the pleasure of working with two very competent fellow graduate students: Tim Parr and Andy Freedman. Both have been a great deal of help with the initial assembly of the apparatus and the running of the experiments. Tim Parr has been a wizard at handling the electronics for the apparatus and the computer.

Finally, I would like to thank my wife and my parents for words of encouragement when things were going poorly.

This work was done under the auspices of the U. S. Energy Research and Development Administration.

TECHNICAL INFORMATION DIVISION
LAWRENCE BERKELEY LABORATORY
UNIVERSITY OF CALIFORNIA
BERKELEY, CALIFORNIA 94720